UiT The Arctic University of Norway

Faculty of Science and Technology

Department of Geosciences

Neoproterozoic orogenesis in south-eastern South America

An examination of pre-orogenic rifting, sedimentation, and mountain building processes recorded in the orogenic foreland of the Dom Feliciano Belt

Jack James Percival

A dissertation for the degree of Philosophiae Doctor

December 2021

Neoproterozoic orogenesis in south-eastern South America

An examination of pre-orogenic rifting, sedimentation, and mountain building processes recorded in the Dom Feliciano Belt

Jack James Percival

A dissertation for the degree of Philosophiae Doctor

UiT The Artic University of Norway

Faculty of Science and Technology

Department of Geosciences

December 2021

Front page image: Folds in the Brusque Complex (Santa Catarina, Brazil) and the Rocha Group (Uruguay).

Acknowledgements

First and foremost, I would like to thank Jiří Konopásek for being an A-grade, world-class supervisor, a passionate and dedicated scientist, and an all-round good bloke. Without your guidance, support, and patience, I may not have made it through. Thank you for inspiring in me a passion for petrology and allowing me to travel the world to pursue my interest in tectonics. Thank you also to Fátima Bitencourt, for your infectious enthusiasm and for welcoming me into your network of brilliant and passionate proteges, you are both inspirational scientists.

I would like to thank the other co-authors of the papers included in this thesis: Jiří Sláma, Robert Anczkiewicz, and Morgan Ganerød for your tireless and masterful geochronological work; Ragnhild Eiesland, Roberto Sacks de Campos, Matheus Battisti, and Pedro Oyhantçabal for your great work in the field, invaluable geological discussions, and much more.

Many thanks as well to all the people who helped with sample preparation, data collection and fieldwork along the way. Thanks (and sorry) to Trine Dahl, Ingvild Hald, and Karina Monsen for making many countless thin sections and tolerating my many questions. Thanks to the fantastic people at the Polish Academy of Sciences in Krakow—Dariusz Sala and Marta Koziarska for all the training and help in the lab, and Akeek Maitra for being a dependable friend during every visit. Thanks also to Radek Škoda and Renata Čopjaková for EMP analyses, and to Martin Whitehouse and Heejin Jeon for their support using the ion microprobe at NordSIM. Finally, thanks to all the amazing geologists in Brazil and Uruguay, without whose help this study would not have been possible—Roberto Sacks de Campos for being so generous with your time, both as a colleague and as a friend; Matheus Battisti and Diego Lira for putting up with me for so long in the field: Giuseppe de Toni for your enthusiasm, intelligent conversation, and for always sharing your chimarrão; and countless others—working with you reminds me why geology is worth studying in the first place.

I am so grateful for all the friendships I have made during my time in Tromsø. Thank you in particular to Louise, Ellery, Naima, Paul, Stephan and Marina for all the cabin trips, festivals, Friday beers, fieldwork, and good times. You are my dear friends, and I am so thankful that you were around through both the difficult and the fun moments. Many thanks also to the many others, too many to list, who made my time in Tromsø enjoyable. Thank you to my family and friends back in Australia, and my new family here in Norway, who helped get me through the final 'corona years' of the PhD. Finally, thank you Mathilde, for your beautiful smile, for all the joy you bring to my life, and for supporting me through everything; meeting you here in Tromsø has made it all worth it.

Preface

This thesis is the result of a four-year PhD project that started in April 2017. The project was funded by the department of Geosciences at the Arctic University of Norway (UiT), with additional funding from Diku Norway and CAPES Brazil (project UTF-2018-10004). The additional funding enabled four fieldtrips to Brazil and Uruguay, where I conducted fieldwork and collected samples for processing and analysis back at UiT and around Europe. Additional funding from the Norwegian Research School for Dynamics and Evolution of Earth and Planets (DEEP), University of Oslo (UiO), also funded three visits to the Institute of Geological Sciences, Polish Academy of Sciences, Kraków, where I spent a total of three months training at the Geochronology and Isotope Geochemistry Laboratory learning techniques in Lu–Hf and Sm–Nd garnet geochronology.

The educational requirements for the PhD program were met by the completion of four short courses run by the DEEP PhD school at UiO (and in collaboration with UiT), as well as a research ethics course and short course in P–T modelling at UiT. One year of the total four-year project was assigned to duty work, which included practical teaching of petrology, structural geology, and field geology courses. Part of this duty work also included maintenance of and responsibility for the rock cutting, crushing and mineral separation labs at the Department of Geosciences, UiT.

Over the course of the PhD, I presented results related to this work at the following international conferences/meetings: *European Geosciences Union (EGU) General Assembly* in Vienna, Austria, in 2019 and 2021 (online); *Thermal and mechanical evolution of collisional and accretionary orogens* in Třešť, Czech Republic. I also attended and presented work at yearly local meetings associated with DEEP and the Geoscience Research Academy of Tromsø (GReAT).

In this work I discuss the evolution of the South Atlantic Neoproterozoic Orogenic System by investigating the pre-orogenic and tectono-metamorphic history of the Dom Feliciano Belt foreland in southern Brazil and Uruguay. The thesis consists of an introduction, including a brief synthesis, and three papers.

The three research articles are as follows:

I. Percival, J. J., Konopásek, J., Eiesland, R., Sláma, J., Campos, R. S., Battisti, M. A., Bitencourt, M. F., 2021, **Pre-orogenic connection of the foreland domains of the Kaoko–Dom Feliciano–Gariep orogenic system**, *Precambrian Research*, vol. 354, pp. 106060, https://doi.org/10.1016/j.precamres.2020.106060

II. Percival, J. J., Konopásek, J., Anczkiewicz, R., Ganerød, M., Sláma, J., Campos, R. S., Battisti, M. A., Bitencourt, M. F., **Tectono-metamorphic evolution of the northern Dom Feliciano Belt foreland, Santa Catarina, Brazil: Implications for models of subduction-driven orogenesis**, in review at *Tectonics*

III. Percival, J. J., Konopásek, J., Oyhantçabal, P., Sláma, J., Anczkiewicz, R., **Diachronous two-stage Neoproterozoic evolution of the southern Dom Feliciano Belt, Uruguay**, in preparation for submission to *Journal of Metamorphic Geology* or *Tectonics*

Contents

SECTION I Synthesis

1 Introduction

Orogeny is a complex process controlled by the interactions between numerous continental and oceanic plates and minor crustal bodies over potentially many tens of millions of years. As such, the final geometry of an orogen can vary significantly depending on the dominant tectonic processes taking place during orogenesis. Three end-member types are generally recognised across both ancient and modern orogens (Fig. 1)—collisional, accretionary and intracontinental (Cawood et al., 2009; Raimondo et al., 2014)—and understanding the timing and conditions of tectonic events within an orogen are integral in developing a consistent tectonic framework within which to describe it. Due to the interrelated nature of the processes driving the three dominant orogen types, recognising identifying characteristic features can be difficult, particularly in ancient orogens where much of the information has been lost. To understand the entire evolution of an orogen, from pre-orogenesis to post-collision, it is essential to develop and integrate robust geochronological, structural, and thermobarometric datasets.

The South Atlantic Neoproterozoic Orogenic System (SANOS, sensu Konopásek et al., 2020) formed from the convergence of a series of continental plates during the amalgamation of Gondwana (Fig. 2a), and is now divided by the South Atlantic Ocean. For many years, the various belts that comprise the SANOS have been predominantly described as collisional or mixed collisional–accretionary orogenic belts preceded by the complete subduction of a large proto-Atlantic oceanic domain known as the

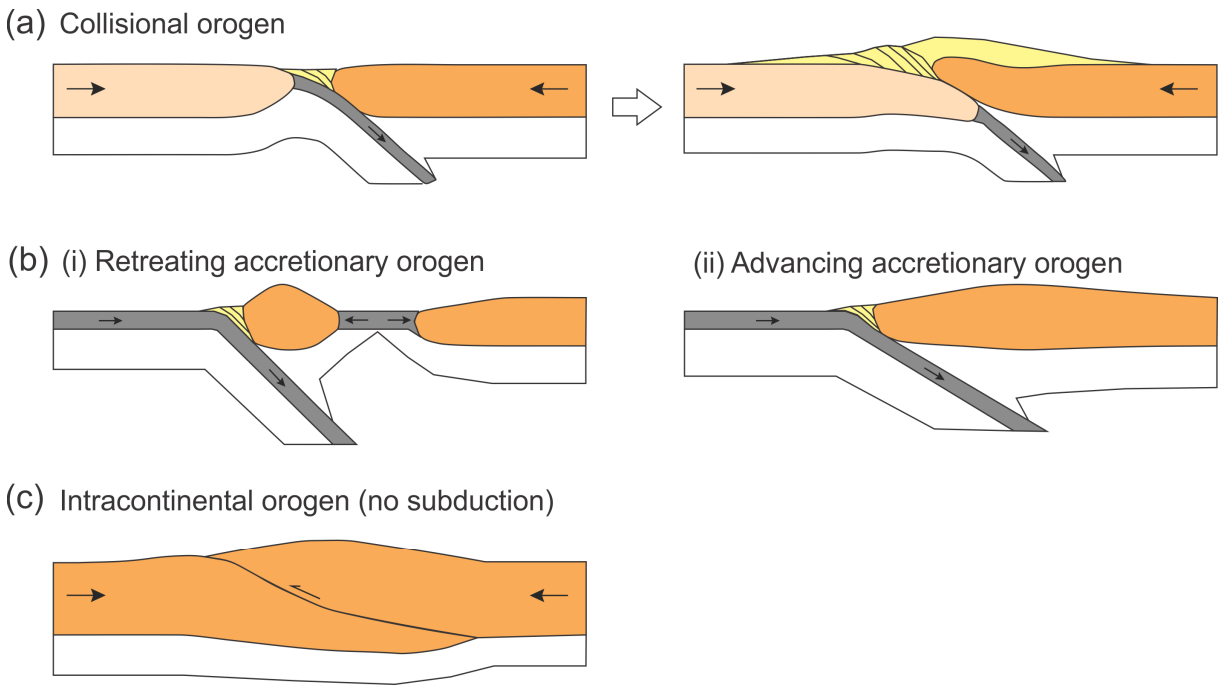

Figure 1. Schematic cross sections depicting the three major orogen types (modified after Cawood et al., 2009). (a) Collisional orogen – subduction leading to collision between two continents; (b) (i) Retreating accretionary orogen – subduction resulting in magmatism, accretion of smaller continental terranes, and back-arc spreading; (ii) Advancing accretionary orogen – subduction resulting in magmatism, accretion of smaller continental terranes, and crustal thickening; (c) Intracontinental orogen – crustal thickening in a within plate setting, far removed from active margins and subduction processes.

Adamastor Ocean (Basei et al., 2000; Hartnady et al., 1985; Heilbron and Machado, 2003; Pedrosa-Soares et al., 1998). A large, pre-orogenic proto-Atlantic Ocean located between the African and South American cratons was first proposed to describe the southern part of the SANOS in terms of continental collision (Porada, 1979), and since then the subduction–collision model has come to dominate the

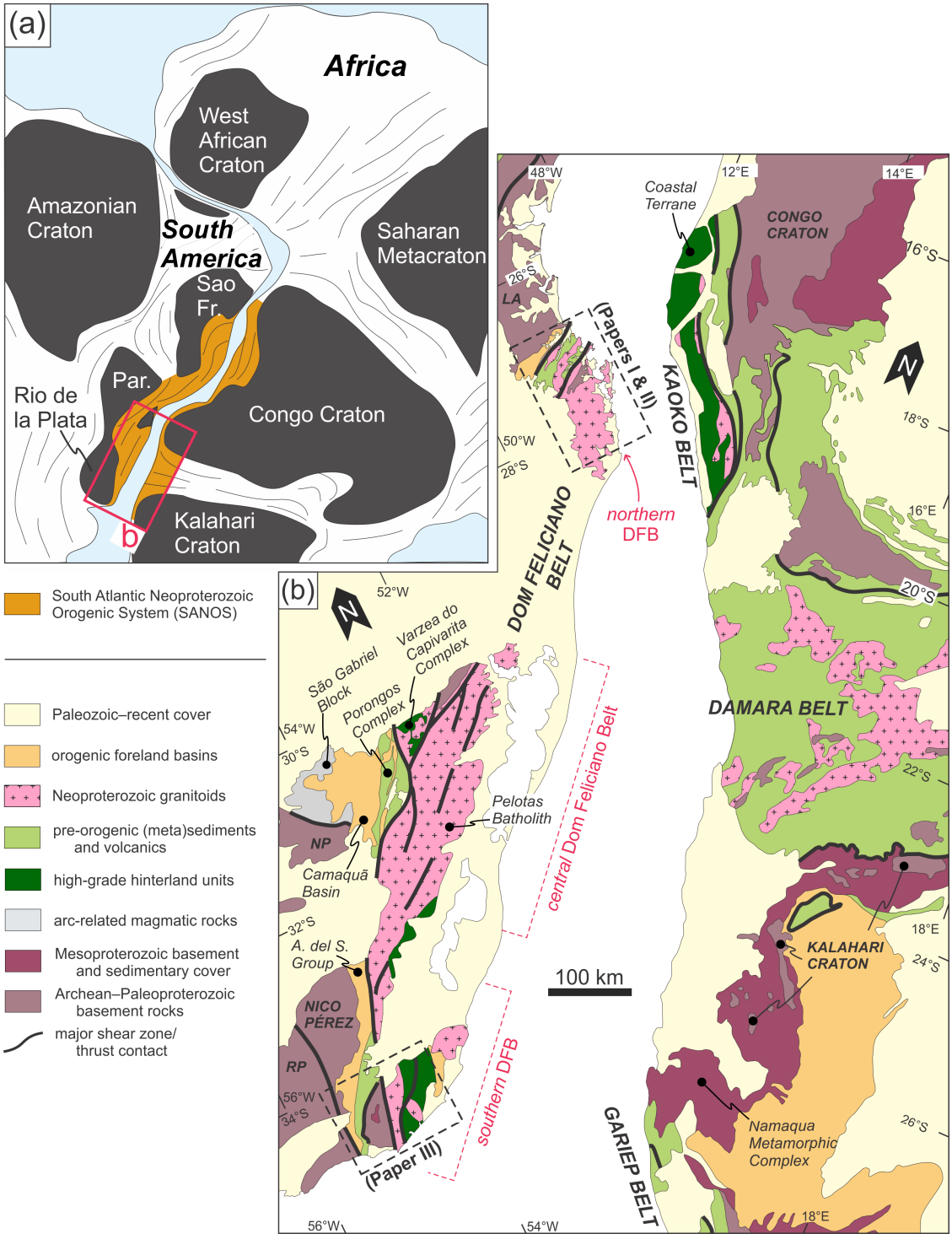

Figure 2. Geological overview of the SANOS. (a) Schematic reconstruction of Western Gondwana showing the location of the SANOS, Par. = Paranapanema Craton, Sao Fr = Sao Francisco Craton (modified after Konopásek et al., 2020). (b) Simplified geology of the southern SANOS (based on Bitencourt and Nardi, 2000; De Toni et al., 2021; Konopásek et al., 2017; McCourt et al., 2013; Oyhantçabal et al., 2011a), showing the position of the African and South American continents at the onset of the opening of the South Atlantic Ocean (after Heine et al., 2013). LA = Luis Alves Craton; NP = Nico Pérez Terrane; RP = Rio de la Plata Craton; DFB = Dom Feliciano Belt.

scientific thinking surrounding the SANOS. However, a growing body of research in recent years suggests that a large Adamastor Ocean may not have existed at all, which has led to increasing support for alternative models involving accretionary orogeny with the SANOS in the back-arc position, or purely intracontinental orogeny (Cavalcante et al., 2019; Fossen et al., 2020; Konopásek et al., 2018; Konopásek et al., 2020; Meira et al., 2019a; Meira et al., 2019b).

The Kaoko–Dom Feliciano–Gariep orogenic system, outcropping along the Atlantic coastlines of Uruguay, southern Brazil, and Namibia, is one such sub-system of the SANOS that is classically characterised as a collisional orogen preceded by the subduction of a large Adamastor Ocean (Hartnady et al., 1985; Porada, 1979, 1989). However, even more so than in the northern SANOS, contrasting interpretations of crucial units have resulted in conflicting models of orogenesis almost since the inception of the concept of the Adamastor Ocean. This conflict is driven primarily by a lack of sufficient geochronological, structural, and metamorphic data.

Constraining the timing and conditions of tectonic events prior to and during orogenesis is key to understanding the evolution of orogenic belts. In particular, the geometric configuration of continental plates prior to orogenesis and the nature of earliest crustal thickening are crucial pieces of information needed to understand the dominant processes that facilitate mountain building. In this study, a multidisciplinary approach was taken to investigate the orogenic evolution of various units within the Dom Feliciano Belt, with particular focus on supracrustal metasedimentary rock of the orogenic foreland. The key study areas are located in Santa Catarina, Brazil, and in south-eastern Uruguay (Fig. 2b).

2 Background

2.1 The South Atlantic Neoproterozoic Orogenic System (SANOS)

The South Atlantic Neoproterozoic Orogenic System (SANOS; sensu Konopásek et al., 2020) comprises the system of Neoproterozoic orogenic belts that outcrop along the coastlines of the South Atlantic Ocean (Fig. 2). The SANOS includes the Dom Feliciano, Ribeira and Araçuaí belts in South America, and the Gariep, Damara, Kaoko and West Congo belts in Africa. The system is generally divided into a northern (Ribeira–Araçuaí–West Congo belts) and a southern (Kaoko–Dom Feliciano–Gariep–Damara belts) domain. Overall, the tectonic structures of the belts fit within the framework of typical orogens, showing internal *hinterland* and external *foreland* domains. The hinterland is characterised by high metamorphic grades and extensive magmatic activity, whereas the foreland is characterised by low- to medium-grade metamorphism and fold-and-thrust tectonics with vergence away from the hinterland. Altogether, the orogenic system is roughly symmetrical, with eastern (African) and western (South American) forelands flanking a single internal hinterland.

Both the eastern and western forelands are comprised of basement domains overlain by variably deformed and metamorphosed supracrustal sequences. The basement consists of Archean–Paleoprotereozoic cratonic crust (Egydio-Silva et al., 2018; Kröner et al., 2004; Oyhantçabal et al., 2018; Passarelli et al., 2018; Seth et al., 1998; Thomas et al., 2016)—including the Congo–Sao Francisco, Kalahari, and Luis Alves cratons, and the Nico Pérez Terrane (Fig. 2a)—and the supracrustal units represent their Paleo–Neoproterozoic volcanosedimentary cover (Frimmel, 2018; Hoffman and Halverson, 2008; Hueck et al., 2018; Juliani et al., 2000; Konopásek et al., 2014; Konopásek et al., 2017; Oriolo et al., 2019). A large proportion of the cover sequences were deposited during the Tonian breakup of Rodinia after major continental rifting starting from ca. 1000 Ma, and are interpreted as rift-related to transitional passive margin successions (Alkmim et al., 2017; Basei et al., 2018; Frimmel, 2018; Pecoits et al., 2016; Philipp et al., 2004; Tack et al., 2001). Deposited on top of these units are syn-orogenic foreland basin sediments (Basei et al., 2000; Guadagnin et al., 2010; Konopásek et al., 2017).

The hinterland consists of amphibolite- to granulite-facies metaigneous and metasedimentary rocks, showing high-temperature and generally moderate- to low-pressure metamorphic conditions (Bento dos Santos et al., 2011; Goscombe and Gray, 2007; Gross et al., 2006; Gross et al., 2009), that are intruded by large volumes of late Neoproterozoic granitic rocks. The igneous protoliths of the metamorphic rocks are largely dated between ca. 860–770 Ma and are interpreted as remnants of large-scale continental rifting (Konopásek et al., 2008; Konopásek et al., 2018; Meira et al., 2019b; Passarelli et al., 2019; Will et al., 2019) or early arc magmatism (De Toni et al., 2020b; Heilbron and Machado, 2003; Heilbron et

al., 2020; Koester et al., 2016; Martil et al., 2017; Masquelin et al., 2011). High-grade metamorphism and partial melting in the hinterland took place between ca. 655–570 Ma (Cavalcante et al., 2018; Franz et al., 1999; Goscombe et al., 2005a; Konopásek et al., 2008; Lenz et al., 2011; Masquelin et al., 2011). The granitoids intruded predominantly between ca. 630–575 Ma along the western part of the hinterland (Florisbal et al., 2012c; Oyhantçabal et al., 2007; Philipp and Machado, 2005; Tedeschi et al., 2016), and between ca. 585–480 Ma along the eastern part (Konopásek et al., 2016; Kröner et al., 2004; Pedrosa-Soares et al., 2011).

2.2 History of the tectonic models of the SANOS

The study of the SANOS has a long history, although it was only with the seminal studies of Porada (1979, 1989) that the tectonic evolution of the system was discussed in detail within an all-encompassing model involving a classic Wilson cycle involving continental rifting, ocean opening, and collisional orogenesis. This discussion followed on naturally from the gradual acceptance of plate tectonic theory, transitioning into a blossoming of studies on both sides of the Atlantic advocating for the novel tectonic processes of subduction, accretion, and plate collision being the driving forces behind orogenesis within the individual belts (e.g. Kröner, 1975; Kröner, 1977; Martin and Porada, 1977). Porada (1979) initially only proposed a genetic connection between the belts of the southern and central SANOS, including the Gariep, Damara, and Kaoko belts in Africa, and the Dom Feliciano and Ribeira belts in South America. They proposed that the evolution of the system began with the opening of a three-armed rift above a mantle plume, from which a ‘proto-South Atlantic Ocean’ opened along the northern and southern branches. The eventual closure of this ocean and subsequent collision between the African and South American cratons, according to this model, is what led to orogenesis (Fig. 3). Porada (1989) further expanded the model to include other belts of the South Atlantic, including the Araçuaí Belt in Brazil and the West Congo Belt in Africa, painting a picture of an extensive but interconnected system of orogenic belts spanning from the easternmost cape of Brazil to the southernmost cape of Africa. However, it was Hartnady et al. (1985) that introduced the term Adamastor Ocean to refer to the hypothetical oceanic domain that was consumed prior to orogenesis, and this title has continued to be in use since.

Since its inception, the Adamastor subduction–collision model has been continuously built upon by researchers on both sides of the South Atlantic and along the entire length of the orogenic system. Having started as a model to explain the evolution of the southern belts (Hartnady et al., 1985; Porada, 1979), the Adamastor Ocean was gradually brought northwards into the Ribeira, Araçuaí, and West Congo belts (Heilbron et al., 2008; Pedrosa-Soares et al., 2001; Pedrosa-Soares et al., 1998; Porada, 1989). However, from the earliest days of the model the direction of subduction remained contentious,

with some researchers advocating for westward subduction of the Adamastor Ocean beneath the South American Cratons and others for eastward subduction beneath the African cratons. Some of the earliest arguments proposed that, based in part on the asymmetry of major deformation structures and clear evidence of nappe transport towards the east in the African foreland, subduction must have been directed towards the west (Fragoso-Cesar, 1980; Frimmel et al., 1996; Frimmel and Frank, 1998; Porada, 1979, 1989). As more of the belt was being studied in the context of collisional orogenesis, others instead interpreted the direction of subduction towards the east, citing thrust structures in the South American foreland with the opposite vergence as indicating nappe transport top-to-the-west, and the voluminous granitic rocks within the belts of South America as indicating arc magmatism resulting from subduction (e.g. Pedrosa-Soares et al., 1998). Both models require the consumption of a large oceanic domain, but notably they differ with respect to the location of the suture between the South American and African cratons. For eastward subduction, this suture is found between the remnants of the proposed arc and the western foreland, whereas with westward subduction the suture must be found between the arc and the eastern foreland.

Along the western side of the orogen, the subduction–collision model hinges on the interpretation of the linear granitic belts as remnant parts of long-lived magmatic arcs active between ca. 860–600 Ma. In

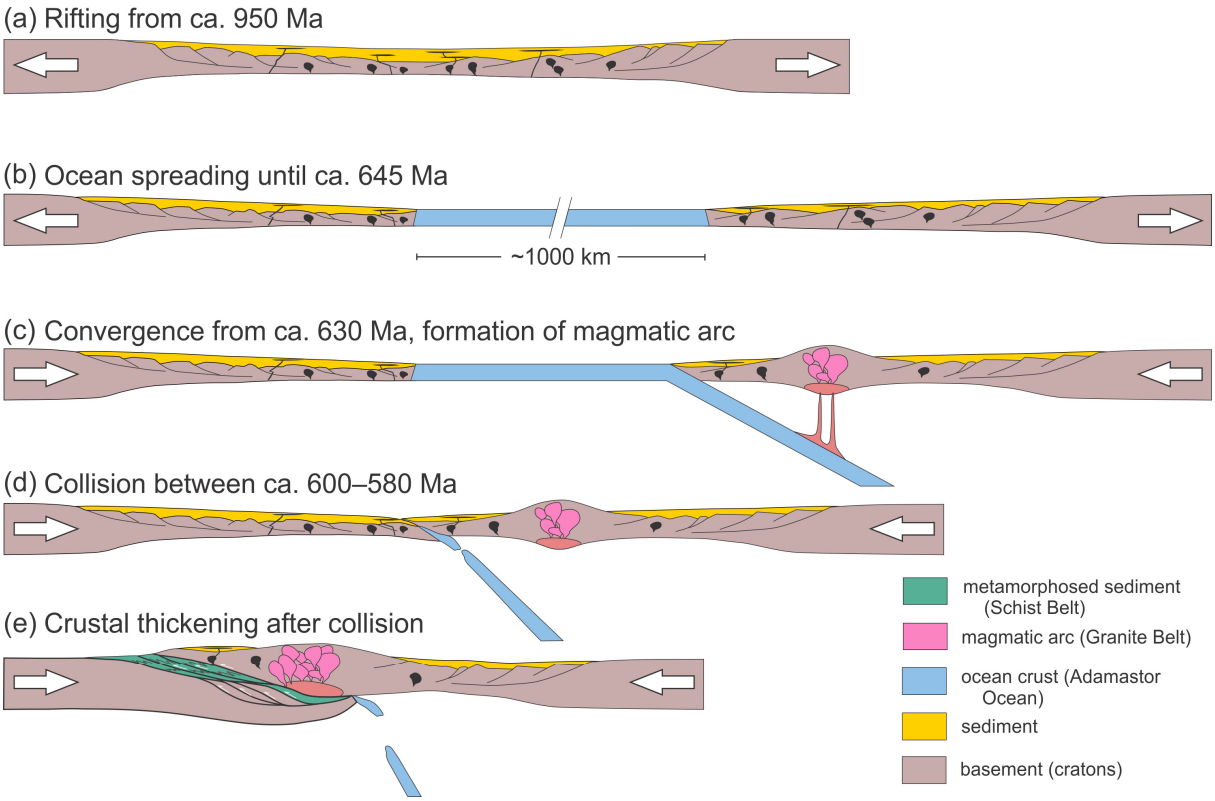

Figure 3. Schematic cross section showing the (west-directed) subduction–collision model for the formation of the SANOS. Time estimates based on reviews in Fossen et al. (2020) and Konopásek et al. (2020), and from Basei et al. (2018). (a-b) Rifting and ocean spreading from ca. 950 Ma (ca. 850 Ma for the southern SANOS) to ca. 645 Ma; (c) Subduction initiation and formation of a magmatic arc from at least 630 Ma, with the start of the Granite Belt; (d) Collision between the arc and the passive margin (the Congo and Kalahari cratons colliding with the Luis Alves and Nico Perez) between ca. 600–580 Ma; (e) Thrusting of the arc over the passive margin, forming the suture between the South American and African cratons, and deformation and metamorphism of the foreland sediment.

the northern SANOS, this is supported by extensive geochemical datasets that, when plotted within tectonic discrimination diagrams, are consistent with arc magmatism (Heilbron et al., 2020; Pedrosa-Soares et al., 2001). In the southern SANOS (the Dom Feliciano Belt) the evidence is less clear, as most geochemical and structural studies interpret large volumes of ca. 635–580 Ma granites, referred to as the Granite Belt (Basei et al., 2000), as the result of post-collisional magmatism (Bitencourt and Nardi, 1993, 2000; Florisbal et al., 2012b; Oyhantçabal et al., 2007). Despite this, there are still a number of studies that posit that the Granite Belt represents the eroded roots of a long lived magmatic arc, and they generally cite thrusting of the Granite Belt to the west over the foreland as indicating eastward subduction (Basei et al., 2000; Basei et al., 2018; Silva et al., 2005b). Several studies also interpret earlier ca. 800–770 Ma igneous activity in the hinterland as indicating arc magmatism associated with much earlier east-directed subduction (De Toni et al., 2020b; Koester et al., 2016; Lenz et al., 2013; Masquelin et al., 2011), which is consistent with the majority of interpretations from the northern SANOS (Heilbron et al., 2020). In support of these subduction–collision models, slivers of amphibolite and ultramafic rocks within the foreland supracrustal sequences are often interpreted as remnants of dismembered ophiolites, and are used as evidence for the location of a suture zone between the hinterland and western foreland (Fig. 3) (Amaral et al., 2020; Arena et al., 2018; Pedrosa-Soares et al., 2001; Pedrosa-Soares et al., 1998).

Ultimately, models involving eastward subduction have come to dominate the literature and is the generally accepted orogenic model in most publications today. However, there still remains some ambiguity, particularly within the southern SANOS. The majority of studies advocating for west-directed subduction of the Adamastor Ocean have come from geological studies along the African side of the southern SANOS (e.g. Diener et al., 2017; Frimmel et al., 1996; Frimmel and Frank, 1998; Germs, 1995; Passchier et al., 2002), and central to this east/west ambiguity is the distinct lack of evidence of high pressure metamorphism in either of the eastern or western belts (Frimmel, 2018). The presence of high pressure/low temperature metamorphic rocks is common across most orogens involving subduction and is thus generally considered indicative of relict subduction (see Fossen et al., 2020 and refernces therein). The absence of such subduction markers along the entire length of the belt is striking, and has, in part, led to models of intracontinental orogeny in place of subduction–collision (Fig. 4), which was notably discussed during the 90s by Trompette (1994, 1997) in the northern SANOS, and Dürr and Dingeldey (1996) in the southern SANOS. The intracontinental orogenic model proposes that instead of long-lived subduction of the Adamastor Ocean preceding crustal thickening, orogenesis was initiated by the inversion of an extended rift basin, with little to no oceanic crust developed between the African and South American cratons (Fig. 4). The discussion of intracontinental orogeny has further picked up speed in recent years, particularly for the belts in the northern SANOS (Araçuaí, Ribeira and West Congo belts) where the long-lived connection between the Congo–São Francisco cratons provides strong evidence for significant intracontinental deformation and a distinct lack in space for the presence

of a large oceanic domain preceding orogenesis (Cavalcante et al., 2018; Cavalcante et al., 2019; Fossen et al., 2020; Konopásek et al., 2020; Meira et al., 2015; Meira et al., 2019a; Meira et al., 2019b). Such arguments are less common in the southern SANOS (Dom Feliciano, Kaoko, Gariep and Damara belts), where relict oceanic crust of the Marmora Terrane obducted over the margin of the Kalahari Craton indicates at least a minor amount of oceanic crust developed after rifting (Konopásek et al., 2020), although some interpretations characterise these rocks as forming within a back-arc tectonic setting (Frimmel, 2018).

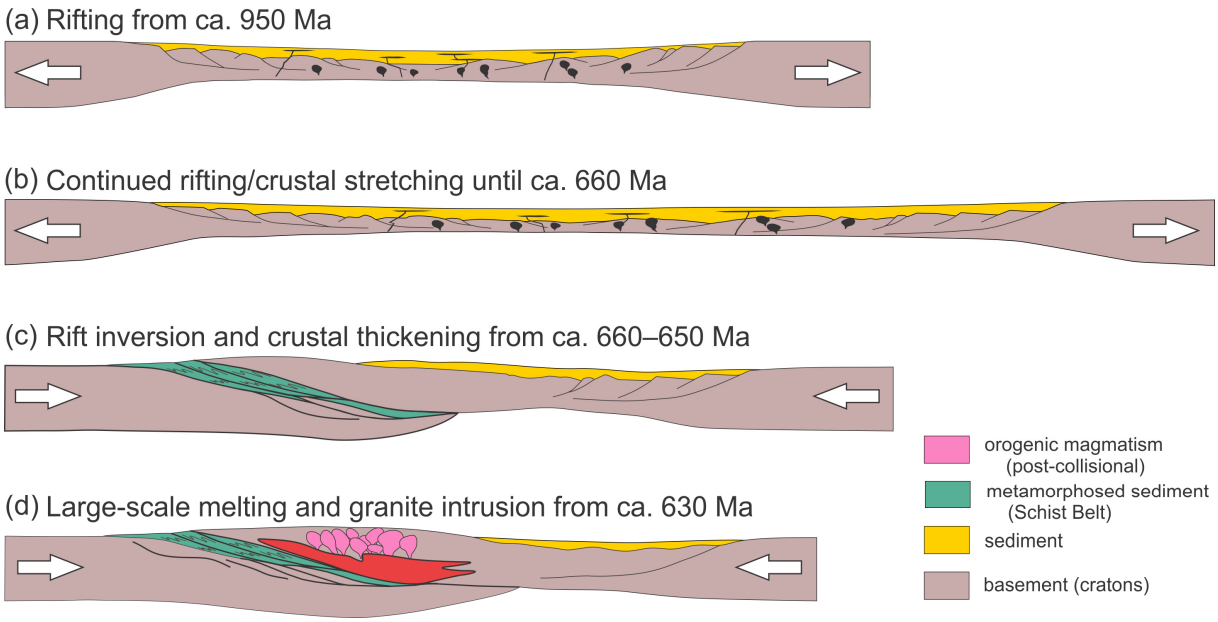

Figure 4. Schematic cross section showing the intracontinental model for the formation of the SANOS. Time estimates based on reviews in Fossen et al. (2020) and Konopásek et al. (2020). (a) Rifting and sedimentation from ca. 950 Ma (ca. 850 Ma for the southern SANOS); (b) Rifting continues throughout the Neoproterozoic without the transition into major ocean floor spreading and continental drift; (c) Rift basin inversion triggers crustal thickening and top-to-the-west directed thrusting at ca. 660–650 Ma; (d) Thermal relaxation leads to lower crustal melting (post-collisional magmatism) from ca. 630 Ma.

2.3 The Dom Feliciano Belt

The Dom Feliciano Belt outcrops along the Atlantic coastlines of southern Brazil and Uruguay and represents the south-westernmost orogenic belt of the SANOS (Fig. 5). The belt is typically grouped with the Kaoko and Gariep belts in Africa, forming part of the larger Kaoko–Dom Feliciano–Gariep orogenic system (Konopásek et al., 2020). This orogenic system was formed by the interactions between four major cratons—the Rio de la Plata and Paranapanema cratons in South American, and the Congo and Kalahari cratons in Africa—and two smaller interstitial cratonic bodies showing close association with the two African cratons (Oriolo et al., 2016b)—the Luis Alves Craton and Nico Pérez Terrane. Given early interpretations of the pre-orogenic setting of the southern SANOS as a three-armed rift system, the Kaoko–Dom Feliciano–Gariep belts, which run predominantly north–south, are often also grouped with the east–west trending Damara Belt located between the Congo and Kalahari cratons (Porada, 1979, 1989). The Dom Feliciano Belt lies along the eastern shoulders of the Luis Alves Craton

and Nico Pérez Terrane, which collectively represent the cratonic foreland of the belt (Fig. 5). The Nico Pérez Terrane and Luis Alves Craton are, in turn, accreted to the eastern margins of the Rio de la Plata (Oriolo et al., 2016b; Oyhantçabal et al., 2018) and Paranapanema cratons (Passarelli et al., 2018), respectively.

The tectono-stratigraphic divisions most commonly used to describe the structure of the Dom Feliciano Belt were defined by Basei et al. (2000), who separated the belt into three major sub-units (excluding the cratonic foreland). These are, from east to west, the Granite Belt, the Schist Belt, and the foreland basins. In addition to these three units, the Coastal–Punta del Este Terrane, which outcrops

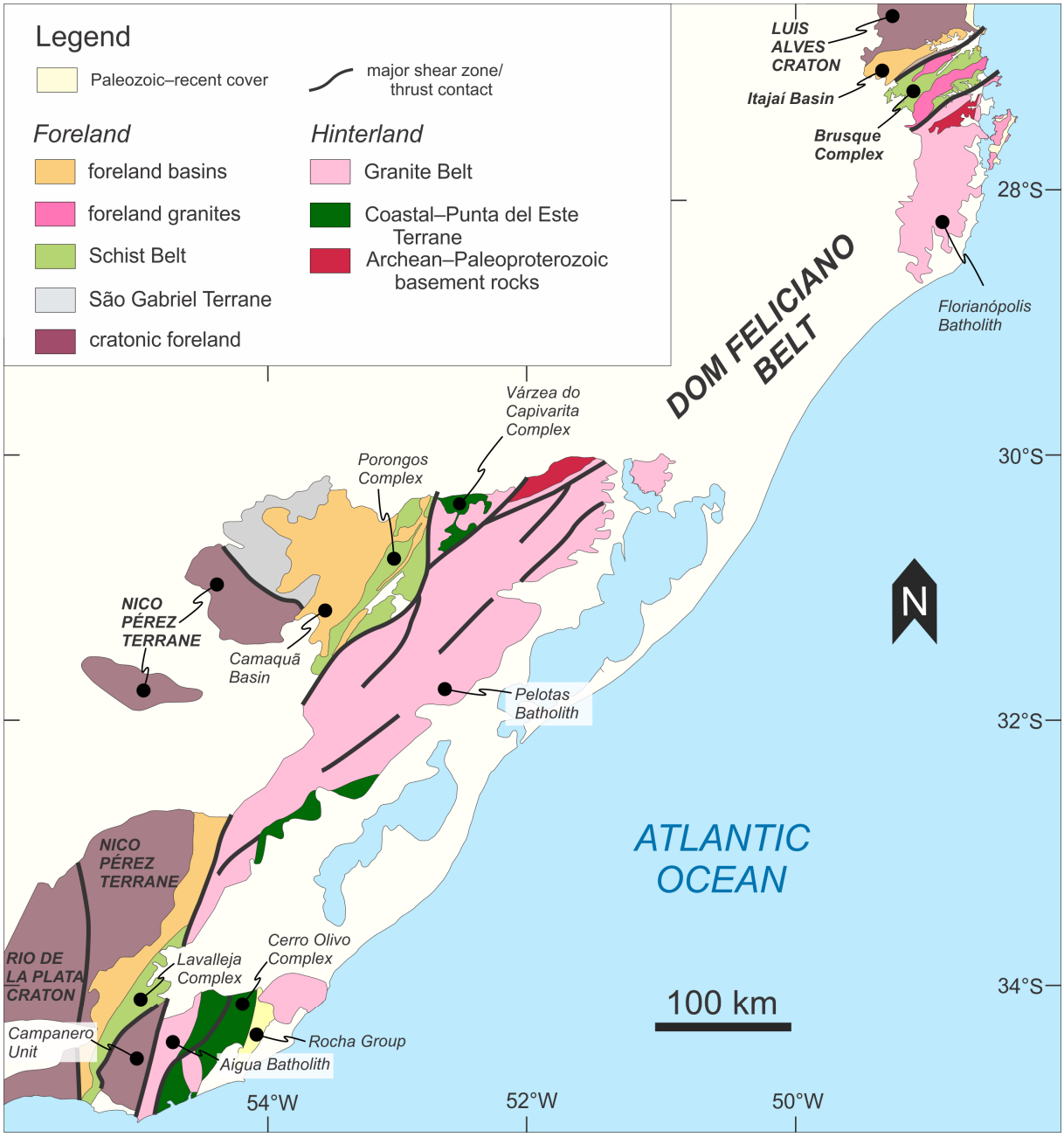

Figure 5. Simplified geological map of the Dom Feliciano Belt in southern Brazil and Uruguay (based on Bitencourt and Nardi, 2000; De Toni et al., 2021; Konopásek et al., 2017; Oyhantçabal et al., 2011a).

predominantly to the east of the Granite Belt, represents the easternmost tectonostratigraphic domain. With few exceptions, this tectonic architecture is consistent along the entire length of the belt (Fig. 5), with one exception being the Sao Gabriel Terrane, which outcrops to the west of the Schist Belt solely in the foreland of the central Dom Feliciano Belt. The belt is typically divided into northern, central, and southern sections based on major exposures in Santa Catarina (Brazil), Rio Grande do Sul (Brazil), and Uruguay, respectively. To facilitate discussion of the orogenic evolution of the belt in the introduction and the three papers that comprise this thesis, the individual tectono-stratigraphic units are further characterised as belonging to the orogenic hinterland or foreland, following the system of Konopásek et al. (2020). In this context, the foreland refers to the units west of and including the Schist Belt, whereas the hinterland comprises the units east of and including the Granite Belt (Fig. 5).

2.3.1 The Granite Belt

The Granite Belt is made up of large volumes of granitic rocks that intruded the Dom Feliciano Belt between ca. 635 and 580 Ma (Chemale et al., 2012; Florisbal et al., 2012c; Frantz et al., 2003; Oyhantçabal et al., 2007), representing much of the exposure of the belt in its central and northern sections (Fig. 5). The Granite Belt is made up of three major batholiths: the Florianópolis, Pelotas and Aiguá batholiths in the northern, central, and southern Dom Feliciano Belt, respectively (Basei et al., 2000). Early interpretations describe the Granite Belt as the exposed roots of a magmatic arc produced by subduction of the Adamastor Ocean (Porada, 1989), and this interpretation has continued to be applied to various models to this day (Basei et al., 2000; Basei et al., 2018). However, since at least the early 90s, marked by the influential study of Bitencourt and Nardi (1993), an alternative interpretation proposes that the Granite Belt represents post-collisional magmatism—that is, magmatism forming after Neoproterozoic collision between the African and South American Cratons (Florisbal et al., 2009; Florisbal et al., 2012a; Florisbal et al., 2012b; Florisbal et al., 2012c; Oyhantçabal et al., 2007). A major focus of **Papers II & III** concerns the nature of the Granite Belt as indirectly determined by the timing and conditions of metamorphism and deformation recorded in the foreland.

2.3.2 The Schist Belt

The Schist Belt is a narrow (<40km) belt of metasedimentary rocks deformed and metamorphosed in the supracrustal foreland position of the Dom Feliciano Belt. The belt consists of a series of metamorphosed sedimentary to volcanosedimentary rocks overlying the reworked cratonic basement of the foreland, primarily consisting of pelitic to psammitic schists and phyllites, metacarbonates, calc-silicates, and meta-mafic to -felsic volcanic and intrusive rocks interlayered within the sediment (Basei et al., 2011a; Basei et al., 2013; Saalmann et al., 2006; Sánchez Bettucci et al., 2001). The protolith of

the Schist Belt is generally accepted to consist of pre-orogenic volcano-sedimentary successions likely deposited from ca. 850 Ma after major rifting and the breakup of Rodinia (Basei et al., 2008a; Basei et al., 2011a), although interpretations of the timing of sedimentation, the number of sedimentary episodes, and the tectonic setting vary (Basei et al., 2000; Battisti et al., 2018; Höfig et al., 2018; Oyhantçabal et al., 2021). The Schist Belt is comprised of the Brusque, Porongos and Lavalleja complexes, outcropping in the northern, central, and southern Dom Feliciano Belt, respectively (Fig. 5), and is the primary focus of the three papers presented in this thesis. Although most studies assume continuation of the Schist Belt across the entirety of the Dom Feliciano Belt based on similarities in deformation, metamorphic grade and lithology, the correlation of these three complexes has so far not been confirmed using concrete geochronological data or modern thermobarometric modelling.

Notably, the timing of metamorphism and deformation in much of the Schist Belt is entirely unknown, and the sources and timing of sedimentation of the protoliths of the Schist Belt are unknown or seemingly inconsistent. Although there is already a large detrital zircon database from the Porongos Complex in the central Dom Feliciano Belt (Höfig et al., 2018; Pertille et al., 2015a; Pertille et al., 2015b; Pertille et al., 2017), and some from the Lavalleja Complex in the south (Oyhantçabal et al., 2021), the same cannot be said for the Brusque Complex which distinctly lacks a robust dataset which could allow a comparison of the sedimentary source regions across the entire Schist Belt. A small number of data are presented by Basei et al. (2008b), who then interpret a sedimentary source from the adjacent Paranapanema Craton. However, they present a total of 22 dates from two samples from the Brusque Complex, which is not particularly statistically convincing. Furthermore, Basei et al. (2011a) constrained the timing of sedimentation of the Brusque Complex protolith to between ca. 640 to 600 Ma based on the youngest individual detrital zircon grains and reported ages of felsic volcanic rocks (Basei et al., 2008b; Silva et al., 2002). However, this age range partly conflicts with the timing of intrusion of major granite batholiths into the complex from ca. 615 Ma (Hueck et al., 2019). In the Porongos Complex, the timing of earliest sedimentation is well constrained by the dating of interlayered volcanic rocks, which provide ages between ca. 810 and 780 Ma (Pertille et al., 2015b; Saalmann et al., 2011). However, major detrital zircon age peaks between ca. 615 and 580 Ma are also recorded in parts of the complex (Pertille et al., 2015a; Pertille et al., 2015b), prompting recent studies proposing that parts of the Schist Belt are comprised of syn-orogenic sedimentary rocks (Battisti et al., 2018; Höfig et al., 2018). Finally, the Lavalleja Complex provides the greatest hurdle in correlating the units of the Schist Belt, as geochronological constraints suggest large parts of the sedimentary record of the complex date to the Mesoproterozoic (Oriolo et al., 2019), which conflicts with estimates of the timing of earliest sedimentation in the Schist Belt protolith as during the early to middle Neoproterozoic (Chemale, 2000; Pertille et al., 2017; Saalmann et al., 2011).

Clearly, based on these observations, the early assumption that all of the metasedimentary rocks of the Schist Belt shared a single paleobasin is likely incorrect. However, establishing to what degree they do have a shared history is key to reconstructing the evolution of the Dom Feliciano Belt and furthering our understanding of the pre-orogenic position of the major cratons. The Brusque Complex is the least studied of the three Schist Belt complexes, lacking both a reliable constraint on the timing of sedimentation and a significant detrital zircon database, therefore representing a distinct gap in knowledge. The focus of **Paper I** is to constrain the timing of sedimentation in the Brusque Complex, and to develop a robust detrital zircon dataset for comparison with the rest of the Schist Belt, as well as with equivalent supracrustal rocks along the eastern foreland of the Kaoko–Dom Feliciano–Gariep orogenic system.

Although there are some estimates of the timing of peak metamorphism in the Schist Belt, they are predominantly based on indirect constraints such as the intrusion of granitic batholiths and detrital zircon ages. There are currently no published studies containing geochronological constraints that can be directly linked to peak metamorphism, although a single, imprecise muscovite–whole rock Rb–Sr age of 658 ± 26 Ma from the Porongos Complex remains the only current estimate of the timing of this event (Lenz, 2006; MSc. thesis). Similarly, the current estimates of peak metamorphic conditions (lower greenschist to lower amphibolite facies) are based primarily on petrological observations of mineral assemblages or classical thermobarometry (Basei et al., 2011a; Campos et al., 2011), and there are currently no studies applying modern methods of thermodynamic modelling to estimate more precise P–T conditions from which we could derive a P–T path. **Papers II & III** address these absences by providing geochronological data and P–T estimates from the forelands of the northern and southern Dom Feliciano Belt.

2.3.3 The Coastal–Punta del Este Terrane

In addition to the three primary tectonostratigraphic units defined by Basei et al. (2000), a fourth unit—the Punta del Este Terrane—is located to the east of the Granite Belt in southern Dom Feliciano Belt in Uruguay (Preciozzi et al., 1999). The Punta del Este Terrane comprises the granulite-facies rocks of the basement Cerro Olivo Complex, as well as low-grade (maximum greenschist facies) metasedimentary syn- to post-orogenic cover sequences known as the Rocha and Sierra de Aguirre formations (Abre et al., 2020; Bossi and Gaucher, 2004; Masquelin et al., 2011; Preciozzi et al., 1999; Silva Lara et al., 2021). The Cerro Olivo Complex is represented by rocks with igneous and sedimentary protoliths recording ages between ca. 800–770 Ma, with a strong high-temperature metamorphic overprint between ca. 655–640 Ma (Lenz et al., 2011; Masquelin et al., 2011; Oyhantçabal et al., 2009; Will et al., 2019).

Hasui et al. (1975) first distinguished these metasedimentary cover units in southern Uruguay as being separate from the Schist Belt primarily based on their location east of the Granite Belt, and their interpretation of the Granite Belt and associated host gneisses as a *median massif*—a major geological division within pre-plate tectonic geosynclinal theory. The exotic nature of these rocks relative to the other supracrustal units of the Dom Feliciano Belt was further emphasised by Basei et al. (2005), who correlated the Rocha Formation with the Oranjemund Formation in the Gariep Belt on the opposite side of the Atlantic. Later, the basement of the Punta del Este Terrane was also identified as having connections with units in Africa, being correlated with the Coastal Terrane of the Kaoko Belt (Basei et al., 2011b; Gross et al., 2009; Oyhantçabal et al., 2009; Oyhantçabal et al., 2011b). Importantly, Oyhantçabal et al. (2009) recognised similarities in age between the igneous protoliths of the Cerro Olivo Complex and the rift-related igneous rocks preserved in the Coastal Terrane (Konopásek et al., 2008). These two units preserve an important magmatic episode between ca. 800–770 Ma, which helps to cement a pre-orogenic connection between the easternmost domain of the Dom Feliciano Belt with the westernmost parts of the African belts. Based on this correlation, the collective unit has been recently referred to as the Coastal–Punta del Este Terrane (Konopásek et al., 2014; Konopásek et al., 2018).

Until recently, the only known rocks of this age in the Dom Feliciano Belt were from the Punta del Este Terrane in Uruguay, and many studies have thus emphasised the uniqueness of the terrane relative to the rest of the belt, asserting that these rocks must have amalgamated against the eastern flank of the Granite Belt sometime after subduction of the Adamastor Ocean and intrusion of the granites (Basei et al., 2011b). Since then, however, rocks of similar age and metamorphic grade to those found in the Cerro Olivo Complex have been identified in the Várzea do Capivarita and Porto Belo complexes in the central and northern Dom Feliciano Belt, respectively (Costa et al., 2020; De Toni et al., 2020b; De Toni et al., 2021; Martil et al., 2017; Philipp et al., 2016). Unlike the Cerro Olivo Complex, the latter two units are located within the western part of the Granite Belt (Fig. 5). If the possible connection between all of these units is accepted, this position within the Granite Belt seemingly contradicts the interpretation that the Coastal–Punta del Este Terrane was juxtaposed against the eastern margin of the Dom Feliciano Belt sometime after intrusion of the granites (e.g. Basei et al., 2011b).

Alternatively, these observations suggest that the Coastal–Punta del Este Terrane may represent surviving relicts of the hinterland of the orogen, forming the country rocks into which intruded the Aiguá Batholith and the other granites of the Granite Belt (Masquelin et al., 2011). High-grade metamorphism recorded in these rocks between ca. 655–640 Ma has been interpreted as early crustal thickening during convergence between the South American and African cratons (Battisti et al., 2018; Lenz et al., 2011). If the Granite Belt represents post-collisional magmatism and not a magmatic arc, then it is possible that this high-grade metamorphic event, occurring some 10 to 25 million years before large-scale

magmatism, marks the timing of early convergence in the Dom Feliciano Belt, and thus may be coeval with thrusting of the hinterland over the foreland of the Dom Feliciano Belt (**Paper II**).

2.3.4 Connection with the Kaoko and Gariep belts

The orogenic connection between the western (Dom Feliciano Belt) and eastern (Kaoko and Gariep belts) parts of the southern SANOS is primarily based on the similarity in ages and lithologies found across both sides of the orogen. As previously mentioned, the syn-orogenic sedimentary cover in the southern Dom Feliciano Belt (Rocha Formation) has been correlated with similar rocks (Oranjemund Group) in the Gariep Belt based on a detrital zircon provenance study (Basei et al., 2005). Similarly, the Coastal Terrane (Kaoko Belt) and the Punta del Este Terrane (southern Dom Feliciano Belt) are correlated based on the ages of their respective igneous protoliths, the age of intrusive rocks similar to the Granite Belt, and the timing and degree of granulite-facies metamorphism (Konopásek et al., 2016; Konopásek et al., 2018; Oyhantçabal et al., 2009; Will et al., 2019). However, the timing of the main phase of transpressive deformation recorded in the Kaoko Belt, between ca. 580–550 Ma, makes it clear that the high temperature metamorphism recorded in the hinterland (Coastal–Punta del Este Terrane) between ca. 655–640 Ma relates to an earlier event, or to a much earlier phase of orogenesis (Goscombe et al., 2005a). The metasedimentary rocks of the Kaoko Belt represent the eastern foreland equivalents of the Schist Belt, comprising a transpressive fold and thrust belt with tectonic vergence to the east (Goscombe et al., 2003a; Goscombe et al., 2003b; Goscombe et al., 2005b). Without any constraints on the timing of deformation and metamorphism in the equivalent part of the Dom Feliciano Belt (the foreland in general, and the Schist Belt in particular), it is not possible to make a connection between the tectonic evolution of the two halves of the belt, or to fully understand the relationship between Cryogenian high temperature metamorphism in the hinterland and Ediacaran transpression in the foreland.

3 Aims and Objectives

The *P–T–D–t* history of the metamorphosed supracrustal rocks of the Dom Feliciano Belt foreland (the Schist Belt) is largely unknown. In particular, works using modern methods for estimating P–T conditions (phase equilibria modelling) and precise geochronological estimates of the timing of metamorphic events are lacking. Furthermore, although there are already reliable constraints showing an orogenic connection between the eastern and western parts of the Kaoko–Dom Feliciano–Gariep orogenic system, their potential pre-orogenic relationship is not so well understood. Thus, the aim of this work is to improve our understanding of the pre-orogenic, metamorphic, and structural history of the Dom Feliciano Belt foreland. With this work, I hope to constrain the relative pre-orogenic positions of the major cratonic bodies involved in Neoproterozoic orogenesis, determine the potential correlation between the foreland supracrustal rocks of the Kaoko–Dom Feliciano–Gariep belts, and help to develop a consistent model of orogenesis in the Dom Feliciano Belt. To achieve this, the following questions were posed:

- What was the pre-orogenic relationship between the foreland supracrustal rocks of the Dom Feliciano, Kaoko and Gariep belts? (**Paper I**)
- What were the relative pre-orogenic positions of the major cratonic bodies involved in orogenesis (Luis Alves, Nico Perez, Congo, and Kalahari cratons)? (**Paper I**)
- What were the conditions of Neoproterozoic metamorphism in the foreland supracrustal rocks, and at what time did metamorphism occur? (**Papers II & III**)
- When did earliest crustal thickening in the orogenic foreland begin? (**Papers II & III**)
- What was the relationship between the hinterland and foreland domains in the Dom Feliciano Belt? (**Papers II & III**)

Paper I presents geochronological data from the Brusque Complex (the northern Schist Belt), exploring the connection between the supracrustal rocks of the forelands of the southern SANOS and the pre-orogenic positions of the cratons. **Paper II** presents the results of structural analysis, thermodynamic modelling, and geochronology from the Brusque Complex, providing an overview of tectonic events from the start to the end of orogenesis in the northern Dom Feliciano Belt. **Paper III** presents the results of thermodynamic modelling and geochronology from the Lavalleja and Campanero complexes (foreland) and the Cerro Olivo Complex (hinterland) in the southern Dom Feliciano Belt. This data is used to explore the relationship between the hinterland and foreland domains, and the paper builds on the results and interpretations from **Papers I & II** to develop a tectonic model for the southern Dom Feliciano Belt that is consistent with the rest of the southern SANOS. Overall, the results of the thesis provide novel data used to better understand the evolution of the Dom Feliciano Belt and southern SANOS in particular, and the SANOS as a whole.

4 Approach and methods

The aims of this thesis are addressed using a combination of analytical and investigative methods including field work, isotope geochronology, phase equilibria modelling, structural analysis, and mineral geochemistry. The motivation behind the use of these wide-ranging techniques is to find a complimentary combination that can help to resolve the complex and long-lived evolution of the Dom Feliciano Belt and the southern SANOS. This section outlines the major approaches and methodologies used during this work.

4.1 Mapping and structural analysis

Four field trips to Santa Catarina, Brazil, and two to southern Uruguay were undertaken between 2017 and 2019 to collect structural data and samples for analysis. The field studies in Santa Catarina form the basis of **Papers I & II**. The fieldwork was focused on mapping and sampling the metasedimentary cover sequences of the foreland (Brusque Complex), including their relationship with adjacent tectonostratigraphic units and major structural features. Fieldwork in Uruguay formed the basis of **Paper III**, with a focus on the foreland supracrustal (Lavalleja Complex) and basement (Campanero Unit) complexes, as well as the hinterland basement (Cerro Olivo Complex).

Due to the poor outcrop situation in southern Brazil and Uruguay, particularly inland away from the coast, collecting a good spread of reliable structural data proved difficult. Partly for this reason, field mapping and structural analysis in the Brusque Complex in Santa Catarina was prioritised over the course of the study due to a distinct lack of published data from this area. This data formed the structural foundations for **Paper II**. The smaller structural dataset obtained from southern Uruguay was supplemented by previously published studies, although the data collected still formed the groundwork for **Paper III**.

4.2 Geochronology and geochemistry

Reliably constraining the timing of major orogenic events is key to developing a consistent and reliable tectonic model. Knowing the timing of sedimentation, deformation, and metamorphism in the foreland of the Dom Feliciano Belt, and correlating these events across the southern SANOS, is vital in answering the main questions posed in this study. Multiple geochronological methods were used to constrain the timing of these events, which involved various analytical techniques in the collection of isotopic data for mineral geochronology.

4.2.1 Zircon and monazite U–Pb

The U–Pb decay system is one of the most widely used geochronometers in the study of tectonics, as well as within many other geological disciplines. This is, in part, because of the extremely robust decay constants evaluated for ^{238}U and ^{235}U, which are considered to be among the most accurate and precise in geochronology (e.g. Mattinson, 2010). Another benefit of the U–Pb system is the independent radioactive decay chains of the parent isotopes ^{238}U and ^{235}U, to the daughter isotopes ^{206}Pb and ^{207}Pb, respectively. The evaluation of both decay systems allows their comparison as an internal check for the reliability of evaluated dates, most commonly using concordia plots. Ideally, given optimal conditions within a given mineral, where the system is closed and there has been no external loss or addition of U or Pb, the results of isotope analysis should plot along a concordia curve, and the combination of multiple analyses can combine to give a concordia age. However, even in the situation when samples are discordant (that is, do not plot along the concordia), the distribution of data within the concordia plot can still be used to infer information about the timing of events, such as Pb loss, that contribute to the discordance.

In **Papers I & III**, laser ablation inductively coupled plasma mass spectrometry (LA-ICP-MS) was used to obtain U–Pb zircon ages, as the method allows the rapid in situ analysis of the large numbers of zircon grains needed for detrital zircon investigations (**Paper I**) and the formation of reliable concordia ages (**Paper III**). For **Paper III**, secondary ion mass spectrometry (SIMS) was used for samples with small numbers of zircon grains, and to confirm one LA-ICP-MS age. Zircon grains were imaged by cathodoluminescence (CL) prior to analysis, and monazite grains were imaged using back-scattered electron (BSE) imaging. For **Papers II & III**, SIMS was used to analyse U–Pb in monazite, due to the small sample sizes and small grain sizes, and the high precision and high spatial resolution of the method.

Monazite trace element chemistry was also analysed to investigate the Rare Earth Element (REE) partitioning between monazite and garnet to establish if they grew in equilibrium. Monazite and garnet directly compete for the heavy REEs during growth, and in general it has been found that the partitioning of these elements into these two minerals is consistent (e.g. Hermann and Rubatto, 2003; Rubatto et al., 2006; Warren et al., 2018). Thus, comparing the trace elements from these minerals within one sample can help determine if they grew together, and thus help to interpret the meaning of analysed ages (**Paper II**).

4.2.2 Garnet Lu–Hf and Sm–Nd

In **Papers II & III**, isotope dilution ICP-MS was used to obtain Lu–Hf and Sm–Nd garnet ages. Garnet Lu–Hf and Sm–Nd geochronology is one of the most useful geochronometers for medium- to high-grade metapelitic rocks, as the timing of garnet growth can often be tied to a specific event or events using microstructural observations and mineral geochemistry (Anczkiewicz et al., 2014; Konopásek et al., 2019; Pollington and Baxter, 2010). Furthermore, the Lu–Hf and Sm–Nd geochronometers can be coupled to constrain the entire timescale of garnet growth, and thus by inference the duration of prograde metamorphism (Lapen et al., 2003; Soldner et al., 2017; Soldner et al., 2020). Garnet is also a key mineral used when employing phase equilibria modelling (e.g. Gaidies et al., 2006), and thus the timing of garnet growth as determined by Lu–Hf and Sm–Nd geochronology can be directly linked to specific pressure and temperature conditions allowing the interpretations of specific tectonic events (Jung et al., 2019; Walczak et al., 2017).

Garnet Lu–Hf and Sm–Nd geochronology does not come without its complications, however. Among the most problematic obstacles are high-Hf/high-REE mineral inclusions. Common inclusions in garnet that can concentrate large amounts of the daughter Hf isotope include zircon and rutile. In the case of zircon, it is common for metasedimentary rocks to contain older inherited grains that did not grow in equilibrium with the matrix assemblage, and therefore do not preserve the same $^{176}Hf/^{177}Hf$ ratio. Because of the high Hf concentrations in zircon, even a small volume of inclusions can completely overwhelm the signal preserved in garnet and result in erroneous ages (Scherer et al., 2000). Similarly, common mineral phases that contain high concentrations of Sm and Nd include REE-bearing minerals such as monazite and apatite. Such minerals, particularly Nd-rich monazite, can overwhelm the Sm/Nd ratio of the garnet and result in an age that is too young and imprecise (Pollington and Baxter, 2010, 2011; Thöni, 2002).

To obtain accurate and precise ages, it is vital to attempt to remove as many of these inclusions from the garnet as possible prior to analysis. Most of the sample preparation for Lu–Hf and Sm–Nd isotope analysis, therefore, is taken up by removal of these inclusions, first by mechanical picking under the microscope to remove visible inclusions and then through dissolution (Anczkiewicz and Thirlwall, 2003; Lagos et al., 2007; Pollington and Baxter, 2011). The first stage of dissolution attempts to dissolve mineral inclusions out of the garnet (for example, monazite), and the second stage is the selective dissolution of the garnet leaving refractory inclusions behind (for example, zircon) which can then be removed mechanically. This final step also prepares the samples for element separation and final isotopic analysis. The methods for sample preparation used in **Papers II & III** follow that of Anczkiewicz et al. (2004).

In **Papers II & III**, trace elements were analysed across garnet grains using LA-ICP-MS to determine the distribution of the isotopes of interest, which are then used to interpret the meaning of the ages. Using the method as described above and in greater detail in **Papers II & III**, the resulting isochron ages will be an average age of the entire growth of the garnet as there is no discrimination between the collection different parts of the garnet during mechanical picking. However, due to the fractionation of Lu over Hf during garnet growth, following a profile predicted by Rayleigh fractionation, garnet tends to concentrate Lu in the cores resulting in much higher Lu to Hf ratios in garnet cores compared to its rims. The preferential Lu enrichment in the cores means that whole-grain garnet Lu–Hf ages tend to be biased towards early garnet growth (Lapen et al., 2003). In contrast, Rayleigh fraction of Sm and Nd suggests that Sm–Nd ages tend to be biased more towards later garnet growth, and thus the combination of Lu–Hf and Sm–Nd geochronology can give a minimum estimate of the duration of garnet growth (Lapen et al., 2003). The trace element profiles are used to determine the true distribution of Lu, Hf, Sm and Nd.

4.2.3 Mica Ar–Ar

In **Paper II**, Ar–Ar geochronology was used to date the cooling of biotite within the Brusque Complex during exhumation, and the recrystallisation of muscovite during late orogenic deformation along sub-vertical high-strain zones. Ar–Ar geochronology of micas is one of the few geochronometers that can be used to date events occurring at low metamorphic conditions and is particularly useful at constraining events along shear zones and faults where the growth and recrystallisation of mica is common. However, because the closure temperature of Ar–Ar within micas is relatively low (~300–400°C; Grove and Harrison, 1996; Harrison et al., 2009), the geochronometers are particularly susceptible to changes in temperature and partial or complete resetting. This is even more problematic in slowly cooling rocks, such as plutonic or metamorphic rocks, and so care needs to be taken when interpreting the meaning of these ages (Schaen et al., 2020).

4.3 Phase equilibria modelling

There are various methods available for estimating the pressure–temperature (P–T) conditions of metamorphic rocks, which all rely on the chemical equilibrium between or within minerals as a function of pressure and temperature. Classical thermobarometry allows the calculation of P or T using individual chemical reactions within or between minerals, and the combination of multiple techniques can result in adequate P–T estimates. Computational phase equilibrium modelling was used to estimate P–T conditions for the rocks in this study, however, as it allows for a broader and more developed

understanding of the stable and metastable mineral assemblages and compositions formed during a rock's metamorphic history. Using this method, assemblage stability diagrams, or *pseudosections*, can be calculated by modelling the phase relations within a constrained bulk composition defined by a given rock, which then represent estimates of the equilibrium assemblages of that rock over P–T space. The mineral assemblage observed in a given rock can then be compared with the calculated pseudosection, defining a range of P–T values that can be used to constrain the conditions at which a rock was metamorphosed. This estimate can be further refined by calculating the compositional and/or modal proportional variation of individual minerals—such as garnet—as *isopleths* within the pseudosection and comparing these values with observed mineral compositions in the rock (Stüwe and Powell, 1995). Ultimately, phase equilibria modelling has the potential to produce reliable estimates of P–T through multiple stages of the metamorphic evolution of a rock, enabling the construction of P–T paths.

4.3.1 Modelling methods and assumptions

For **Papers II & III** I have used the Perplex (ver. 6.9.0) modelling software of Connolly (2005) in combination with the thermodynamic dataset DS6.22 of Holland and Powell (2011). Perplex is one of the leading thermodynamic modelling packages available for phase equilibria modelling and receives regular updates and fixes. The solution models we used were predominantly those from White et al. (2014), as they were calibrated with the dataset of Holland and Powell (2011) and made specifically for modelling of metapelitic rocks. Some exceptions are outlined in **Papers II & III**.

Bulk rock compositions were analysed using inductively coupled plasma emission spectroscopy (ICP-ES) and atomic absorption spectroscopy (AAS) (**Papers II & III**). One major assumption made when constraining the bulk rock composition in this way is that the analysed bulk rock accurately reflects the effective composition of the sample examined under thin section. Many metamorphic rocks show significant heterogeneity, which is particularly obvious in low- to medium-grade, layered schists such as those studied in **Paper II**. Using the mineral assemblage observed in a thin section that was cut from part of the sample that is not representative of the average bulk composition may result in an erroneous pseudosection and/or modal compositional isopleths that do not intersect. Attempts were made to avoid this by cutting multiple thin sections from different parts of the sample and analysing mineral compositions across each of these sections to get a broad overview of the mineral assemblage and chemistries within the rock.

The mineral assemblage observed in a metamorphic rock ideally represents the stable assemblage formed at the metamorphic climax, which typically occurs when a rock reaches a peak in temperature and is at its least hydrated state. However, unless the rock has very rapidly cooled from this peak temperature, or has somehow otherwise escaped further metamorphism, there will often be signs of

retrograde metamorphic reactions as the rock attempts to maintain thermodynamic equilibrium with changing P–T conditions. This requires careful petrological study of the samples to determine what, if anything, remains of the relict peak mineral assemblage, and what represents retrograde or secondary overprint.

It is also possible that thin sections reveal small sub-domains within a sample that contain isolated mineral assemblages that are not in equilibrium with the matrix assemblage, which can potentially reveal the P–T conditions during earlier stages of metamorphism. One sample from this study (**Paper III**) showed such features, and in this case the effective bulk composition of the isolated domain was determined by thin section 2D volume estimation in combination with mineral compositional analysis.

Another assumption made for the modelling in this study is the conversion of all analysed iron into FeO (with the exception of one sample in **Paper II**), effectively ignoring Fe_2O_3 in the system. Iron analysed during whole rock compositional analysis is typically reported as Fe_2O_3 (Fe^{3+}) due to the oxidation of FeO (Fe^{2+}) during sample preparation. The conversion of Fe_2O_3 to FeO was done with samples containing no significant Fe_2O_3-bearing phases, as the absence of such minerals implies that the small amount of Fe_2O_3 present in the rock will have a negligible effect on the chemical equilibrium of the system. This assumption is supported by studies investigating the effect of Fe_2O_3 on modelling of metapelitic rocks (e.g. Diener and Powell, 2010; Forshaw and Pattison, 2021). For the one sample in this study containing a significant proportion of Fe_2O_3-bearing phases (**Paper II**), the concentrations of Fe_2O_3 and FeO were separately analysed by titration and used for pseudosection modelling. In this case, the relatively large proportion of Fe_2O_3-bearing phases (in particular, hematite and magnetite) indicated the importance of Fe^{3+} for the chemical system.

5 Summary of papers

Paper I

Percival, J. J., Konopásek, J., Eiesland, R., Sláma, J., Campos, R. S., Battisti, M. A., Bitencourt, M. F., 2021, **Pre-orogenic connection of the foreland domains of the Kaoko–Dom Feliciano–Gariep orogenic system**, *Precambrian Research*, vol. 354, pp. 106060, https://doi.org/10.1016/j.precamres.2020.106060

The supracrustal rocks of the Schist Belt in the Dom Feliciano Belt have long assumed to be a continuous unit with a shared pre-orogenic sedimentary history (Basei et al., 2000). More recently, studies have further proposed a pre-orogenic connection with rocks from the hinterland (Battisti et al., 2018), as well as with the foreland supracrustal rocks of the Kaoko Belt in Namibia (Konopásek et al., 2020). However, data from the central and southern parts of the Schist Belt has recently challenged this view, with the finding that parts of the Schist Belt record markedly different ages of sedimentation; age constraints from the central Schist Belt suggests predominantly Neoproterozoic sedimentation, whereas the southern Schist Belt records Mesoproterozoic sedimentation (Oriolo et al., 2019; Pertille et al., 2017; Saalmann et al., 2011). To investigate the potential correlation of these units across the southern SANOS, **Paper I** is focused on the pre-orogenic history of the Brusque Complex metasediments that comprise the foreland supracrustal sequences of the northern Dom Feliciano Belt. The Brusque Complex is the least studied of the Schist Belt sub-units, and available constraints on the timing and sources of sedimentation are imprecise or inconsistent (Basei et al., 2005; Basei et al., 2011a). Furthermore, the current position of the northern Dom Feliciano Belt implies close proximity to the Kaoko Belt prior to the opening of the Atlantic, and thus represents the best location to study a possible connection between the African and South American supracrustal sequences (Fig. 2b). The study is based on the interpretation of zircon U–Pb data from the Brusque Complex, including detrital and igneous zircon from metapelitic, metapsammitic and metavolcanic rocks.

A concordia age of 811 ± 6 Ma was obtained from igneous zircon within a deformed and metamorphosed felsic dyke intruding the sedimentary protolith of the Brusque Complex, which constrains the minimum timing of earliest sedimentation into the paleo-basin to sometime before ca. 811 Ma. This is close to estimates for the timing of rifting (i.e. basin formation) at ca. 835 Ma (Basei et al., 2008a), and is consistent with age constraints from the central Schist Belt (Porongos Complex) of ca. 810–780 Ma (Pertille et al., 2017; Saalmann et al., 2011). Furthermore, it matches the timing of igneous activity in the hinterland (Coastal–Punta del Este Terrane) between ca. 820–770 Ma (Konopásek et al., 2008; Konopásek et al., 2018; Lenz et al., 2011; Oyhantçabal et al., 2009).

Detrital zircon analysis reveals that the Brusque Complex metasedimentary rocks fall into two distinct groups based on age patterns: one group containing only Paleoproterozoic-aged zircon between 2.2–2.0 Ga, and another with both Paleo- to Mesoproterozoic age peaks of between ca. 2.1–1.8 and ca. 1.6–1.0 Ga. The detrital zircon ages from the Paleoproterozoic sample group are consistent with erosion of the adjacent Luis Alves Craton. This sedimentary source is unsurprising assuming that the current relative positions of the supracrustal rocks and the Luis Alves craton reflects their past positions during sedimentation, and it confirms interpretations that the Brusque Complex was deposited along the shoulder of the craton. The Mesoproterozoic ages from the second group of samples, however, are not known from basement rocks in southern South America, and instead are more consistent with the igneous provinces and/or sedimentary cover sequences of the African cratonic margins (the Congo and Kalahari cratons). This suggests a major sedimentary source of African affinity. The detrital zircon ages and patterns are nearly identical to those from the central Dom Feliciano Belt (Porongos Complex), indicating a shared sedimentary source. Similarities are also found when compared with the eastern foreland supracrustal rocks in the Kaoko Belt, and to a lesser extent in the Gariep Belt.

We interpret this data as indicating that sedimentation occurred in a shared system of basins at the onset of, and during, rifting between the African and South American Cratonic blocks during the Tonian. This implies that the cratons involved in late-Neoproterozoic orogenesis were in close proximity prior to rifting and intracontinental basin formation at ca. 810 Ma, which has major implications for pre-orogenic plate reconstructions.

Paper II

Percival, J. J., Konopásek, J., Anczkiewicz, R., Ganerød, M., Sláma, J., Campos, R. S., Battisti, M. A., Bitencourt, M. F., 2021, **Tectono-metamorphic evolution of the northern Dom Feliciano Belt foreland, Santa Catarina, Brazil: Implications for models of subduction-driven orogenesis**, in review at *Tectonics*

The metamorphosed supracrustal rocks within the foreland of the Dom Feliciano Belt (the Schist Belt) occupy a unique position along the western edge of the SANOS, potentially recording the structural and metamorphic evolution of Neoproterozoic orogenesis from its earliest stages. In particular, the Schist Belt should be an ideal candidate to test subduction–collision models of orogenesis, as it lies immediately to the west of the proposed suture (e.g. Basei et al., 2018). Thus, if the Adamastor subduction–collision model is accurate, the Schist Belt should record collision between the arc (the Granite Belt) with the South American passive margin (the Schist Belt). Although there are various studies describing deformation and metamorphism affecting the Schist Belt during Neoproterozoic orogenesis (e.g. Basei et al., 2011a; Saalmann et al., 2006; Sánchez Bettucci et al., 2001), there are

currently no reliable constraints on the timing or conditions of these events, and detailed study of the tectono-metamorphic history of the foreland supracrustal rocks in the northern Dom Feliciano Belt (the Brusque Complex) is almost completely lacking. Unravelling orogenic events as recorded within the Brusque Complex can hopefully also shed light on the validity of alternative tectonic models.

Structural mapping of the Brusque Complex reveals that early deformation occurred during top-to-NW thrusting with tectonic transport near-perpendicular to the trend of the orogenic belt. This deformation was associated with prograde regional metamorphism along a geothermal gradient of ~25°C/km, reaching peak conditions of 540–570°C and 5.5–6.7 kbar. These observations suggest earliest deformation and metamorphism in the Schist Belt occurred during early orogenic crustal thickening driven by thrusting and tectonic burial. We used garnet–whole rock Lu–Hf geochronology to date the timing of earliest garnet growth in the highest-grade rocks of the Brusque Complex, which constrains prograde metamorphism, and by inference the timing of thrusting, to between ca. 660–650 Ma. A combination of garnet–whole rock Sm–Nd and monazite U–Pb geochronology constrains the end of this event to between ca. 650–645 Ma. Finally, a biotite Ar–Ar cooling age suggests that thrust-driven exhumation of the Brusque Complex resulted in cooling at ca. 635 Ma.

Structural mapping further reveals a second set of major deformation structures that are oriented parallel with the primary NE–SW trend of the belt. These consist of upright folds, crenulations, and axial planar cleavages showing association with retrograde overprint of the earlier fabric. This style of deformation contrasts with the dextral strike-slip dominated deformation recorded in the Major Gercino Shear zone at the south-eastern boundary with the Granite Belt. These observations are consistent with a transition from thrusting to partitioned transpression as reported by De Toni et al. (2020a), where the pure shear component of transpression is concentrated in the foreland and the simple shear strike-slip component is concentrated in the hinterland. Large granitic batholiths aged between ca. 615–585 Ma intrude the Brusque Complex parallel to the orientation of these structures (Hueck et al., 2019), indicating intrusion during or after deformation. P–T modelling and garnet dating from a metavolcanic rock adjacent to these intrusions shows that at least parts of the complex were at pressures of ~2.2–3.2 kbar by ca. 600 Ma. Muscovite Ar–Ar ages from shear zones within the complex indicate localised deformation continued until at least ca. 570 Ma.

Our results show that the foreland reached metamorphic conditions typical for orogenic crustal thickening ca. 20–30 million years prior to the onset of massive magmatic activity in the hinterland characterised by the intrusion of the Granite Belt. This unequivocally indicates that early deformation and peak metamorphism in the northern Schist Belt does not record collision with the Granite Belt, suggesting the absence of a large Adamastor Ocean between the hinterland and foreland domains prior to convergence. Instead, based on this data, we believe it is more likely that crustal thickening as the result of convergence between the Congo and Luis Alves Cratons began ca. 660–650 Ma with thrusting

of a high-grade metamorphic hinterland over the foreland, and that granitic magmatism was the result of post-collisional melting processes and not arc magmatism (Bitencourt and Nardi, 1993, 2000; Florisbal et al., 2009; Florisbal et al., 2012a; Florisbal et al., 2012b; Florisbal et al., 2012c; Lara et al., 2017; Oyhantçabal et al., 2007). Such a delay of ca. 20–30 Myr between the timing of earliest recorded crustal thickening and large-scale melting is typical of hot, internal parts of orogens (England and Thompson, 1986; Jamieson et al., 2011; Jamieson and Beaumont, 2013). We suggest that orogenesis in the northern Dom Feliciano Belt was initiated by rift-basin inversion driven by far-field forces transmitted through the crust in an intracontinental or back-arc rift setting (e.g. De Toni et al., 2020b; Konopásek et al., 2018; Konopásek et al., 2020).

Paper III

Percival, J. J., Konopásek, J., Oyhantçabal, P., Sláma, J., Anczkiewicz, R. 2021, **Diachronous two-stage Neoproterozoic evolution of the southern Dom Feliciano Belt, Uruguay**, in preparation for submission to *Journal of Metamorphic Geology* or *Tectonics*

Like the Brusque Complex in the northern Dom Feliciano Belt, the southern part of the Schist Belt (the Lavalleja Complex) potentially records tectonic events from throughout the entire evolution of the orogen. Furthermore, the southern Dom Feliciano Belt contains the largest exposure of Tonian-aged rocks in the hinterland, which are preserved in the basement of the Punta del Este Terrane (the Cerro Olivo Complex). By studying and comparing the tectono-metamorphic histories of the hinterland and foreland domains of the southern Dom Feliciano Belt, we hope to see if the tectonic model presented in **Paper II** is applicable along the entire length of the belt, and if not, what this can tell us about the tectonic evolution of the southern SANOS in general. One noticeable difference in the southern foreland compared to the northern and central sections is the presence of a sliver of Paleoproterozoic basement thrust over the Schist Belt (Mallmann et al., 2007; Oyhantçabal et al., 2018; Rossini and Legrand, 2003), which already alludes to differing tectonic processes between the various parts of the belt. As such, the aim of **Paper III** is to determine the conditions and timing of metamorphism and deformation in 1) the Tonian-aged, high-grade hinterland rocks (Cerro Olivo Complex), 2) the foreland supracrustal rocks (Schist Belt), and 3) the foreland basement nappe (Campanero Unit). To do this, we use a combination of structural mapping, phase equilibria modelling, and geochronology.

Previous studies have shown that the Cerro Olivo Complex hinterland rocks experienced granulite-facies metamorphism associated with top-to-W thrusting (Masquelin et al., 2011). Our P–T modelling shows that the hinterland rocks experienced near-isothermal decompression from ~10 kbar and ~770°C, down to ~6 kbar, which we interpret to reflect rapid thrust-driven exhumation. Garnet Lu–Hf and zircon U–Pb geochronology constrains the timing of this event to between ca. 655–640 Ma, which is consistent

with the timing of crustal thickening recorded in the northern foreland, as discussed in **Paper II**. After high-T metamorphism and associated thrust-dominated deformation in the hinterland at ca. 650 Ma, sub-vertical dextral strike-slip shear zones developed along the boundary between the hinterland and foreland, and the foreland and the Rio de le Plata Craton, such as is observed in the northern part of the belt (**Paper II**). Intrusion of the Granite Belt from ca. 630 Ma was focused along the Sierra Ballena Shear Zone between the hinterland and foreland (Lara et al., 2017; Oyhantçabal et al., 2007).

In contrast, P–T modelling of the Lavalleja Complex revealed that prograde metamorphism in the foreland supracrustal rocks reached up to only lower amphibolite facies conditions, between ~6–7kbar and ~550–570°C, similar to the schists in the Brusque Complex (**Paper II**). However, the timing of this event is dated by garnet Lu–Hf geochronology at 582 ± 23 Ma, which, although imprecise, indicates that garnet growth (and thus peak metamorphism) occurred much later in the southern foreland than in the hinterland and northern foreland. P–T modelling of the foreland basement nappe (the Campanero Unit) indicates similar pressures but higher temperature conditions of ~4–9 kbar and ~670–770°C, and monazite U–Pb dating shows that this high-T metamorphism and partial melting occurred close to timing of metamorphism in the Lavalleja Complex, at ca. 585–570 Ma. These observations support previous interpretations that the Campanero Unit represents a deep part of the foreland basement thrust over the more distal foreland supracrustal rocks. Deformation within the foreland at this time appears to have been dominated by NW-directed thrusting. We interpret this as reflecting a transpressional structure similar to a restraining bend contractional duplex, where the foreland is caught between two major sinistral shear zones at the boundaries with the Rio de la Plata Craton and the hinterland, developing thrusts with movement oblique to the trend of the orogen.

This metamorphic event from ca. 585 Ma is also coeval with the intrusion of large volumes of magmatic rocks into the southern foreland (Lara et al., 2017) and the sinistral reactivation of previously dextral major strike-slip shear zones bordering the foreland (Oriolo et al., 2016a; Oriolo et al., 2016c). Thus, unlike in the northern Dom Feliciano Belt, a significant amount of sinistral transpressional deformation in the southern section appears to have occurred from ca. 585 Ma, which is coeval with sinistral transpressional orogenesis in the Kaoko and Gariep belts (Frimmel, 2018; Goscombe et al., 2003a; Goscombe et al., 2003b; Goscombe et al., 2005a; Goscombe et al., 2005b; Goscombe and Gray, 2008). This diachronous two-stage orogenic history, marked by 1) early thrusting and crustal thickening transitioning into dextral transpression, followed by 2) sinistral transpression, suggests a major tectonic shift within the southern SANOS, which appears to be recorded heterogeneously along the length of the orogen. We suggest that this tectonic shift was driven by the convergence and incorporation of the Kalahari Craton into orogenesis (e.g. Oriolo et al., 2016a).

6 Concluding remarks and future research

Prior to the completion of this thesis, there were no significant detrital zircon data from the Brusque Complex to allow a comparison and correlation between the central and northern Schist Belts, or to demonstrate a clear pre-orogenic connection between the western and eastern foreland supracrustal rocks. **Paper I** provides a contribution for further research into the evolution of the southern SANOS, as well as for Neoproterozoic plate tectonic reconstructions of the transition from Rodinia to Gondwana. This work also provides the first geochronological constraints for the timing of sedimentation (**Paper I**) and metamorphism (**Paper II**) in the Brusque Complex of the northern Dom Feliciano Belt foreland, as well as metamorphism in the southern foreland (**Paper III**) (summarised in Fig. 6). With these data, it is possible to further correlate records of pre-orogenic rifting in the foreland with that seen in the hinterland, as well as to correlate crustal thickening in the northern foreland with high temperature, decompressive metamorphism and thrusting in the hinterland (**Papers II & III**). Metamorphism in the southern foreland, in contrast, shows a stronger temporal connection with later transpressive orogenesis

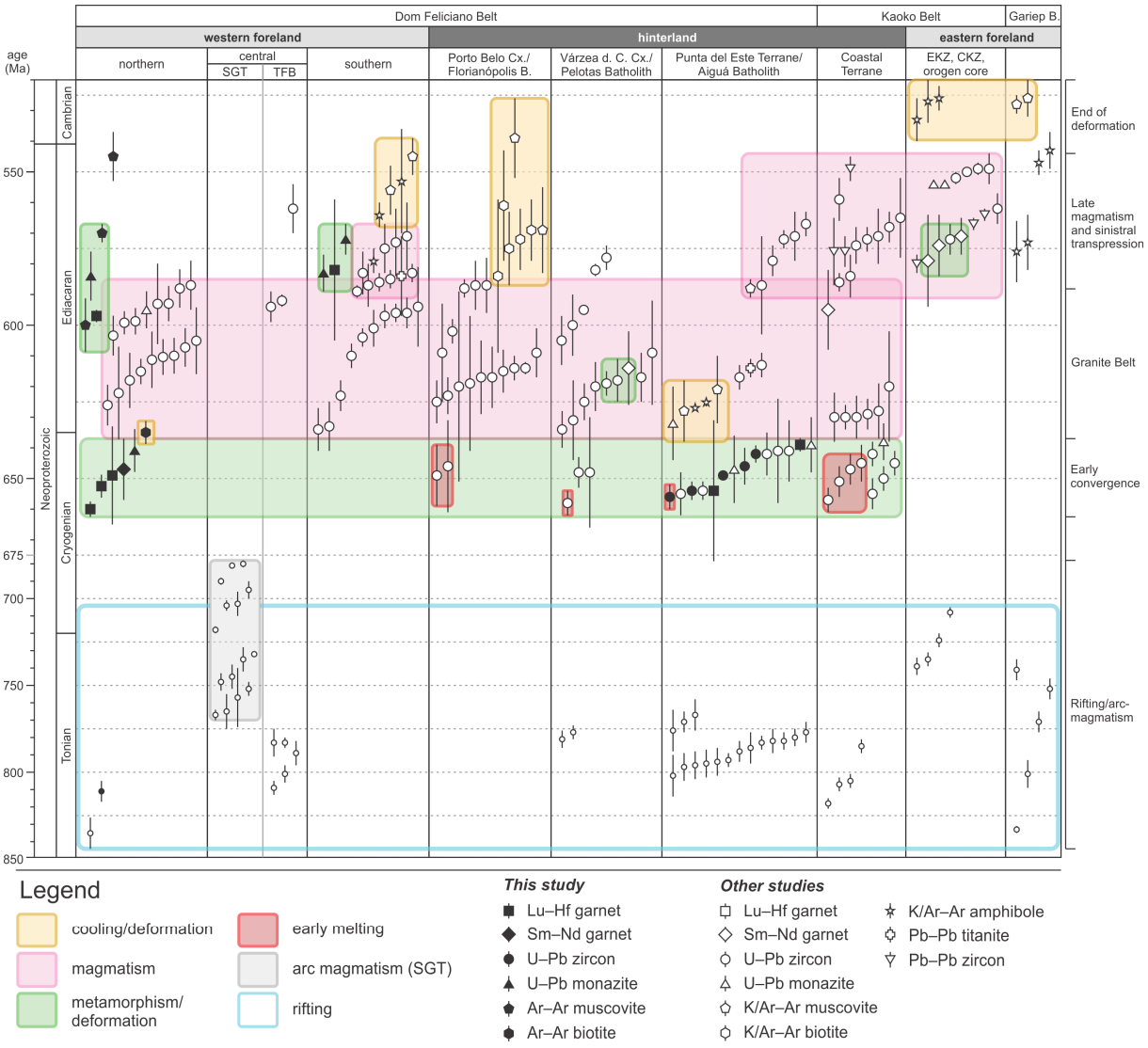

Figure 6. *(previous page)* Summary of major tectonic events using available geochronological data from the southern SANOS. Data from this work (**Papers I, II & III**) are represented by filled shapes, and data from other works are represented by unfilled shapes. Data are grouped by location from the western to eastern forelands (left to right), and within these domains they are grouped from north to south (left to right). SGT = São Gabriel Terrane; TFB = Tijucas Fold Belt; EKZ = Eastern Kaoko Zone; CKZ = Central Kaoko Zone. Sources for data: **northern foreland** – Basei et al. (2008a); Basei et al. (2011a); Campos et al. (2012); Florisbal et al. (2012c); Hueck et al. (2019); Silva et al. (2003); Silva et al. (2005b); Vlach et al. (2009), **central foreland** – Cerva-Alves et al. (2021); Chemale (2000); Gubert et al. (2016); Hartmann et al. (2011); Pertille et al. (2017); Remus et al. (1999); Remus et al. (2000a); Remus et al. (2000b); Saalmann et al. (2011); Silva et al. (2005a); Siviero et al. (2021), **southern foreland** – Gaucher et al. (2008); Hartmann et al. (2002); Lara et al. (2017); Lara et al. (2020); Oriolo et al. (2016c); Oyhantçabal et al. (2007); Oyhantçabal et al. (2009); Oyhantçabal et al. (2012); Rapalini et al. (2015), **northern hinterland** – Chemale et al. (2012); Florisbal et al. (2012c); Passarelli et al. (2010), **central hinterland** – Babinski et al. (1997); Frantz et al. (2003); Gross et al. (2006); Gruber et al. (2016); Koester et al. (2016); Martil (2016); Oliveira et al. (2015); Philipp et al. (2016); Silva et al. (1999); Völz et al. (2020), **southern hinterland** – Basei et al. (2000); Hartmann et al. (2002); Lara et al. (2020); Lenz et al. (2011); Masquelin et al. (2011); Oyhantçabal et al. (2007); Oyhantçabal et al. (2009); Will et al. (2019), **Coastal Terrane and Kaoko Belt** – (Franz et al., 1999); Goscombe et al. (2003b); Goscombe et al. (2005a); Konopásek et al. (2008); Konopásek et al. (2016); Konopásek et al. (2018); Kröner et al. (2004); Seth et al. (1998), **Gariep Belt** – Frimmel and Frank (1998).

in the eastern foreland, where the hinterland is thrust over the foreland in the Kaoko Belt and a small amount of oceanic crust is thrust over the foreland in the Gariep Belt (Fig. 6). The results presented in this thesis highlight the importance of the development and integration of robust geochronological and structural datasets, and thermodynamic modelling, for the study of orogenic belts.

6.1 Future work

6.1.1 Further fieldwork and detailed structural analysis in the southern foreland

The direction of thrusting of the Campanero Unit is difficult to ascertain given the presence of two lineations in the high-T S1 foliation, and detailed structural analysis is hindered by poor outcrop exposure. Although it is not possible to rule out that L2 is the result of pure shear stretching orthogonal to the shear direction, assuming consistent transport-parallel stretching lineations there are two possible scenarios supported by the combined geochronological and structural data: 1) S1 and L1 were produced by an early (ca. 640─630 Ma) low-angle shear event, possibly correlated with west-directed thrusting seen in the Cerro Olivo Complex, and this was followed much later by NNE-directed low-angle thrusting during transpression and sinistral reactivation of the Sierra Ballena Shear Zone, producing L2 by overprinting S1, and developing E─W-trending S2; 2) both lineations developed during the period ca. 585─570 Ma, where L1 and NW-directed thrusting immediately preceded L2 and NNE-directed thrusting, with the direction of tectonic transport rotating during the transpressional episode at ca. 585─570 Ma. Whichever scenario is considered, orogen-parallel stretching contributed significantly to the Neoproterozoic tectono-metamorphic evolution of the Nico Perez Terrane. Such a scenario could be explained through lateral extrusion of the foreland between the restrictive Sarandí del Yí and Sierra Ballena shear zones during oblique transpression, like what is described in the Kaoko Belt (Goscombe et al., 2005b). Further complicating the model are the undeformed, ca. 630 Ma granites that appear to

be intruding the Zanja del Tigre Complex (Oyhantçabal et al., 2009). Exactly how these granitic bodies escaped the ca. 580 Ma transpressional event without being deformed together with the schists is currently unexplained by our model, although possibly they represent underlying rocks exposed as basement inliers beneath another thrust sheet comprised of the Zanja del Tigre Complex supracrustal rocks, and deformation of the overlying schists simply reflects thin skinned tectonics. Ultimately, further detailed strain analysis of the Campanero Unit and adjacent rocks is needed to develop a more robust model.

6.1.2 Intracontinental or back-arc rifting?

One of the primary findings put forth in this study is the high likelihood that orogenic crustal thickening (i.e., continental convergence between the Luis Alves–Nico Perez and the Congo–Kalahari) was already underway by ca. 660–650 Ma, and the low likelihood that subduction arc magmatism was responsible for formation of large volumes of magmatic rocks intruding the orogenic hinterland (the Granite Belt) between ca. 630–580 Ma. This implies the absence of a large Adamastor Ocean, and probably the tectonic setting at the onset of convergence was more similar to an extended rift basin with little to no oceanic crust. However, what cannot be fully answered by the data collected in this study is whether this rift basin was the result of intracontinental or back-arc rifting. Many recent studies in the northern SANOS advocate for intracontinental rifting, which greatly simplifies the geological evolution of the orogen and explains many contradictions and data unexplained by the various subduction–collision models (Cavalcante et al., 2019; Fossen et al., 2020; Konopásek et al., 2020; Meira et al., 2015; Meira et al., 2019b). In contrast, the predominant alternative model in the southern SANOS is that the pre-orogenic tectonic setting for the Dom Feliciano Belt was an arc or back-arc active between ca. 900 and 700 Ma (De Toni et al., 2020b; Koester et al., 2016; Lenz et al., 2013; Martil et al., 2017). These interpretations are supported by the presence of the Sao Gabriel Terrane in the central Dom Feliciano Belt preserving arc magmatism between ca. 900 and 700 Ma (Philipp et al., 2018), as well as the reported arc-like geochemistry of igneous rocks in the hinterland of the belt. However, some studies propose that these latter rocks could well be entirely rift-related, and simply inheriting arc-like geochemistry from the melting of their source rocks (Konopásek et al., 2020). This would place the evolution of the southern SANOS more in line with recently proposed intracontinental orogenic models for the northern sections. In any case, further work is needed to integrate the existing data into a fully realised model, or to find further evidence supporting those that currently exist.

7 References

Abre P., Blanco G., Gaucher C., Frei D. & Frei R., 2020. Provenance of the Late Ediacaran Rocha Formation, Cuchilla Dionisio Terrane, Uruguay: Tectonic implications on the assembly of Gondwana. Precambrian Res., vol. 342, p. 105704. https://doi.org/10.1016/j.precamres.2020.105704.

Alkmim F. F., Kuchenbecker M., Reis H. L. S. & Pedrosa-Soares A. C., 2017. The Araçuaí Belt. In Heilbron M., Cordani U. G. & Alkmim F. F. eds. São Francisco Craton, Eastern Brazil: Tectonic Genealogy of a Miniature Continent. pp. 255-276. Cham: Springer International Publishing https://doi.org/10.1007/978-3-319-01715-0_14.

Amaral L., Caxito F. d. A., Pedrosa-Soares A. C., Queiroga G., Babinski M., Trindade R., Lana C. & Chemale F., 2020. The Ribeirão da Folha ophiolite-bearing accretionary wedge (Araçuaí orogen, SE Brazil): New data for Cryogenian plagiogranite and metasedimentary rocks. Precambrian Res., vol. 336, p. 105522. https://doi.org/10.1016/j.precamres.2019.105522.

Anczkiewicz R. & Thirlwall M. F., 2003. Improving precision of Sm-Nd garnet dating by H2SO4 leaching: a simple solution to the phosphate inclusion problem. Geological Society, London, Special Publications, vol. 220, no. 1, pp. 83–91. https://10.1144/GSL.SP.2003.220.01.05.

Anczkiewicz R., Platt J. P., Thirlwall M. F. & Wakabayashi J., 2004. Franciscan subduction off to a slow start: evidence from high-precision Lu–Hf garnet ages on high grade-blocks. Earth Planet. Sci. Lett., vol. 225, no. 1, pp. 147–161. https://doi.org/10.1016/j.epsl.2004.06.003.

Anczkiewicz R., Chakraborty S., Dasgupta S., Mukhopadhyay D. & Kołtonik K., 2014. Timing, duration and inversion of prograde Barrovian metamorphism constrained by high resolution Lu–Hf garnet dating: A case study from the Sikkim Himalaya, NE India. Earth Planet. Sci. Lett., vol. 407, pp. 70–81. http://dx.doi.org/10.1016/j.epsl.2014.09.035.

Arena K. R., Hartmann L. A. & Lana C., 2018. U–Pb–Hf isotopes and trace elements of metasomatic zircon delimit the evolution of neoproterozoic Capané ophiolite in the southern Brasiliano Orogen. Int. Geol. Rev., pp. 1-18. https://doi.org/10.1080/00206814.2017.1355269.

Babinski M., Chemale F., Van Schmus W. R., Hartmann L. A. & Da Silva L. C., 1997. U-Pb and Sm-Nd geochronology of the neoproterozoic granitic-gneissic Dom Feliciano belt, Southern Brazil. J. S. Am. Earth Sci., vol. 10, no. 3, pp. 263-274. https://doi.org/10.1016/S0895-9811(97)00021-7.

Basei M. A. S., Siga Jr O., Masquelin H., Harara O. M., Reis Neto J. M. & Preciozzi F., 2000. The Dom Feliciano Belt of Brazil and Uruguay and its Foreland Domain, the Rio de la Plata Craton: framework, tectonic evolution and correlation with similar provinces of Southwestern Africa. In Cordani U. G., et al. eds. Tectonic Evolution of South America. pp. 311─334. Rio de Janeiro, Brazil: Geological Society http://10.13140/RG.2.1.5109.4567.

Basei M. A. S., Frimmel H. E., Nutman A. P., Preciozzi F. & Jacob J., 2005. A connection between the Neoproterozoic Dom Feliciano (Brazil/Uruguay) and Gariep (Namibia/South Africa) orogenic belts - Evidence from a reconnaissance provenance study. Precambrian Res., vol. 139, no. 3-4, pp. 195-221. https://www.doi.org/10.1016/j.precamres.2005.06.005.

Basei M. A. S., Grasso C. B., Vlach S. R. F., Nutman A., Siga Jr. O. & Osaki L. S., 2008a. A-type rift-related granite and the lower cryogenian age for the beginning of the Brusque Belt basin. Proceedings of South American Symposium on Isotope Geology. San Carlos de Bariloche, Argentina.

Basei M. A. S., Frimmel H. E., Nutman A. P. & Preciozzi F., 2008b. West Gondwana amalgamation based on detrital zircon ages from Neoproterozoic Ribeira and Dom Feliciano belts of South America and comparison with coeval sequences from SW Africa. Geol. Soc. Spec. Publ., vol. 294, no. 1, pp. 239-256. https://www.doi.org/10.1144/SP294.13.

Basei M. A. S., Campos Neto M. C., Castro N. A., Nutman A. P., Wemmer K., Yamamoto M. T., Hueck M., Osako L., Siga Jr O. & Passarelli C. R., 2011a. Tectonic evolution of the Brusque Group, Dom Feliciano belt, Santa Catarina, Southern Brazil. J. S. Am. Earth Sci., vol. 32, no. 4, p. 324─350. https://doi.org/10.1016/j.jsames.2011.03.016.

Basei M. A. S., Peel E., Sánchez Bettucci L., Preciozzi F. & Nutman A. P., 2011b. The basement of the Punta del Este Terrane (Uruguay): an African Mesoproterozoic fragment at the eastern border

of the South American Río de La Plata craton. Int. J. Earth Sci., vol. 100, pp. 289-304. https://www.doi.org/10.1007/s00531-010-0623-1.

Basei M. A. S., Campos Neto M. d. C., Lopes A. P., Nutman A. P., Liu D. & Sato K., 2013. Polycyclic evolution of Camboriú Complex migmatites, Santa Catarina, Southern Brazil: integrated Hf isotopic and U-Pb age zircon evidence of episodic reworking of a Mesoarchean juvenile crust. Brazilian Journal of Geology, vol. 43, no. 3, pp. 427-443. https://doi.org/10.5327/Z2317-48892013000300002.

Basei M. A. S., Frimmel H. E., Campos Neto M. d. C., de Araujo C. E. G., de Castro N. A. & Passarelli C. R., 2018. The Tectonic History of the Southern Adamastor Ocean Based on a Correlation of the Kaoko and Dom Feliciano Belts. In Siegesmund S., et al. eds. Geology of Southwest Gondwana. pp. 63─85. 1st ed. Cham: Springer International Publishing https://doi.org/10.1007/978-3-319-68920-3_3.

Battisti M. A., Bitencourt M. F., De Toni G. B., Nardi L. V. S. & Konopásek J., 2018. Metavolcanic rocks and orthogneisses from Porongos and Várzea do Capivarita complexes: A case for identification of tectonic interleaving at different crustal levels from structural and geochemical data in southernmost Brazil. J. S. Am. Earth Sci., vol. 88, p. 253─274. https://doi.org/10.1016/j.jsames.2018.08.009.

Bento dos Santos T. M., Munhá J. M., Tassinari C. C. G., Fonseca P. E. & Neto C. D., 2011. Metamorphic P-T evolution of granulites in the central Ribeira Fold Belt, SE Brazil. Geosciences Journal, vol. 15, no. 1, pp. 27-51. https://doi.org/10.1007/s12303-011-0004-1.

Bitencourt M. F. & Nardi L. V. S., 1993. Late- to Post-collisional Brasiliano Magmatism in Southernmost Brazil. Anais da Academia Brasileira de Ciências, vol. 65, p. 3─16. https://10.25249/0375-7536.2000301186189.

Bitencourt M. F. & Nardi L. V. S., 2000. Tectonic setting and sources of magmatism related to the southern Brazilian shear belt. Revista Brasileira de Geociencias, vol. 30, no. 1, p. 186─189.

Bossi J. & Gaucher C., 2004. The Cuchilla Dionisio Terrane, Uruguay: An Allochthonous Block Accreted in the Cambrian to SW-Gondwana. Gondwana Res., vol. 7, no. 3, pp. 661-674. https://doi.org/10.1016/S1342-937X(05)71054-6.

Campos R. S., Philipp R. P., Massonne H.-J., Chemale Jr F. & Theye T., 2011. Petrology and isotope geology of mafic to ultramafic metavolcanic rocks of the Brusque Metamorphic Complex, southern Brazil. Int. Geol. Rev., vol. 54, no. 6, p. 686─713. https://doi.org/10.1080/00206814.2011.569393.

Campos R. S., Philipp R. P., Massonne H.-J. & Chemale Jr F., 2012. Early post-collisional Brasiliano magmatism in Botuverá region, Santa Catarina, southern Brazil: Evidence from petrology, geochemistry, isotope geology and geochronology of the diabase and lamprophyre dikes. J. S. Am. Earth Sci., vol. 37, p. 266─278. https://doi.org/10.1016/j.jsames.2012.02.005.

Cavalcante C., Hollanda M. H., Vauchez A. & Kawata M., 2018. How long can the middle crust remain partially molten during orogeny? Geology, vol. 46, no. 10, pp. 839–842. https://doi.org/10.1130/g45126.1.

Cavalcante C., Fossen H., de Almeida R. P., Hollanda M. H. B. M. & Egydio-Silva M., 2019. Reviewing the puzzling intracontinental termination of the Araçuaí-West Congo orogenic belt and its implications for orogenic development. Precambrian Res., vol. 322, pp. 85–98. https://doi.org/10.1016/j.precamres.2018.12.025.

Cawood P. A., Kröner A., Collins W. J., Kusky T. M., Mooney W. D. & Windley B. F., 2009. Accretionary orogens through Earth history. Geological Society, London, Special Publications, vol. 318, no. 1, pp. 1–36. https://doi.org/10.1144/SP318.1.

Cerva-Alves T., Hartmann L. A., Lana C., Queiroga G. N., Maciel L. A. C., Leandro C. G. & Savian J. F., 2021. Rutile and zircon age and geochemistry in the evolution of the juvenile São Gabriel Terrane early in the Brasiliano Orogeny. J. S. Am. Earth Sci., vol. 112, p. 103505. https://doi.org/10.1016/j.jsames.2021.103505.

Chemale F., Jr, 2000. Evolução geológica do Escudo Sul-rio-grandense. Geologia e Estratigrafia do Rio Grande do Sul, pp. 3-44.

Chemale F., Jr, Mallmann G., Bitencourt M. F. & Kawashita K., 2012. Time constraints on magmatism along the Major Gercino Shear Zone, southern Brazil: Implications for West Gondwana

reconstruction. Gondwana Res., vol. 22, no. 1, pp. 184–199. https://doi.org/10.1016/j.gr.2011.08.018.
Connolly J. A. D., 2005. Computation of phase equilibria by linear programming: A tool for geodynamic modeling and its application to subduction zone decarbonation. Earth Planet. Sci. Lett., vol. 236, no. 1–2, pp. 524–541. https://doi.org/10.1016/j.epsl.2005.04.033.
Costa E. O. d., Gomes E. M., Bitencourt M. d. F., De Toni G. B. & Nardi L. V. S., 2020. Reassessing the PT conditions of Neoproterozoic collisional metamorphism and partial melting in southernmost Brazil. J. S. Am. Earth Sci., vol. 100, p. 102584. https://doi.org/10.1016/j.jsames.2020.102584.
De Toni G. B., Bitencourt M. F., Konopásek J., Martini A., Andrade P. H. S., Florisbal L. M. & Campos R. S., 2020a. Transpressive strain partitioning between the Major Gercino Shear Zone and the Tijucas Fold Belt, Dom Feliciano Belt, Santa Catarina, southern Brazil. J. Struct. Geol., vol. 136, p. 104058. https://doi.org/10.1016/j.jsg.2020.104058.
De Toni G. B., Bitencourt M. F., Nardi L. V. S., Florisbal L. M., Almeida B. S. & Geraldes M., 2020b. Dom Feliciano Belt orogenic cycle tracked by its pre-collisional magmatism: The Tonian (ca. 800 Ma) Porto Belo Complex and its correlations in southern Brazil and Uruguay. Precambrian Res., vol. 342, p. 105702. https://doi.org/10.1016/j.precamres.2020.105702.
De Toni G. B., Bitencourt M. F., Konopásek J., Battisti M. A., Oliveira da Costa E. & Savian J. F., 2021. Autochtonous origin of the Encruzilhada Block, Dom Feliciano Belt, southern Brazil, based on aerogeophysics, image analysis and PT-paths. JGeo, vol. 144, p. 101825. https://doi.org/10.1016/j.jog.2021.101825.
Diener J. F. A. & Powell R., 2010. Influence of ferric iron on the stability of mineral assemblages. Journal of Metamorphic Geology, vol. 28, no. 6, pp. 599-613. https://doi.org/10.1111/j.1525-1314.2010.00880.x.
Diener J. F. A., Thomas R. J. & Macey P. H., 2017. Pan-African accretionary metamorphism in the Sperrgebiet Domain, Gariep Belt, SW Namibia. Precambrian Res., vol. 292, pp. 152-162. https://doi.org/10.1016/j.precamres.2017.02.006.
Dürr S. B. & Dingeldey D. P., 1996. The Kaoko belt (Namibia): Part of a late Neoproterozoic continental-scale strike-slip system. Geology, vol. 24, no. 6, pp. 503-506. https://doi.org/10.1130/0091-7613(1996)024<0503:Tkbnpo>2.3.Co;2.
Egydio-Silva M., Vauchez A., Fossen H., Gonçalves Cavalcante G. C. & Xavier B. C., 2018. Connecting the Araçuaí and Ribeira belts (SE – Brazil): Progressive transition from contractional to transpressive strain regime during the Brasiliano orogeny. J. S. Am. Earth Sci., vol. 86, pp. 127-139. https://doi.org/10.1016/j.jsames.2018.06.005.
England P. C. & Thompson A., 1986. Some thermal and tectonic models for crustal melting in continental collision zones. Geological Society, London, Special Publications, vol. 19, no. 1, p. 83. https://doi.org/10.1144/GSL.SP.1986.019.01.05.
Florisbal L. M., Bitencourt M. F., Nardi L. V. S. & Conceição R. V., 2009. Early post-collisional granitic and coeval mafic magmatism of medium- to high-K tholeiitic affinity within the Neoproterozoic Southern Brazilian Shear Belt. Precambrian Res., vol. 175, no. 1–4, pp. 135–148. https://doi.org/10.1016/j.precamres.2009.09.003.
Florisbal L. M., Janasi V. A., Bitencourt M. F., Nardi L. V. S. & Heaman L. M., 2012a. Contrasted crustal sources as defined by whole-rock and Sr–Nd–Pb isotope geochemistry of neoproterozoic early post-collisional granitic magmatism within the Southern Brazilian Shear Belt, Camboriú, Brazil. J. S. Am. Earth Sci., vol. 39, pp. 24–43. https://doi.org/10.1016/j.jsames.2012.06.013.
Florisbal L. M., Bitencourt M. F., Janasi V. A., Nardi L. V. S. & Heaman L. M., 2012b. Petrogenesis of syntectonic granites emplaced at the transition from thrusting to transcurrent tectonics in post-collisional setting: Whole-rock and Sr–Nd–Pb isotope geochemistry in the Neoproterozoic Quatro Ilhas and Mariscal Granites, Southern Brazil. Lithos, vol. 153, pp. 53–71. https://doi.org/10.1016/j.lithos.2012.04.031.
Florisbal L. M., Janasi V. A., Bitencourt M. F. & Heaman L. M., 2012c. Space–time relation of post-collisional granitic magmatism in Santa Catarina, southern Brazil: U–Pb LA-MC-ICP-MS zircon geochronology of coeval mafic–felsic magmatism related to the Major Gercino Shear Zone. Precambrian Res., vol. 216–219, pp. 132–151. https://doi.org/10.1016/j.precamres.2012.06.015.

Forshaw J. B. & Pattison D. R. M., 2021. Ferrous/ferric (Fe2+/Fe3+) partitioning among silicates in metapelites. Contributions to Mineralogy and Petrology, vol. 176, no. 9, p. 63. https://doi.org/10.1007/s00410-021-01814-4.

Fossen H., Cavalcante C., Konopásek J., Tieppo Meira V., Almeida R., Hollanda M. & Trompette R., 2020. A critical discussion of the subduction-collision model for the Neoproterozoic Araçuaí-West Congo orogen. Precambrian Res., p. 105715. https://doi.org/10.1016/j.precamres.2020.105715.

Fragoso-Cesar A. R. S., 1980. O craton do Rio de la Plata eo cinturao Dom Feliciano no escudo Uruguaio-Sul-Riograndense. Congresso Brasileiro de Geologia. pp. 2879-2882. Anais Camboriú.

Frantz J., McNaughton N. J., Marques J., Hartmann L. A., Botelho N. & Caravaca G., 2003. Shrimp U-Pb zircon ages of granitoids from southernmost Brazil: constraints on the temporal evolution on the Dorsal do Canguçu transcurrent shear zone and the eastern Dom Feliciano Belt. IV South American Symposium on Isotope Geology, pp. 174-177.

Franz L., Romer R. L. & Dingeldey D. P., 1999. Diachronous Pan-African granulite-facies metamorphism (650 Ma and 550 Ma) in the Kaoko Belt, NW Namibia. European Journal of Mineralogy, vol. 11, no. 1, pp. 167-180. https://doi.org/10.1127/ejm/11/1/0167.

Frimmel H. E., Hartnady C. J. H. & Koller F., 1996. Geochemistry and tectonic setting of magmatic units in the Pan-African Gariep Belt, Namibia. Chem. Geol., vol. 130, no. 1-2, pp. 101-121. https://doi.org/10.1016/0009-2541(95)00188-3.

Frimmel H. E. & Frank W., 1998. Neoproterozoic tectono-thermal evolution of the Gariep Belt and its basement, Namibia and South Africa. Precambrian Res., vol. 90, no. 1, pp. 1-28. https://doi.org/10.1016/S0301-9268(98)00029-1.

Frimmel H. E., 2018. The Gariep Belt. In Siegesmund S., et al. eds. Geology of Southwest Gondwana. pp. 353-386. 1st ed. Cham: Springer International Publishing https://www.doi.org/10.1007/978-3-319-68920-3_13.

Gaidies F., Abart R., De Capitani C., Schuster R., Connolly J. A. D. & Reusser E., 2006. Characterization of polymetamorphism in the Austroalpine basement east of the Tauern Window using garnet isopleth thermobarometry. Journal of Metamorphic Geology, vol. 24, no. 6, pp. 451-475. https://doi.org/10.1111/j.1525-1314.2006.00648.x.

Gaucher C., Finney S. C., Poiré D. G., Valencia V. A., Grove M., Blanco G., Pamoukaghlián K. & Peral L. G., 2008. Detrital zircon ages of Neoproterozoic sedimentary successions in Uruguay and Argentina: Insights into the geological evolution of the Río de la Plata Craton. Precambrian Res., vol. 167, no. 1, pp. 150-170. https://doi.org/10.1016/j.precamres.2008.07.006.

Germs G. J. B., 1995. The Neoproterozoic of southwestern Africa, with emphasis on platform stratigraphy and paleontology. Precambrian Res., vol. 73, no. 1, pp. 137-151. https://doi.org/10.1016/0301-9268(94)00075-3.

Goscombe B., Hand M. & Gray D., 2003a. Structure of the Kaoko Belt, Namibia: progressive evolution of a classic transpressional orogen. J. Struct. Geol., vol. 25, no. 7, pp. 1049-1081. https://www.doi.org/10.1016/S0191-8141(02)00150-5.

Goscombe B., Hand M., Gray D. & Mawby J. O., 2003b. The Metamorphic Architecture of a Transpressional Orogen: the Kaoko Belt, Namibia. J. Petrol., vol. 44, no. 4, pp. 679-711. https://www.doi.org/10.1093/petrology/44.4.679.

Goscombe B., Gray D., Armstrong R., Foster D. A. & Vogl J., 2005a. Event geochronology of the Pan-African Kaoko Belt, Namibia. Precambrian Res., vol. 140, no. 3–4, pp. 103.e1–103.e41. https://doi.org/10.1016/j.precamres.2005.07.003.

Goscombe B., Gray D. & Hand M., 2005b. Extrusional Tectonics in the Core of a Transpressional Orogen; the Kaoko Belt, Namibia. J. Petrol., vol. 46, no. 6, pp. 1203-1241. https://www.doi.org/10.1093/petrology/egi014.

Goscombe B. & Gray D., 2007. The Coastal Terrane of the Kaoko Belt, Namibia: Outboard arc-terrane and tectonic significance. Precambrian Res., vol. 155, no. 1, pp. 139-158. https://doi.org/10.1016/j.precamres.2007.01.008.

Goscombe B. & Gray D., 2008. Structure and strain variation at mid-crustal levels in a transpressional orogen: A review of Kaoko Belt structure and the character of West Gondwana amalgamation

and dispersal. Gondwana Res., vol. 13, no. 1, pp. 45–85. https://doi.org/10.1016/j.gr.2007.07.002.
Gross A. O. M. S., Porcher C. C., Fernandes L. A. D. & Koester E., 2006. Neoproterozoic low-pressure/high-temperature collisional metamorphic evolution in the Varzea do Capivarita Metamorphic Suite, SE Brazil: Thermobarometric and Sm/Nd evidence. Precambrian Res., vol. 147, no. 1, pp. 41-64. https://doi.org/10.1016/j.precamres.2006.02.001.
Gross A. O. M. S., Droop G. T. R., Porcher C. C. & Fernandes L. A. D., 2009. Petrology and thermobarometry of mafic granulites and migmatites from the Chafalote Metamorphic Suite: New insights into the Neoproterozoic P–T evolution of the Uruguayan—Sul-Rio-Grandense shield. Precambrian Res., vol. 170, no. 3–4, pp. 157–174. https://doi.org/10.1016/j.precamres.2009.01.011.
Grove M. & Harrison T. M., 1996. 40Ar* diffusion in Fe-rich biotite. Am. Mineral., vol. 81, no. 7–8, pp. 940–951. https://doi.org/10.2138/am-1996-7-816.
Gruber L., Porcher C. C., Koester E., Bertotti A. L., Lenz C., Fernandes L. A. D. & Remus M. V. D., 2016. Isotope geochemistry and geochronology of syn-depositional volcanism in Porongos Metamorphic Complex, Santana da Boa Vista Antiform, Dom Feliciano Belt, Brazil: Onset of an 800 Ma continental arc. J. Sediment. Environ., vol. 1, no. 2, pp. 196-215. https://www.doi.org/10.12957/jse.2016.22722.
Guadagnin F., Chemale Jr F., Dussin I. A., Jelinek A. R., dos Santos M. N., Borba M. L., Justino D., Bertotti A. L. & Alessandretti L., 2010. Depositional age and provenance of the Itajaí Basin, Santa Catarina State, Brazil: Implications for SW Gondwana correlation. Precambrian Res., vol. 180, no. 3–4, pp. 156–182. https://doi.org/10.1016/j.precamres.2010.04.002.
Gubert M. L., Philipp R. P. & Stipp Basei M. A., 2016. The Bossoroca Complex, São Gabriel Terrane, Dom Feliciano Belt, southernmost Brazil: UPb geochronology and tectonic implications for the neoproterozoic São Gabriel Arc. J. S. Am. Earth Sci., vol. 70, pp. 1-17. https://doi.org/10.1016/j.jsames.2016.04.006.
Harrison T. M., Célérier J., Aikman A. B., Hermann J. & Heizler M. T., 2009. Diffusion of 40Ar in muscovite. Geochimica et Cosmochimica Acta, vol. 73, no. 4, pp. 1039–1051. https://doi.org/10.1016/j.gca.2008.09.038.
Hartmann L. A., Santos J. O. S., Bossi J., Campal N., Schipilov A. & McNaughton N. J., 2002. Zircon and titanite U–Pb SHRIMP geochronology of Neoproterozoic felsic magmatism on the eastern border of the Rio de la Plata Craton, Uruguay. J. S. Am. Earth Sci., vol. 15, no. 2, pp. 229-236. https://doi.org/10.1016/S0895-9811(02)00030-5.
Hartmann L. A., Philipp R. P., Santos J. O. S. & McNaughton N. J., 2011. Time frame of 753–680 Ma juvenile accretion during the São Gabriel orogeny, southern Brazilian Shield. Gondwana Res., vol. 19, no. 1, pp. 84-99. https://doi.org/10.1016/j.gr.2010.05.001.
Hartnady C., Joubert P. & Stowe C., 1985. Proterozoic Crustal Evolution in Southwestern Africa. International Union of Geological Sciences, vol. 8, no. 4, pp. 236–244. https://doi.org/10.18814/epiiugs/1985/v8i4/003.
Hasui Y., Carneiro C. D. R. & Coimbra A. M., 1975. The Ribeira Folded Belt. Revista Brasileira de Geociências, vol. 5, no. 4, pp. 257-266.
Heilbron M. & Machado N., 2003. Timing of terrane accretion in the Neoproterozoic–Eopaleozoic Ribeira orogen (se Brazil). Precambrian Res., vol. 125, no. 1, pp. 87–112. https://doi.org/10.1016/S0301-9268(03)00082-2.
Heilbron M., Valeriano C. M., Tassinari C. C. G., Almeida J., Tupinambá M., Siga O. & Trouw R., 2008. Correlation of Neoproterozoic terranes between the Ribeira Belt, SE Brazil and its African counterpart: comparative tectonic evolution and open questions. Geological Society, London, Special Publications, vol. 294, no. 1, p. 211. https://doi.org/10.1144/SP294.12.
Heilbron M., de Morisson Valeriano C., Peixoto C., Tupinambá M., Neubauer F., Dussin I., Corrales F., Bruno H., Lobato M., Horta de Almeida J. C. & Guilherme do Eirado Silva L., 2020. Neoproterozoic magmatic arc systems of the central Ribeira belt, SE-Brazil, in the context of the West-Gondwana pre-collisional history: A review. J. S. Am. Earth Sci., vol. 103, p. 102710. https://doi.org/10.1016/j.jsames.2020.102710.
Heine C., Zoethout J. & Müller R. D., 2013. Kinematics of the South Atlantic rift. Solid Earth, vol. 4, no. 2, pp. 215–253. https://doi.org/10.5194/se-4-215-2013.

Hermann J. & Rubatto D., 2003. Relating zircon and monazite domains to garnet growth zones: age and duration of granulite facies metamorphism in the Val Malenco lower crust. Journal of Metamorphic Geology, vol. 21, no. 9, pp. 833–852. https://doi.org/10.1046/j.1525-1314.2003.00484.x.

Hoffman P. F. & Halverson G. P., 2008. Otavi Group of the western Northern Platform, the Eastern Kaoko Zone and the western Northern Margin Zone. In Miller R. M. ed. The Geology of Namibia. pp. 69-136. Namibia: Geological Survey Namibia.

Höfig D. F., Marques J. C., Basei M. A. S., Giusti R. O., Kohlrausch C. & Frantz J. C., 2018. Detrital zircon geochronology (U-Pb LA-ICP-MS) of syn-orogenic basins in SW Gondwana: New insights into the Cryogenian-Ediacaran of Porongos Complex, Dom Feliciano Belt, southern Brazil. Precambrian Res., vol. 306, pp. 189–208. https://doi.org/10.1016/j.precamres.2017.12.031.

Holland T. J. B. & Powell R., 2011. An improved and extended internally consistent thermodynamic dataset for phases of petrological interest, involving a new equation of state for solids. Journal of Metamorphic Geology, vol. 29, no. 3, pp. 333–383. https://doi.org/10.1111/j.1525-1314.2010.00923.x.

Hueck M., Oyhantçabal P., Basei M. & Siegesmund S., 2018. The Dom Feliciano Belt in Southern Brazil and Uruquay. In Siegesmund S., et al. eds. Geology of Southwest Gondwana. pp. 267–302. 1st ed. Cham: Springer International Publishing https://doi.org/10.1007/978-3-319-68920-3_11.

Hueck M., Basei M. A. S. & Castro N. A. d., 2019. Tracking the sources and the evolution of the late Neoproterozoic granitic intrusions in the Brusque Group, Dom Feliciano Belt, South Brazil: LA-ICP-MS and SHRIMP geochronology coupled to Hf isotopic analysis. Precambrian Res., vol. 338, p. 105566. https://doi.org/10.1016/j.precamres.2019.105566.

Jamieson R. A., Unsworth M. J., Harris N. B. W., Rosenberg C. L. & Schulmann K., 2011. Crustal Melting and the Flow of Mountains. Elements, vol. 7, no. 4, pp. 253–260. https://doi.org/10.2113/gselements.7.4.253.

Jamieson R. A. & Beaumont C., 2013. On the origin of orogens. Geological Society of America Bulletin, vol. 125, no. 11–12, pp. 1671–1702. https://doi.org/10.1130/b30855.1.

Juliani C., Hackspacher P., Dantas E. L. & Fetter A. H., 2000. The mesoproterozoic volcano-sedimentary Serra do Itaberaba Group of the Central Ribeira Belt, São Paulo State, Brazil: implications for the age of the overlying São Roque Group. Revista brasileira de geociências, vol. 30, no. 1, pp. 82-86. https://doi.org/10.25249/0375-7536.2000301082086.

Jung S., Brandt S., Bast R., Scherer E. E. & Berndt J., 2019. Metamorphic petrology of a high-T/low-P granulite terrane (Damara belt, Namibia) – Constraints from pseudosection modelling and high-precision Lu–Hf garnet-whole rock dating. Journal of Metamorphic Geology, vol. 37, no. 1, pp. 41-69. https://doi.org/10.1111/jmg.12448.

Koester E., Porcher C. C., Pimentel M. M., Fernandes L. A. D., Vignol-Lelarge M. L., Oliveira L. D. & Ramos R. C., 2016. Further evidence of 777 Ma subduction-related continental arc magmatism in Eastern Dom Feliciano Belt, southern Brazil: The Chácara das Pedras Orthogneiss. J. S. Am. Earth Sci., vol. 68, pp. 155–166. https://doi.org/10.1016/j.jsames.2015.12.006.

Konopásek J., Kosler J., Tajčmanová L., Ulrich S. & Kitt S., 2008. Neoproterozoic igneous complex emplaced along major tectonic boundary in the Kaoko Belt (NW Namibia): ion probe and LA-ICP-MS dating of magmatic and metamorphic zircons. J. Geol. Soc. Lond., vol. 165, no. 1, pp. 153–165. https://doi.org/10.1144/0016-76492006-192.

Konopásek J., Košler J., Sláma J. & Janoušek V., 2014. Timing and sources of pre-collisional Neoproterozoic sedimentation along the SW margin of the Congo Craton (Kaoko Belt, NW Namibia). Gondwana Res., vol. 26, no. 1, pp. 386–401. https://doi.org/10.1016/j.gr.2013.06.021.

Konopásek J., Sláma J. & Košler J., 2016. Linking the basement geology along the Africa-South America coasts in the South Atlantic. Precambrian Res., vol. 280, pp. 221–230. https://doi.org/10.1016/j.precamres.2016.05.011.

Konopásek J., Hoffmann K.-H., Sláma J. & Košler J., 2017. The onset of flysch sedimentation in the Kaoko Belt (NW Namibia) – Implications for the pre-collisional evolution of the Kaoko–Dom

Feliciano–Gariep orogen. Precambrian Res., vol. 298, pp. 220–234. http://dx.doi.org/10.1016/j.precamres.2017.06.017.
Konopásek J., Janoušek V., Oyhantçabal P., Sláma J. & Ulrich S., 2018. Did the circum-Rodinia subduction trigger the Neoproterozoic rifting along the Congo–Kalahari Craton margin? Int. J. Earth Sci., vol. 107, no. 5, pp. 1859–1894. https://doi.org/10.1007/s00531-017-1576-4.
Konopásek J., Anczkiewicz R., Jeřábek P., Corfu F. & Žáčková E., 2019. Chronology of the Saxothuringian subduction in the West Sudetes (Bohemian Massif, Czech Republic and Poland). Journal of the Geological Society, vol. 176, no. 3, pp. 492-504. https://doi.org/10.1144/jgs2018-173.
Konopásek J., Cavalcante C., Fossen H. & Janoušek V., 2020. Adamastor – an ocean that never existed? Earth-Sci. Rev., vol. 205, p. 103201. https://doi.org/10.1016/j.earscirev.2020.103201.
Kröner A., 1975. Late Precambrian formations in the western Richtersveld, northern Cape Province. Transactions of the Royal Society of South Africa, vol. 41, no. 4, pp. 375-433. https://doi.org/10.1080/00359197509519451.
Kröner A., 1977. Precambrian mobile belts of southern and eastern Africa — ancient sutures or sites of ensialic mobility? A case for crustal evolution towards plate tectonics, vol. 40, pp. 101-136.
Kröner S., Konopásek J., Kröner A., Passchier C. W., Poller U., Wingate M. T. D. & Hofmann K. H., 2004. U-Pb and Pb-Pb zircon ages for metamorphic rocks in the Kaoko Belt of Northwestern Namibia: A Palaeo- to Mesoproterozoic basement reworked during the Pan-African orogeny. S. Afr. J. Geol., vol. 107, no. 3, pp. 455-476. https://www.doi.org/10.2113/107.3.455.
Lagos M., Scherer E. E., Tomaschek F., Münker C., Keiter M., Berndt J. & Ballhaus C., 2007. High precision Lu–Hf geochronology of Eocene eclogite-facies rocks from Syros, Cyclades, Greece. Chem. Geol., vol. 243, no. 1, pp. 16-35. https://doi.org/10.1016/j.chemgeo.2007.04.008.
Lapen T. J., Johnson C. M., Baumgartner L. P., Mahlen N. J., Beard B. L. & Amato J. M., 2003. Burial rates during prograde metamorphism of an ultra-high-pressure terrane: an example from Lago di Cignana, western Alps, Italy. Earth Planet. Sci. Lett., vol. 215, no. 1, pp. 57–72. https://doi.org/10.1016/S0012-821X(03)00455-2.
Lara P., Oyhantçabal P. & Dadd K., 2017. Post-collisional, Late Neoproterozoic, high-Ba-Sr granitic magmatism from the Dom Feliciano Belt and its cratonic foreland, Uruguay: Petrography, geochemistry, geochronology, and tectonic implications. Lithos, vol. 277, pp. 178-198. https://doi.org/10.1016/j.lithos.2016.11.026.
Lara P., Oyhantçabal P. & Belousova E., 2020. Two distinct crustal sources for Late Neoproterozoic granitic magmatism across the Sierra Ballena Shear Zone, Dom Feliciano Belt, Uruguay: Whole-rock geochemistry, zircon geochronology and Sr-Nd-Hf isotope evidence. Precambrian Res., vol. 341, p. 105625. https://doi.org/10.1016/j.precamres.2020.105625.
Lenz C., 2006. Evolução metamórfica dos metapelitos da antiforme Serra dos Pedrosas: condições e idades do metamorfismo. Instituto de Geociências. Universidade Federal do Rio Grande do Sul.
Lenz C., Fernandes L. A. D., McNaughton N. J., Porcher C. C. & Masquelin H., 2011. U–Pb SHRIMP ages for the Cerro Bori Orthogneisses, Dom Feliciano Belt in Uruguay: Evidences of a ∼800Ma magmatic and ∼650Ma metamorphic event. Precambrian Res., vol. 185, no. 3, pp. 149–163. https://doi.org/10.1016/j.precamres.2011.01.007.
Lenz C., Porcher C., Fernandes L., Masquelin H., Koester E. & Conceição R., 2013. Geochemistry of the Neoproterozoic (800–767 Ma) Cerro Bori orthogneisses, Dom Feliciano Belt in Uruguay: tectonic evolution of an ancient continental arc. Mineral. Petrol., vol. 107, pp. 785–806. https://doi.org/10.1007/s00710-012-0244-4.
Mallmann G., Chemale Jr F., Ávila J. N., Kawashita K. & Armstrong R. A., 2007. Isotope geochemistry and geochronology of the Nico Pérez Terrane, Rio de la Plata Craton, Uruguay. Gondwana Res., vol. 12, no. 4, pp. 489-508. https://doi.org/10.1016/j.gr.2007.01.002.
Martil M. M. D., 2016. O Magmatismo De Arco Continental Pré-colisional (790 Ma) E a Reconstituição Espaço-temporal Do Regime Transpressivo (650 Ma) No Complexo Várzea Do Capivarita, Sul Da Província Mantiqueira. Universidade Federal do Rio Grande do Sul, Available at: https://www.lume.ufrgs.br/handle/10183/149194.
Martil M. M. D., Bitencourt M. F., Nardi L. V. S., Koester E. & Pimentel M. M., 2017. Pre-collisional, Tonian (ca. 790 Ma) continental arc magmatism in southern Mantiqueira Province, Brazil:

Geochemical and isotopic constraints from the Várzea do Capivarita Complex. Lithos, vol. 274–275, pp. 39–52. https://doi.org/10.1016/j.lithos.2016.11.011.

Martin H. & Porada H., 1977. The intracratonic branch of the Damara Orogen in South West Africa I. Discussion of geodynamic models. Precambrian Res., vol. 5, no. 4, pp. 311-338. https://doi.org/10.1016/0301-9268(77)90039-0.

Masquelin H., Fernandes L., Lenz C., Porcher C. C. & McNaughton N. J., 2011. The Cerro Olivo Complex: A pre-collisional Neoproterozoic magmatic arc in Eastern Uruguay. Int. Geol. Rev., vol. 54, pp. 1161-1183. https://www.doi.org/10.1080/00206814.2011.626597.

Mattinson J. M., 2010. Analysis of the relative decay constants of 235U and 238U by multi-step CA-TIMS measurements of closed-system natural zircon samples. Chem. Geol., vol. 275, no. 3, pp. 186-198. https://doi.org/10.1016/j.chemgeo.2010.05.007.

McCourt S., Armstrong R., Jelsma H. & Mapeo R., 2013. New U-Pb SHRIMP ages from the Lubango region, SW Angola: Insights into the Palaeoproterozoic evolution of the Angolan Shield, southern Congo Craton, Africa. Geol. Soc. Spec. Publ., vol. 170, no. 2, pp. 353–363. https://doi.org/10.1144/jgs2012-059.

Meira V. T., García-Casco A., Juliani C., Almeida R. P. & Schorscher J. H. D., 2015. The role of intracontinental deformation in supercontinent assembly: insights from the Ribeira Belt, Southeastern Brazil (Neoproterozoic West Gondwana). Terra Nova, vol. 27, no. 3, pp. 206-217. https://doi.org/10.1111/ter.12149.

Meira V. T., Garcia-Casco A., Juliani C. & Schorscher J. H. D., 2019a. Late Tonian within-plate mafic magmatism and Ediacaran partial melting and magmatism in the Costeiro Domain, Central Ribeira Belt, Brazil. Precambrian Res., vol. 334, p. 105440. https://doi.org/10.1016/j.precamres.2019.105440.

Meira V. T., Garcia-Casco A., Hyppolito T., Juliani C. & Schorscher J. H. D., 2019b. Tectono-Metamorphic Evolution of the Central Ribeira Belt, Brazil: A Case of Late Neoproterozoic Intracontinental Orogeny and Flow of Partially Molten Deep Crust During the Assembly of West Gondwana. Tectonics, vol. 38, no. 8, pp. 3182–3209. https://doi.org/10.1029/2018tc004959.

Oliveira D. S. d., Sommer C. A., Philipp R. P., Lima E. F. d. & Basei M. Â. S., 2015. Post-collisional subvolcanic rhyolites associated with the Neoproterozoic Pelotas Batholith, southern Brazil. J. S. Am. Earth Sci., vol. 63, pp. 84-100. https://doi.org/10.1016/j.jsames.2015.05.009.

Oriolo S., Oyhantçabal P., Wemmer K., Heidelbach F., Pfänder J., Basei M. A. S., Hueck M., Hannich F., Sperner B. & Siegesmund S., 2016a. Shear zone evolution and timing of deformation in the Neoproterozoic transpressional Dom Feliciano Belt, Uruguay. J. Struct. Geol., vol. 92, pp. 59-78. https://doi.org/10.1016/j.jsg.2016.09.010.

Oriolo S., Oyhantçabal P., Basei M. A. S., Wemmer K. & Siegesmund S., 2016b. The Nico Pérez Terrane (Uruguay): From Archean crustal growth and connections with the Congo Craton to late Neoproterozoic accretion to the Río de la Plata Craton. Precambrian Res., vol. 280, pp. 147–160. https://doi.org/10.1016/j.precamres.2016.04.014.

Oriolo S., Oyhantçabal P., Wemmer K., Basei M. A. S., Benowitz J., Pfänder J., Hannich F. & Siegesmund S., 2016c. Timing of deformation in the Sarandí del Yí Shear Zone, Uruguay: Implications for the amalgamation of western Gondwana during the Neoproterozoic Brasiliano-Pan-African Orogeny. Tectonics, vol. 35, no. 3, pp. 754–771. https://doi.org/10.1002/2015tc004052.

Oriolo S., Oyhantçabal P., Konopásek J., Basei M. A. S., Frei R., Sláma J., Wemmer K. & Siegesmund S., 2019. Late Paleoproterozoic and Mesoproterozoic magmatism of the Nico Pérez Terrane (Uruguay): Tightening up correlations in southwestern Gondwana. Precambrian Res., vol. 327, pp. 296-313. https://doi.org/10.1016/j.precamres.2019.04.012.

Oyhantçabal P., Siegesmund S., Wemmer K., Frei R. & Layer P., 2007. Post-collisional transition from calc-alkaline to alkaline magmatism during transcurrent deformation in the southernmost Dom Feliciano Belt (Braziliano–Pan-African, Uruguay). Lithos, vol. 98, no. 1–4, p. 141─159. https://doi.org/10.1016/j.lithos.2007.03.001.

Oyhantçabal P., Siegesmund S., Wemmer K., Presnyakov S. & Layer P., 2009. Geochronological constraints on the evolution of the southern Dom Feliciano Belt (Uruguay). Journal of the

Geological Society, vol. 166, no. 6, p. 1075─1084. https://doi.org/10.1144/0016-76492008-122.

Oyhantçabal P., Siegesmund S. & Wemmer K., 2011a. The Río de la Plata Craton: a review of units, boundaries, ages and isotopic signature. Int. J. Earth Sci., vol. 100, no. 2, p. 201─220. https://doi.org/10.1007/s00531-010-0580-8.

Oyhantçabal P., Siegesmund S., Wemmer K. & Passchier C. W., 2011b. The transpressional connection between Dom Feliciano and Kaoko Belts at 580–550 Ma. Int. J. Earth Sci., vol. 100, p. 379─390. https://doi.org/10.1007/s00531-010-0577-3.

Oyhantçabal P., Wagner-Eimer M., Wemmer K., Schulz B., Frei R. & Siegesmund S., 2012. Paleo- and Neoproterozoic magmatic and tectonometamorphic evolution of the Isla Cristalina de Rivera (Nico Pérez Terrane, Uruguay). Int. J. Earth Sci., vol. 101, no. 7, pp. 1745-1762. https://doi.org/10.1007/s00531-012-0757-4.

Oyhantçabal P., Oriolo S., Philipp R. P., Wemmer K. & Siegesmund S., 2018. The Nico Pérez Terrane of Uruguay and Southeastern Brazil. In Siegesmund S., et al. eds. Geology of Southwest Gondwana. pp. 161-188. Cham: Springer International Publishing https://doi.org/10.1007/978-3-319-68920-3_7.

Oyhantçabal P., Oriolo S., Wemmer K., Basei M. A. S., Frei D. & Siegesmund S., 2021. Provenance of metasedimentary rocks of the western Dom Feliciano Belt in Uruguay: Insights from U–Pb detrital zircon geochronology, Hf and Nd model ages, and geochemical data. J. S. Am. Earth Sci., vol. 108, p. 103139. https://doi.org/10.1016/j.jsames.2020.103139.

Passarelli C. R., Basei M. A. S., Siga O., Reath I. M. & Campos Neto M. d. C., 2010. Deformation and geochronology of syntectonic granitoids emplaced in the Major Gercino Shear Zone, southeastern South America. Gondwana Res., vol. 17, no. 4, p. 688─703. https://doi.org/10.1016/j.gr.2009.09.013.

Passarelli C. R., Basei M. A. S., Siga O. & Harara O. M. M., 2018. The Luis Alves and Curitiba Terranes: Continental Fragments in the Adamastor Ocean. In Siegesmund S., et al. eds. Geology of Southwest Gondwana. pp. 189-215. Cham: Springer International Publishing https://www.doi.org/10.1007/978-3-319-68920-3_8.

Passarelli C. R., Verma S. K., McReath I., Basei M. A. S. & Siga O., 2019. Tracing the history from Rodinia break-up to the Gondwana amalgamation in the Embu Terrane, southern Ribeira Belt, Brazil. Lithos, vol. 342-343, pp. 1-17. https://doi.org/10.1016/j.lithos.2019.05.024.

Passchier C. W., Trouw R. A. J., Ribeiro A. & Paciullo F. V. P., 2002. Tectonic evolution of the southern Kaoko belt, Namibia. J. Afr. Earth Sci., vol. 35, no. 1, pp. 61-75. https://doi.org/10.1016/S0899-5362(02)00030-1.

Pecoits E., Aubet N. R., Heaman L. M., Philippot P., Rosière C. A., Veroslavsky G. & Konhauser K. O., 2016. UPb detrital zircon ages from some Neoproterozoic successions of Uruguay: Provenance, stratigraphy and tectonic evolution. J. S. Am. Earth Sci., vol. 71, pp. 108-130. https://doi.org/10.1016/j.jsames.2016.07.003.

Pedrosa-Soares A. C., Noce C. M., Wiedemann C. M. & Pinto C. P., 2001. The Araçuaí-West-Congo Orogen in Brazil: an overview of a confined orogen formed during Gondwanaland assembly. Precambrian Res., vol. 110, no. 1, p. 307─323. https://doi.org/10.1016/S0301-9268(01)00174-7.

Pedrosa-Soares A. C., De Campos C. P., Noce C., Silva L. C., Novo T., Roncato J., Medeiros S., Castañeda C., Queiroga G., Dantas E., Dussin I. & Alkmim F., 2011. Late Neoproterozoic-Cambrian granitic magmatism in the Araçuaí orogen (Brazil), the Eastern Brazilian Pegmatite Province and related mineral resources. Geological Society, London, Special Publications, vol. 350, no. 1, p. 25. https://doi.org/10.1144/SP350.3.

Pedrosa-Soares A. n. C., Vidal P., Leonardos O. H. & de Brito Neves B. B., 1998. Neoproterozoic oceanic remnants in eastern Brazil: Further evidence and refutation of an exclusively ensialic evolution for the Araçuaí–West Congo orogen. Geology, vol. 26, no. 6, pp. 519-522. https://doi.org/10.1130/0091-7613(1998)026<0519:Norieb>2.3.Co;2.

Pertille J., Hartmann L. A., Philipp R. P., Petry T. S. & de Carvalho Lana C., 2015a. Origin of the Ediacaran Porongos Group, Dom Feliciano Belt, southern Brazilian Shield, with emphasis on whole rock and detrital zircon geochemistry and U–Pb, Lu–Hf isotopes. J. S. Am. Earth Sci., vol. 64, pp. 69-93. https://www.doi.org/10.1016/j.jsames.2015.09.001.

Pertille J., Hartmann L. A. & Philipp R. P., 2015b. Zircon U–Pb age constraints on the Paleoproterozoic sedimentary basement of the Ediacaran Porongos Group, Sul-Riograndense Shield, southern Brazil. J. S. Am. Earth Sci., vol. 63, pp. 334-345. https://doi.org/10.1016/j.jsames.2015.08.005.

Pertille J., Hartmann L. A., Santos J. O. S., McNaughton N. J. & Armstrong R., 2017. Reconstructing the Cryogenian–Ediacaran evolution of the Porongos fold and thrust belt, Southern Brasiliano Orogen, based on Zircon U–Pb–Hf–O isotopes. Int. Geol. Rev., vol. 59, no. 12, p. 1532─1560. https://doi.org/10.1080/00206814.2017.1285257.

Philipp R. P., Mallmann G., Bitencourt M. F., Souza E. R., Liz J. D., Wild F., Arendt S., Oliveira A. S., Duarte L. C., Rivera C. B. & Prado M., 2004. Caracterização Litológica e Evolução Metamórfica da Porção Leste do Complexo Metamórfico Brusque, Santa Catarina. Revista Brasileira de Geociências, vol. 34, p. 21─34. https://doi.org/10.25249/0375-7536.20043412134.

Philipp R. P. & Machado R., 2005. The Late Neoproterozoic granitoid magmatism of the Pelotas Batholith, southern Brazil. J. S. Am. Earth Sci., vol. 19, no. 4, p. 461─478. https://doi.org/10.1016/j.jsames.2005.06.010.

Philipp R. P., Bom F. M., Pimentel M. M., Junges S. L. & Zvirtes G., 2016. SHRIMP U-Pb age and high temperature conditions of the collisional metamorphism in the Várzea do Capivarita Complex: Implications for the origin of Pelotas Batholith, Dom Feliciano Belt, southern Brazil. J. S. Am. Earth Sci., vol. 66, pp. 196-207. https://doi.org/10.1016/j.jsames.2015.11.008.

Philipp R. P., Pimentel M. M. & Basei M. A. S., 2018. The Tectonic Evolution of the São Gabriel Terrane, Dom Feliciano Belt, Southern Brazil: The Closure of the Charrua Ocean. In Siegesmund S., et al. eds. Geology of Southwest Gondwana. pp. 243─265. Cham: Springer International Publishing https://doi.org/10.1007/978-3-319-68920-3_10.

Pollington A. D. & Baxter E. F., 2010. High resolution Sm–Nd garnet geochronology reveals the uneven pace of tectonometamorphic processes. Earth Planet. Sci. Lett., vol. 293, no. 1, p. 63─71. https://doi.org/10.1016/j.epsl.2010.02.019.

Pollington A. D. & Baxter E. F., 2011. High precision microsampling and preparation of zoned garnet porphyroblasts for Sm–Nd geochronology. Chem. Geol., vol. 281, no. 3, pp. 270-282. https://doi.org/10.1016/j.chemgeo.2010.12.014.

Porada H., 1979. The Damara-Ribeira orogen of the Pan-African─Brasiliano cycle in Namibia (Southwest Africa) and Brazil as interpreted in terms of continental collision. Tectonophysics, vol. 57, no. 2, p. 237─265. https://doi.org/10.1016/0040-1951(79)90150-1.

Porada H., 1989. Pan-African rifting and orogenesis in southern to equatorial Africa and eastern Brazil. Precambrian Res., vol. 44, no. 2, p. 103─136. https://doi.org/10.1016/0301-9268(89)90078-8.

Preciozzi F., Masquelin H. & Basei M., 1999. The namaqua/grenville terrane of eastern Uruguay: 2nd South American symposium on isotope geology. Argentina, pp. 338-340.

Raimondo T., Hand M. & Collins W. J., 2014. Compressional intracontinental orogens: Ancient and modern perspectives. Earth-Sci. Rev., vol. 130, p. 128─153. https://doi.org/10.1016/j.earscirev.2013.11.009.

Rapalini A. E., Tohver E., Bettucci L. S., Lossada A. C., Barcelona H. & Pérez C., 2015. The late Neoproterozoic Sierra de las Ánimas Magmatic Complex and Playa Hermosa Formation, southern Uruguay, revisited: Paleogeographic implications of new paleomagnetic and precise geochronologic data. Precambrian Res., vol. 259, pp. 143-155. https://doi.org/10.1016/j.precamres.2014.11.021.

Remus M. V. D., McNaughton N. J., Hartmann L. A., Koppe J. C., Fletcher I. R., Groves D. I. & Pinto V. M., 1999. Gold in the Neoproterozoic juvenile Bossoroca Volcanic Arc of southernmost Brazil: isotopic constraints on timing and sources. J. S. Am. Earth Sci., vol. 12, no. 4, pp. 349-366. https://doi.org/10.1016/S0895-9811(99)00026-7.

Remus M. V. D., Hartmann L. A., McNaughton N. J., Groves D. I. & Reischl J. L., 2000a. Distal Magmatic-Hydrothermal Origin for the Camaquã Cu (Au-Ag) and Santa Maria Pb, Zn (Cu-Ag) Deposits, Southern Brazil. Gondwana Res., vol. 3, no. 2, pp. 155-174. https://doi.org/10.1016/S1342-937X(05)70094-0.

Remus M. V. D., Hartmann L. A., McNaughton N. J., Groves D. I. & Fletcher I. R., 2000b. The link between hydrothermal epigenetic copper mineralization and the Caçapava Granite of the

Brasiliano Cycle in southern Brazil. J. S. Am. Earth Sci., vol. 13, no. 3, pp. 191-216. https://doi.org/10.1016/S0895-9811(00)00017-1.

Rossini C. A. & Legrand J. M., 2003. Tecto-metamorphic events in the Carapé group: a model for its Neoproterozoic evolution. Revista de la Sociedad Uruguaya de Geología, vol. 1, p. 49─67.

Rubatto D., Hermann J. & Buick I. S., 2006. Temperature and Bulk Composition Control on the Growth of Monazite and Zircon During Low-pressure Anatexis (Mount Stafford, Central Australia). J. Petrol., vol. 47, no. 10, p. 1973─1996. https://doi.org/10.1093/petrology/egl033.

Saalmann K., Remus M. V. D. & Hartmann L. A., 2006. Structural evolution and tectonic setting of the Porongos belt, southern Brazil. Geological Magazine, vol. 143, no. 1, p. 59─88. https://doi.org/10.1017/S0016756805001433.

Saalmann K., Gerdes A., Lahaye Y., Hartmann L., Remus M. & Läufer A., 2011. Multiple accretion at the eastern margin of the Rio de la Plata craton: the prolonged Brasiliano orogeny in southernmost Brazil. Int. J. Earth Sci., vol. 100, p. 355─378. https://doi.org/10.1007/s00531-010-0564-8.

Sánchez Bettucci L., Cosarinsky M. & Ramos V. A., 2001. Tectonic Setting of the Late Proterozoic Lavalleja Group (Dom Feliciano Belt), Uruguay. Gondwana Res., vol. 4, no. 3, pp. 395-407. https://doi.org/10.1016/S1342-937X(05)70339-7.

Schaen A. J., Jicha B. R., Hodges K. V., Vermeesch P., Stelten M. E., Mercer C. M., Phillips D., Rivera T. A., Jourdan F., Matchan E. L., Hemming S. R., Morgan L. E., Kelley S. P., Cassata W. S., Heizler M. T., Vasconcelos P. M., Benowitz J. A., Koppers A. A. P., Mark D. F., Niespolo E. M., Sprain C. J., Hames W. E., Kuiper K. F., Turrin B. D., Renne P. R., Ross J., Nomade S., Guillou H., Webb L. E., Cohen B. A., Calvert A. T., Joyce N., Ganerød M., Wijbrans J., Ishizuka O., He H., Ramirez A., Pfänder J. A., Lopez-Martínez M., Qiu H. & Singer B. S., 2020. Interpreting and reporting 40Ar/39Ar geochronologic data. Geological Society of America Bulletin, vol. 133, no. 3–4, pp. 461–487. https://doi.org/10.1130/B35560.1.

Scherer E. E., Cameron K. L. & Blichert-Toft J., 2000. Lu–Hf garnet geochronology: closure temperature relative to the Sm–Nd system and the effects of trace mineral inclusions. Geochimica et Cosmochimica Acta, vol. 64, no. 19, pp. 3413–3432. https://doi.org/10.1016/S0016-7037(00)00440-3.

Seth B., Kröner A., Mezger K., Nemchin A. A., Pidgeon R. T. & Okrusch M., 1998. Archaean to Neoproterozoic magmatic events in the Kaoko belt of NW Namibia and their geodynamic significance. Precambrian Res., vol. 92, no. 4, pp. 341-363. https://doi.org/10.1016/S0301-9268(98)00086-2.

Silva Lara H., Siegesmund S., Wemmer K., Hueck M., Basei M. A. S. & Oyhantçabal P., 2021. The Sierra de Aguirre Formation, Uruguay: Post-collisional Ediacaran volcanism in the southernmost Dom Feliciano Belt. J. S. Am. Earth Sci., vol. 107, p. 103118. https://doi.org/10.1016/j.jsames.2020.103118.

Silva L. C., Hartmann L. A., McNaughton N. J. & Fletcher I. R., 1999. SHRIMP U/Pb Zircon Dating of Neoproterozoic Granitic Magmatism and Collision in the Pelotas Batholith, Southernmost Brazil. Int. Geol. Rev., vol. 41, no. 6, pp. 531-551. https://doi.org/10.1080/00206819909465156.

Silva L. C., Armstrong R., Pimentel M. M., Scandolara J., Ramgrab G., Wildner W., Angelim L. A. d. A., Vasconcelos A. M., Rizzoto G., Quadros M. L. d. E. S., Sander A. & de Rosa A. L. Z., 2002. Reavaliacao da evolucao geologica em terrenos pre-cambrianos brasileiros com base em novos dados U/Pb SHRIMP Parte III, Provincias Borborema, Mantiqueira meridional e Rio Negro-Juruena. Revista Brasileira de Geociencias, vol. 32, no. 4, pp. 529-544. https://doi.org/10.25249/0375-7536.2002324529544.

Silva L. C., McNaughton N. J., Hartmann L. & Fletcher I. R., 2003. Contrasting Zircon Growth Patterns in Neoproterozoic Granites of Southern Brazil Revealed by Shrimp U-Pb Analyses and SEM Imaging: Consequences for the Discrimination of Emplacement and Inheritance Ages. Short Papers - IV South American Symposium on Isotope Geology. pp. 689-690.

Silva L. C., McNaughton N. J., Armstrong R., Hartmann L. A. & Fletcher I. R., 2005a. The neoproterozoic Mantiqueira Province and its African connections: a zircon-based U–Pb geochronologic subdivision for the Brasiliano/Pan-African systems of orogens. Precambrian Res., vol. 136, no. 3, pp. 203-240. https://doi.org/10.1016/j.precamres.2004.10.004.

Silva L. C., McNaughton N. J. & Fletcher I. R., 2005b. SHRIMP U–Pb zircon geochronology of Neoproterozoic crustal granitoids (Southern Brazil): A case for discrimination of emplacement and inherited ages. Lithos, vol. 82, no. 3–4, pp. 503–525. https://doi.org/10.1016/j.lithos.2004.09.029.

Siviero R. S., Bruguier O., D'ávila Fernandes L. A., Koester E., Porcher C. C. & Kraemer G., 2021. Age and geochemistry of Cambaí Complex, São Gabriel Terrane, Brazil: Arc-related TTG-like rocks. J. S. Am. Earth Sci., vol. 108, p. 103165. https://doi.org/10.1016/j.jsames.2021.103165.

Soldner J., Oliot E., Schulmann K., Štípská P., Kusbach V. & Anczkiewicz R., 2017. Metamorphic P–T–t–d evolution of (U)HP metabasites from the South Tianshan accretionary complex (NW China) — Implications for rock deformation during exhumation in a subduction channel. Gondwana Res., vol. 47, pp. 161-187. https://doi.org/10.1016/j.gr.2016.07.007.

Soldner J., Štípská P., Schulmann K., Yuan C., Anczkiewicz R., Sala D., Jiang Y., Zhang Y. & Wang X., 2020. Coupling of P–T–t–D histories of eclogite and metagreywacke—Insights to late Ordovician–Silurian crustal folding events recorded in the Beishan Orogen (NW China). Journal of Metamorphic Geology, vol. 38, no. 6, pp. 555-591. https://doi.org/10.1111/jmg.12531.

Stüwe K. & Powell R., 1995. PT Paths from modal proportions: application to the Koralm Complex, Eastern Alps. Contributions to Mineralogy and Petrology, vol. 119, no. 1, pp. 83-93. https://doi.org/10.1007/BF00310719.

Tack L., Wingate M. T. D., Liégeois J. P., Fernandez-Alonso M. & Deblond A., 2001. Early Neoproterozoic magmatism (1000–910 Ma) of the Zadinian and Mayumbian Groups (Bas-Congo): onset of Rodinia rifting at the western edge of the Congo craton. Precambrian Res., vol. 110, no. 1, pp. 277-306. https://doi.org/10.1016/S0301-9268(01)00192-9.

Tedeschi M., Novo T., Pedrosa-Soares A., Dussin I., Tassinari C., Silva L. C., Gonçalves L., Alkmim F., Lana C., Figueiredo C., Dantas E., Medeiros S., De Campos C., Corrales F. & Heilbron M., 2016. The Ediacaran Rio Doce magmatic arc revisited (Araçuaí-Ribeira orogenic system, SE Brazil). J. S. Am. Earth Sci., vol. 68, pp. 167–186. https://doi.org/10.1016/j.jsames.2015.11.011.

Thomas R. J., Macey P. H., Spencer C., Dhansay T., Diener J. F. A., Lambert C. W., Frei D. & Nguno A., 2016. The Sperrgebiet Domain, Aurus Mountains, SW Namibia: A ~2020–850Ma window within the Pan-African Gariep Orogen. Precambrian Res., vol. 286, pp. 35-58. https://doi.org/10.1016/j.precamres.2016.09.023.

Thöni M., 2002. Sm–Nd isotope systematics in garnet from different lithologies (Eastern Alps): age results, and an evaluation of potential problems for garnet Sm–Nd chronometry. Chem. Geol., vol. 185, no. 3, pp. 255-281. https://doi.org/10.1016/S0009-2541(01)00410-7.

Trompette R., 1994. Geology of Western Gondwana (2000 - 500 Ma): Pan-African-Brasiliano Aggregation of South America and Africa (translated by A. V. Carozzi, Univ. of Illinois, USA). Milton: Taylor & Francis Group, Milton.

Trompette R., 1997. Neoproterozoic (~600 Ma) aggregation of Western Gondwana: a tentative scenario. Precambrian Res., vol. 82, no. 1, pp. 101-112. https://doi.org/10.1016/S0301-9268(96)00045-9.

Vlach S., Basei M. & Castro N. A., 2009. Idade U-Th-Pb de monazita por microssonda eletrônica do Granito Nova Trento, Grupo Brusque, SC. Simpósio 45 anos de Geocronologia no Brasil, Boletim de Resumos Expandidos. São Paulo, Brasil, pp. 325-327.

Völz W. M., Koester E., Pinto V. M., Debruyne D., Cardozo E., Vieira D. T., Dal Olmo-Barbosa L. & Bastos V. A., 2020. Geochemistry and U–Pb (SHRIMP) geochronology of Grupelli Granite: New constraints on the cessation of felsic magmatism in the Pelotas Batholith, Dom Feliciano Belt. J. S. Am. Earth Sci., vol. 103, p. 102746. https://doi.org/10.1016/j.jsames.2020.102746.

Walczak K., Anczkiewicz R., Szczepański J., Rubatto D. & Košler J., 2017. Combined garnet and zircon geochronology of the ultra-high temperature metamorphism: Constraints on the rise of the Orlica-Śnieżnik Dome, NE Bohemian Massif, SW Poland. Lithos, vol. 292-293, pp. 388-400. https://doi.org/10.1016/j.lithos.2017.09.013.

Warren C. J., Greenwood L. V., Argles T. W., Roberts N. M. W., Parrish R. R. & Harris N. B. W., 2018. Garnet-monazite rare earth element relationships in sub-solidus Metapelites: A case study from Bhutan. Geol. Soc. Spec. Publ., vol. 478, no. 1, pp. 145–166. https://doi.org/10.1144/SP478.1.

White R. W., Powell R., Holland T. J. B., Johnson T. E. & Green E. C. R., 2014. New mineral activity–composition relations for thermodynamic calculations in metapelitic systems. Journal of Metamorphic Geology, vol. 32, no. 3, pp. 261–286. https://doi.org/10.1111/jmg.12071.

Will T. M., Gaucher C., Ling X. X., Li X. H., Li Q. L. & Frimmel H. E., 2019. Neoproterozoic magmatic and metamorphic events in the Cuchilla Dionisio Terrane, Uruguay, and possible correlations across the South Atlantic. Precambrian Res., vol. 320, pp. 303–322. https://doi.org/10.1016/j.precamres.2018.11.004.

SECTION II Research papers

Paper I

Precambrian Research 354 (2021) 106060

Contents lists available at ScienceDirect

Precambrian Research

journal homepage: www.elsevier.com/locate/precamres

Pre-orogenic connection of the foreland domains of the Kaoko–Dom Feliciano–Gariep orogenic system

Jack James Percival [a,*], Jiří Konopásek [a,b], Ragnhild Eiesland [a], Jiří Sláma [c], Roberto Sacks de Campos [d], Matheus Ariel Battisti [e], Maria de Fátima Bitencourt [e]

[a] Department of Geosciences, UiT–The Arctic University of Norway, Dramsveien 201, 9037 Tromsø, Norway
[b] Czech Geological Survey, Klárov 3, 118 21 Prague 1, Czech Republic
[c] Institute of Geology of the Czech Academy of Sciences, Rozvojová 269, 165 00 Prague 6, Czech Republic
[d] Programa de Pós-graduação em Geologia (PPGGeologia), Universidade Federal de Santa Catarina (UFSC), Florianópolis, SC, Brazil
[e] Programa de Pós-graduação em Geociências, Instituto de Geociências, Universidade Federal do Rio Grande do Sul, Porto Alegre, Brazil

ARTICLE INFO

Keywords:
Gondwana
Rodinia
Dom Feliciano Belt
Kaoko Belt
Neoproterozoic
Rifting

ABSTRACT

Neoproterozoic metasedimentary rocks in the foreland domains of the Kaoko–Dom Feliciano–Gariep orogenic system record sedimentation from the breakup of Rodinia to the amalgamation of Gondwana, and thus provide ideal subjects for investigation of the mutual pre-orogenic positions of rifted margins of the African and South American cratonic blocks. U–Pb isotopic dating of zircon in the Brusque Complex of the northern Dom Feliciano Belt, Brazil, provides new constraints on the timing and sources of Neoproterozoic sedimentation along the eastern margin of the Luis Alves Craton. The minimum age of sedimentation is constrained by a U–Pb zircon age of 811 ± 6 Ma from a dyke cross-cutting the Brusque Complex. U–Pb detrital zircon analysis reveals two distinct groups: one with ages ca. 2.2–2.0 Ga consistent with erosion of the adjacent Luis Alves Craton, and another with ages ca. 2.1–1.8 and 1.6–1.0 Ga consistent with erosion of Paleoproterozoic to Mesoproterozoic igneous provinces and/or supracrustal sequences at the edge of the Congo Craton. The age distributions match with analogous rocks of the central Dom Feliciano Belt and the Kaoko Belt, and show similarities with the Gariep Belt, suggesting deposition in a system of coeval and spatially related paleobasins around the time of Rodinia breakup. The absence of Neoproterozoic detrital zircon close to the age of sedimentation suggests deposition in an intracontinental rift or passive margin. A third group contains a significant proportion of Neoproterozoic ca. 670–560 Ma zircon, suggesting similarities with the adjacent Itajaí Basin syn-orogenic foreland sedimentary rocks. This indicates that foreland basin sediments were partly tectonically interleaved with the pre-orogenic metasediments of the Brusque Complex during late-stage orogenic deformation. The findings support an intracontinental rifting model for the formation of the Kaoko–Dom Feliciano–Gariep basin system. The data further indicate that the Luis Alves Craton was in close proximity to the Congo Craton, and likely with the Nico Pérez Terrane and the Kalahari Craton, at the onset of Tonian rifting and the breakup of Rodinia.

1. Introduction

The period between the breakup of Rodinia and the amalgamation of Gondwana during the Neoproterozoic (ca. 800 to 500 Ma) is interpreted to involve the reconfiguration of many of Earth's major cratonic blocks (Johansson, 2014; Li et al., 2008; Merdith et al., 2017a, 2017b). Paleogeographic reconstructions at the time of Rodinia breakup vary significantly in the placement of continental blocks that now belong to the African and South American continents. Some models place the African and South American cratons as close neighbours (Johansson, 2014; Li et al., 2008, 2013), and in other models they are far apart with a large oceanic domain between them (Evans, 2009; Gray et al., 2008; Merdith et al., 2017a). The latter models contrast with tectonic reconstructions of the orogenic belts exposed today along the South Atlantic coastlines, in which authors assume that there was no major reconfiguration of continental blocks and instead suggest that pairs of previously rifted continental margins came back together during their convergent evolution (Basei et al., 2018; Frimmel et al., 2011;

* Corresponding author at: Department of Geosciences, UiT – The Arctic University of Norway, Dramsveien 201, 9037 Tromsø, Norway.
E-mail address: jack.j.percival@uit.no (J.J. Percival).

https://doi.org/10.1016/j.precamres.2020.106060
Received 18 August 2020; Received in revised form 7 December 2020; Accepted 7 December 2020
Available online 30 December 2020

Konopásek et al., 2018, 2020; Oriolo et al., 2016; Porada, 1989).

The breakup of Rodinia and the transition into what would become Western Gondwana began with extensive early-Neoproterozoic rifting at ca. 840–800 Ma (Basei et al., 2008b; Frimmel et al., 2001, 2011; Hueck et al., 2018a; Konopásek et al., 2014, 2018; Porada, 1989), which developed by way of convergence into orogenesis active between ca. 650–550 Ma (Hueck et al., 2018b; Konopásek et al., 2008; Lenz et al., 2011; Oyhantçabal et al., 2009), leaving behind a ca. 3000 km long orogen recently named the South Atlantic Neoproterozoic Orogenic System (SANOS) (Konopásek et al., 2020). The southern part of this system (Fig. 1) is an orogenic triple junction comprised of multiple orogenic belts: the Kaoko, Dom Feliciano and Gariep belts forming a North–South oriented belt continuous with the rest of the SANOS, and the Damara Belt forming an offshoot junction on the African side of the orogen. In the Kaoko–Dom Feliciano–Gariep part of this system, orogenesis was the result of convergence between the Congo and Kalahari cratons on the African side, and the Rio de la Plata craton and other smaller crustal blocks such as the Luis Alves Craton and Nico Pérez and Curitiba terranes on the South American side (Basei et al., 2000, 2009; Frimmel et al., 2011; Frimmel, 2018; Goscombe et al., 2003b; Hueck et al., 2018b; Oriolo et al., 2016). The pre-convergent evolution of this orogenic system is an extensively discussed topic, as it provides context in linking through time the breakup of Rodinia and the amalgamation of Western Gondwana. Central to these discussions is whether early-Neoproterozoic rifting culminated in breakup of the crust and the development of a large ocean known as the Adamastor Ocean (see Fig. 2 in Konopásek et al., 2020; and references therein), and thus the exact pre-orogenic connections between the African and South American parts of the Kaoko–Dom Feliciano–Gariep orogen remains an important line of research (e.g. Basei et al., 2005, 2011c; Oyhantçabal et al., 2018). Recent works have correlated the convergent history of rocks of the orogenic hinterland across both the Kaoko and Dom Feliciano Belts (Gross et al., 2009; Konopásek et al., 2016; Oyhantçabal et al., 2009, 2011a); however, connecting the pre-convergence histories of the two belts so far remains problematic.

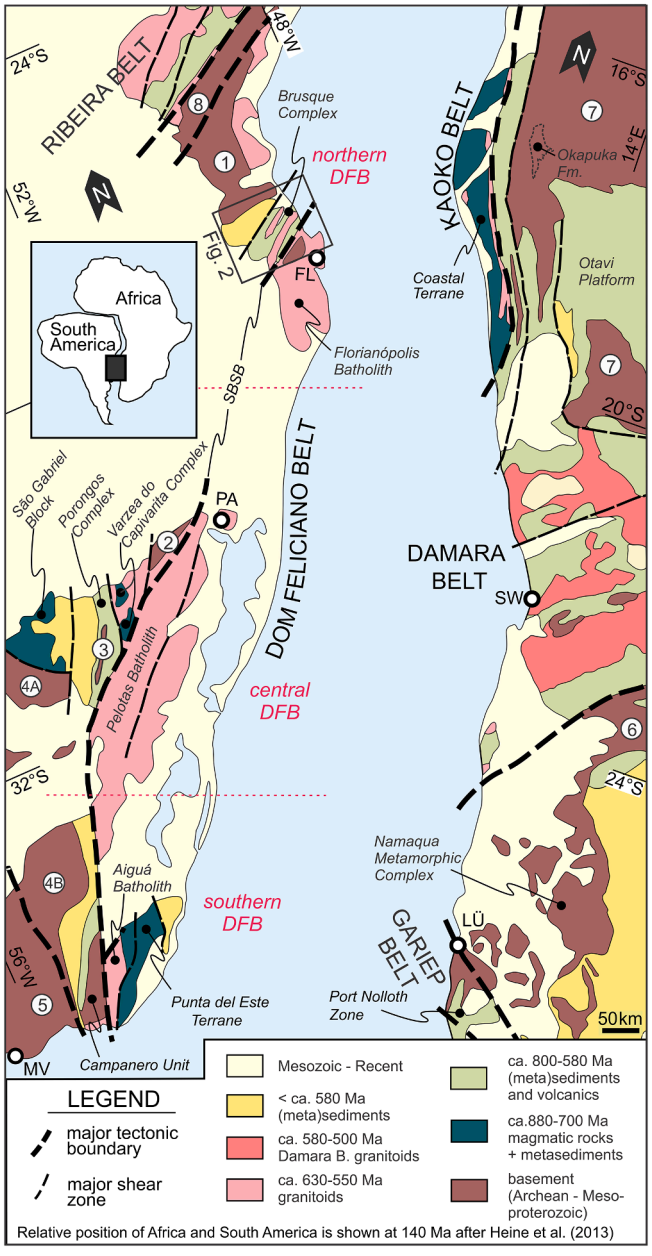

Fig. 1. Overview geological sketch of the Kaoko–Dom Feliciano–Gariep orogenic system (modified after Konopásek et al., 2017). 1—Luis Alves Craton, 2—Arroio dos Ratos Complex, 3—Encantadas Complex, 4A—Nico Pérez Terrane (Taquarembó Block), 4B—Nico Pérez Terrane, 5—Rio de la Plata Craton, 6—Kalahari Craton, 7—Congo Craton, 8—Curitiba Terrane. SBSB—Southern Brazilian Shear Belt, FL—Florianópolis, PA—Porto Alegre, MV—Montevideo, LÜ—Lüderitz, SW—Swakopmund.

Some of the most promising targets for investigation of the early history of the orogen are the supracrustal schist belts that run the length of the orogen, and that outcrop on both sides of the Atlantic Ocean. These units are interpreted as rifting-related basin deposits (Basei et al., 2008b; Campos et al., 2011; Frimmel and Fölling, 2004; Frimmel, 2018; Konopásek et al., 2014; Saalmann et al., 2006) that were later deformed and metamorphosed in the foreland positions of the orogen (Basei et al., 2011b; Frimmel et al., 2011; Frimmel, 2018; Goscombe et al., 2003b; Saalmann et al., 2006). As such, they should contain a record of the pre-convergence history from rifting to the onset of orogenesis.

The aim of this work is to discuss the mutual pre-orogenic positions of rifted margins of the Congo and Luis Alves cratons by studying the depositional history and potential source regions of the supracrustal rocks of the northern Dom Feliciano Belt using U–Pb detrital zircon geochronology. If the African and South American cratons represented one coherent crustal block at the beginning of rifting, the provenance record of metamorphosed rifting-related sediments on top of them should correlate. Studies with large datasets have been published investigating the timing of sedimentation and potential sources for these supracrustal rocks in the African counterpart of the belt (the Kaoko and Gariep orogenic belts) (Andersen et al., 2018a; Hofmann et al., 2014; Konopásek et al., 2014, 2017). Similarly, the central parts of the Dom Feliciano Belt are well studied (Gruber et al., 2011, 2016; Höfig et al., 2018; Pertille et al., 2015a, 2015b, 2017) (for a current review of the relevant provenance record in Western Gondwana, see Zimmermann, 2018). However, there is little data for the northern part of the belt (Basei et al., 2008a; Hartmann et al., 2003), which represents the direct counterpart to the Kaoko Belt in a pre-Atlantic setting (Fig. 1). We present a robust dataset of detrital zircon ages from metamorphosed clastic sedimentary and igneous rocks of the northern Dom Feliciano foreland that enables comparison and possible correlation of syn-rifting evolution with the Kaoko Belt in Africa, as well as with the central and southern Dom Feliciano Belt.

2. Geological setting

2.1. The Kaoko–Dom Feliciano–Gariep orogenic system

The Kaoko, Dom Feliciano and Gariep belts (Fig. 1) are three geographically separate orogenic belts that, prior to the opening of the Atlantic Ocean, represented a continuous orogenic system formed during the Neoproterozoic Brasiliano/Pan African orogenic cycle (Porada, 1989). The system crops out along the South Atlantic coastlines of South

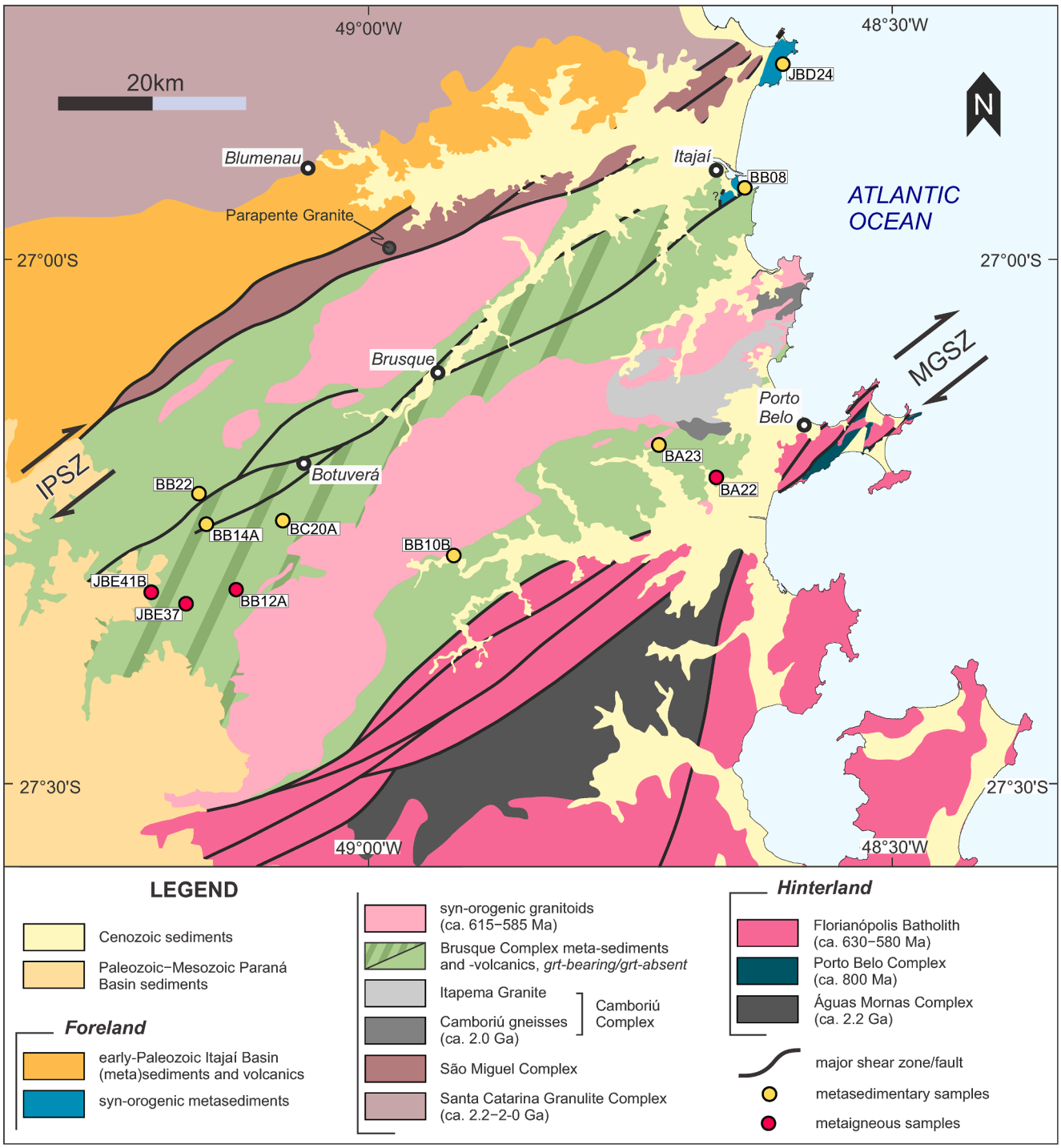

Fig. 2. Geological map of the northern Dom Feliciano Belt foreland. MGSZ = Major Gercino Shear Zone, IPSZ = Itajaí–Perimbó Shear Zone. Modified after Basei et al. (2006); Campos et al. (2011); De Toni et al. (2020a); Florisbal et al. (2012b); Hueck et al. (2018b). See text for geochronological references.

America and Africa, and forms the southern part of the larger South Atlantic Neoproterozoic Orogenic System (*sensu* Konopásek et al., 2020). The Kaoko–Dom Feliciano–Gariep orogenic system is structurally symmetric, with an eastern and western foreland domain lying either side of an internal orogenic hinterland (Fig. 1). Both foreland domains contain fold-and-thrust belts incorporating early- to middle-Neoproterozoic rift-related volcano-sedimentary rocks and associated basement, overlain by syn-orogenic flysch and molasse deposits (Frimmel, 2018; Goscombe et al., 2003b; Hueck et al., 2018b).

The basement of the eastern foreland consists of the Archean–Paleoproterozoic Congo and Kalahari cratons, and associated Mesoproterozoic crust exposed along the cratons' western edges (Kröner and Rojas-Agramonte, 2017; Kröner et al., 2004; Macey et al., 2018; Seth et al., 1998) (Fig. 1). In the Kaoko Belt, the eastern-most part of the foreland consists of autochthonous early- to middle-Neoproterozoic sedimentary successions lying directly on the Congo Craton basement, named the Otavi Carbonate Platform (Hoffman and Halverson, 2008). The low-grade Otavi Carbonate Platform is overridden by an imbricated fold-and-thrust belt, the Central Kaoko Zone, which consists of deformed and metamorphosed early- to middle-Neoproterozoic sedimentary

successions interlayered with slices of the basement, and overlain by late-Neoproterozoic syn-orogenic sedimentary rocks (Konopásek et al., 2014, 2017). The equivalent unit in the Gariep Belt is the para-autochthonous Port Nolloth Zone, which comprises all Neoproterozoic sedimentary rocks within the fold-and-thrust belt including rift-related basin deposits overlain by foredeep sediments (Frimmel et al., 1996; Frimmel, 2018 and references therein). The Port Nolloth Zone is overridden by the allochthonous Marmora Terrane, consisting of post-rift oceanic metabasalts overlain by late-Neoproterozoic siliciclastic and carbonate sedimentary rocks (Frimmel and Fölling, 2004; Frimmel, 2018).

The orogenic hinterland outcrops on both sides of the Atlantic Ocean, and consists of tectonically interleaved orthogneisses, paragneisses and migmatites intruded by numerous late-Neoproterozoic plutons. It is represented by the Coastal Terrane in the Kaoko Belt (Goscombe et al., 2005b), and the Cerro Olivo Complex of the Punta del Este Terrane, the Várzea do Capivarita Complex, and the Porto Belo and Águas Mornas Complexes in the southern, central and northern Dom Feliciano Belt respectively (Fig. 1) (Battisti et al., 2018; De Toni et al., 2020a; Gross et al., 2009; Oyhantçabal et al., 2009; Silva et al., 2000). The protoliths of the metamorphic hinterland consist of Paleoproterozoic cratonic basement intruded by early-Neoproterozoic bimodal magmatic rocks that are interpreted as remnants of arc-related (De Toni et al., 2020a; Koester et al., 2016; Lenz et al., 2013; Martil et al., 2017; Philipp et al., 2016) or rift-related (Konopásek et al., 2018; Oyhantçabal et al., 2009; Will et al., 2019) magmatism, and associated sedimentary cover. The episodic crustal stretching, melting and basin sedimentation that formed the early-Neoproterozoic parts of the hinterland rocks occurred from ca. 840 Ma to at least ca. 710 Ma (Basei et al., 2011c; De Toni et al., 2020a; Konopásek et al., 2014; Lenz et al., 2011; Martil et al., 2017; Oyhantçabal et al., 2009), and likely up to ca. 660–650 Ma ending shortly before the onset of orogenesis (Konopásek et al., 2017, 2018; Kröner et al., 2004). Orogenesis coincides with a strong metamorphic overprint in the hinterland rocks at ca. 670–640 Ma (Chemale et al., 2012; Masquelin et al., 2012; Oyhantçabal et al., 2009).

Along the western edge of the hinterland, in the Dom Feliciano Belt, is the Granite Belt: an extensive belt of late-Neoproterozoic, syn- and post-collisional granitoid batholiths (Fig. 1) (Bitencourt and Nardi, 1993, 2000; Florisbal et al., 2009, 2012a, 2012b; Hueck et al., 2018b; Oyhantçabal et al., 2007; Philipp and Machado, 2005; Philipp et al., 2013), that intrude the Paleoproterozoic to early-Neoproterozoic units of the high-grade hinterland (De Toni et al., 2020a; Koester et al., 2016; Lenz et al., 2013; Martil et al., 2017; Masquelin et al., 2012). The granitoids predominantly intruded between ca. 630–580 Ma (Florisbal et al., 2012b; Lara et al., 2020; Philipp and Machado, 2005), with scattered evidence of early magmatism at ca. 660–650 Ma (Chemale et al., 2012; Frantz et al., 2003).

The Granite Belt is in tectonic contact with the western foreland, separated by a large strike-slip dominated shear zone system running the entire length of the Dom Feliciano Belt, known as the Southern Brazilian Shear Belt (Fig. 1) (Bitencourt and Nardi, 2000). The foreland consists of a fold-and-thrust belt comprised of pre-orogenic rift-related sedimentary successions – known as the Schist Belt – and their associated basement rocks (Basei et al., 2011b; Bettucci et al., 2001; Saalmann et al., 2006), and a system of foreland basins (Fig. 1) (Almeida et al., 2010; Basei et al., 2011a; Guadagnin et al., 2010; Hueck et al., 2018b). The Schist Belt is comprised of the Brusque, Porongos and Lavalleja complexes in the Northern, Central and Southern Dom Feliciano Belt respectively. The Schist Belt and foreland basins lie on Archean–Paleoproterozoic basement units (Fig. 1). In Uruguay, the basement of the Dom Feliciano Belt foreland is the Nico Pérez Terrane (Oriolo et al., 2016; Oyhantçabal et al., 2011b). In the Central Dom Feliciano Belt, the basement of the foreland is exposed as tectonic windows in the Schist Belt (Saalmann et al., 2006).

2.2. The northern Dom Feliciano Belt

The foreland basement of the northern Dom Feliciano Belt is the Luis Alves Craton, which is predominantly comprised of Paleoproterozoic granulitic gneisses of the Santa Catarina Granulite Complex (Fig. 2) (Basei et al., 2009; Hartmann et al., 2015; Passarelli et al., 2018). The complex is made up of ca. 2.2–2.0 Ga orthogneisses, interspersed with mafic–ultramafic enclaves and subordinate paragneisses (Basei et al., 1998a, 2009; Hartmann et al., 1999, 2000). The southern margin of the Luis Alves Craton is covered by the Itajaí Basin (Fig. 2) (Basei et al., 2009; Passarelli et al., 2018), which consists of volcano-sedimentary successions deposited in an orogenic foreland environment (Basei et al., 2011a) with a maximum age of deposition constrained by U–Pb zircon dating of interlayered volcanics at ca. 560–550 Ma (Guadagnin et al., 2010). The Itajaí Basin is weakly deformed, with deformation increasing south-eastwards towards the Itajaí–Perimbó Shear Zone where it is in contact with the foreland fold-and-thrust belt (Fig. 2) (Basei et al., 2011a).

The fold-and-thrust belt is predominantly comprised of metamorphosed volcano-sedimentary sequences of the Brusque Complex intruded by a series of Neoproterozoic granitoids between ca. 630–585 Ma (Fig. 2) (Florisbal et al., 2012b; Hueck et al., 2019). A narrow sliver of crystalline basement of unknown age and origin, known as the São Miguel Complex, is exposed at the north-western contact with the Itajaí Basin (Fig. 2) (Basei et al., 2011b). Syenogranites intruding this foreland basement have been dated at 835 ± 9 Ma and 843 ± 12 Ma (U–Pb zircon), and are interpreted as A-type granitoids marking the beginning of rifting that lead to the formation of the Brusque Complex paleobasin (Parapente Granite, see Fig. 2) (Basei et al., 2008b). This is within error of a 833 ± 3 Ma (U–Pb zircon) age found in granitic to syenitic rocks of the Richtersveld Igneous Complex in the Gariep Belt, which is similarly interpreted as evidence of the earliest crustal thinning in the region marking the beginning of continental breakup (Frimmel et al., 2001).

A basement inlier—the Camboriú Complex—outcrops along the coast in central part of the Brusque Complex (Fig. 2). The Camboriú Complex is predominantly comprised of migmatitic felsic orthogneisses interleaved with amphibolites (Martini et al., 2019), which predominantly show U–Pb zircon ages of 2.2–2.0 Ga comparable with the Luis Alves Craton (Hartmann et al., 2003; Silva et al., 2000, 2005).

The southern border of the Brusque Complex is in tectonic contact with the Florianópolis Batholith, and the two units are separated by the large-scale Major Gercino Shear Zone (Fig. 2). The Florianópolis Batholith is the northern exposure of the Granite Belt (Fig. 1), and is comprised of a vast series of Neoproterozoic granitoids that intruded the western edge of the hinterland represented by the ca. 800 Ma migmatitic orthogneisses of the Porto Belo Complex (De Toni et al., 2020a) and the Paleoproterozoic Águas Mornas Complex (Fig. 2) (Silva et al., 2005). The granitoids were emplaced predominantly between ca. 630–590 Ma (Chemale et al., 2012; Florisbal et al., 2012b).

2.3. Early evolution of the Brusque Complex

The rocks in this study belong to the metamorphosed volcano-sedimentary successions of the Brusque Complex, which forms a NE–SW oriented belt of predominantly pelitic schists divided into a northern and southern section by an elongate syn-orogenic granitic batholith (Fig. 2) (Valsungana Batholith). Metamorphism in the Brusque Complex is characterised by a general increase in metamorphic grade from NW–SE (Basei et al., 2011b; Campos et al., 2011, 2012). In the NW, the Brusque Complex metapelites are dominated by lower-greenschist facies chlorite – mica schists and phyllites, and a narrow garnet zone in the centre and southern parts of the belt suggests metamorphic conditions reached maximum lowermost amphibolite facies (Fig. 2). The Brusque Complex rocks are intensely deformed, showing evidence of multiple deformation structures associated with its prolonged contractional history (Basei et al., 2011b; Campos et al., 2011).

There is little published work available concerning the early evolution of the Brusque Complex, as poor exposure and the intensity of deformation makes any stratigraphic subdivision difficult. Despite this, three sequences are generally described based on the presence or absence of volcanic sub-units (e.g. Basei et al., 2006, 2011b). The lowermost and upper-most formations—the Rio do Oliveira and Rio da Areia sequences respectively—are described as being dominated by metasedimentary rocks, with some mafic and rare felsic metavolcanics interlayered within (Basei et al., 2011b; Campos et al., 2011). The upper sequence is described as containing a large proportion of metacarbonate rocks, and the lower sequence frequently containing calc-silicate lenses of volcanogenic origin (Basei et al., 2011b; Campos et al., 2011). The middle formation—the Botuverá sequence—is described as entirely clastic, varying in composition between metapelitic and metapsammitic and containing no metavolcanic or metacarbonate rocks (Basei et al., 2011b).

There is also little published data to constrain the timing of sedimentation of the Brusque Complex protolith. The upper limit is loosely placed at ca. 840 Ma at the start of basin formation (Basei et al., 2008b), but within the Brusque Complex itself there are currently no reliable constraints on the upper limit of sedimentation. Basei et al. (2008a) reported a minimum age at ca. 570–540 Ma based on the two youngest detrital zircon grains from pelitic schists of the Brusque Complex. However, this age is contradicted by the well-constrained age of intrusion of granitic plutons and dykes into the Brusque Complex metasediments between ca. 620 and 580 Ma (Campos et al., 2012; Hueck et al., 2019). Currently, these post-metamorphic magmatic rocks remain the only robust constraint on the minimum age of sedimentation into the Brusque Complex paleobasin.

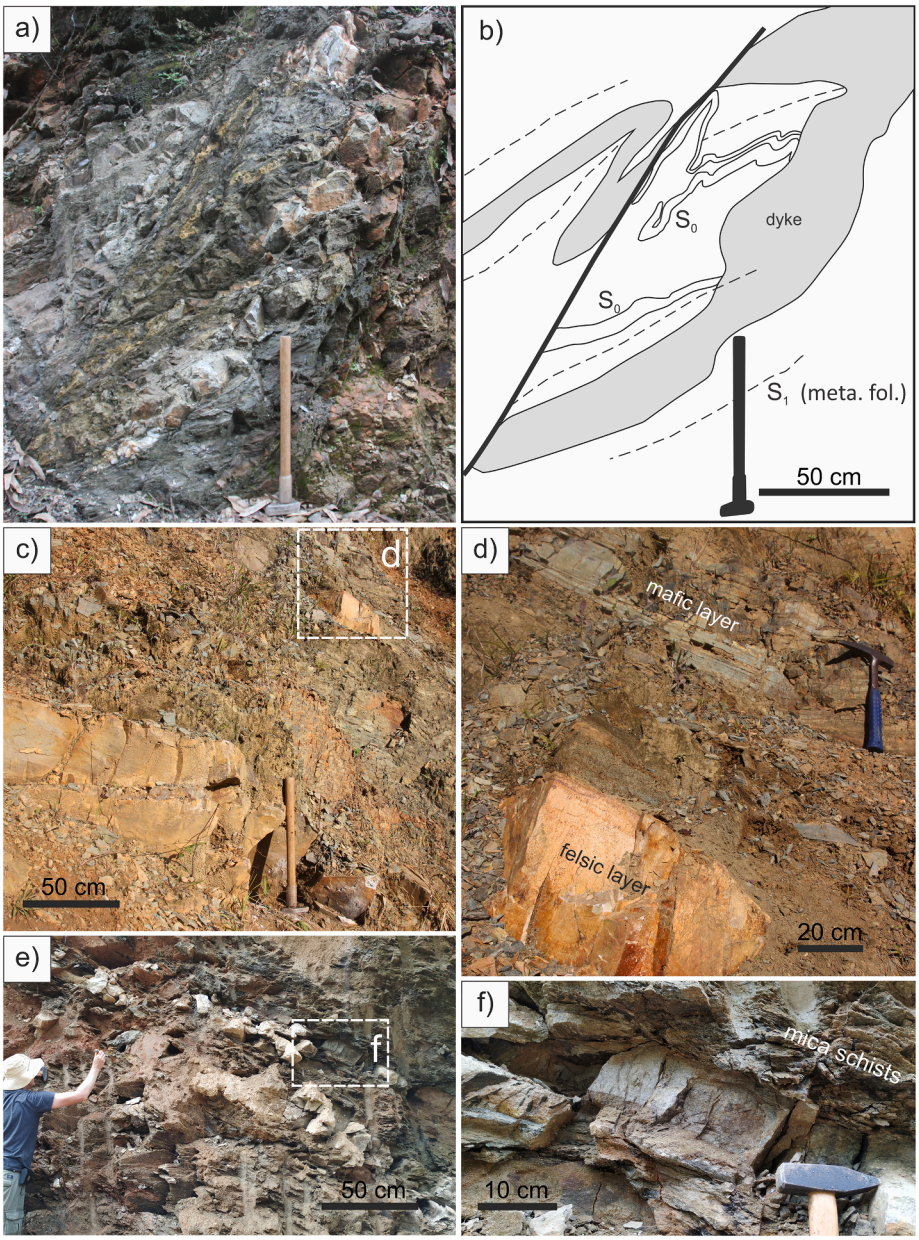

Fig. 3. Outcrops of metaigneous rocks: a) photo of the metamorphosed and deformed felsic dyke BB12A, b) an accompanying sketch of the same road-cut outcrop outlining the cross-cutting nature of the dyke relative to remnant S_0, c) road-cut outcrop BA22, d) detail of outcrop BA22 showing bimodal volcanics, e) outcrop JBE37, f) detail of outcrop JBE37 showing foliation-parallel nature of felsic rock.

3. Geochronology

3.1. Materials and methods

Zircon U–Pb ages were determined at the Institute of Geology of the Czech Academy of Sciences, Prague, Czech Republic, using laser ablation inductively coupled plasma mass spectrometry (LA-ICP-MS), and the complete isotopic dataset is presented in Electronic Appendix A. For detrital zircon data, U–Pb age spectra are presented as cumulative distribution curves with 95% confidence intervals after Andersen et al. (2016) and using the visualisation package (*detzrcr*) of Andersen et al. (2018b), and as frequency histograms with 30 Ma binwidths and adaptive kernel density estimate (KDE) curves as described in Vermeesch et al. (2016) using the software package (*densityplotter* version 8.4) of Vermeesch (2012). Only concordant dates with calculated discordance within ± 10%, are included. Concordance is calculated from ages, using ($^{206}Pb/^{238}U$) / ($^{207}Pb/^{206}Pb$) for $^{207}Pb/^{206}Pb$, and using ($^{206}Pb/^{238}U$) / ($^{207}Pb/^{235}U$) for $^{206}Pb/^{238}U$. $^{207}Pb/^{206}Pb$ dates are reported for data > 1.0 Ga, and $^{206}Pb/^{238}U$ dates for data < 1.0 Ga. Description of zircon separation and analytical methods is provided in Electronic Appendix B. Locations of analysed samples are plotted in Fig. 2.

3.2. Description of metaigneous samples and results of U–Pb zircon dating

3.2.1. Sample BB12A

Sample BB12A (Fig. 2) (27° 18.940′ S, 49° 07.682′ W) was collected from a felsic dyke intrusive in metapelitic schists. The dyke is approximately 30 cm thick, and is folded and metamorphosed together with the schists indicating intrusion prior to deformation and metamorphism of the host rock (Fig. 3a and b). The metamorphic mineral assemblage is dominated by quartz, plagioclase and K-feldspar, with minor white mica, chlorite and biotite, and accessory opaque minerals. Chlorite pseudomorphs after garnet completely replace poikiloblastic garnet, suggesting overprint at lower metamorphic conditions. The original magmatic texture has been almost completely overprinted by metamorphism and deformation, although K-feldspar crystals much larger than those in the matrix remain as inclusions in garnet pseudomorphs suggesting that the magmatic fabric is locally preserved.

From 42 spot analyses in oscillatory-zoned parts of the zircon grains, 25 concordant dates combine in a concordia U–Pb age of 811 ± 6 Ma (Fig. 4a and b), interpreted as the age of intrusion and crystallisation of the dyke. Zircon grains range from ca. 60 to 150 μm in length, and most are idiomorphic and show oscillatory zoning in cathodoluminescence (CL) images (Fig. 4c). Some grains show truncated zoning at the edges, which are likely fractured and abraded inherited zircons. Of the remaining 17 analyses, three are discordant likely due to lead loss at an unspecified time, and the rest are older than the major cluster of dates and likely represent inherited grains.

3.2.2. Sample BA22

Sample BA22 (27° 12.195′ S, 48° 39.853′ W) is a fine-grained metarhyolite, consisting of quartz, plagioclase, K-feldspar, minor amounts of muscovite, and with accessory garnet and opaque minerals. The outcrop consists of a series of metamorphosed, interlayered mafic and felsic volcanic rocks interspersed with metapelitic schists (Fig. 3c and d). The outcrop shows a penetrative metamorphic foliation, overprinting any previous magmatic texture. However, due to layering of the mafic, felsic and pelitic layers, and the presence of abundant K-feldspar, we interpret the sample as a metamorphosed felsic volcanic rock.

Only a small number of zircon grains were recovered from the sample, varying between 70 and 190 μm in length and 60 and 130 μm in width. The grains predominantly show sector zoning, with minor oscillatory zoning, and are strongly fractured and rounded. Of 22 grains analysed, 19 yielded concordant dates. Four grains were analysed twice, and repeated dates were not plotted. The data are plotted in Fig. 5a, and show that the dates mainly cluster at ca. 2.05 Ga. Due to similarities with the surrounding samples (see below), we interpret all zircon grains as inherited.

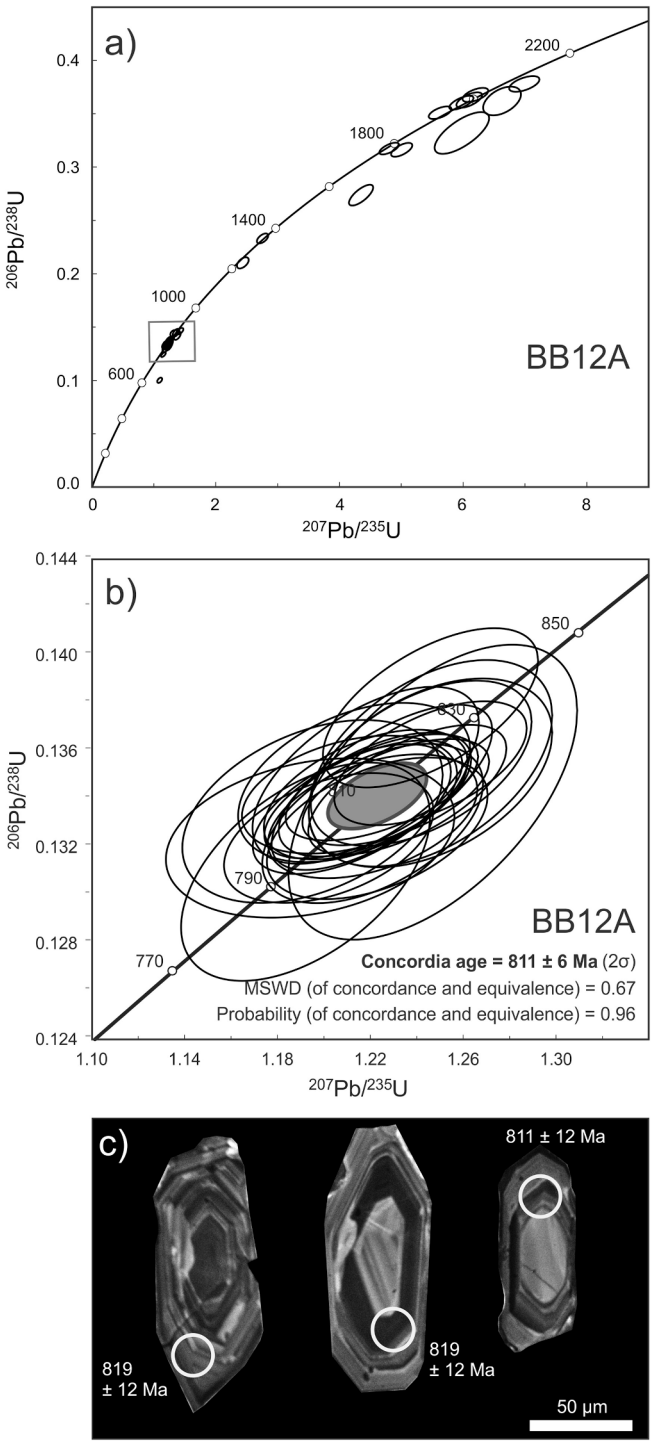

Fig. 4. Results of U–Pb zircon dating of sample BB12A: a) zircon U–Pb concordia plot for sample BB12A (analysed by LA–ICP–MS), b) detail of inset showing combined 25 data points used for calculation of the concordia age (data point error ellipses are plotted at 2σ level, MSWD = mean square weighted deviation), and c) cathodoluminescence images and individual dates of example zircon grains.

3.2.3. Sample JBE41B and JBE37

Samples JBE41B (27° 19.083′ S, 49° 12.516′ W) and JBE37 (27°

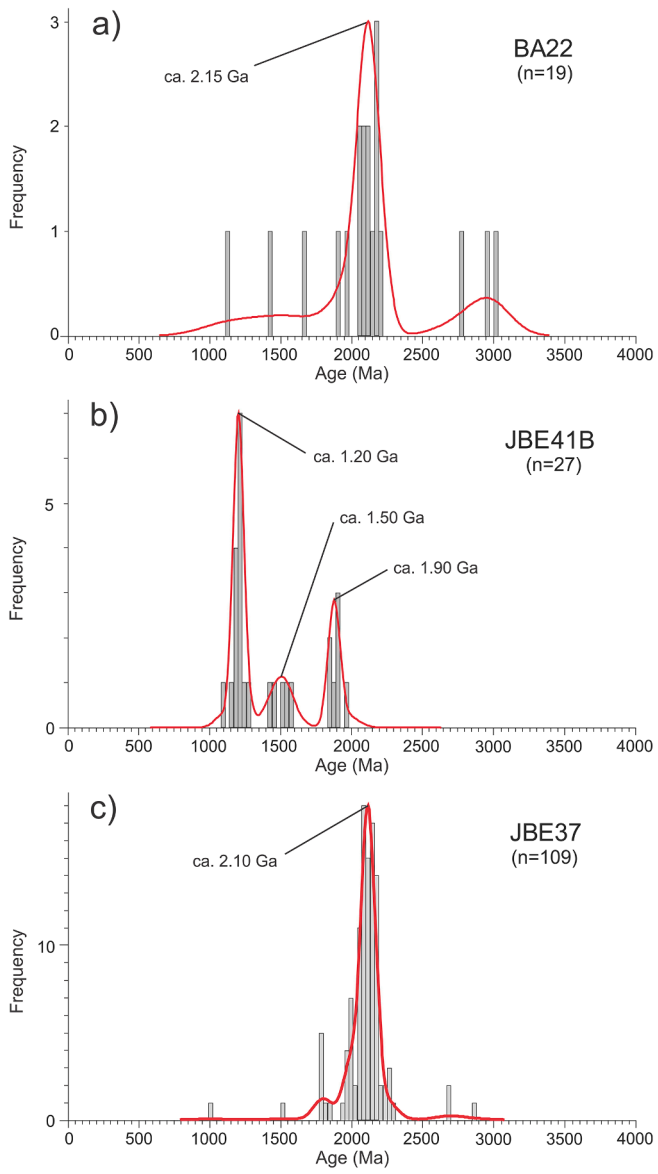

Fig. 5. U-Pb zircon age data for analysed metaigneous samples, presented as frequency histograms and KDEs. n = number of data.

20.192′ S, 49° 10.536′ W) were collected from approximately foliation-parallel felsic layers within the garnet-schists of the Brusque Complex. Both outcrops consist of a series of felsic layers approximately 10–30 cm thick, interlayered with garnet-bearing schists. The samples contain the mineral assemblage quartz, plagioclase and K-feldspar, with subordinate biotite, white mica, chlorite and opaque minerals. Chlorite pseudomorphs after garnet in sample JBE37 contain K-feldspar inclusions similar to sample BB12A. Based on field observations and the presence of blastoporphyritic K-feldspar, we interpret the protoliths of the samples as metamorphosed felsic volcanic rocks. However, due to metamorphic overprint it remains difficult to conclusively differentiate them from a meta-arkose.

For sample JBE41B, 28 zircon grains were analysed and 27 yielded concordant dates with 2σ uncertainty ≤ 10%. The data are plotted in Fig. 5b, and the resulting spectrum shows age peaks at ca. 1.90, 1.50 and 1.20 Ga. All of the zircon grains are interpreted as inherited/detrital.

For sample JBE37, analysis of 112 zircon grains produced 109 concordant dates with 2σ uncertainty ≤ 10%. The data are plotted in Fig. 5c, and the resulting spectrum shows a single dominant age peak centred at ca. 2.10 Ga, with a much smaller peak at ca. 1.80 Ga, and some individual data between ca. 3.00–1.00 Ga. All of the zircon grains are also interpreted as inherited/detrital.

3.3. Description of metasedimentary samples and results of U–Pb detrital zircon dating

3.3.1. Sample JBD24

Sample JBD24 (26° 48.324′ S, 48° 35.838′ W) is a micaceous quartzite collected from within the Itajaí–Perimbó Shear Zone, close to the northern contact with the underlying basement (Basei et al., 2011b) (Fig. 2). The rock is intensely folded and deformed, though weakly metamorphosed, containing quartz, muscovite, biotite, chlorite and plagioclase, with accessory opaque minerals. Zircon grains are mostly ca. 50 to 120 μm in length, and show varying degrees of fragmentation from whole, prismatic crystals to small, abraded fragments. The majority show oscillatory zoning, and often with truncated edges likely due to transport and abrasion. No grains appear to have metamorphic overgrowth rims, and few show sector zoning or no zoning at all.

Analysis of 140 grains yielded 118 concordant dates. The spectrum of dates (Fig. 6a) shows distinct peaks at ca. 2.20 Ga and 660 Ma, with individual data in the intervals between ca. 2.10–0.80 Ga, and ca. 3.60–2.30 Ga.

3.3.2. Sample BB08

Sample BB08 (26° 55.544′ S, 48° 38.055′ W) is a carbonate-bearing phyllitic metarhythmite collected from a coastal outcrop within the southern part of the Itajaí–Perimbó Shear Zone (Fig. 2). The rock is strongly deformed, with a primary metamorphic foliation containing intrafolial folding that is overprinted by a steep, pervasive crenulation cleavage parallel to the Itajaí–Perimbó Shear Zone. The style of deformation at this outcrop is consistent with other high-strain parts of the Brusque Complex (Basei et al., 2011b).

The rock contains quartz, muscovite, biotite, chlorite, plagioclase and calcite, with accessory opaque minerals. Zircon grains vary between ca. 60 and 200 μm in length. Most of the grains show oscillatory zoning, with some showing sector zoning and other more complex internal structures. The majority of grains are abraded and fragmented, and some show thin CL-bright overgrowth rims.

101 analysed zircon grains yielded 82 concordant dates. The data show a similar bimodal distribution to sample JBD24, with distinct peaks at ca. 2.15 Ga and 670 Ma, and minor peaks at ca. 625 and 560 Ma (Fig. 6b). Individual data appear over the intervals between ca. 2.95–1.75 Ga and ca. 750–500 Ma. The two youngest individual zircon grains are ca. 84 Ma and 375 Ma, which are significant outliers. These two grains are likely from contamination, either from beach sediment cemented onto the rock by dissolution and precipitation of calcite, or otherwise introduced during the separation process.

3.3.3. Sample BA23

Sample BA23 (27° 10.511′ S, 48° 43.054′ W) was collected in the southeast section of the Brusque Complex from a large, loose block at the foot of an isolated steep slope (not in situ, but inferred to be close to its original position on the hill above). The sample is a weakly foliated micaceous quartzite containing quartz, muscovite, biotite, chlorite and garnet, with accessory opaque minerals. Zircon grains range between ca. 80 and 150 μm in length, and are mostly fragmented and abraded. Most grains have oscillatory or sector zoning, and many show featureless overgrowth rims. A smaller number show complex zoning patterns or no zoning at all.

Isotopic dating yielded 136 concordant dates from 140 analysed zircon grains. The age spectrum (Fig. 6c) shows the majority of dates cluster at a single peak ca. 2.00 Ga. A minor, long-wavelength peak centred at 2.70 Ga encompasses a series of individual dates between ca. 3.15–2.30 Ga.

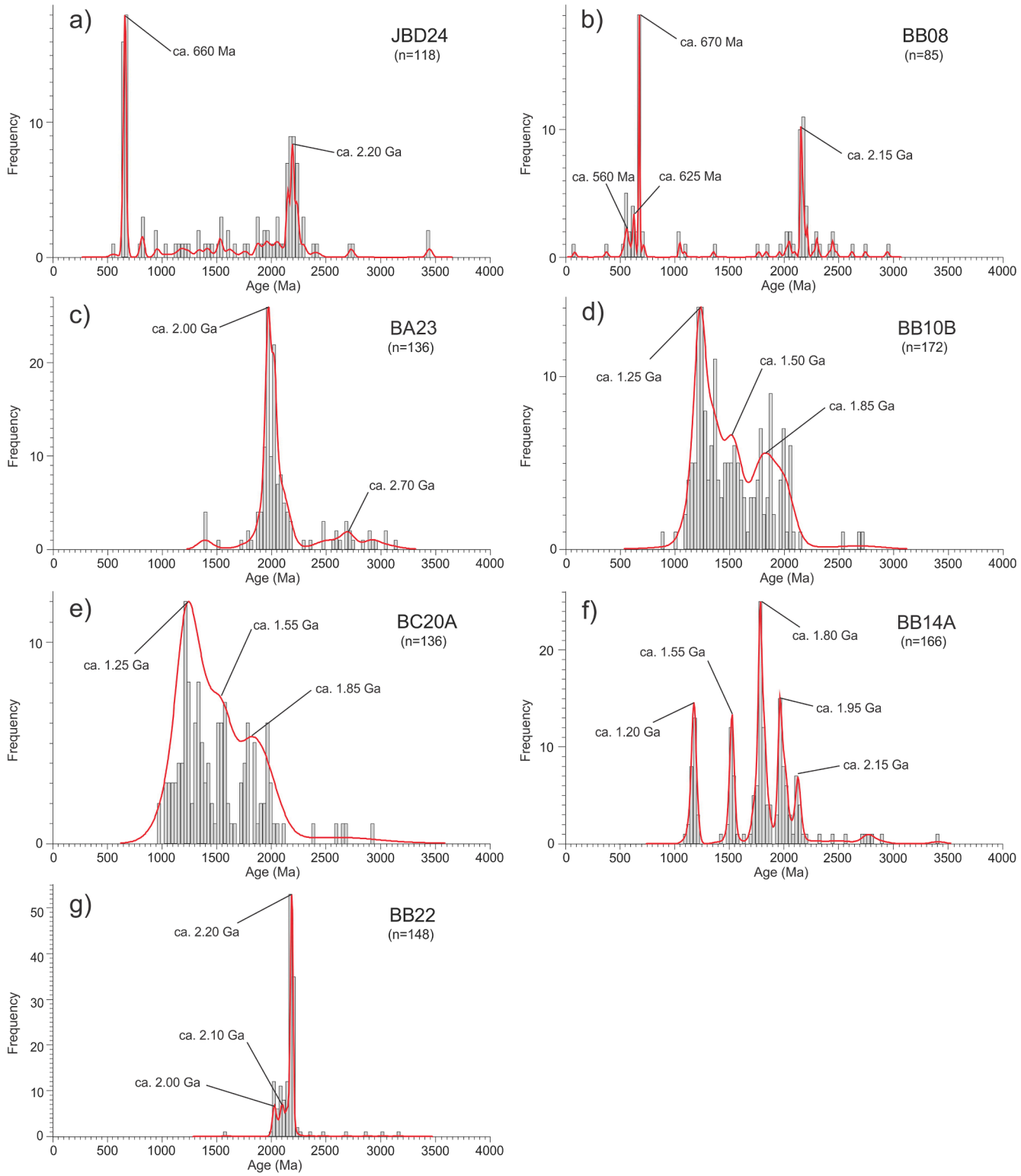

Fig. 6. U-Pb detrital zircon data for analysed metasedimentary samples, presented as frequency histograms and KDEs. n = number of data.

3.3.4. Sample BB10B

Sample BB10B (27° 16.964′ S, 48° 55.006′ W) was collected from the southern-central part of the Brusque Complex, from a strongly foliated quartz-rich schist containing quartz, muscovite, biotite, and chlorite, with accessory opaque minerals. Zircon grains range from ca. 50 to 120 μm in length, and ca. 30 to 50 μm in width. Many grains are elongate and euhedral, showing sector or oscillatory zoning. Thin, CL-bright overgrowth rims are common.

Analysis of 182 zircon grains yielded 172 concordant dates. The spectrum of ages (Fig. 6d) shows a broad distribution of dates from ca. 2.20–1.00 Ga, with the highest proportion centred at a peak at ca. 1.25 Ga. The remaining data are distributed between ca. 2.20–1.30 Ga with minor peaks at ca. 2.00, 1.80, 1.50 and 1.35 Ga.

3.3.5. Sample BC20A

Sample BC20A (27° 14.919′ S, 49° 04.959′ W) was collected from a strongly deformed garnet-bearing schist in the south-western part of the Brusque Complex. The sample contains quartz, garnet, muscovite, biotite, chlorite and plagioclase, with accessory tourmaline and opaque minerals. Zircon grains range from ca. 50 to 200 μm in length. Grains vary in shape and structure: some are euhedral with oscillatory zoning, while others have abraded edges, are often fractured, and with complex internal structures.

Isotopic analysis of 140 zircon grains produced 136 concordant dates. The data (Fig. 6e) show a broad distribution of dates between ca. 2.10 Ga and 900 Ma, with a major peak at ca. 1.25 Ga and minor peaks at ca. 1.95, 1.80, 1.55 and 1.35 Ga.

3.3.6. Sample BB14A

Sample BB14A (27° 15.128′ S, 49° 09.412′ W) is a quartzite collected from the western part of the Brusque Complex. The sample contains quartz, muscovite and biotite, with accessory rutile and opaque minerals. Zircon grains range from ca. 80 to 200 μm in length, and are predominantly elongate and rounded. Most grains show oscillatory zoning, with only a few showing sector or complex zoning patterns. The grains are mostly fragmented and abraded

From 168 zircon grains analysed, 166 produced concordant U–Pb dates. The resulting age spectrum (Fig. 6f) shows distinct peaks at ca. 2.15, 1.95, 1.80, 1.55 and 1.15 Ga.

3.3.7. Sample BB22

Sample BB22 (27° 13.358′ S, 49° 09.847′ W) is a quartzite collected from the low-grade section of the Brusque Complex in the north-west. The sample contains quartz and muscovite, with accessory titanite and opaque minerals. Zircon grains range from 70 to 250 μm in length, and are predominantly elongate and rounded. Most grains show oscillatory zoning, and are mostly fragmented and abraded. Some grains show more complex zoning patterns.

Isotopic analysis of 154 zircon grains produced 148 concordant U–Pb dates. The corresponding age spectrum (Fig. 6g) shows the majority of dates centred at a large peak at ca. 2.20 Ga, with two minor peaks at ca. 2.10 and 2.05 Ga.

4. Discussion

4.1. Constraining the age of sedimentation

The concordia U–Pb zircon age of 811 ± 6 Ma from sample BB12A represents the youngest cluster of data in the sample, and likely the crystallisation age of the dyke. Because the youngest detrital zircon grains from neighbouring samples (e.g. BB10B and BC20A; Fig. 2) are ca. 1.00 Ga, it is not likely that the ca. 800 Ma zircons in sample BB12A represent xenocrystic grains. Furthermore, considering that the rock is deformed and metamorphosed together with the host schists, we interpret that the dyke intruded the Brusque Complex protolith prior to the onset of orogenic evolution at ca. 650 Ma. Due to issues with stratigraphy, there is no constraint on what level of the Brusque Complex basin is represented by these metasediments, though it suggests that at least part of the Brusque Complex protolith was deposited prior to ca. 811 Ma.

This age is close to estimates of earliest sedimentation in the Porongos Complex of the central Dom Feliciano Belt foreland, which has been constrained to ca. 810–770 Ma by dating of syn-depositional volcanics (Pertille et al., 2017; Saalmann et al., 2011). These ages also correlate well with ca. 820–785 Ma syn-sedimentary magmatism in the Coastal Terrane of the Kaoko Belt hinterland (Konopásek et al., 2008, 2018), ca. 800 Ma magmatism in the Porto Belo Complex of the northern Dom Feliciano Belt hinterland (De Toni et al., 2020a), and ca. 790 Ma magmatism in the Várzea do Capivarita Complex of the central Dom Feliciano Belt hinterland (Martil et al., 2017), suggesting a genetic relationship between the early Neoproterozoic rocks of the foreland and hinterland domains (e.g. Battisti et al., 2018). Importantly, the dyke post-dates estimates for the beginning of continental rifting, and thus basin formation, in the Kaoko–Dom Feliciano–Gariep orogenic system at ca. 840 Ma (Basei et al., 2008b; Frimmel et al., 2001). All these data constrain the beginning of sedimentation in the Brusque Complex to between ca. 840–811 Ma.

None of the other potential metaigneous samples (BA22, JBE41B and JBE37) produced a cluster of dates that could be interpreted as a magmatic age. Thus, the ca. 811 Ma age obtained from sample BB12A provides the current best constraint for the minimum age of sedimentation of the Brusque Complex protolith.

4.2. Detrital zircon age patterns

Three distinct detrital zircon age patterns are identified within the studied samples (Fig. 7a). Sample BA22 contained too few zircons to confidently assign to a group, and so is not included in any further analysis.

The first pattern shows a polymodal age distribution, as seen in samples BB10B, BC20A, BB14A and JBE41B (Fig. 7b). These samples have age peaks predominantly within a range from ca. 2.10 to 1.00 Ga (Fig. 7b), with major Paleoproterozoic peaks at ca. 2.10, 1.95 and 1.80 Ga, and a series of peaks in the Mesoproterozoic at ca. 1.55, 1.35 and 1.20 Ga. Using the *1-O* parameter of Andersen et al. (2016) to statistically determine likeness between samples, samples BC20A, BB10B and JBE41B all show a perfect match within the sample confidence intervals (*1-O* = 0.00 for each comparison), and sample BB14A matches poorly with each (*1-O* = 0.11 for each comparison).

The next is a unimodal distribution pattern seen in samples BA23, BB22 and JBE37. The data show detrital zircon ages almost entirely within the Paleoproterozoic, and the pooled KDE (Fig. 7c) is dominated by a large, narrow peak at 2.20 Ga, with a series of smaller peaks between ca. 2.15–2.00 Ga. Sample JBE37 shows a good match with samples BA23 and BB22 (*1-O* = 0.03 and 0.02 respectively), and sample BA23 matches well with BB22 (*1-O* = 0.05). The pooled data do not show a strictly unimodal distribution pattern, but individually the samples show generally unimodal distributions (Fig. 5-c, 6-c, -g). The most noticeable difference when comparing the polymodal and the unimodal sample groups is the complete absence of Mesoproterozoic zircon age peaks in the latter, and the absence of a 2.20 Ga peak in the former.

Finally, an approximately bimodal distribution pattern is seen in samples JBD24 and BB08, and when these samples are pooled (Fig. 7d) the data show significant peaks at ca. 665 Ma and ca. 2.20 Ga, a minor peak at ca. 560 Ma, and individual dates distributed between ca. 2.10–0.80 Ga and between ca. 3.50–2.30 Ga. These two samples match perfectly within their confidence intervals (*1-O* = 0.00).

4.3. Polymodal detrital zircon pattern and its possible sources

When pooled, the major peaks in the polymodal pattern at ca. 2.10, 1.95, 1.80, 1.55, 1.35 and 1.20 Ga are distinct (Fig. 7b). Notably, there is no peak at 2.20 Ga, which is the dominant Paleoproterozoic age peak seen in the unimodal and bimodal pooled relative frequency plots (Fig. 7c and d). The oldest peaks in the pooled polymodal plot are at ca. 2.10 and 2.00 Ga, which correlate with magmatic ages of ca. 2.05–1.95 Ga from the Congo Craton basement of the Kaoko Belt (Kröner et al., 2004), as well as with similar ages reported from basement rocks of the Luis Alves Craton (Basei et al., 1999, 2009) and the Camboriú Complex (Silva et al., 2000). As the most proximal cratonic basement rocks to the Brusque Complex, the Luis Alves Craton would be the most likely candidate for protosource material for the Brusque Complex sediments. However, the absence of a ca. 2.20 Ga age peak suggests a closer affinity to the Congo Craton basement, which, unlike the Luis Alves Craton, does not contain a record of ca. 2.20 Ga activity.

The presence of Mesoproterozoic zircon grains in the polymodal

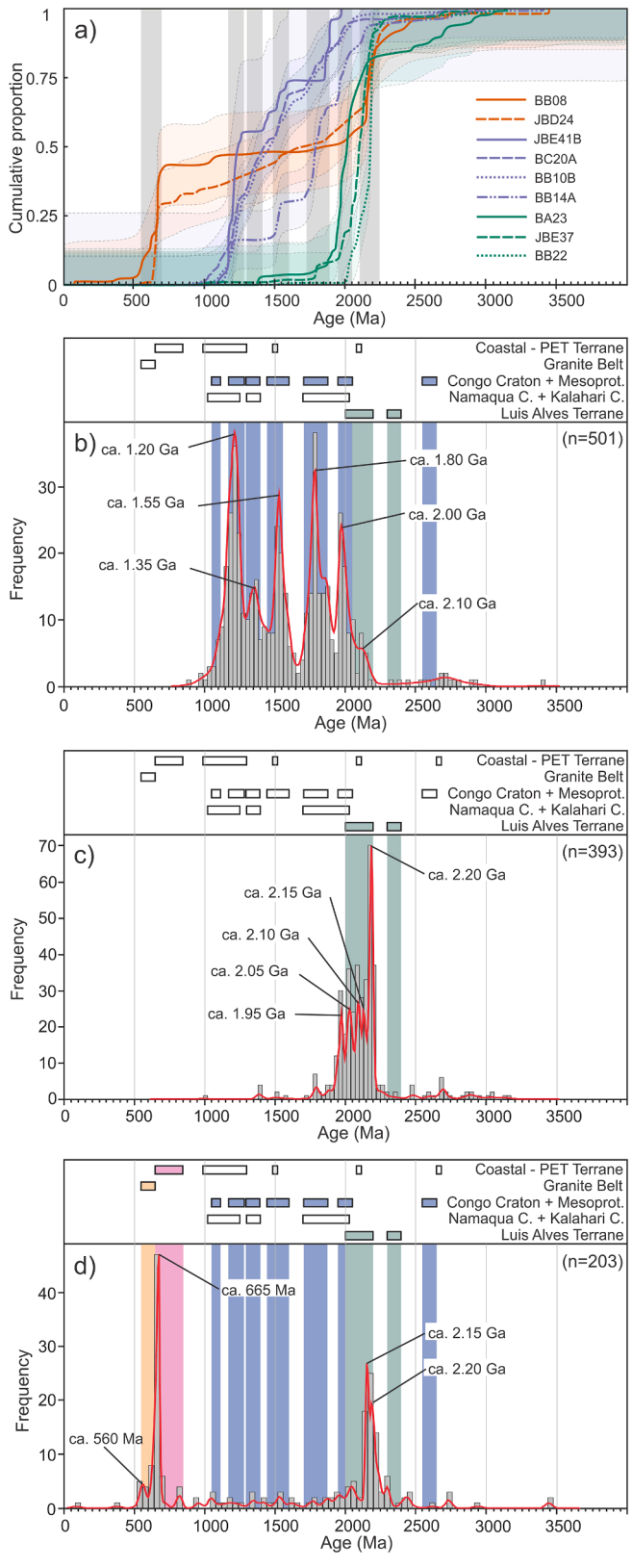

(caption on next column)

Fig. 7. Brusque Complex U–Pb detrital zircon data grouped into three patterns: a) cumulative proportion curves of each sample with 95% confidence intervals (shaded columns delineate major common age fractions), b) pooled polymodal group (samples BC20A, BB10B, BB14A and JBE41B), c) unimodal group (samples BA23, BB22 and JBE37), and d) bimodal group (samples BB08 and JBD24). Bars at the top of figures b, c and d show age ranges of relevant protosources, and the coloured columns behind the data show the best fit protosources for each group that correlate to major age fractions. Data for reference bars: Congo Craton + Mesoprot. from Kröner et al. (2015, 2004); Kröner and Rojas-Agramonte (2017); Seth et al. (1998, 2003), Namaqua Metamorphic Complex from Becker et al. (2006); Bial et al. (2015); Clifford et al. (2004), Luis Alves Craton from Basei et al. (2009); (Hartmann et al., 1999); Hartmann et al. (2000), Coastal–PET Terrane from Basei et al. (2011c); Goscombe et al. (2005a); Konopásek et al. (2008); Lenz et al. (2011); Oyhantçabal et al. (2009), Granite Belt from Florisbal et al. (2012b); Lara et al. (2020); Philipp and Machado (2005).

sample group indicates a significant contribution from Mesoproterozoic-aged protosource rocks, which were otherwise almost entirely absent during sedimentation of the protoliths of the unimodal sample group. However, rocks of this age are so far unknown from the basement rocks exposed in the northern Dom Feliciano Belt. In the southern Dom Feliciano Belt (Fig. 1), rocks with ages corresponding to the Mesoproterozoic peaks in the polymodal pattern, at ca. 1.50 and 1.40 Ga, are known only from the Nico Pérez Terrane in Uruguay (Gaucher et al., 2011; Mallmann et al., 2007; Oriolo et al., 2019; Oyhantçabal et al., 2018; Sánchez-Bettucci et al., 2004). A ca. 1.55 Ga crystallisation age is also recorded within the Capivarita Anorthosite in the exposed basement of the Granite Belt in the central part of the Dom Feliciano Belt in Rio Grande do Sul (Chemale et al., 2011). Given their distal nature to the northern Dom Feliciano Belt, though, it is unlikely that these rocks directly contributed to sedimentation into the Brusque Complex paleobasin.

The 1.55–1.40 Ga ages are common, however, in Mesoproterozoic magmatic rocks intruding the Congo Craton of Namibia and SW Angola (e.g. Bybee et al., 2019; Lehmann et al., 2020; Luft et al., 2011; Seth et al., 1998), providing possible protosources for the Brusque Complex sediment. The best-fit source rocks for the observed ages in the polymodal group come from metamorphosed supracrustal rocks of the Okapuka Formation and the underlying Epupa Metamorphic Complex in the Kaoko Belt (Fig. 7b). Part of the Congo Craton, the Epupa Metamorphic Complex is dated at ca. 1.85–1.75 Ga (Kröner et al., 2010, 2015), and is intruded by granitoid rocks with ages primarily clustered at ca. 1.50, 1.35 and 1.20 Ga (Drüppel et al., 2007; Kröner et al., 2015; Kröner and Rojas-Agramonte, 2017; Seth et al., 2003). These basement rocks are overlain by the ca. 1.35 Ga volcano-sedimentary Okapuka Formation (Fig. 1), which contains detrital zircon spanning ca. 2.05–1.40 Ga that was likely sourced from the nearby basement. The formation is intruded by magmatic rocks with ages between ca. 1.20–1.05 Ga (Kröner and Rojas-Agramonte, 2017).

The underlying Paleoproterozoic basement may represent part of the source for the Brusque Complex sediments, however it is equally likely that these rocks represent the protosource and that the Brusque Complex sediment is sourced directly from the Mesoproterozoic sedimentary cover (Okapuka Fm.) and associated intrusive rocks. Recycling of older sedimentary successions has been proposed by Andersen et al. (2018a) to explain the detrital zircon record in equivalent rocks in the Gariep Belt, and they point to preserved fragments of Meso- and Paleoproterozoic sedimentary cover on the surrounding cratonic basement as evidence of this recycling system. Similarly, Konopásek et al. (2017) and Konopásek et al. (2018) inferred an extensive Mesoproterozoic sedimentary cover sequence as the source for the Neoproterozoic successions of the Kaoko Belt foreland. Given the presumed pre-Atlantic proximity of the Kaoko Belt to the northern Dom Feliciano Belt (Konopásek et al., 2017; Porada, 1989), we judge this inferred extensive Mesoproterozoic cover sequence as the most likely candidate for the

Mesoproterozoic zircon populations in the Brusque Complex rocks.

4.4. Unimodal detrital zircon pattern and its possible sources

Zircon ages at ca. 2.20 Ga, corresponding to the largest peak in the unimodal pooled zircon age distribution pattern (Fig. 7c), are known from local basement rocks of the Luis Alves Craton, the Camboriú Complex and the Águas Mornas Complex (Basei et al., 2009; Hartmann et al., 1999, 2000; Silva et al., 2000, 2005). The closest basement unit of the Luis Alves Craton is the Santa Catarina Granulite Complex, which outcrops immediately to the north of the Itajaí Basin (Fig. 1). Zircon grains from granulitic gneisses of this complex mostly preserve U–Pb ages of ca. 2.20–2.10 Ga, with less common ca. 2.40–2.30 Ga ages and minor occurrences of ca. 2.00 Ga zircon (Basei et al., 2009; Hartmann et al., 1999, 2000). Ages corresponding to the smaller peaks at ca. 2.10 and 2.00 Ga are also known from the Camboriú Complex (Silva et al., 2000, 2005), as well as from exposed Congo Craton basement in the Kaoko Belt (Kröner et al., 2004). As the samples from the unimodal group contain only single zircon age peaks, which correspond to ages in the local basement, we interpret the unimodal group as reflecting first generation detrital zircon and thus direct erosion of the basement.

The Brusque Complex contains both local basement-derived sediment and recycled sediment, however the absence of a 2.20 Ga age peak in the polymodal group suggests that these two sources did not mix. This indicates that the inferred Mesoproterozoic sedimentary cover source was completely eroded before any of the local basement was exposed. Inferring from this that the sediment was sourced locally implies also that the Mesoproterozoic sedimentary sequences covered the Luis Alves basement prior to erosion into the Brusque Complex paleobasin, and thus that the Congo and Luis Alves cratons were in close proximity prior to Neoproterozoic rifting.

Both the unimodal and polymodal sample groups do not contain zircon age peaks younger than 1.20 Ga, and even the youngest individual zircons are no older than ca. 0.9–1.0 Ga (Fig. 7b and c). Considering the minimum age of sedimentation at ca. 810 Ma, the Brusque Complex metasediments therefore contain no zircon grains sourced from syn-sedimentary igneous rocks. This is typical of rift basin or passive margin environments, where the influx of material into the basin is dominated by older grains sourced from the surrounding craton (Cawood et al., 2012).

4.5. Bimodal detrital zircon pattern and its possible sources

The two samples with bimodal age distribution contain the youngest zircon grains of all the studied samples, with between one third and one half of the total analysed grains dated in the Neoproterozoic. Using the youngest zircon age peak as a conservative estimate of the timing of sedimentation (Dickinson and Gehrels, 2009), the maximum age of sedimentation of the protolith is ca. 560 Ma (Fig. 7d). However, the much more robust peak at ca. 665 Ma is a safer benchmark for the maximum sedimentation age, considering the possibility of lead loss in the small number of younger grains during late-stage orogenic deformation or modern weathering. This post-dates the ca. 811 Ma minimum age of sedimentation constrained in this study by at least ca. 150 million years, implying the presence of two temporally distinct sedimentary protoliths. This observation remains difficult to confirm in the field, as the younger rocks appear to be metamorphosed at similar greenschist facies conditions as the low-grade Brusque Complex rocks, and they exhibit a deformation style indistinguishable from the high-strain zones of the Brusque Complex further inland (see Basei et al., 2011b). Indeed, it is possible that ancient lead loss could account for the Neoproterozoic zircon peaks by skewing Mesoproterozoic ages along the concordia towards younger values (e.g. Andersen et al., 2019). However, the large Neoproterozoic fraction (up to ca. 45%), the low-grade metamorphic conditions, and the remarkable similarity of the detrital signature to that of the adjacent Itajaí Basin (see section 4.6) favours the former interpretation. Further, two distinct depositional episodes have also recently been identified in the Porongos Complex of the central Dom Feliciano Belt foreland (Battisti et al., 2018; Höfig et al., 2018).

The ca. 2.20 Ga age peak and the spread of individual Mesoproterozoic and Paleoproterozoic dates between ca. 2.10–1.00 Ga (Fig. 7d) show similarities with the unimodal and polymodal groups respectively (Fig. 7b and c). The ca. 665 Ma age fits well with earliest estimates of the timing of orogenesis in the Dom Feliciano Belt (De Toni et al., 2020b), and thus the most likely protosource for the ca. 665 peak is the orogenic hinterland. The hinterland rocks record ca. 650–645 Ma zircon ages (Chemale et al., 2012) associated with orogenesis in the northern Dom Feliciano Belt, and up to ca. 665–660 Ma (Frantz et al., 2003; Masquelin et al., 2012) in the southern Dom Feliciano Belt. The number of grains between ca. 640–600 Ma fit with known ages from the Granite Belt, which intruded the orogenic hinterland between ca. 640–580 Ma (Chemale et al., 2012; Florisbal et al., 2012b).

Considering this possible protosource, the distribution pattern shown in Fig. 7d can thus be explained by a combination of recycled (meta) sedimentary rocks with a detrital zircon content matching the unimodal and polymodal sample groups of the Brusque Complex, and syn-orogenic rocks sourced directly from the orogenic hinterland.

4.6. Comparison with the Itajaí basin

The data suggest that the sedimentary protoliths of the bimodal sample group were sourced from erosion of the rising orogen, and thus they possibly represent syn-orogenic flysch- or molasse-type sediments similar to the Itajaí Basin. In support of this, the data from the Itajaí Basin show remarkably similar detrital zircon patterns, with the same primary age fractions with major peaks at ca. 650–550 Ma and

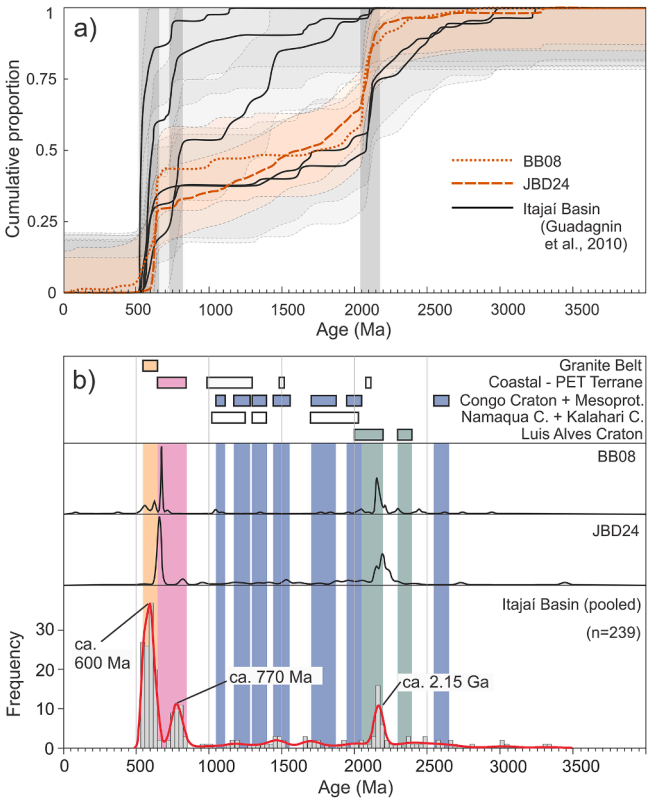

Fig. 8. Comparison between detrital zircon signatures of samples BB08, JBD24, and the Itajaí Basin: a) individual cumulative distribution curves with 95% confidence intervals (shaded columns delineate major common age fractions) b) KDEs and frequency histograms, with pooled Itajaí Basin data. Data for Itajaí Basin from Guadagnin et al. (2010). See Fig. 7 for age range references.

2.20–2.05 Ga, and a distribution of individual ages between ca. 2.00–1.00 Ga (Fig. 8a and b). Further, the ages corresponding to the small peak at ca. 560 Ma in the KDE curve are known from syn-sedimentary volcanism in the Itajaí Basin (Guadagnin et al., 2010), although the small number of grains younger than 600 Ma (8 grains) make this correlation only speculative.

The Itajaí Basin shows a typical orogenic foreland deformation style (e.g. Condie, 2016), with the margin closest to the foreland fold and thrust belt (i.e. the Schist Belt) showing stronger deformation than the opposite margin (Basei et al., 1998b; Guadagnin et al., 2010). Given the proposed source rocks and similarities with the Itajaí Basin sediments, we interpret samples JBD24 and BB08 as belonging to syn-orogenic sediments deposited in a foreland basin setting similar to the Itajaí Basin, or possibly part of the Itajaí Basin itself. The proximity and structural correlation of these rocks to the Itajaí–Perimbó Shear Zone (Fig. 2) lends support to this interpretation, as parts of the foreland basin closest to the leading edge of the fold-and-thrust belt would likely become tectonically interleaved with the Brusque Complex, making the deformation history between the two distinct protoliths indistinguishable.

4.7. Comparing the Kaoko–Dom Feliciano–Gariep Neoproterozoic foreland units

The Brusque Complex zircon distribution shares many similarities with the foreland fold-and-thrust belt cover sequences of the central Dom Feliciano Belt (Porongos Complex), the Kaoko Belt and the Gariep Belt. Fig. 9 compares detrital zircon data from these four regions, showing pooled data from various published detrital zircon studies (Andersen et al., 2018a; Gruber et al., 2011; Höfig et al., 2018; Hofmann et al., 2014; Konopásek et al., 2014, 2017; Pertille et al., 2015a, 2017), with samples grouped together based on the patterns as recognized in this study. The same two detrital zircon age distribution patterns as seen in the Brusque Complex are recorded in each of the other regions, with only minor differences (Fig. 9a and b). The Lavalleja Complex in Uruguay is often interpreted as the continuation of the Schist Belt in the southern Dom Feliciano Belt (Basei et al., 2008a). However, due to the small number of published detrital zircon datasets and poor age constraints (see Hueck et al., 2018b), the potential correlation of the Lavalleja Complex with the rest of the Schist Belt will not be further discussed.

The pooled polymodal group of the Porongos Complex samples matches well with the Brusque Complex rocks of this study (Fig. 9a and c). Using the *1-O* parameter of Andersen et al. (2016), they show a perfect pairwise overlap within 95% confidence intervals (*1-O* = 0.00). Like the Brusque Complex, the pooled data of the Porongos Complex is missing a 2.20 Ga peak, suggesting a majority African affinity for the sedimentary protosources (Fig. 9c). The similarities between the units imply that they shared the same source, which supports the interpretation that the Schist Belt of the Dom Feliciano Belt represents sediment deposited into a coeval and spatially related system of paleobasins.

The Porongos Complex unimodal group also shows a good match with the equivalent Brusque Complex rocks (Fig. 9b) (pairwise overlap *1-O* = 0.04). The Paleoproterozoic peaks between ca. 2.20–2.00 Ga in the samples with unimodal distribution have been linked with local basement rocks of the Encantadas Complex (Pertille et al., 2015a, 2017), and can also be correlated with ca. 2.50–2.00 Ga basement rocks of the Taquarembó Block, part of the Nico Pérez Terrane (Fig. 9d) (Oyhantçabal et al., 2011b, 2018 and references therein). The similarities in age between the Brazilian Nico Pérez Terrane (Taquarembó Block) and the Luis Alves Craton, most notably the presence of ca. 2.20 Ga rocks which are absent on the African side of the orogen, suggests that these cratonic blocks may represent a continuous basement unit.

For the Kaoko Belt, the two sample groups are pooled based on the patterns as recognised in this study and as constrained by the local stratigraphy (Fig. 9b and c) (Konopásek et al., 2014, 2017). Konopásek et al. (2017) showed that the pre-orogenic stratigraphic position of the Kaoko Belt metasedimentary rocks can be distinguished based on their detrital zircon signatures, with the lower sequences containing both Paleoproterozoic and Mesoproterozoic ages, and the upper sequences dominated by Paleoproterozoic ages only. The Kaoko Belt polymodal group shows strong similarities to the Brusque and Porongos Complexes (Fig. 9a) (pairwise overlap *1-O* = 0.03 and 0.02 respectively). The Mesoproterozoic peaks at ca. 1.55, 1.40 and 1.20 Ga match well with those from the Brusque Complex, and the same with the Paleoproterozoic peaks between ca. 2.10–1.80 Ga and the notable absence of ca. 2.20 Ga zircon. The only significant difference between the Mesoproterozoic detrital signals of the Kaoko and Dom Feliciano Belts is the presence of a ca. 1.05 Ga peak in the Kaoko Belt rocks (Fig. 9c), which can also be found in the foreland supra-crustal rocks of the Gariep Belt (Basei et al., 2005; Hofmann et al., 2014, 2015).

The pooled unimodal group shows a prominent Paleoproterozoic peak similar to the Brusque and Porongos complexes (Fig. 9d). However, the peak is centred at 1.80 Ga, resulting in a poor pairwise overlap comparison (Fig. 9b) (*1-O* = 0.11). This age peak fits with erosion of the local Congo Craton basement (Kröner et al., 2004; Luft et al., 2011).

Konopásek et al. (2017) recognised the gradual disappearance of Mesoproterozoic zircon from the upper parts of the Kaoko Belt supracrustal sequences, and suggested that this reflects the complete erosion of Mesoproterozoic supracrustal source rocks into the lower parts of the paleobasin, with the upper sequences representing erosion of the exposed local basement. Given evident similarities in detrital zircon signatures, it is possible that the Brusque Complex protolith was deposited in the same way; the rocks with polymodal zircon distribution representing the lower strata, and those with unimodal distribution the upper strata of the basin. This interpretation would necessitate a complete revision of the current stratigraphy of the Brusque Complex (Basei et al., 2006, 2011b), as the samples with polymodal and unimodal patterns come from all known stratigraphic levels. However, given problems with exposure in the northern Dom Feliciano Belt, it remains difficult to test this hypothesis, and is otherwise beyond the scope of this study.

Data from the Port Nolloth Zone of the Gariep Belt (Andersen et al., 2018a; Hofmann et al., 2014) also fit into unimodal and polymodal groups (Fig. 9 a and b). The polymodal group contains the same late Mesoproterozoic age peaks at ca. 1.30, 1.20 and 1.10 Ga (Fig. 9c), however there is a conspicuous absence of early Mesoproterozoic ages ca. 1.50 Ga, resulting in poor pairwise overlap comparisons (*1-O*: Brusque Complex = 0.18, Porongos Complex = 0.22, Kaoko Belt = 0.22). The Namaqua Metamorphic Complex outcropping along the western edge of the Kalahari Craton contains abundant Mesoproterozoic rocks dated between ca. 1.30–1.00 Ga (Becker et al., 2006; Bial et al., 2015; Clifford et al., 2004), and has no record of 1.50 Ga events, making these rocks the most likely protosource. The Gariep unimodal group is dominated by a single Paleoproterozoic peak at 1.90 Ga, which fits with basement of the Kalahari Craton (Fig. 9d) and closely matches the Kaoko Belt unimodal group (pairwise overlap *1-O* = 0.04). Andersen et al. (2018a) interpret the Gariep Belt detrital zircon signature as the result of mixing of various protosources during sedimentary recycling events prior to Neoproterozoic rifting, similar to the inferred Mesoproterozoic sedimentary cover of Konopásek et al. (2017). However, the differences between the Gariep Belt and the rest of the orogen clearly shows there is local variation in the recycled sediment protosources,

The similarities in detrital signatures strongly suggest that the pre-orogenic supracrustal rocks of the Brusque Complex, Porongos Complex and the Kaoko Belt partly shared the same source, and that the Gariep Belt shared at least some of the same protosources. The protosources for the polymodal group are clearly of African affinity, with no clear equivalent in the South American rock record, suggesting that the sediment was sourced from Mesoproterozoic (volcano-)sedimentary sequences containing recycled African detritus.

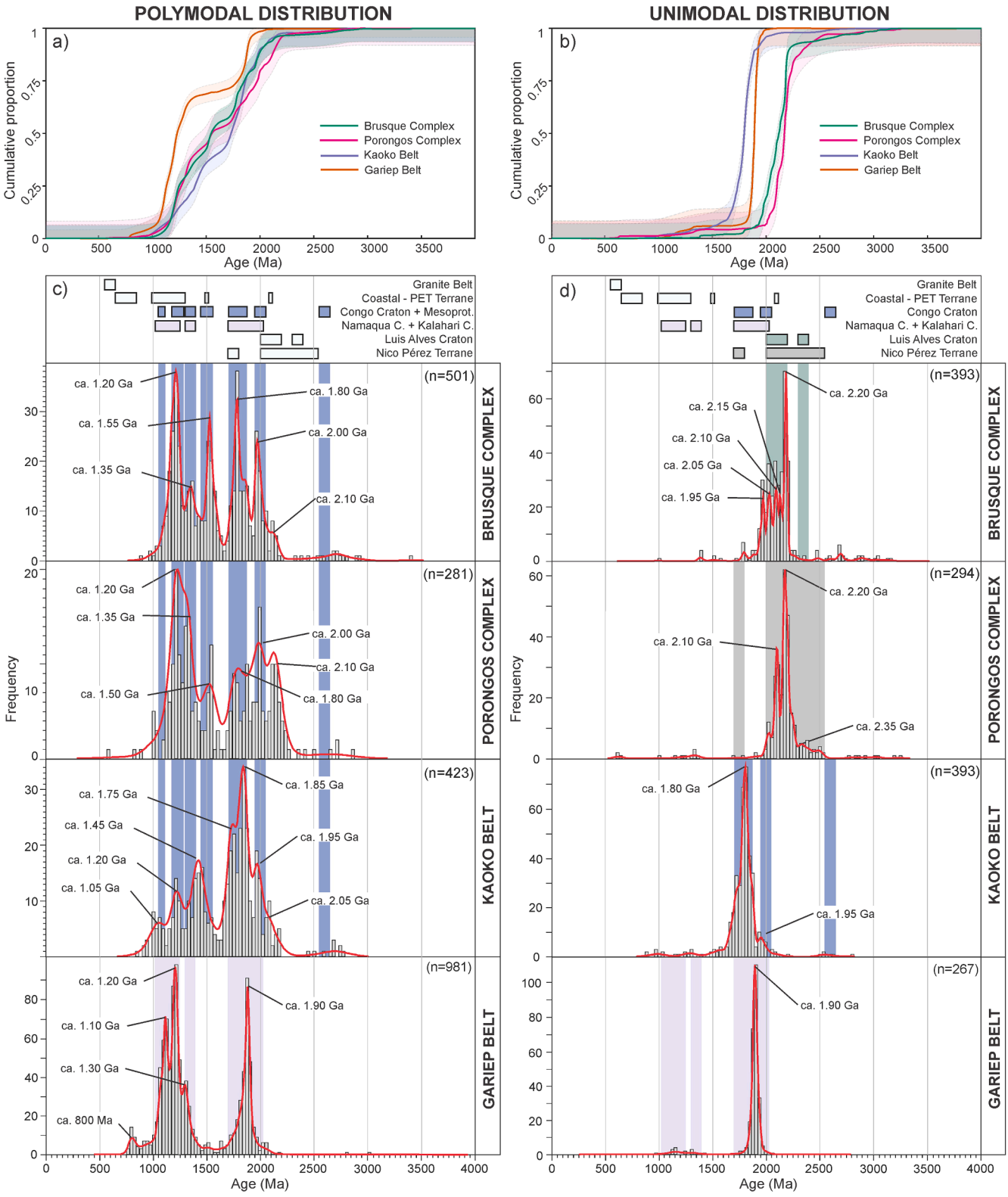

Fig. 9. Comparison between detrital zircon data of the pre-orogenic metasediments of the Brusque Complex, the Porongos Complex, the Kaoko Belt and the Gariep Belt (Porth Nolloth Zone): a) cumulative distribution curves for pooled polymodal group, b) cumulative distribution curves for pooled unimodal group, c) KDEs and histograms for polymodal group and d) KDEs and histograms for unimodal group. Data are grouped according to the patterns as identified in this study. Data sources: Brusque Complex from this study, Porongos Complex from Gruber et al. (2011); Höfig et al. (2018); Pertille et al. (2015a, 2015b, 2017), Kaoko Belt from Konopásek et al. (2014, 2017), Gariep Belt from Andersen et al. (2018a); Hofmann et al. (2014). Nico Pérez age range from Oyhantçabal et al. (2018) and references therein. See Fig. 7 for references for the remaining age-range bars.

4.8. Tectonic setting and evolution of the Schist Belt

Fig. 10 shows schematic cross sections across the northern Dom Feliciano Belt and the Kaoko Belt, outlining the proposed evolution of the Schist Belt as inferred from the Brusque Complex U–Pb zircon data and correlations with the other units. During the pre-rifting stage at ca. 1.0 Ga–850 Ma, the Congo and Luis Alves cratons were connected, accompanied by Mesoproterozoic terranes and cover sequences associated with the amalgamation of Rodinia (Fig. 10a) (Bial et al., 2015; Miller, 2012). The lack of detrital zircon close to the age of

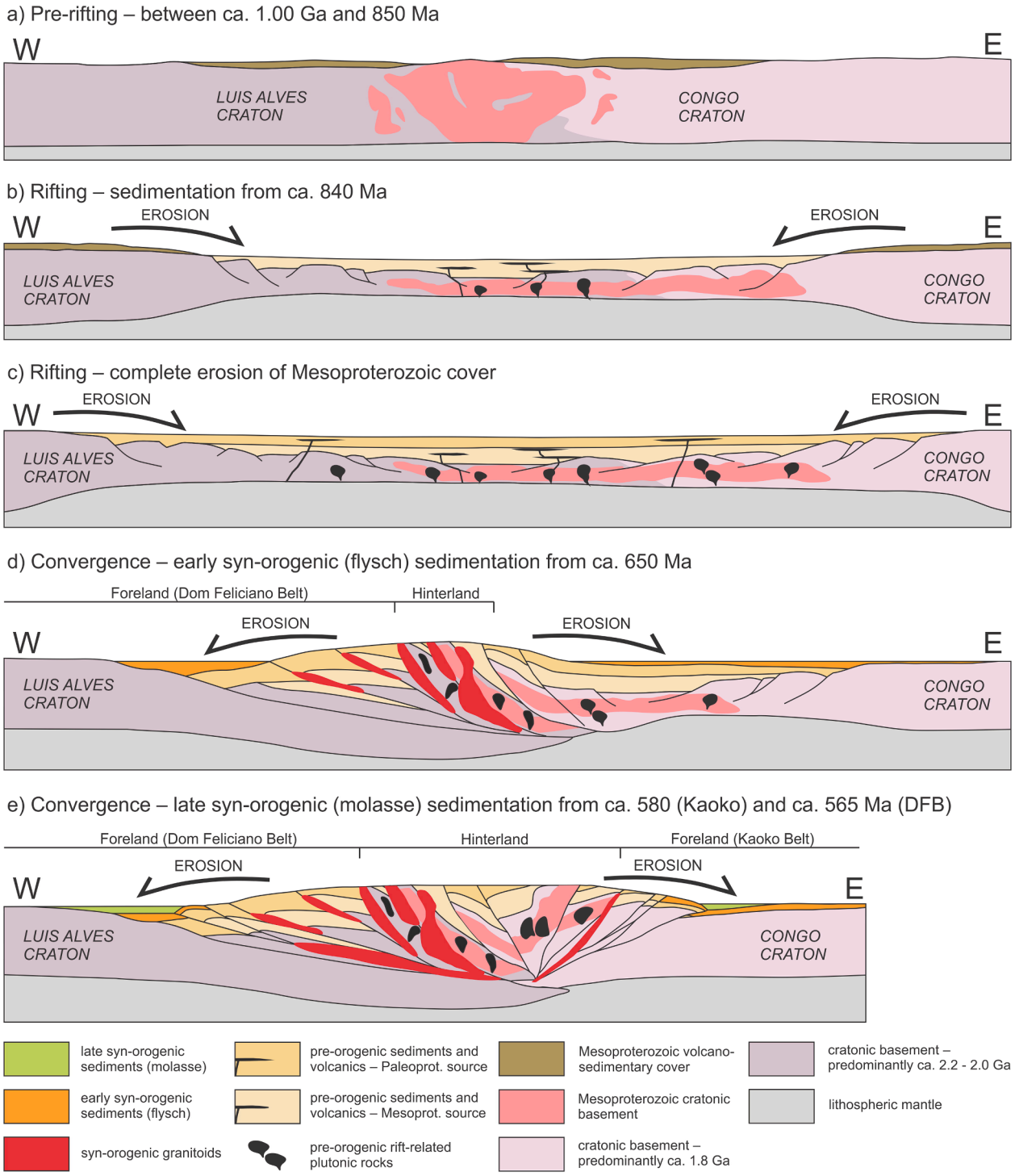

Fig. 10. Schematic cross sections outlining the proposed evolution of the Kaoko–Dom Feliciano Belt as inferred from U–Pb detrital zircon data: a) pre-rifting stage ca. 1.0 Ga–850 Ma, the Congo and Luis Alves cratons are connected, together with Mesoproterozoic terranes and cover sequences associated with Rodinia amalgamation, b) rifting from ca. 840 Ma, erosion of an extensive Mesoproterozoic cover sequence, sedimentation into the rift basin from at least ca. 810 Ma, c) rifting continues, complete erosion of the Mesoproterozoic cover and erosion of the Luis Alves and Congo Craton Basement, d) rift inversion and convergence leads to orogenesis at ca. 650, and the erosion of the rising hinterland leads to sedimentation (flysch) into *syn*-orogenic basins, e) continued convergence leads to the movement of the orogenic front towards the east and the formation of the Kaoko Belt, more sedimentation into both foreland basins, and late deformation in the west leads to deformation and metamorphism of the *syn*-orogenic sediments in the Brusque Complex.

sedimentation within the pre-orogenic sediments of the Kaoko–Dom Feliciano–Gariep Belt indicates the absence of magmatic activity on the crust of either basin margin at this time. Based on the model of Cawood et al. (2012), the pre-orogenic sediments of the Brusque Complex, Porongos Complex, Kaoko Belt and Gariep Belt best fit into an extensional setting, as the youngest 5% of zircon are>150 m.y. older than the age of sedimentation (Fig. 11). This finding supports a pure intracontinental rifting model for the formation of the Kaoko–Dom Feliciano–Gariep basin (Konopásek et al., 2018, 2020), and is in disagreement with various proposed subduction-collision models that place arc-magmatism inside and/or at the margin of the basin during or before its opening (De Toni et al., 2020a; Koester et al., 2016; Lenz et al., 2013; Martil et al., 2017). Based on this interpretation, the basin formed by intracontinental rifting from ca. 840 Ma (Basei et al., 2008b), with sedimentation into the Brusque Complex paleobasin from at least ca. 810 Ma (Fig. 10b). The complete erosion of the Mesoproterozoic cover sequences on the South American side, and the near-complete erosion on the African side, led to erosion of the Luis Alves and Congo cratons into the rift basin (Fig. 10c).

The period prior to convergence and orogenesis consisted of either 1) rift-drift transition and the development of the Adamastor Ocean (e.g. Basei et al., 2018 and references therein), or 2) continued intracontinental rifting and little to no oceanic spreading (e.g. Konopásek et al., 2020). Due to the continued lack of geochronological constraints on sedimentation into the Brusque Complex paleobasin, the duration of rifting cannot be inferred from our data. However, based on the lack of evidence of late-Neoproterozoic subduction-related metamorphism, the syn- to post- collisional nature of the Granite Belt (Bitencourt and Nardi, 1993, 2000; Florisbal et al., 2012a, 2012b), and evidence in the Kaoko Belt of crustal stretching and sedimentation up to ca. 660 Ma (Konopásek et al., 2020), the latter model is favoured for this interpretation.

Based on similarities with the Itajaí Basin, we interpret the syn-orogenic sediments of the Brusque Complex as belonging to a collisional foreland setting (Fig. 11). This suggests that, after rift inversion and convergence led to orogenesis at ca. 650 Ma (De Toni et al., 2020b), the eroding rising hinterland fed into proximal syn-orogenic basins (Fig. 10d). Finally, continued convergence led to the movement of the orogenic front towards the east (Fig. 10e), where the hinterland overrode the Congo Craton margin and led to the development of the Kaoko Belt from ca. 580 Ma (Goscombe et al., 2003a; Konopásek et al., 2008). This late-stage convergence is reflected in the northern Dom Feliciano belt by the deformation of syn-orogenic sediments and their possible incorporation into the Brusque Complex (Fig. 10e).

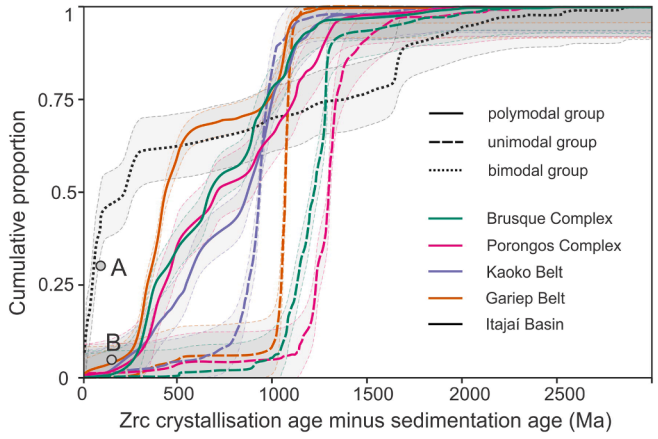

Fig. 11. Summary cumulative distribution function plot (with 95% confidence intervals) showing the difference between the detrital zircon crystallisation age and the sedimentation age of the various sample groups in this study. Point A and B are from Cawood et al. (2012), showing the points used to predict tectonic setting: A–youngest 30% of grains with < 100 M.y. difference suggests convergent tectonic setting, >100 M.y. difference suggests collisional foreland setting; B–youngest 5% of grains with < 150 M.y. difference suggests collisional foreland setting, >150 M.y. difference suggests extensional setting. Sedimentation ages are based on this study and from other sources in the text.

4.9. Tectonic implications for pre-orogenic configuration

Based on pre-Atlantic plate reconstructions (Heine et al., 2013), and correlations between basement units (Konopásek et al., 2016), the Brusque Complex and Kaoko Belt foreland fold-and-thrust belts were located at approximately similar positions on either side of the orogenic hinterland (Fig. 12). The identification of a single source for significant parts of the pre-orogenic supracrustal rocks of the Dom Feliciano and Kaoko belts provides strong evidence to also correlate these rocks prior to early-Neoproterozoic rifting. Considering their deposition into a system of coeval, spatially related paleobasins, the Congo Craton, Luis Alves Craton and Nico Pérez Terrane must have been in close proximity at the onset of early-Neoproterozoic rifting (Fig. 10). Despite differences in protosources, the similarities in sedimentation history of the Gariep Belt suggests the involvement of the Kalahari Craton as well.

This means that, considering the correlation between the northern and central parts of the Schist Belt (Fig. 12), the rifting stage beginning at ca. 840–830 Ma (Basei et al., 2008b; Frimmel et al., 2001) may have involved a combined Luis Alves – Nico Pérez terrane rifting from the Congo and Kalahari cratons (Johansson, 2014; Konopásek et al., 2018). Although some authors argue that these cratonic fragments were separated by wide oceanic domains at the time of sedimentation (e.g. Foster et al., 2015), the data from this study support tectonic models that place these crustal blocks together in Rodinia at the onset of rifting (e.g. Konopásek et al., 2020; Oriolo et al., 2016; Oyhantçabal et al., 2011a; Philipp et al., 2016; Rapela et al., 2011).

The results of this study also contradict suggestions that the Major Gercino Shear Zone, and possibly the rest of the Southern Brazilian Shear Belt, separates distinct sedimentary rocks of African affinity on one side, and South American affinity on the other (Basei et al., 2000, 2008a). Although there are differences in source region for parts of the sedimentary protoliths that correlate with local African or South American basement, the Mesoproterozoic detrital zircon ages in both belts show a shared source with clear African affinity, and based on this study there is no indication that the Major Gercino Shear Zone represents a syn-sedimentary, pre-orogenic structure that separated basins with entirely different source regions.

5. Conclusions

1) U–Pb zircon dating of a felsic dyke intruding sedimentary rocks of the Brusque Complex constrains the minimum age of sedimentation into the Brusque Complex paleobasin at 811 ± 6 Ma. This age correlates with sedimentation age constraints in the Porongos Complex, Kaoko Belt and Gariep Belt, and with the age of pre-orogenic magmatism and sedimentation in the orogenic hinterland.
2) U–Pb detrital zircon dating of metamorphosed magmatic and sedimentary rocks of the Brusque Complex reveals three distinct sample groups. The first group shows a polymodal age distribution, with peaks in both the Meso- and Paleoproterozoic. The second group contains only Paleoproterozoic ages, dominated by a single age peak. The third group shows a mostly bimodal age distribution, with a major Neoproterozoic age fraction.
3) Potential protosources for the Mesoproterozoic zircon grains in the polymodal sample group are all of African affinity. The most likely source for the sediment was Mesoproterozoic sedimentary cover of the Congo Craton bearing recycled zircon grains. We suggest that the Mesoproterozoic sediment also covered the Luis Alves Craton prior to Neoproterozoic rifting. The Paleoproterozoic zircon grains from the unimodal sample group were likely sourced from local basement represented by the Luis Alves Craton and Camboriú Complex.

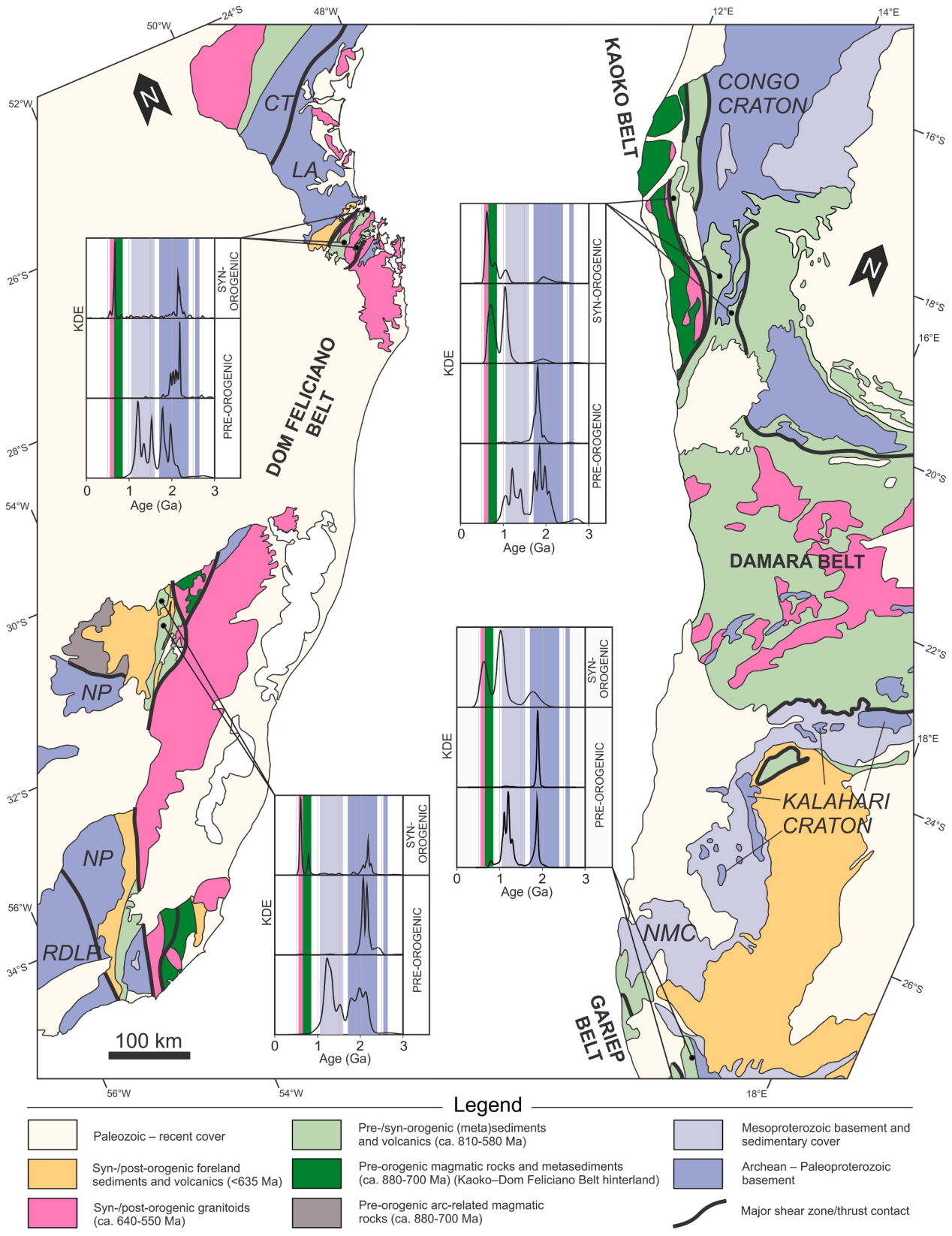

Fig. 12. Overview map showing the correlation of metasedimentary rocks of the Kaoko–Dom Feliciano Belt orogenic forelands (modified after Hueck et al., 2018b; Konopásek et al., 2017; McCourt et al., 2013; Oyhantçabal et al., 2011b; and Passarelli et al., 2018). NMC = Namaqua Metamorphic Complex, RDLP = Rio de la Plata Craton, NP = Nico Pérez Terrane, LA = Luis Alves Craton, CT = Curitiba Terrane. For KDE figures see Fig. 7 for references. Coloured bars behind KDE curves represent probable protosource regions, and the colours correspond to those regions as shown in the map.

4) The Neoproterozoic zircon grains in the bimodal sample group post-date sedimentation in the Brusque Complex paleobasin as constrained in this study, suggesting that these rocks belong to a later paleobasin formed in a different tectonic environment. Similarities with the Itajaí Basin suggest that they represent parts of a syn-orogenic foreland basin, with sediment sourced from the rising orogenic hinterland. The rocks were likely tectonically interleaved with the Brusque Complex during late-stage orogenic deformation.
5) The absence of Neoproterozoic zircon at or close to the age of sedimentation in the pre-orogenic sediments of the Brusque Complex implies that the paleobasin did not evolve within a convergent tectonic setting, supporting a pure intracontinental rifting model for basin formation.
6) Comparison of pre-orogenic Brusque Complex detrital zircon data with equivalent rocks in the Porongos Complex, Kaoko Belt and Gariep Belt indicates a shared source and/or shared basin evolution, implying that these sediments were deposited into a system of coeval and spatially related paleobasins. The data imply that the Luis Alves Craton, Congo Craton, Nico Pérez Terrane and Kalahari Craton were in close proximity at the start of Neoproterozoic rifting and the breakup of Rodinia.

CRediT authorship contribution statement

Jack James Percival: Conceptualization, Methodology, Formal analysis, Investigation, Writing - original draft, Visualization. **Jiří Konopásek:** Conceptualization, Methodology, Resources, Funding acquisition, Writing - review & editing, Project administration, Supervision. **Ragnhild Eiesland:** Conceptualization, Methodology, Formal analysis, Investigation. **Jiří Sláma:** Investigation, Formal analysis, Validation, Data curation. **Roberto Sacks de Campos:** Investigation, Writing - review & editing. **Matheus Ariel Battisti:** Investigation, Writing - review & editing. **Maria de Fátima Bitencourt:** Supervision, Writing - review & editing.

Declaration of Competing Interest

The authors declare that they have no known competing financial interests or personal relationships that could have appeared to influence the work reported in this paper.

Acknowledgements

This work was supported by the Norwegian Centre for International Cooperation in Education (SIU), the Norwegian Agency for International Cooperation and Quality Enhancement in Higher Education (Diku), and the Coordenação de Aperfeicoamento de Pessoal de Nível Superior (CAPES) in Brazil through the grant projects no. UTF-2016-CAPES-SIU10024 and UTF-2018-CAPES-Diku-10004. J. Konopásek acknowledges financial support of the Czech Science Foundation, grant no. 18-24281S. J. Sláma was supported by the ASCR institutional support RVO 67985831. Acknowledgements and thanks to D. Lyra for fieldwork assistance. The authors are grateful to T. Andersen and an anonymous reviewer for their helpful reviews.

Appendix A. Supplementary data

Supplementary data to this article can be found online at https://doi.org/10.1016/j.precamres.2020.106060.

References

Almeida, R.P., Janikian, L., Fragoso-Cesar, A.R.S., Fambrini, G.L., 2010. The Ediacaran to Cambrian Rift System of Southeastern South America: tectonic Implications. J. Geol. 118 (2), 145–161. https://www.doi.org/10.1086/649817.

Andersen, T., Elburg, M., Cawthorn-Blazeby, A., 2016. U-Pb and Lu–Hf zircon data in young sediments reflect sedimentary recycling in eastern South Africa. J. Geol. Soc. 173 (2), 337–351. https://doi.org/10.1144/jgs2015-006.

Andersen, T., Elburg, M.A., van Niekerk, H.S., Ueckermann, H., 2018a. Successive sedimentary recycling regimes in southwestern Gondwana: Evidence from detrital zircons in Neoproterozoic to Cambrian sedimentary rocks in southern Africa. Earth-Sci. Rev., vol. 181, pp. 43-60. Doi: 10.1016/j.earscirev.2018.04.001.

Andersen, T., Kristoffersen, M., Elburg, M.A., 2018b. Visualizing, interpreting and comparing detrital zircon age and Hf isotope data in basin analysis – a graphical approach. Basin Res., vol. 30, no. 1, pp. 132-147. Doi: 10.1111/bre.12245.

Andersen, T., Elburg, M.A., Magwaza, B.N., 2019. Sources of bias in detrital zircon geochronology: Discordance, concealed lead loss and common lead correction. Earth-Sci. Rev. 197, 102899 https://doi.org/10.1016/j.earscirev.2019.102899.

Basei, M.A.S., McReath, I., Siga Jr., O., 1998a. The Santa Catarina Granulite Complex of Southern Brazil: A Review. Gondwana Res. 1 (3–4), 383–391. https://www.doi.org/10.1016/S1342-937X(05)70854-6.

Basei, M.A.S., Citroni, S.B., Siga Jr, O., 1998b. Stratigraphy and age of fini-Proterozoic basins of Parana and Santa Catarina States, southern Brazil. Boletim IG-USP, Serie Cientifica 29, 195–216.

Basei, M.A.S., Siga, Jr O., Reis Neto, J.M.d., Passarelli, C.R., Prazeres, H., Kaulfuss, G., Sato, K., Lima, P.S., 1999. Paleoproterozoic granulitic belts of the Brazilian southern region (PR-SC). II South American Symposium on Isotope Geology. pp. 291-294. Cordoba, Argentina: Subsecretaría de Minería de la Nación.

Basei, M.A.S., Siga, Jr O., Masquelin, H., Harara, O.M., Reis Neto, J.M., Preciozzi, F., 2000. The Dom Feliciano Belt of Brazil and Uruguay and its Foreland Domain, the Rio de la Plata Craton: framework, tectonic evolution and correlation with similar provinces of Southwestern Africa. In Cordani U. G., et al. eds. Tectonic Evolution of South America. pp. 311-334. Rio de Janeiro, Brazil: Geological Society.

Basei, M.A.S., Frimmel, H.E., Nutman, A.P., Preciozzi, F., Jacob, J., 2005. A connection between the Neoproterozoic Dom Feliciano (Brazil/Uruguay) and Gariep (Namibia/South Africa) orogenic belts - Evidence from a reconnaissance provenance study. Precambrian Res. 139 (3–4), 195–221. https://www.doi.org/10.1016/j.precamres.2005.06.005.

Basei, M.A.S., Campos Neto, M.C., Castro, N.A., Santos, P.R., Siga, Jr. O., Passarelli, C.R., 2006. Mapa Geológico 1:100.000 das Folhas Brusque e Vidal Ramos, SC, Convênio USP-CPRM. XLII Congresso Brasileiro de Geologia, Aracaju, SE.

Basei, M.A.S., Frimmel, H.E., Nutman, A.P., Preciozzi, F., 2008a. West Gondwana amalgamation based on detrital zircon ages from Neoproterozoic Ribeira and Dom Feliciano belts of South America and comparison with coeval sequences from SW Africa. Geol. Soc. Spec. Publ. 294 (1), 239–256. https://www.doi.org/10.1144/SP294.13.

Basei, M.A.S., Grasso, C.B., Vlach, S.R.F., Nutman, A., Siga, Jr. O., Osaki, L.S., 2008b. A-type rift-related granite and the lower cryogenian age for the beginning of the Brusque Belt basin. Proceedings of South American Symposium on Isotope Geology. San Carlos de Bariloche, Argentina.

Basei, M.A.S., Nutman, A., Siga, Jr O., Passarelli, C.R., Drukas, C.O., 2009. The Evolution and Tectonic Setting of the Luis Alves Microplate of Southeastern Brazil: An Exotic Terrane during the Assembly of Western Gondwana. In Gaucher C., et al. eds. Developments in Precambrian Geology. pp. 273-291. Elsevier Doi: 10.1016/S0166-2635(09)01620-X.

Basei, M.A.S., Drukas, C.O., Nutman, A.P., Wemmer, K., Dunyi, L., Santos, P.R., Passarelli, C.R., Campos Neto, M.C., Siga Jr O., Osako, L., 2011a. The Itajaí foreland basin: A tectono-sedimentary record of the Ediacaran period, Southern Brazil. Int. J. Earth Sci., vol. 100, pp. 543–569. https://www.doi.org/10.1007/s00531-010-0604-4.

Basei, M.A.S., Campos Neto, M.C., Castro, N.A., Nutman, A.P., Wemmer, K., Yamamoto, M.T., Hueck, M., Osako, L., Siga, Jr O., Passarelli, C.R., 2011b. Tectonic evolution of the Brusque Group, Dom Feliciano belt, Santa Catarina, Southern Brazil. J. S. Am. Earth Sci., vol. 32, no. 4, pp. 324-350. https://www.doi.org/10.1016/j.jsames.2011.03.016.

Basei, M.A.S., Peel, E., Sánchez, Bettucci L., Preciozzi, F., Nutman, A.P., 2011c. The basement of the Punta del Este Terrane (Uruguay): an African Mesoproterozoic fragment at the eastern border of the South American Río de La Plata craton. Int. J. Earth Sci. 100, 289–304. https://doi.org/10.1007/s00531-010-0623-1.

Basei, M.A.S., Frimmel, H.E., Campos Neto, M.d.C., de Araujo, C.E.G., de Castro, N.A., Passarelli, C.R., 2018. The Tectonic History of the Southern Adamastor Ocean Based on a Correlation of the Kaoko and Dom Feliciano Belts. In Siegesmund S., et al. eds. Geology of Southwest Gondwana. pp. 63-85. 1st ed. Cham: Springer International Publishing Doi: 10.1007/978-3-319-68920-3_3.

Battisti, M.A., Bitencourt, M.F., De Toni, G.B., Nardi, L.V.S., Konopásek, J., 2018. Metavolcanic rocks and orthogneisses from Porongos and Várzea do Capivarita complexes: A case for identification of tectonic interleaving at different crustal levels from structural and geochemical data in southernmost Brazil. J. S. Am. Earth Sci. 88, 253–274. https://doi.org/10.1016/j.jsames.2018.08.009.

Becker, T., Schreiber, U., Kampunzu, A.B., Armstrong, R., 2006. Mesoproterozoic rocks of Namibia and their plate tectonic setting. J. Afr. Earth Sci. 46 (1–2), 112–140. https://doi.org/10.1016/j.jafrearsci.2006.01.015.

Bettucci, L.S., Cosarinsky, M., Ramos, V.A., 2001. Tectonic Setting of the Late Proterozoic Lavalleja Group (Dom Feliciano Belt). Uruguay. Gondwana Res. 4 (3), 395–407. https://doi.org/10.1016/S1342-937X(05)70339-7.

Bial, J., Büttner, S.H., Frei, D., 2015. Formation and emplacement of two contrasting late-Mesoproterozoic magma types in the central Namaqua Metamorphic Complex (South Africa, Namibia): Evidence from geochemistry and geochronology. Lithos 224–225, 272–294. https://doi.org/10.1016/j.lithos.2015.02.021.

Bitencourt, M.F., Nardi, L., 1993. Late- to Post-collisional Brasiliano Magmatism in Southernmost Brazil. Anais da Academia Brasileira de Ciências 65, 3–16.

Bitencourt, M.F., Nardi, L.V.S., 2000. Tectonic setting and sources of magmatism related to the southern Brazilian shear belt. Rev. Brasil. Geocienc. 30 (1), 186–189.
Bybee, G.M., Hayes, B., Owen-Smith, T.M., Lehmann, J., Ashwal, L.D., Brower, A.M., Hill, C.M., Corfu, F., Manga, M., 2019. Proterozoic massif-type anorthosites as the archetypes of long-lived (≥100 Myr) magmatic systems—New evidence from the Kunene Anorthosite Complex (Angola). Precambrian Res. 332, 105393 https://doi.org/10.1016/j.precamres.2019.105393.
Campos, R.S., Philipp, R.P., Massonne, H.-J., Chemale Jr, F., Theye, T., 2011. Petrology and isotope geology of mafic to ultramafic metavolcanic rocks of the Brusque Metamorphic Complex, southern Brazil. Int. Geol. Rev. 54 (6), 686–713. https://doi.org/10.1080/00206814.2011.569393.
Campos, R.S., Philipp, R.P., Massonne, H.-J., Chemale Jr, F., 2012. Early post-collisional Brasiliano magmatism in Botuverá region, Santa Catarina, southern Brazil: Evidence from petrology, geochemistry, isotope geology and geochronology of the diabase and lamprophyre dikes. J. S. Am. Earth Sci. 37, 266–278. https://doi.org/10.1016/j.jsames.2012.02.005.
Cawood, P.A., Hawkesworth, C.J., Dhuime, B., 2012. Detrital zircon record and tectonic setting. Geology 40 (10), 875–878. https://doi.org/10.1130/g32945.1.
Chemale, F., Philipp, R.P., Dussin, I.A., Formoso, M.L.L., Kawashita, K., Berttotti, A.L., 2011. Lu–Hf and U-Pb age determination of Capivarita Anorthosite in the Dom Feliciano Belt. Brazil. Precambrian Res. 186 (1–4), 117–126. https://doi.org/10.1016/j.precamres.2011.01.005.
Chemale, F., Mallmann, G., Bitencourt, M.F., Kawashita, K., 2012. Time constraints on magmatism along the Major Gercino Shear Zone, southern Brazil: Implications for West Gondwana reconstruction. Gondwana Res. 22 (1), 184–199. https://doi.org/10.1016/j.gr.2011.08.018.
Clifford, T.N., Barton, E.S., Stern, R.A., Duchesne, J.-C., 2004. U-Pb Zircon Calendar for Namaquan (Grenville) Crustal Events in the Granulite-facies Terrane of the O'okiep Copper District of South Africa. J. Petrol. 45 (4), 669–691. https://doi.org/10.1093/petrology/egg097.
Condie, K.C., 2016. Chapter 3 - Tectonic Settings. In: Condie, K.C. (Ed.), Earth as an Evolving Planetary System (Third Edition). Academic Press, pp. 43–88. https://doi.org/10.1016/B978-0-12-803689-1.00003-1.
De Toni, G.B., Bitencourt, M.F., Nardi, L.V.S., Florisbal, L.M., Almeida, B.S., Geraldes, M., 2020a. Dom Feliciano Belt orogenic cycle tracked by its pre-collisional magmatism: The Tonian (ca. 800 Ma) Porto Belo Complex and its correlations in southern Brazil and Uruguay. Precambrian Res. 342, 105702 https://doi.org/10.1016/j.precamres.2020.105702.
De Toni, G.B., Bitencourt, M.F., Konopásek, J., Martini, A., Andrade, P.H.S., Florisbal, L.M., Campos, R.S., 2020b. Transpressive strain partitioning between the Major Gercino Shear Zone and the Tijucas Fold Belt, Dom Feliciano Belt, Santa Catarina, southern Brazil. J. Struct. Geol. 136, 104058 https://doi.org/10.1016/j.jsg.2020.104058.
Dickinson, W.R., Gehrels, G.E., 2009. Use of U-Pb ages of detrital zircons to infer maximum depositional ages of strata: A test against a Colorado Plateau Mesozoic database. Earth Planet. Sci. Lett. 288 (1–2), 115–125. https://doi.org/10.1016/j.epsl.2009.09.013.
Drüppel, K., Littmann, S., Romer, R.L., Okrusch, M., 2007. Petrology and isotope geochemistry of the Mesoproterozoic anorthosite and related rocks of the Kunene Intrusive Complex. NW Namibia. Precambrian Res. 156 (1–2), 1–31. https://doi.org/10.1016/j.precamres.2007.02.005.
Evans, D.A.D., 2009. The palaeomagnetically viable, long-lived and all-inclusive Rodinia supercontinent reconstruction. Geol. Soc. Spec. Publ. 327 (1), 371. https://doi.org/10.1144/SP327.16.
Florisbal, L.M., Bitencourt, M.F., Nardi, L.V.S., Conceição, R.V., 2009. Early post-collisional granitic and coeval mafic magmatism of medium- to high-K tholeiitic affinity within the Neoproterozoic Southern Brazilian Shear Belt. Precambrian Res. 175 (1–4), 135–148. https://doi.org/10.1016/j.precamres.2009.09.003.
Florisbal, L.M., Bitencourt, M.F., Janasi, V.d.A., Nardi, L.V.S., Heaman, L.M., 2012a. Petrogenesis of syntectonic granites emplaced at the transition from thrusting to transcurrent tectonics in post-collisional setting: Whole-rock and Sr–Nd–Pb isotope geochemistry in the Neoproterozoic Quatro Ilhas and Mariscal Granites, Southern Brazil. Lithos, vol. 153, pp. 53-71. Doi: 10.1016/j.lithos.2012.04.031.
Florisbal, L.M., de Assis Janasi, V., Bitencourt, M.F., Heaman, L.M., 2012b. Space–time relation of post-collisional granitic magmatism in Santa Catarina, southern Brazil: U-Pb LA-MC-ICP-MS zircon geochronology of coeval mafic–felsic magmatism related to the Major Gercino Shear Zone. Precambrian Res. 216–219, 132–151. https://doi.org/10.1016/j.precamres.2012.06.015.
Foster, D.A., Goscombe, B.D., Newstead, B., Mapani, B., Mueller, P.A., Gregory, L.C., Muvangua, E., 2015. U-Pb age and Lu–Hf isotopic data of detrital zircons from the Neoproterozoic Damara Sequence: Implications for Congo and Kalahari before Gondwana. Gondwana Res. 28 (1), 179–190. https://doi.org/10.1016/j.gr.2014.04.011.
Frantz, J., McNaughton, N.J., Marques, J., Hartmann, L.A., Botelho, N., Caravaca, G., 2003. Shrimp U-Pb zircon ages of granitoids from southernmost Brazil: constraints on the temporal evolution on the Dorsal do Canguçu transcurrent shear zone and the eastern Dom Feliciano Belt. IV South American Symposium on Isotope Geology, pp. 174-177.
Frimmel, H.E., Hartnady, C.J.H., Koller, F., 1996. Geochemistry and tectonic setting of magmatic units in the Pan-African Gariep Belt. Namibia. Chem. Geol. 130 (1–2), 101–121. https://doi.org/10.1016/0009-2541(95)00188-3.
Frimmel, H.E., Zartman, R.E., Späth, A., 2001. The Richtersveld Igneous Complex, South Africa: U-Pb Zircon and Geochemical Evidence for the Beginning of Neoproterozoic Continental Breakup. J. Geol. 109 (4), 493–508. https://doi.org/10.1086/320795.
Frimmel, H.E., Fölling, P.G., 2004. Late Vendian Closure of the Adamastor Ocean: Timing of Tectonic Inversion and Syn-orogenic Sedimentation in the Gariep Basin. Gondwana Res. 7 (3), 685–699. https://doi.org/10.1016/S1342-937X(05)71056-X.
Frimmel, H.E., Basei, M.A.S., Gaucher, C., 2011. Neoproterozoic geodynamic evolution of SW-Gondwana: a southern African perspective. Int. J. Earth Sci. 100, 323–354. https://doi.org/10.1086/320795.
Frimmel, H.E., 2018. The Gariep Belt. In: Siegesmund, S. (Ed.), Geology of Southwest Gondwana, 1st ed. Springer International Publishing, Cham, pp. 353–386.
Gaucher, C., Frei, R., Chemale Jr, F., Frei, D., Bossi, J., Martínez, G., Chiglino, L., Cernuschi, F., 2011. Mesoproterozoic evolution of the Río de la Plata Craton in Uruguay: at the heart of Rodinia? Int. J. Earth Sci. 100 (2), 273–288. https://doi.org/10.1007/s00531-010-0562-x.
Goscombe, B., Hand, M., Gray, D., Mawby, J.O., 2003a. The Metamorphic Architecture of a Transpressional Orogen: the Kaoko Belt. Namibia. J. Petrol. 44 (4), 679–711. https://doi.org/10.1093/petrology/44.4.679.
Goscombe, B., Hand, M., Gray, D., 2003b. Structure of the Kaoko Belt, Namibia: progressive evolution of a classic transpressional orogen. J. Struct. Geol. 25 (7), 1049–1081. https://doi.org/10.1016/S0191-8141(02)00150-5.
Goscombe, B., Gray, D., Armstrong, R., Foster, D.A., Vogl, J., 2005a. Event geochronology of the Pan-African Kaoko Belt. Namibia. Precambrian Res. 140 (3–4), 103.e1–103.e41. https://doi.org/10.1016/j.precamres.2005.07.003.
Goscombe, B., Gray, D., Hand, M., 2005b. Extrusional Tectonics in the Core of a Transpressional Orogen; the Kaoko Belt. Namibia. J. Petrol. 46 (6), 1203–1241. https://doi.org/10.1093/petrology/egi014.
Gray, D.R., Foster, D.A., Meert, J.G., Goscombe, B.D., Armstrong, R., Trouw, R.A.J., Passchier, C.W., 2008. A Damara Orogen perspective on the assembly of southwestern Gondwana. In: Pankhurst, R.J. (Ed.), West Gondwana: Pre-Cenozoic Correlations Across the South Atlantic Region. Geological Society Special Publications, London, pp. 257–278. Doi: 10.1144/SP294.14.
Gross, A.O.M.S., Droop, G.T.R., Porcher, C.C., Fernandes, L.A.D., 2009. Petrology and thermobarometry of mafic granulites and migmatites from the Chafalote Metamorphic Suite: New insights into the Neoproterozoic P-T evolution of the Uruguayan—Sul-Rio-Grandense shield. Precambrian Res. 170 (3–4), 157–174. https://doi.org/10.1016/j.precamres.2009.01.011.
Gruber, L., Porcher, C., Lenz, C., Fernandes, L., 2011. Proveniência de metassedimentos das sequências Arroio Areião, Cerro Cambará e Quartzo Milonitos no Complexo Metamórfico Porongos, Santana da Boa Vista. RS. Pesquisas em Geociencias 38 (3), 205–224. https://doi.org/10.22456/1807-9806.35157.
Gruber, L., Porcher, C.C., Koester, E., Bertotti, A.L., Lenz, C., Fernandes, L.A.D., Remus, M.V.D., 2016. Isotope geochemistry and geochronology of syn-depositional volcanism in Porongos Metamorphic Complex, Santana da Boa Vista Antiform, Dom Feliciano Belt, Brazil: Onset of an 800 Ma continental arc. J. Sediment. Environ. 1 (2), 196–215. https://doi.org/10.12957/jse.2016.22722.
Guadagnin, F., Chemale Jr, F., Dussin, I.A., Jelinek, A.R., dos Santos, M.N., Borba, M.L., Justino, D., Bertotti, A.L., Alessandretti, L., 2010. Depositional age and provenance of the Itajaí Basin, Santa Catarina State, Brazil: Implications for SW Gondwana correlation. Precambrian Res. 180 (3–4), 156–182. https://doi.org/10.1016/j.precamres.2010.04.002.
Hartmann, L.A., Basei, M.A.S., Simas, M.W., 1999. Geochemistry of the Lower Proterozoic granulite-facies Grant syenite gneiss, Barra Velha, Santa Catarina State, southern Brazil. Pesquisas em Geociencias 25, 3–9.
Hartmann, L.A., Santos, J.O.S., McNaughton, N.J., Vasconcellos, M.A.Z., da Silva, L.C., 2000. Ion microprobe (SHRIMP) dates complex granulite from Santa Catarina, southern Brazil. Anais da Academia Brasileira de Ciencias 72 (4), 559–572. https://doi.org/10.1590/S0001-37652000000400007.
Hartmann, L.A., Bitencourt, M.F., Santos, J.O.S., McNaughton, N.J., Rivera, C.B., Betiollo, L., 2003. Prolonged Paleoproterozoic magmatic participation in the Neoproterozoic Dom Feliciano belt, Santa Catarina, Brazil, based on zircon U-Pb SHRIMP geochronology. J. S. Am. Earth Sci. 16 (6), 477–492. https://doi.org/10.1016/j.jsames.2003.04.001.
Hartmann, L.A., Savian, J.F., Lopes, W.R., 2015. Airborne geophysical characterization of geotectonic relationships in the southern Ribeira Belt, Luís Alves Craton, and northern Dom Feliciano Belt. Brazilian Shield. Int. Geol. Rev. 58 (4), 471–488. https://doi.org/10.1080/00206814.2015.1089424.
Heine, C., Zoethout, J., Müller, R.D., 2013. Kinematics of the South Atlantic rift. Solid Earth 4 (2), 215–253. https://doi.org/10.5194/se-4-215-2013.
Hoffman, P.F., Halverson, G.P., 2008. Otavi Group of the western Northern Platform, the Eastern Kaoko Zone and the western Northern Margin Zone. In: Miller, R.M. (Ed.), The Geology of Namibia. Geological Survey Namibia, Namibia, pp. 69–136.
Höfig, D.F., Marques, J.C., Basei, M.A.S., Giusti, R.O., Kohlrausch, C., Frantz, J.C., 2018. Detrital zircon geochronology (U-Pb LA-ICP-MS) of syn-orogenic basins in SW Gondwana: New insights into the Cryogenian-Ediacaran of Porongos Complex, Dom Feliciano Belt, southern Brazil. Precambrian Res. 306, 189–208. https://doi.org/10.1016/j.precamres.2017.12.031.
Hofmann, M., Linnemann, U., Hoffmann, K.-H., Gerdes, A., Eckelmann, K., Gärtner, A., 2014. The Namuskluft and Dreigratberg sections in southern Namibia (Kalahari Craton, Gariep Belt): a geological history of Neoproterozoic rifting and recycling of cratonic crust during the dispersal of Rodinia until the amalgamation of Gondwana. Int. J. Earth Sci. 103 (5), 1187–1202. https://doi.org/10.1007/s00531-013-0949-6.
Hofmann, M., Linnemann, U., Hoffmann, K.-H., Germs, G., Gerdes, A., Marko, L., Eckelmann, K., Gärtner, A., Krause, R., 2015. The four Neoproterozoic glaciations of southern Namibia and their detrital zircon record: The fingerprints of four crustal growth events during two supercontinent cycles. Precambrian Res. 259, 176–188. https://doi.org/10.1016/j.precamres.2014.07.021.
Hueck, M., Basei, M.A.S., Wemmer, K., Oriolo, S., Heidelbach, F., Siegesmund, S., 2018a. Evolution of the Major Gercino Shear Zone in the Dom Feliciano Belt, South Brazil,

and implications for the assembly of southwestern Gondwana. Int. J. Earth Sci. 108 (2), 403–425. https://doi.org/10.1007/s00531-018-1660-4.
Hueck, M., Oyhantçabal, P., Basei, M., Siegesmund, S., 2018b. The Dom Feliciano Belt in Southern Brazil and Uruquay. In: Siegesmund, S. (Ed.), Geology of Southwest Gondwana, 1st ed. Springer International Publishing, Cham, pp. 267–302.
Hueck, M., Basei, M.A.S., Castro, N.A.d., 2019. Tracking the sources and the evolution of the late Neoproterozoic granitic intrusions in the Brusque Group, Dom Feliciano Belt, South Brazil: LA-ICP-MS and SHRIMP geochronology coupled to Hf isotopic analysis. Precambrian Res. 338, 105566 https://doi.org/10.1016/j.precamres.2019.105566.
Johansson, Å., 2014. From Rodinia to Gondwana with the 'SAMBA' model—A distant view from Baltica towards Amazonia and beyond. Precambrian Res. 244, 226–235. https://doi.org/10.1016/j.precamres.2013.10.012.
Koester, E., Porcher, C.C., Pimentel, M.M., Fernandes, L.A.D., Vignol-Lelarge, M.L., Oliveira, L.D., Ramos, R.C., 2016. Further evidence of 777 Ma subduction-related continental arc magmatism in Eastern Dom Feliciano Belt, southern Brazil: The Chácara das Pedras Orthogneiss. J. S. Am. Earth Sci. 68, 155–166. https://www.doi.org/10.1016/j.jsames.2015.12.006.
Konopásek, J., Kosler, J., Tajcmanova, L., Ulrich, S., Kitt, S., 2008. Neoproterozoic igneous complex emplaced along major tectonic boundary in the Kaoko Belt (NW Namibia): ion probe and LA-ICP-MS dating of magmatic and metamorphic zircons. J. Geol. Soc. London 165 (1), 153–165.
Konopásek, J., Košler, J., Sláma, J., Janoušek, V., 2014. Timing and sources of pre-collisional Neoproterozoic sedimentation along the SW margin of the Congo Craton (Kaoko Belt, NW Namibia). Gondwana Res. 26 (1), 386–401. https://www.doi.org/10.1016/j.gr.2013.06.021.
Konopásek, J., Sláma, J., Košler, J., 2016. Linking the basement geology along the Africa-South America coasts in the South Atlantic. Precambrian Res. 280, 221–230. https://www.doi.org/10.1016/j.precamres.2016.05.011.
Konopásek, J., Hoffmann, K.-H., Sláma, J., Košler, J., 2017. The onset of flysch sedimentation in the Kaoko Belt (NW Namibia) – Implications for the pre-collisional evolution of the Kaoko-Dom Feliciano–Gariep orogen. Precambrian Res. 298, 220–234. https://doi.org/10.1016/j.precamres.2017.06.017.
Konopásek, J., Janoušek, V., Oyhantçabal, P., Sláma, J., Ulrich, S., 2018. Did the circum-Rodinia subduction trigger the Neoproterozoic rifting along the Congo-Kalahari Craton margin? Int. J. Earth Sci. 107 (5), 1859–1894. https://www.doi.org/10.1007/s00531-017-1576-4.
Konopásek, J., Cavalcante, C., Fossen, H., Janoušek, V., 2020. Adamastor – an ocean that never existed? Earth-Sci. Rev. 205, 103201 https://doi.org/10.1016/j.earscirev.2020.103201.
Kröner, A., Rojas-Agramonte, Y., Hegner, E., Hoffmann, K.H., Wingate, M.T.D., 2010. SHRIMP zircon dating and Nd isotopic systematics of Palaeoproterozoic migmatitic orthogneisses in the Epupa Metamorphic Complex of northwestern Namibia. Precambrian Res. 183 (1), 50–69. https://doi.org/10.1016/j.precamres.2010.06.018.
Kröner, A., Rojas-Agramonte, Y., Wong, J., Wilde, S.A., 2015. Zircon reconnaissance dating of Proterozoic gneisses along the Kunene River of northwestern Namibia. Tectonophysics 662, 125–139. https://doi.org/10.1016/j.tecto.2015.04.020.
Kröner, A., Rojas-Agramonte, Y., 2017. Mesoproterozoic (Grenville-age) granitoids and supracrustal rocks in Kaokoland, northwestern Namibia. Precambrian Res. 298, 572–592. https://doi.org/10.1016/j.precamres.2017.07.008.
Kröner, S., Konopásek, J., Kröner, A., Passchier, C.W., Poller, U., Wingate, M.T.D., Hofmann, K.H., 2004. U-Pb and Pb-Pb zircon ages for metamorphic rocks in the Kaoko Belt of Northwestern Namibia: A Palaeo- to Mesoproterozoic basement reworked during the Pan-African orogeny. S. Afr. J. Geol. 107 (3), 455–476. https://www.doi.org/10.2113/107.3.455.
Lara, P., Oyhantçabal, P., Belousova, E., 2020. Two distinct crustal sources for Late Neoproterozoic granitic magmatism across the Sierra Ballena Shear Zone, Dom Feliciano Belt, Uruguay: Whole-rock geochemistry, zircon geochronology and Sr-Nd-Hf isotope evidence. Precambrian Res. 341, 105625 https://doi.org/10.1016/j.precamres.2020.105625.
Lehmann, J., Bybee, G.M., Hayes, B., Owen-Smith, T.M., Belyanin, G., 2020. Emplacement of the giant Kunene AMCG complex into a contractional ductile shear zone and implications for the Mesoproterozoic tectonic evolution of SW Angola. Int. J. Earth Sci. 109 (4), 1463–1485. https://doi.org/10.1007/s00531-020-01837-5.
Lenz, C., Fernandes, L.A.D., McNaughton, N.J., Porcher, C.C., Masquelin, H., 2011. U-Pb SHRIMP ages for the Cerro Bori Orthogneisses, Dom Feliciano Belt in Uruguay: Evidences of a ~800Ma magmatic and ~650Ma metamorphic event. Precambrian Res. 185 (3), 149–163. https://doi.org/10.1016/j.precamres.2011.01.007.
Lenz, C., Porcher, C., Fernandes, L., Masquelin, H., Koester, E., Conceição, R., 2013. Geochemistry of the Neoproterozoic (800–767 Ma) Cerro Bori orthogneisses, Dom Feliciano Belt in Uruguay: tectonic evolution of an ancient continental arc. Mineral. Petrol. 107, 785–806. https://www.doi.org/10.1007/s00710-012-0244-4.
Li, Z.-X., Bogdanova, S.V., Collins, A.S., Davidson, A., De Waele, B., Ernst, R.E., Fitzsimons, I.C.W., Fuck, R.A., Gladkochub, D.P., Jacobs, J., Karlstrom, K.E., Lu, S., Natapov, L.M., Pease, V., Pisarevsky, S.A., Thrane, K., Vernikovsky, V., 2008. Assembly, configuration, and break-up history of Rodinia: A synthesis. Precambrian Res. 160 (1), 179–210. https://doi.org/10.1016/j.precamres.2007.04.021.
Li, Z.-X., Evans, D.A.D., Halverson, G.P., 2013. Neoproterozoic glaciations in a revised global palaeogeography from the breakup of Rodinia to the assembly of Gondwanaland. Sediment. Geol. 294, 219–232. https://doi.org/10.1016/j.sedgeo.2013.05.016.
Luft, J.L., Chemale Jr, F., Armstrong, R., 2011. Evidence of 1.7- to 1.8-Ga Collisional Arc in the Kaoko Belt. NW Namibia. Int. J. Earth Sci. 100, 305–321. https://www.doi.org/10.1007/s00531-010-0591-5.
Macey, P.H., Abrahams, Y., Miller, J.A., 2018. Lithostratigraphy of the Mesoproterozoic Stolzenfels Enderbite (Komsberg Suite), South Africa and Namibia. S. Afr. J. Geol. 121 (2), 217–226. https://www.doi.org/10.25131/sajg.121.0016.
Mallmann, G., Chemale Jr, F., Ávila, J.N., Kawashita, K., Armstrong, R.A., 2007. Isotope geochemistry and geochronology of the Nico Pérez Terrane, Rio de la Plata Craton. Uruguay. Gondwana Res. 12 (4), 489–508. https://doi.org/10.1016/j.gr.2007.01.002.
Martil, M.M.D., Bitencourt, M.F., Nardi, L.V.S., Koester, E., Pimentel, M.M., 2017. Pre-collisional, Tonian (ca. 790 Ma) continental arc magmatism in southern Mantiqueira Province, Brazil: Geochemical and isotopic constraints from the Várzea do Capivarita Complex. Lithos 274–275, 39–52. https://doi.org/10.1016/j.lithos.2016.11.011.
Martini, A., Bitencourt, M.F., Weinberg, R.F., De Toni, G.B., Lauro, V.S.N., 2019. From migmatite to magma - crustal melting and generation of granite in the Camboriú Complex, south Brazil. Lithos 340–341, 270–286. https://www.doi.org/10.1016/j.lithos.2019.05.017.
Masquelin, H., Fernandes, L., Lenz, C., Porcher, C.C., McNaughton, N.J., 2012. The Cerro Olivo Complex: A pre-collisional Neoproterozoic magmatic arc in Eastern Uruguay. Int. Geol. Rev. 54, 1161–1183. https://www.doi.org/10.1080/00206814.2011.626597.
McCourt, S., Armstrong, R., Jelsma, H., Mapeo, R., 2013. New U-Pb SHRIMP ages from the Lubango region, SW Angola: Insights into the Palaeoproterozoic evolution of the Angolan Shield, southern Congo Craton. Africa. Geol. Soc. Spec. Publ. 170 (2), 353–363. https://www.doi.org/10.1144/jgs2012-059.
Merdith, A.S., Collins, A.S., Williams, S.E., Pisarevsky, S., Foden, J.D., Archibald, D.B., Blades, M.L., Alessio, B.L., Armistead, S., Plavsa, D., Clark, C., Müller, D.R., 2017a. A Full-Plate Global Reconstruction of the Neoproterozoic. Gondwana Res. 50, 84–134. https://www.doi.org/10.1016/j.gr.2017.04.001.
Merdith, A.S., Williams, S.E., Müller, R.D., Collins, A.S., 2017b. Kinematic constraints on the Rodinia to Gondwana transition. Precambrian Res. 299, 132–150. https://doi.org/10.1016/j.precamres.2017.07.013.
Miller, R.M., 2012. Review of Mesoproterozoic magmatism, sedimentation and terrane amalgamation in southwestern Africa. S. Afr. J. Geol. 115 (4), 417–448. https://www.doi.org/10.2113/gssajg.115.4.417.
Oriolo, S., Oyhantçabal, P., Basei, M.A.S., Wemmer, K., Siegesmund, S., 2016. The Nico Pérez Terrane (Uruguay): From Archean crustal growth and connections with the Congo Craton to late Neoproterozoic accretion to the Río de la Plata Craton. Precambrian Res. 280, 147–160. https://doi.org/10.1016/j.precamres.2016.04.014.
Oriolo, S., Oyhantçabal, P., Konopásek, J., Basei, M.A.S., Frei, R., Sláma, J., Wemmer, K., Siegesmund, S., 2019. Late Paleoproterozoic and Mesoproterozoic magmatism of the Nico Pérez Terrane (Uruguay): Tightening up correlations in southwestern Gondwana. Precambrian Res. 327, 296–313. https://doi.org/10.1016/j.precamres.2019.04.012.
Oyhantçabal, P., Siegesmund, S., Wemmer, K., Frei, R., Layer, P., 2007. Post-collisional transition from calc-alkaline to alkaline magmatism during transcurrent deformation in the southernmost Dom Feliciano Belt (Braziliano–Pan-African, Uruguay). Lithos 98 (1–4), 141–159. https://doi.org/10.1016/j.lithos.2007.03.001.
Oyhantçabal, P., Siegesmund, S., Wemmer, K., Presnyakov, S., Layer, P., 2009. Geochronological constraints on the evolution of the southern Dom Feliciano Belt (Uruguay). J. Geol. Soc. 166 (6), 1075–1084. https://www.doi.org/10.1144/0016-76492008-122.
Oyhantçabal, P., Siegesmund, S., Wemmer, K., Passchier, C.W., 2011a. The transpressional connection between Dom Feliciano and Kaoko Belts at 580–550 Ma. Int. J. Earth Sci. 100, 379–390. https://www.doi.org/10.1007/s00531-010-0577-3.
Oyhantçabal, P., Siegesmund, S., Wemmer, K., 2011b. The Río de la Plata Craton: a review of units, boundaries, ages and isotopic signature. Int. J. Earth Sci. 100 (2), 201–220. https://www.doi.org/10.1007/s00531-010-0580-8.
Oyhantçabal, P., Oriolo, S., Philipp, R.P., Wemmer, K., Siegesmund, S., 2018. The Nico Pérez Terrane of Uruguay and Southeastern Brazil. In: Siegesmund, S. (Ed.), Geology of Southwest Gondwana. Springer International Publishing 10.1007/978-3-319-68920-3_7, Cham, pp. 161–188.
Passarelli, C.R., Basei, M.A.S., Siga, O., Harara, O.M.M., 2018. The Luis Alves and Curitiba Terranes: Continental Fragments in the Adamastor Ocean. In: Siegesmund, S. (Ed.), Geology of Southwest Gondwana. Springer International Publishing, Cham, pp. 189–215 https://www.doi.org/10.1007/978-3-319-68920-3_8.
Pertille, J., Hartmann, L.A., Philipp, R.P., 2015a. Zircon U-Pb age constraints on the Paleoproterozoic sedimentary basement of the Ediacaran Porongos Group, Sul-Riograndense Shield, southern Brazil. J. S. Am. Earth Sci. 63, 334–345. https://doi.org/10.1016/j.jsames.2015.08.005.
Pertille, J., Hartmann, L.A., Philipp, R.P., Petry, T.S., de Carvalho Lana, C., 2015b. Origin of the Ediacaran Porongos Group, Dom Feliciano Belt, southern Brazilian Shield, with emphasis on whole rock and detrital zircon geochemistry and U-Pb, Lu–Hf isotopes. J. S. Am. Earth Sci. 64, 69–93. https://www.doi.org/10.1016/j.jsames.2015.09.001.
Pertille, J., Hartmann, L.A., Santos, J.O.S., McNaughton, N.J., Armstrong, R., 2017. Reconstructing the Cryogenian-Ediacaran evolution of the Porongos fold and thrust belt, Southern Brasiliano Orogen, based on Zircon U-Pb–Hf–O isotopes. Int. Geol. Rev. 59 (12), 1532–1560. https://www.doi.org/10.1080/00206814.2017.1285257.
Philipp, R.P., Machado, R., 2005. The Neoproterozoic to Cambrian granitic magmatism of the Pelotas Batholith, Southern Brazil. J. S. Am. Earth Sci. 19, 461–478.
Philipp, R.P., Massonne, H.-J., de Campos, R.S., 2013. Peraluminous leucogranites of the Cordilheira Suite: A record of Neoproterozoic collision and the generation of the Pelotas Batholith, Dom Feliciano Belt, Southern Brazil. J. S. Am. Earth Sci. 43, 8–24. https://www.doi.org/10.1016/j.jsames.2012.10.006.
Philipp, R.P., Pimentel, M.M., Chemale Jr, F., 2016. Tectonic evolution of the Dom Feliciano Belt in Southern Brazil: Geological relationships and U-Pb geochronology.

Braz. J. Geol. 46, 83–104. https://www.doi.org/10.1590/2317-488920162015001 6.
Porada, H., 1989. Pan-African rifting and orogenesis in southern to equatorial Africa and eastern Brazil. Precambrian Res. 44 (2), 103–136. https://doi.org/10.1016/0301-9268(89)90078-8.
Rapela, C.W., Fanning, C.M., Casquet, C., Pankhurst, R.J., Spalletti, L., Poiré, D., Baldo, E.G., 2011. The Rio de la Plata craton and the adjoining Pan-African/brasiliano terranes: Their origins and incorporation into south-west Gondwana. Gondwana Res. 20 (4), 673–690. https://doi.org/10.1016/j.gr.2011.05.001.
Saalmann, K., Remus, M.V.D., Hartmann, L.A., 2006. Structural evolution and tectonic setting of the Porongos belt, southern Brazil. Geol. Mag. 143 (1), 59–88. https://www.doi.org/10.1017/S0016756805001433.
Saalmann, K., Gerdes, A., Lahaye, Y., Hartmann, L., Remus, M., Läufer, A., 2011. Multiple accretion at the eastern margin of the Rio de la Plata craton: the prolonged Brasiliano orogeny in southernmost Brazil. Int. J. Earth Sci. 100, 355–378. https://www.doi.org/10.1007/s00531-010-0564-8.
Sánchez-Bettucci, L., Oyhantçabal, P., Loureiro, J., Ramos, V.A., Preciozzi, F., Basei, M.A. S., 2004. Mineralizations of the Lavalleja Group (Uruguay), a Probable Neoproterozoic Volcano-sedimentary Sequence. Gondwana Res. 7 (3), 745–751. https://www.doi.org/10.1016/S1342-937X(05)71060-1.
Seth, B., Kröner, A., Mezger, K., Nemchin, A.A., Pidgeon, R.T., Okrusch, M., 1998. Archaean to Neoproterozoic magmatic events in the Kaoko belt of NW Namibia and their geodynamic significance. Precambrian Res. 92 (4), 341–363. https://doi.org/10.1016/S0301-9268(98)00086-2.
Seth, B., Armstrong, R.A., Brandt, S., Villa, I.M., Kramers, J.D., 2003. Mesoproterozoic U-Pb and Pb–Pb ages of granulites in NW Namibia: reconstructing a complete orogenic cycle. Precambrian Res. 126 (1–2), 147–168. https://doi.org/10.1016/S0301-9268(03)00193-1.
Silva, L.C., Hartmann, L.A., McNaughton, N.J., Fletcher, I., 2000. Zircon U-Pb SHRIMP dating of a Neoproterozoic overprint in Paleoproterozoic granitic-gneissic terranes, southern Brazil. Am. Mineral. 85 (5–6), 649–667. https://www.doi.org/10.2138/am-2000-5-602.
Silva, L.C., McNaughton, N.J., Fletcher, I.R., 2005. SHRIMP U-Pb zircon geochronology of Neoproterozoic crustal granitoids (Southern Brazil): A case for discrimination of emplacement and inherited ages. Lithos 82 (3–4), 503–525. https://doi.org/10.1016/j.lithos.2004.09.029.
Vermeesch, P., 2012. On the visualisation of detrital age distributions. Chem. Geol. 312–313, 190–194. https://doi.org/10.1016/j.chemgeo.2012.04.021.
Vermeesch, P., Resentini, A., Garzanti, E., 2016. An R package for statistical provenance analysis. Sediment. Geol. 336, 14–25. https://doi.org/10.1016/j.sedgeo.2016.01.009.
Will, T.M., Gaucher, C., Ling, X.X., Li, X.H., Li, Q.L., Frimmel, H.E., 2019. Neoproterozoic magmatic and metamorphic events in the Cuchilla Dionisio Terrane, Uruguay, and possible correlations across the South Atlantic. Precambrian Res. 320, 303–322. https://doi.org/10.1016/j.precamres.2018.11.004.
Zimmermann, U., 2018. The Provenance of Selected Neoproterozoic to Lower Paleozoic Basin Successions of Southwest Gondwana: A Review and Proposal for Further Research. In: Siegesmund, S. (Ed.), Geology of Southwest Gondwana. Springer International Publishing, Cham, pp. 561–591. https://doi.org/10.1007/978-3-319-68920-3_7.

Paper II

Tectono-Metamorphic Evolution of the Northern Dom Feliciano Belt Foreland, Santa Catarina, Brazil: Implications for Models of Subduction-Driven Orogenesis

Jack James Percival[1], Jiří Konopásek[1,2], Robert Anczkiewicz[3], Morgan Ganerød[4], Jiří Sláma[5], Roberto Sacks de Campos[6], Maria de Fátima Bitencourt[7]

[1] Department of Geosciences, UiT–The Arctic University of Norway, Dramsveien 201, 9037 Tromsø, Norway,

[2] Czech Geological Survey, Klárov 3, 118 21 Prague 1, Czech Republic

[3] Institute of Geological Sciences, Polish Academy of Sciences, Kraków Research Centre, Senacka 1, PL 31-002, Kraków, Poland

[4] Geological Survey of Norway, Leiv Erikssonsvei 39, 7040 Trondheim, Norway

[5] Institute of Geology of the Czech Academy of Sciences, Rozvojová 269, 165 00 Prague 6, Czech Republic

[6] Programa de Pós-graduação em Geologia (PPGGeologia), Universidade Federal de Santa Catarina (UFSC), Florianópolis, SC, Brazil

[7] Programa de Pós-graduação em Geociências, Instituto de Geociências, Universidade Federal do Rio Grande do Sul, Porto Alegre, Brazil

Corresponding author: Jack Percival (jack.j.percival@gmail.com, jack.j.percival@uit.no)

Key Points:

- Clockwise P─T evolution of the northern Dom Feliciano Belt foreland records early crustal thickening and subsequent thrust-driven exhumation
- The foreland reached peak regional metamorphic conditions ca. 660–645 Ma, ~20–30 million years before voluminous magmatism in the hinterland
- The results imply the absence of a large oceanic domain between the foreland and hinterland, pointing to a rift setting prior to convergence

Abstract

The Dom Feliciano Belt in southern Brazil and Uruguay represents the western half of a Neoproterozoic orogenic belt located in the southern portion of the South Atlantic Neoproterozoic Orogenic System. Current interpretations are divided as to the nature of orogenesis in this belt, in part owing to lacking geochronological constraints. Metamorphosed and deformed supracrustal sequences of the Brusque Complex in the northern Dom Feliciano Belt, representing part of the orogenic foreland, record the onset and duration of crustal thickening. Structural analysis and pressure–temperature estimates indicate that the complex reached peak regional metamorphic conditions of 540–570°C and 5.5–6.7 kbar during thrusting and burial, consistent with orogenic metamorphism and early crustal thickening. Garnet–whole rock Lu–Hf and Sm–Nd isochron ages date this event to between circa 660–650 Ma. Ar–Ar dating of mica suggests that exhumation was completed by circa 635 Ma, and that localised deformation occurred into the late Ediacaran. Our results show that the orogenic foreland reached metamorphic conditions typical for crustal thickening 20–30 million years prior to the onset of massive magmatic activity in the hinterland. Such a delay is typical of hot, internal parts of orogens, which supports interpretations that hinterland magmatism in the northern Dom Feliciano Belt represents post-collisional magmatism and not arc magmatism above a subduction zone. Instead, we suggest that orogenesis in the northern Dom Feliciano Belt was initiated by rift-basin inversion driven by far-field forces transmitted through the crust in an intracontinental or back-arc rift setting.

1 Introduction

Orogenic systems vary widely in terms of their geometry, duration, and scale. The classic collisional orogen can be described using models that involve the termination of a Wilson cycle, where the opening and closing of a large ocean basin between continental bodies culminates in continental collision. Accretionary orogens, in contrast, form at continental–oceanic convergent plate boundaries in the absence of continental collision, and develop during continuous subduction by crustal thickening due to short-term coupling across the subduction plate boundary (Cawood et al., 2009). Within-plate deformation can also occur away from plate margins, triggered by the transmission of stress from active plate boundaries through the lithosphere (Aitken et al., 2013; Raimondo et al., 2014). Large-scale intracontinental orogens are comparatively less common than collisional or accretionary orogens, but examples are recognised in both ancient and modern settings (Cunningham, 2005; Faure et al., 2009; Hand & Sandiford, 1999). Although the defining characteristics of collisional, accretionary, and intracontinental orogens make them distinct, Cawood et al. (2009) proposed that they represent three interrelated endmembers between which lies a wide spectrum of orogen types. Thus, continental collision at the termination of a Wilson cycle is genetically linked to preceding accretionary orogeny. Similarly, tectonic switching during accretionary orogeny can produce large-scale crustal thickening in within-plate settings (Lister & Forster, 2009), resulting in orogens that develop as the consequence of intracratonic rift inversion, similar to what occurs within an accretionary back-arc setting but at a distance from the developing arc (Collins, 2002; Thompson et al., 2001).

The South Atlantic Neoproterozoic Orogenic System (SANOS, sensu Konopásek et al., 2020) comprises an extensive system of orogenic belts that formed during the late Neoproterozoic amalgamation of Western Gondwana (Fig. 1a). The SANOS is situated along the Atlantic coastlines of South America and Africa, and includes the Dom Feliciano, Ribeira and Araçuaí belts on the South American side, and the Gariep, Kaoko and West Congo belts on the African side of the orogen. Porada (1979, 1989) first interpreted this orogenic system as having formed by collisional orogenesis after closure of a hypothetical proto-South Atlantic Ocean. This hypothesis was later expanded upon by Hartnady et al.

(1985), who proposed that orogenesis was preceded by the closure of a large oceanic domain they titled the Adamastor Ocean.

In recent years, models involving long-lived subduction of a large Adamastor Ocean, culminating in continental collision at ca. 600 Ma, have dominated much of the research surrounding formation of the SANOS (Basei et al., 2018; Basei et al., 2000; Heilbron et al., 2020; Heilbron & Machado, 2003). The primary evidence used to support this argument is a linear series of granitic batholiths intruding the western hinterland of the orogenic system, which are interpreted as the exhumed roots of magmatic arcs (Basei et al., 2018; Basei et al., 2000; Caxito et al., 2021; Heilbron & Machado, 2003; Pedrosa-Soares et al., 2001; Tedeschi et al., 2016). These include the Granite Belt in the Dom Feliciano Belt (sensu Basei et al., 2000), the Rio Doce arc in the Araçuaí Belt (Tedeschi et al., 2016), and various magmatic complexes in the Ribeira Belt (Heilbron et al., 2020). However, in the northern SANOS, some researchers have recently moved away from standard subduction-collision models entirely, arguing that an absence of sufficient space between continental blocks precludes the formation of a large oceanic domain and long-lived subduction between the South American and African cratonic blocks (Cavalcante et al., 2019; Cavalcante et al., 2018; Fossen et al., 2020; Fossen et al., 2017; Konopásek et al., 2020; Konopásek et al., 2017; Meira et al., 2019). The existence of a large-scale Adamastor Ocean has been similarly challenged in the Dom Feliciano Belt of the southern SANOS, where evidence of the post-collisional nature of the Granite Belt (e.g. Bitencourt & Nardi, 2000; Florisbal, Janasi, Bitencourt, & Heaman, 2012; Oyhantçabal et al., 2007), and of collisional metamorphism pre-dating intrusion of the Granite Belt (Battisti et al., 2018; Koester et al., 2016; Oyhantçabal et al., 2009), casts doubt on its origins within a supra-subduction zone magmatic arc. Owing to this, some authors have proposed that the Kaoko–Dom Feliciano–Gariep orogenic system formed from inversion of a back-arc to intracontinental rift basin where subduction occurred much earlier and further to the west (De Toni, Bitencourt, Nardi, et al., 2020; Konopásek et al., 2020; Konopásek et al., 2018; Oriolo, Oyhantçabal, Basei, et al., 2016; Oriolo, Oyhantçabal, Wemmer, Basei, et al., 2016).

Despite a generally good understanding of the Dom Feliciano Belt hinterland, owing in part to a large dataset from the Granite Belt, there are currently insufficient geochronological and P–T constraints in

the foreland to develop a complete orogenic model. To investigate the above-described controversy, we have undertaken a multidisciplinary study focusing on the pressure–temperature–time–deformation (P–T–t–D) paths of supracrustal rocks of the northern Dom Feliciano Belt foreland. By dating the growth of P–T-sensitive metamorphic minerals, in particular garnet, it is possible to constrain the timing and conditions of specific tectonic processes (Anczkiewicz et al., 2014; Baxter & Scherer, 2013), enabling reliable estimates of the timing and duration of crustal thickening during orogenesis (Godet et al., 2021; Leech et al., 2005; Smit et al., 2014). Thus, detailed structural and petrographic observations, thermodynamic modelling, Lu–Hf and Sm–Nd isotopic dating of garnet, U–Pb dating of monazite, and Ar–Ar dating of micas were utilized to constrain the conditions and timing of major tectonic events. Our results are compared with previous studies, and integrated to discuss the tectonic evolution of the southern SANOS.

2 Geological setting

2.1 The Dom Feliciano Belt

The Dom Feliciano Belt represents the western half of the southern SANOS extending along the coastlines of southern Brazil and Uruguay (Fig. 1b). The Dom Feliciano Belt is the counterpart to the Kaoko Belt and the Gariep Belt in southern Africa (Fig. 1b), with the three belts sharing a common pre- and syn-orogenic evolution (Konopásek et al., 2016; Oyhantçabal, Siegesmund, Wemmer, et al., 2011; Percival et al., 2021). The structure of the Kaoko–Dom Feliciano–Gariep orogenic system is approximately symmetric, comprising an internal *hinterland* domain characterised by high-temperature metamorphism and voluminous magmatism, bordered by western and eastern external *foreland* domains characterised by low- to medium-grade metamorphism and fold-and-thrust tectonics. The Dom Feliciano Belt is generally separated into northern, central, and southern regions located in the Brazilian states of Santa Catarina and Rio Grande do Sul, and in Uruguay, respectively (Fig. 1b).

The hinterland is the easternmost domain of the Dom Feliciano Belt, and comprises granulites, paragneisses and orthogneisses of various high-grade metamorphic complexes including the Cerro Olivo, Várzea do Capivarita, and Porto Belo complexes (De Toni, Bitencourt, Nardi, et al., 2020; Gross et al., 2009; Oyhantçabal et al., 2009). Pre-orogenic magmatism and basin sedimentation in these units occurred between ca. 810–770 Ma (De Toni, Bitencourt, Nardi, et al., 2020; Lenz et al., 2011; Martil et al., 2017; Oyhantçabal et al., 2009; Will et al., 2019). Low-pressure granulite-facies metamorphism between ca. 650–630 is interpreted as recording either the start of crustal thickening (De Toni, Bitencourt, Konopásek, et al., 2020; De Toni, Bitencourt, Nardi, et al., 2020; Konopásek et al., 2020; Lenz et al., 2011), or the inversion of plate motions leading to subduction initiation and thickening at an active plate margin (Basei et al., 2018; Frimmel et al., 2011). Voluminous granitoid magma—the Granite Belt (Fig. 1b)—intruded the hinterland metamorphic complexes predominantly between ca. 630–580 Ma (Florisbal, Janasi, Bitencourt, & Heaman, 2012; Lara et al., 2020; Philipp & Machado, 2005). Some authors interpret the Granite Belt as resulting from pre-collisional arc-related magmatism above a subduction zone, with eastward subduction culminating in collision between the foreland and

hinterland at ca. 615–600 Ma (Basei et al., 2021; Basei et al., 2018; Hueck et al., 2019). Other authors instead argue that the Granite Belt represents syn- to post-collisional magmatism related in time and space to syn-orogenic NE-trending strike-slip shear zones (e.g. the Major Gercino Shear Zone) (Bitencourt & Nardi, 1993, 2000; Florisbal et al., 2009; Florisbal, Janasi, Bitencourt, & Heaman, 2012; Florisbal, Janasi, Bitencourt, Nardi, et al., 2012; Oyhantçabal et al., 2007; Peternell et al., 2010; Philipp et al., 2013).

The foreland domain of the Dom Feliciano Belt comprises Archean–Paleoproterozoic crust of the Nico Pérez and Luis Alves terranes, which is overlain by metamorphosed Mesoproterozoic and Neoproterozoic sedimentary cover (the Schist Belt) and late-Neoproterozoic synorogenic foreland basin sequences (Basei et al., 2009; Basei et al., 2000; Guadagnin et al., 2010; Oyhantçabal et al., 2018; Oyhantçabal et al., 2021; Percival et al., 2021). In addition, along the northern margin of the Nico Pérez Terrane in the central Dom Feliciano Belt lies the São Gabriel Terrane, which is comprised of a complex association of Neoproterozoic magmatic arcs (the ca. 890 to 860 Ma Passinho Arc and the ca. 770 to 680 Ma São Gabriel Arc), and metasedimentary and relict ophiolite complexes (Philipp et al., 2018). The Schist Belt consists of a narrow (~ 40 km wide) belt of deformed and metamorphosed volcano-sedimentary sequences, with early sedimentation constrained to ca. 810–770 Ma within a series of pre-orogenic rift basins (Percival et al., 2021; Pertille et al., 2017; Saalmann et al., 2011). Early deformation and peak metamorphism in the Schist Belt is thought to be the result of crustal thickening during convergence (Battisti et al., 2018), typical of fold-and-thrust belts in convergent orogen. Although there are currently no reliable age constraints for the timing of this event, some authors have used the metamorphism in the hinterland at ca. 650 Ma as an indirect maximum age constraint (e.g. Chemale et al., 2011; De Toni, Bitencourt, Konopásek, et al., 2020), whereas Ar–Ar and K–Ar cooling ages between ca. 625–600 Ma (Oriolo, Oyhantçabal, Wemmer, Heidelbach, et al., 2016) and the intrusion of granites into the Schist Belt from ca. 615 Ma (Hueck et al., 2019) provide minimum age constraints. Synorogenic foreland basin deposits overlie the cratonic basement and parts of the Schist Belt (Fig. 1b). These units consist of volcanosedimentary sequences deposited between ca. 570–540 Ma (Guadagnin et al., 2010;

Oliveira et al., 2014), parts of which are metamorphosed and tectonically interleaved with metasedimentary rocks of the Schist Belt (Battisti et al., 2018; Höfig et al., 2018; Percival et al., 2021).

2.2 The northern Dom Feliciano Belt and the Brusque Complex

The hinterland and foreland domains of the northern Dom Feliciano Belt are delineated by the Major Gercino Shear Zone (Fig. 1b, c). The hinterland, lying to the east of the shear zone, is predominantly comprised of the Florianópolis Batholith, which intruded between ca. 625–590 Ma and represents the northern extent of the Granite Belt (Basei et al., 2000; Chemale et al., 2012; Florisbal, Janasi, Bitencourt, & Heaman, 2012; Passarelli et al., 2010). Relicts of Paleoproterozoic basement and pre-orogenic Neoproterozoic magmatic rocks can be found within the Águas Mornas and Porto Belo complexes, respectively, which outcrop as xenoliths and roof pendants within the batholith (De Toni, Bitencourt, Nardi, et al., 2020; Silva et al., 2000). To the west of the Major Gercino Shear Zone lies the northern exposure of the Schist Belt, referred to as the Brusque Complex (Basei et al., 2000). Reworked basement units are exposed as windows within, and at the northern margin of, the Schist Belt, known as the Camboriú and São Miguel complexes, respectively (Basei et al., 2011; Silva et al., 2000). The basement and supracrustal units are intruded by Ediacaran granitoids that are partly contemporaneous with the rocks of the Florianópolis Batholith, although differences in geochemistry and inherited zircon ages suggest that the two magmatic associations were sourced from distinct reservoirs (Florisbal, Janasi, Bitencourt, & Heaman, 2012; Hueck et al., 2019). To the west of the Schist Belt, separated by the Itajaí—Perimbó Shear Zone, is the foreland basement of the Luis Alves Craton. Finally, overlying the foreland basement is the Itajaí Basin—a succession of syn-orogenic foreland volcanosedimentary rocks (Basei et al., 2000).

The Brusque Complex comprises a succession of volcanosedimentary rocks metamorphosed at greenschist to amphibolite facies conditions (Basei et al., 2000). The predominant rock types are metapelitic phyllites and schists, often showing narrow, alternating quartz-rich and mica-rich layering, and occasionally containing garnet. Metapsammitic and carbonate-rich layers and lenses are found

throughout the complex and in some places dominate the lithology. The metavolcanic rocks are predominantly mafic to ultramafic in composition, occasionally associated with minor calc-silicate layers, and are interlayered within the metasedimentary rocks (Basei et al., 2011; Campos et al., 2011; De Toni, Bitencourt, Konopásek, et al., 2020). Minor layers, lenses and dykes of felsic volcanic to subvolcanic rocks are also found throughout the complex (Percival et al., 2021).

The Brusque Complex protolith is characterised as a series of Tonian rift-related (Campos et al., 2011; Percival et al., 2021), transitional rift to passive margin (Basei et al., 2011; Philipp et al., 2004), or entirely passive margin volcanosedimentary successions (Basei et al., 2018). Early sedimentation in the Brusque Complex basin is constrained to somewhat before ca. 810 Ma (Percival et al., 2021), and regional metamorphism is constrained to sometime before ca. 615 Ma by overprinting contact metamorphism caused by the intrusion of voluminous syn-orogenic granitic rocks (Basei et al., 2011; Hueck et al., 2016). Up to four separate deformation phases have been identified within the Brusque Complex (Basei et al., 2011; Campos et al., 2012; Philipp et al., 2004). Most studies describe a pervasive transposition foliation as the dominant structure in the Brusque Complex, and NW-verging asymmetric folding of this fabric is interpreted to record early top-to-NW thrusting during oblique convergence (Basei et al., 2011; De Toni, Bitencourt, Konopásek, et al., 2020; Fischer et al., 2019; Philipp et al., 2004). This foliation is interpreted as forming during regional metamorphism associated with tectonic burial, reaching maximum upper-greenschist to lower-amphibolite facies conditions (Basei et al., 2011; Campos et al., 2011; Philipp et al., 2004). According to De Toni, Bitencourt, Konopásek, et al. (2020), early thrusting was followed by the progressive transition into strike-slip dominated tectonics, leading to the development of high-angle shear zones of the Major Gercino Shear Zone, where the majority of strain was concentrated during the later stages of convergence from ca. 625 Ma (De Toni, Bitencourt, Konopásek, et al., 2020; Hueck, Basei, et al., 2018). In the Brusque Complex, deformation during the late transpressional stage is expressed by the development of upright folds and a steep crenulation cleavage. Although there are currently no reliable age constraints for this deformation in the Brusque Complex, both the early thrusting and later strike-slip shearing are thought to have occurred during the same orogenic event (Basei et al., 2011; De Toni, Bitencourt, Konopásek, et al., 2020)

3 Results

3.1 Structural geology

Figure 2 presents the results of structural mapping and analysis in the Brusque Complex. Structural data are presented as strike/dip using the right-hand rule for plane data, and plunge/plunge direction for line data.

Field and petrological observations confirm previous studies describing the primary structural feature of the Brusque Complex as a pervasive metamorphic foliation striking NE–SW, parallel with the orogenic trend of the belt (Fig. 2a & b). The fabric is defined by oriented white mica and chlorite in areas of low metamorphic grade, and white mica and biotite in areas of medium metamorphic grade. The foliation often contains intrafolial rootless folds (F_1), indicative of a transposition foliation (Fig. 3b). Although previous studies assign this transposed fabric as the earliest S_1 (Basei et al., 2011; Philipp et al., 2004), it is unclear whether it is truly a previous metamorphic fabric or simply relicts of sedimentary S_0. Furthermore, the transposition features are consistent with synkinematic progressive shearing during primary foliation development, and thus can be characterised as an early stage of the same foliation (sensu Fossen et al., 2019). Therefore, we choose to define the fabric as a whole, including transposed relicts, as S_1.

Structural domain analysis (after Vollmer, 1990) reveals two km-scale regions that diverge from the primary NE–SW trend (Fig. 2d & e). The rocks in Region 1 (Fig. 2a) are typically only weakly affected by later folding and cleavage overprint, thus best preserving the earlier orientation of the S_1 metamorphic fabric. Here, S_1 is predominantly shallowly-dipping, with the main cluster of data showing an average orientation of 135/30W (Fig. 2d). Based on this region, and similar isolated locations elsewhere, the S_1 fabric appears to be gently-dipping. NW/SE-plunging quartz stretching lineations (L_1, Fig. 2c) and associated kinematic indicators, such as asymmetric quartz sigma-clasts (Fig. 3a), mica fish, rotated garnet porphyroblasts, and quartz pressure shadows (Fig. 4a), indicate horizontal tangential shearing and a top-to-NW shear sense. The S_1 foliation is deformed by upright to inclined folds (F_2) and an axial plane-parallel crenulation cleavage (S_2) (Fig. 3b). Meso-scale F_2 folding is predominantly tight, upright,

and asymmetric verging to the NW (Fig. 3b). This is reflected in the complex-wide S_1 foliation trend, where folding constructed from a best fit great circle is slightly asymmetric with an axial plane parallel to the S_2 crenulation cleavage (average orientation of 055/85E), and with a fold axis plunging shallowly to the SW (~05/235) (Fig. 2b). A small domain in the centre of the complex (Region 2, Fig. 2a), however, shows S_1 plotting along a great circle consistent with F_2 folding with an axis plunging moderately towards the NE (35/050; Fig. 2e), opposite to the average trend in the majority of the complex (Fig. 2b). This suggests that, on a larger-scale, F_2 folding is non-cylindrical. The apparent non-cylindricity of F_2 folding is also evident in the doubly plunging nature of meso-scale F_2 fold axes (Fig. 2b).

Near-complete transposition of S_1 into S_2 cleavage, predominantly defined by muscovite ± chlorite, is observed in regions of high strain (Fig. 3c). S_2-parallel mylonites and phyllonites indicate even higher strain in some regions, which are most common close to the Major Gercino and Itajaí—Perimbó shear zones, although narrow phyllonitic zones are also observed in the centre of the complex (Fig. 2a). Where present, L_2 stretching lineations on S_2 planes in the central shear zones consist of dismembered fold limbs and other stretched quartz aggregates, and mainly plunge shallowly to the NE and SW (Fig. 2c). Kinematic indicators show a predominantly dextral shear sense (Fig. 4c), consistent with the major regional shear zones (Hueck, Basei, et al., 2018), although occasional symmetric and sinistral shear sense indicators are also present. The southernmost part of the Brusque Complex represents a structural domain dominated by high-strain S_2 overprint (Region 3, Fig. 2a & f), where mylonites and phyllonites likely represent extensions of the Major Gercino Shear Zone into the Brusque Complex. Here, S_2 is predominantly steeply dipping and striking ~040°, although a subordinate cluster of data striking ~100° suggests the presence of conjugate shear zones (Fig. 2f), consistent with previous observations of anastomosing mylonitic foliations within the Major Gercino Shear Zone (Passarelli et al., 2010).

The Itajaí–Perimbó Shear Zone, where the Brusque Complex is in contact with basement gneisses of the São Miguel Complex, is characterised by mylonites and strong transposition foliation. The dominant foliation (S_2) is steeply dipping and strikes ENE (Fig. 2a), consistent with the orientation of S_2 elsewhere in the complex. Like in the Major Gercino Shear Zone, there are variations in the strike of S_2 consistent with a network of interconnected anastomosing high-strain zones typical of a mature shear zone (Fossen

& Cavalcante, 2017). Shear sense indicators suggest predominantly dextral strike-slip movement, although moderately to steeply plunging stretching lineations at some outcrops reveal a strong top-to-WNW thrust component (Fig. 4d).

A NW–SE-oriented crenulation cleavage (S_3) oriented perpendicular to the average S_2 orientation is also observed across most of the Brusque Complex (Fig. 2b). This cleavage is much less ubiquitous than the previously described deformation fabrics, appearing of markedly lower strain and grade. The S_3 crenulation occasionally shows a conjugate pair at the outcrop scale (Fig. 3d), which is also observed regionally where poles–to-plane data show two maxima at 320/65E and 125/50W giving a ~60° interplanar angle (Fig. 2b). The S_3 cleavage is occasionally associated with meso-scale folding (F_3), which together with F_2 folds can produce dome-and-basin and other complex fold interference patterns. Macro-scale F_3 fold interference may be responsible for the spread of S_1 foliation data and F_2 fold axes away from cylindricity (Fig. 2b).

3.2 Relationship between deformation and metamorphism

Based on field and petrographic observations, regional metamorphism in the Brusque Complex metasedimentary rocks reached maximum lower-amphibolite facies conditions. There is an apparent increase in metamorphic grade from the hinterland towards the centre of the complex, from low-grade chlorite-biotite-schists south of the Valsungana Batholith to medium-grade garnet-schists to the north (Fig. 1c). There is then a sudden decrease in metamorphic grade near the centre of the complex, with predominantly low-grade chlorite-schists again in the NW. The medium-grade rocks are dominated by garnet-bearing metapelitic schists, and the presence of porphyroblastic garnet is used as the principal marker defining the medium-grade zone.

In the medium-grade domain, garnet porphyroblasts often contain oriented inclusion trails (S_i) showing continuation with the primary S_1 matrix foliation (Figs. 4a & 5a–b), and occasionally contain cores with randomly-oriented, equidimensional inclusions (Fig. 5a & b). The overprinting S_2 crenulation cleavage is often associated with parallel chlorite overgrowth (Fig. 4b), in which chlorite overprints the

lepidoblastic mica-rich matrix at a high angle to the S_1 foliation (Fig. 4b). Similarly, in places where there is stronger S_2 and F_2 overprint, garnet porphyroblasts often show extensive replacement by thick chlorite rims. In regions with complete transposition of S_1 by S_2, the mineral assemblage is dominated by muscovite and chlorite (Fig. 4c). In the low-grade domains, the metamorphic mineral assemblage is predominantly comprised of quartz and muscovite, ± biotite and chlorite. In the northern low-grade domain (Fig. 1c), regions of apparent low strain show no indication of relict garnet, or evidence of earlier higher-grade conditions. In contrast, some outcrops in the southern low-grade domain contain garnet-bearing assemblages (e.g. sample BA23) and evidence of relict garnet pseudomorphs.

3.3 Sample petrography and mineral chemistry

Six metasedimentary samples and one metaigneous sample were collected from the Brusque Complex, and one deformed granite was collected from the underlying São Miguel Complex basement (Fig. 1c). An overview of mineral chemistry data for samples used in thermodynamic modelling is given in Table 1, and the full dataset can be found in the online Supporting Information. Mineral abbreviations follow Whitney and Evans (2010). Mineral compositions and endmember mole fractions are reported as follows: X_{Mg}=Mg/(Mg+Fe), X_{Sps}=Mn/(Mn+Fe+Mg+Ca), X_{Alm}=Fe/(Mn+Fe+Mg+Ca), X_{Prp}=Mg/(Mn+Fe+Mg+Ca), X_{Grs}=Ca/(Mn+Fe+Mg+Ca), X_{An}=Ca/(Ca+Na+K).

3.3.1 Garnet-bearing metapelitic samples

Samples BC43 and BB11 are medium-grained pelitic schists collected from the central medium-grade zone of the Brusque Complex (Fig. 1c). Sample BC43 (S 27.39615°, W 49.16711°; all coordinates in WGS84) contains the mineral assemblage garnet (X_{Mg} = 0.05–0.10), biotite (X_{Mg} = 0.41–0.44), muscovite, plagioclase (X_{An} = 0.12), ilmenite and quartz, with accessory chlorite (X_{Mg} = 0.47), paragonite and rutile, and trace amounts of tourmaline. The primary foliation (S_1) is segregated into layers of ~2−5 mm thickness, comprised of alternating mica+garnet-rich, and feldspar+quartz-rich domains. Garnet porphyroblasts reach up to 4 mm in diameter, often showing straight crystal faces and

occasionally with thin chlorite reaction rims (Fig. 5a). Garnet is an almandine-rich solid solution, with strong variation in composition from core to rim ($Sps_{0.12}Alm_{0.75}Prp_{0.04}Grs_{0.09}$ – $Sps_{0.02}Alm_{0.83}Prp_{0.09}Grs_{0.06}$). The garnet shows typical prograde U-shaped zoning of the Prp and bell-shaped zoning of the Sps components (Fig. 5a), and there is a general trend of increasing Alm and decreasing Grs components from core to rim (Fig. 5a, Table 1).

Sample BB11 (S 27.31695°, W 49.12598°) contains the mineral assemblage quartz, garnet (X_{Mg} = 0.04–0.09), biotite (X_{Mg} = 0.38–0.43), muscovite, chlorite (X_{Mg} = 0.41–0.45) and ilmenite, with trace amounts of plagioclase (X_{An} = 0.06–0.07), monazite and zircon. The matrix is dominated by micas, with a strong S_2 crenulation and retrograde chlorite overprint (Fig. 4b). Garnet porphyroblasts are rounded, reaching up to 3 mm in diameter with inclusions of quartz and ilmenite (Fig. 5b). Compositional zoning in garnet is consistent with prograde growth, with decreasing Sps and Grs and increasing Prp and Alm components from core to rim ($Sps_{0.15}Alm_{0.60}Prp_{0.03}Grs_{0.22}$ – $Sps_{0.02}Alm_{0.74}Prp_{0.08}Grs_{0.17}$) (Fig. 5b). Most garnet porphyroblasts show significant chlorite replacement rims (Fig. 5b).

Sample BA23 (S 27.17519°, W 48.70610°) is a weakly foliated, medium-grained metapsammitic schist collected from the southern low-grade zone of the Brusque Complex (Fig. 1c). The sample contains the mineral assemblage quartz, muscovite, hematite, magnetite and garnet (X_{Mg} = 0.18–0.29), with trace amounts of biotite (X_{Mg} = 0.74), chlorite, rutile and tourmaline. The matrix is dominated by quartz, with abundant interstitial hematite, and occasional narrow (1mm) lenses of muscovite and chlorite (Fig. 5c). Garnet is mostly poikilitic and is found within lenses together with muscovite (Fig. 5c). The mica-rich lenses show evidence of a weak S_2 crenulation, with recrystallised white mica oriented parallel to S_2. Hematite grains (<50 μm) are oriented parallel to the primary foliation and are present as inclusions within garnet porphyroblasts. Relict magnetite is found within larger hematite grains. Garnet in sample BA23 is a spessartine-rich solid solution and shows prograde core to rim compositional zoning (Fig. 5c; $Sps_{0.70}Alm_{0.19}Prp_{0.04}Grs_{0.06}$ – $Sps_{0.60}Alm_{0.25}Prp_{0.10}Grs_{0.05}$).

3.3.2 Low-grade metapelitic samples

Samples BC30 and JBD14 are metapelitic phyllites collected from the northern low-grade zone of the Brusque Complex (Fig. 1c). Both samples contain the mineral assemblage quartz, muscovite, chlorite, plagioclase, and oxides. Sample BC30 (S 27.16005°, W 48.99434°) was collected from a steeply dipping high-strain shear zone in the centre of the Brusque Complex (Figs. 1c & 2a). It is fine-grained and strongly foliated, containing foliation-parallel stretched quartz veins, sigma-shaped quartz porphyroclasts, mica-fish, and S-C-C' shear fabrics indicating predominantly dextral strike-slip kinematics (Fig. 4c). Neoformed quartz in shear bands cutting across quartz veins show evidence of bulging dynamic recrystallisation, indicating deformation at low-temperature conditions between ~280−400°C (Stipp et al., 2002).

Sample JBD14 (S 26.92420°, W 48.63520°) was collected on the coast, along-strike from sample BC30 in a similarly steeply dipping high-strain zone (Fig. 1c). The sample is coarser-grained than sample BC30 and contains a lower proportion of matrix phyllosilicates. The microstructure involves thin phyllosilicate-rich domains anastomosing around lenses of quartz aggregates, with individual quartz grains ranging from ~50−250 μm in width.

3.3.3 Metaigneous samples

Sample BA22 (S 27.20325°, W 48.66032°) is a fine-grained, weakly foliated metavolcanic rock collected from the low-grade domain of the Brusque Complex, close to the Major Gercino Shear Zone (Fig. 1c). The sample contains the mineral assemblage quartz, albite (X_{An} = 0.00–0.10) and muscovite, with minor garnet (X_{Mg} = 0.01), biotite (X_{Mg} = 0.28–0.29) and ilmenite, and trace amounts of tourmaline. Garnet grains are small (~100μm) and rounded, with no visible inclusions (Fig. 5d). Garnet is a spessartine- and almandine-rich solid solution, with no significant pyrope component (Fig. 5d), and shows only minor zoning from core to rim ($Sps_{0.46}Alm_{0.50}Prp_{0.00}Grs_{0.3}$ – $Sps_{0.40}Alm_{0.56}Prp_{0.00}Grs_{0.04}$). Biotite shows poor analytical results due to alteration (see Table 1).

Sample JBD09 (S 26.9780°, W 48.9567°) is a ca. 840 Ma (Basei et al., 2008), now mylonitic granite collected from within the Itajaí–Perimbó Shear Zone (Fig. 1c). The sample contains the mineral assemblage quartz, muscovite, plagioclase, and K-feldspar, with minor oxides. The matrix comprises ~80% of the sample, and predominantly consists of fine-grained white mica and quartz, with relict K-feldspar porphyroclasts up to 0.5mm. Quartz porphyroclasts up to 5mm in length show evidence of bulging and sub-grain rotation dynamic recrystallisation, suggesting deformation at temperatures between ~300−450°C (Stipp et al., 2002). The foliation is steeply-dipping, and sigma-shaped quartz porphyroclasts and stretched quartz tails indicate oblique dextral strike-slip shear kinematics with a strong top-to-WNW thrust component (Fig. 4d).

3.4 Phase equilibria modelling

P–T estimates for four garnet-bearing samples from the Brusque Complex were calculated using the PerpleX software package of Connolly (2005) (ver. 6.9.0) with the thermodynamic dataset DS6.22 of Holland and Powell (2011). The following solution models were used for all pseudosections: garnet, chlorite, white mica, biotite and staurolite of White et al. (2014), and ternary feldspar of Fuhrman and Lindsley (1988). In addition, a solution model for ilmenite (White et al., 2000) was used to calculate pseudosections for samples BC43, BB11 and BA22, stilpnomelane (ad hoc model: Connolly, 2005) for samples BA23 and BA22, and spinel (White et al., 2002) for sample BA23.

For all four samples, an initial pseudosection was calculated using measured whole-rock major element compositions (Table S1), which were determined at Bureau Veritas Mineral Laboratories in Vancouver, Canada, and the Czech Geological Survey in Prague, Czech Republic. Pseudosections for samples BC43, BB11 and BA22 were calculated in a simplified MnNCKFMASHT system as they do not contain Fe^{3+}-rich phases. For these samples, Fe_2O_3 from whole-rock analysis was converted to FeO. Given abundant hematite and magnetite present in sample BA23, FeO and Fe_2O_3 concentrations were measured directly via titration, and pseudosections were calculated in the MnNCKFMASHTO system. For all pseudosections, H_2O was considered a saturated component. All samples contain accessory apatite, thus

CaO corrections were applied based on measured P_2O_5 (except sample BB11, as discussed in section 3.4.2).

Because garnet grains in samples BC43, BB11 and BA23 show strong compositional zoning (Fig. 5a, b & c), pseudosections calculated using effective bulk-rock compositions can only confidently estimate *P–T* conditions for garnet core growth (Evans, 2004). Thus, garnet fractionation routines were applied using PerpleX, where modelled garnet cores were subtracted from the bulk composition and the resulting fractionated bulk compositions were used for further modelling. The starting conditions for garnet fractionation were estimated from the intersection of garnet endmember compositional isopleths from garnet cores. The end of the garnet fractionation path was estimated at the point when modelled garnet compositions most closely resembled measured rim values before the complete consumption of Mn from the bulk rock. As the actual P–T paths that the rocks followed are unknown, we chose to fractionate along linear gradients from surface conditions and intersecting the garnet core estimates. Exploratory models using varying fractionation paths (not shown) revealed a negligible effect of the steepness of the slope on the composition of the fractionating garnet and the resulting bulk composition, thus suggesting that the chosen paths are adequate estimates. Pseudosections using the fractionated bulk rock compositions are presented with the pseudosections using measured bulk compositions. Fractionation routines were not conducted for sample BA22, as the garnet grains are small and only weakly zoned (Fig. 5d).

3.4.1 Sample BC43

A pseudosection calculated for sample BC43 using measured bulk rock values (Fig. 6a) shows modelled garnet core compositional isopleths for X_{Sps} (0.12 ± 0.01), X_{Alm} (0.73 ± 0.01) and X_{Grs} (0.11 ± 0.01) intersecting at ~540–550°C and 5.1–6.2 kbar. The X_{Prp} isopleths (0.03± 0.01) do not intersect, plotting at lower temperature conditions (Fig. 6a). This inconsistency suggests that the analysis used for the garnet core composition is not from the exact centre of the garnet, and/or implies problems with the bulk

composition used for modelling (Evans, 2004). Despite this, the intersecting modal compositional isopleths provide an adequate estimate for garnet core *P–T* conditions.

After garnet fractionation, compositional isopleths for X_{Sps} (0.01 ± 0.01), X_{Grs} (0.08 ± 0.01), X_{Alm} (0.81 ± 0.01) and X_{Prp} (0.09 ± 0.01) intersect within error at 560–570°C and 5.5–6.5 kbar, within the phase field containing the observed assemblage Pl+Chl+Grt+Ms+Pg+Ilm+Qz (Fig. 6b). The model does not predict stable rutile; however, it is only present as inclusions in garnet and thus may have been stable during earlier growth, or reflect local compositional heterogeneity. Although the analysed garnet rim compositions show good fit with the model, the compositional variables for biotite X_{Mg}, chlorite X_{Mg}, and plagioclase X_{An} do not exactly match the analysed values (see Table 2). This either reflects issues with the solution models or indicates the re-equilibration of these minerals after growth of the garnet. Despite these discrepancies, we consider the *P–T* conditions of 560–570°C and 5.5–6.5 kbar as best representing the estimate of peak metamorphic conditions for sample BC43.

3.4.2 Sample BB11

A pseudosection calculated for sample BB11 using the apatite-adjusted measured bulk rock composition shows garnet core isopleths for X_{Sps} (0.15 ± 0.01), X_{Alm} (0.60 ± 0.01), X_{Grs} (0.22 ± 0.01) and X_{Prp} (0.03 ± 0.01) intersecting at 510–520°C and 5.7–6.3 kbar (see Figure S1a). After garnet fractionation and modelling using the fractioned bulk composition, the resulting pseudosection showed poorly intersecting garnet compositional isopleths and garnet stability only within Pl-absent phase fields (see Figure S1b), suggesting that the modelled system was too CaO-poor. The measured bulk rock composition prior to apatite CaO adjustment already showed low CaO concentrations (Table S1), and plagioclase is only observed in trace amounts, indicating that small changes in CaO concentrations to the bulk composition can have a large effect on the model. It is likely that the initial apatite adjustment removed too much CaO, and that the assumption that all measured P2O5 comes from apatite is incorrect, which is supported by the presence of monazite in the sample. Using the measured bulk-rock CaO concentration instead of the apatite-adjusted CaO resulted in a pseudosection with comparable phase

fields, and the intersection of garnet core compositional isopleths at 510–520°C and 5.5–6.0 kbar (Fig. 6c) matches closely that from the CaO-adjusted model. After garnet fractionation (Fig. 6d), garnet rim compositional isopleths for observed X_{Sps} (0.02 ± 0.01), X_{Grs} (0.18 ± 0.01), X_{Alm} (0.74 ± 0.01) and X_{Prp} (0.06 ± 0.01) intersect at 540–550°C and 6.4–6.7 kbar within a field containing the observed assemblage of Pl+Grt+Chl+Ms+Bt+Ilm+Qz, notably including plagioclase. Modelled compositional variables for biotite X_{Mg} and plagioclase X_{An} do not exactly match the observed values (see Table 2). Despite this, we consider this as best representing the peak metamorphic conditions for sample BB11.

3.4.3 Sample BA23

A pseudosection calculated for sample BA23 using the analysed bulk-rock composition is presented in Figure 7a. Compositional isopleths for X_{Sps} (0.67 ± 0.01), X_{Mg} (0.21–0.23 ± 0.01) and X_{Grs} (0.05–0.06 ± 0.01) in garnet cores intersect between 475–500°C and 3–7 kbar (Fig. 7a). Although the garnet isopleths do not allow for a precise pressure estimate, exploratory modelling (not shown) using garnet fractionation paths through the higher end of the pressure range, or with a steeper gradient not intersecting surface conditions, result in the destabilisation of garnet before reaching the observed X_{Sps} compositional range, and the best-fit P–T path is through the lower end of this pressure estimate (3.0–4.5 kbar).– After garnet fractionation, isopleths for garnet X_{Sps} (0.60–0.62 ± 0.01) and X_{Mg} (0.29–0.30 ± 0.01), and biotite X_{Mg} (0.72–0.75) intersect within error at 535–555°C and 4.2–6.0 kbar within the phase field containing the observed mineral assemblage of Chl+Grt+Ms+Bt+Mag+Hem+Rt (Fig. 7b). Although the X_{Grs} isopleths (0.03–0.05 ± 0.01) do not intersect at this point, we still interpret this to be an adequate estimate of peak metamorphic conditions based on the intersection of the other compositional isopleths.

3.4.4 Sample BA22

The calculated pseudosection for sample BA22 shows stability of the observed mineral assemblage (Pl+Ab+Grt+Ms+Bt+Ilm) over a large *P–T* range (Fig. 7c). Modelled compositional variables for

plagioclase X_{An} do not match observed values (see Table 2), and do not intersect with those for the garnet endmembers. However, garnet compositional isopleths for X_{Sps} (0.40–0.46), X_{Alm} (0.50–0.56) and X_{Grs} (0.03–0.04) intersect at 510–520°C and 2.3–3.3 kbar, which we interpret as the best estimate of *P–T* conditions for garnet growth.

3.5 Garnet Lu–Hf and Sm–Nd geochronology and trace element chemistry

The results of garnet Lu–Hf and Sm–Nd isotopic dating and trace element analysis are summarised in Table 3 and Fig. 8 and presented in the online Supporting Information. Sample preparation and mass spectrometry procedures are summarised in Anczkiewicz et al. (2004) and Anczkiewicz and Thirlwall (2003). Standards reproducibility and constants used for the calculations are given in the footnote to Table 3. Four samples were analysed by isotope dilution, each producing a Lu–Hf isochron from two to three garnet aliquots and one representative whole rock powder. One sample further produced a Sm–Nd isochron from three garnet aliquots and one whole rock powder. We obtained Lu–Hf isochron ages of 652.5 ± 3.6 Ma, 660.0 ± 2.3 Ma, 649 ± 16 Ma, and 596.9 ± 1.7 Ma for samples BC43, BB11, BA23, and BA22, respectively (Fig. 8a–d), and a Sm–Nd isochron age of 647 ± 10 Ma for sample BC43 (Fig. 8e). One garnet fraction was rejected from sample BB11 (Grt1, see section 4.1.1).

Trace elements were analysed along rim-to-rim transects across representative garnets from each sample to determine the potential influence of inclusions on bulk mineral separate isotopic systematics, and the influence of zonation on age interpretation. The analytical methods are presented in the Supporting Information Text S1. A summary of the results is presented in Figure 8f–j, and the full dataset can be found in the online Supporting Information. The apparatus and analytical protocols are provided in Anczkiewicz et al. (2012). We used NIST 612 glass as a primary standard and BCR2G glass was measured for quality control. GEOREM recommended values were applied (Jochum et al., 2016; Jochum et al., 2011).

In sample BC43, Lu is strongly enriched in garnet cores and decreases sharply towards the rims (Fig. 8f), and Sm and Nd show the opposite trend with enrichment away from the core (Fig. 8j), which is consistent with Rayleigh fractionation during garnet growth (Hollister, 1966). Large peaks in the Sm and Nd profiles correspond to inclusions of accessory minerals such as monazite and allanite. Garnet grains from sample BB11 show Lu-enriched cores and depleted rims (Fig. 8g), although concentrations are significantly lower than sample BC43. Samples BA23 and BA22 have similar Lu concentrations to sample BB11 but show flatter Lu zonation with no systematic variation from core to rim (Fig. 8h & i). In all four samples, the average concentration of Hf in clean parts of the garnet (without mixed analyses from mineral inclusions) is generally around 0.2 ppm and does not vary significantly across or between grains. Peaks in Hf and Zr correspond to inclusions of zircon, which is further discussed in section 4.1.

3.6 Monazite U–Pb geochronology and trace element chemistry

To complement garnet Lu–Hf and Sm–Nd ages, monazite grains from sample BC43 were separated and analysed for trace elements and dated by U–Pb LA–ICP–MS method, with the results presented in Figure 9. A Thermo Scientific Element 2 sector field ICP-MS coupled to a 193 nm ArF excimer laser (Teledyne CETAC Analyte Excite laser), at the Institute of Geology of the Czech Academy of Sciences, was used to measure the Pb/U, Pb/Th and Pb isotopic ratios, and rare earth element and Y (REE+Y) concentrations in monazite. Details of the mineral separation procedures are provided in Supporting Information Text S1. Full results and analytical details are provided in the online Supporting Information.

Trace element composition maps of representative monazite grains show some zoning/variation across individual grains (Fig. 9a and b). Chondrite-normalised REE patterns (Fig. 9c) show typical monazite REE distribution pattern with decreasing concentration from the light to the heavy REEs, and all grains show a negative Eu-anomaly. The REE patterns show two distinct groups, with one group showing significantly higher HREE concentration of at least one order of magnitude (Fig. 9c).

From U–Pb analysis of 6 grains, two age groups were identified corresponding to the two trace element patterns (Fig. 9d). Analysis of four spots from one grain showing the high-HREE pattern yielded a combined concordia age of 583.9 ± 8.0 Ma (2σ, MSWD = 0.24; Fig. 9b). From the analysis of 14 spots in five grains showing the low-HREE pattern, 12 yielded concordant dates that combined to give a $^{207}Pb/^{235}U$–$^{206}Pb/^{238}U$ concordia age of 640.9 ± 7.0 Ma (95% conf., MSWD = 11.4; Fig. 9c).

3.7 $^{40}Ar/^{39}Ar$ mica geochronology

Four samples were selected for $^{40}Ar/^{39}Ar$ geochronology of biotite (sample BC43) and muscovite (samples JBD14, BC30 and JBD09). Biotite was separated and analysed from sample BC43 with the intention of constraining the timing of exhumation of the S_1 fabric prior to F_2 folding, as this sample represents part of the medium-grade zone showing very little S_2 overprint (Region 1; Fig. 2a). Two samples were collected from high-strain zones within the Brusque Complex to constrain the timing of deformation associated with the development of the S_2 fabric (JBD14 and BC30, Fig. 1c). The muscovite in these samples consists of neocrystallised grains lying parallel to the overprinting S_2 fabric (e.g. Fig. 4c). One sample was collected from a high-strain zone within the Itajaí–Perimbó Shear Zone (JBD09, Fig. 1c) to constrain the timing of movement along the northern boundary of the Brusque Complex. Details of sample preparation and analytical methods are provided in the Supporting Information Text S1.

The results from $^{40}Ar/^{39}Ar$ analysis of biotite and muscovite are presented in Figure 10. Five heating steps for biotite from sample BC43 released ~50% ^{39}Ar and defines a plateau age of 635 ± 4 Ma (MSWD = 0.93) (Fig. 10a). Ten heating steps on muscovite from sample JBD14 released ~80% ^{39}Ar, defining a plateau age of 601 ± 9 Ma (MSWD = 0.70) (Fig. 10b). Thirteen heating steps on muscovite from sample BC30 released ~85% ^{39}Ar and defines a plateau age of 571 ± 3 Ma (MSWD = 0.28) (Fig. 10c). Five heating steps for muscovite from sample JBD09 released ~60% ^{39}Ar and defines a plateau age of 545 ± 4 Ma (MSWD = 1.55) (Fig. 10d). Complete results and analytical details are presented in the online Supporting Information.

4 Discussion

4.1 Interpretation of geochronological results

4.1.1 Lu–Hf and Sm–Nd garnet ages and their meaning

Garnet analysed by isotopic dilution in samples BC43 and BA23 shows Hf concentrations between 4.13–4.55 and 1.52–1.70 ppm, respectively (Table 3), which is considered high for garnet in typical metamorphic rocks (Anczkiewicz et al., 2014; Cheng, 2019; Scherer et al., 2000). This is significantly higher than results obtained by LA-ICP-MS analysis from inclusion-free parts of individual garnet porphyroblasts, which show Hf concentrations between ~0.05–0.40 ppm for both samples. In contrast, garnet isotope dilution of sample BB11 shows Hf concentrations ~0.2 ppm (Table 3), which is comparable to estimates from LA-ICP-MS analysis of between ~0.05–0.10 ppm. This disparity between measured Hf concentrations is likely attributed to contamination from Hf-rich accessory mineral inclusions in garnet, such as ilmenite, rutile, and possibly zircon. The presence of sub-micron inclusions of zircon in garnet is confirmed from all four samples by corresponding spikes in U and Hf (Fig. 8f–i), and the presence of ilmenite is obvious from petrographic observations. Despite efforts to reduce the presence of such inclusions in garnet aliquots through manual picking and hotplate dissolution (after Anczkiewicz et al., 2004), the high total Hf and low $^{176}Lu/^{177}Hf$ ratios in samples BC43 and BA23 (Table 3) indicate that some Hf-rich phases were dissolved with the garnet. In contrast, sample BB11 shows a good match between Hf concentrations as measured by isotope dilution (0.18–0.21ppm) and LA-ICP-MS (~0.2 ppm), suggesting such high-Hf inclusions were successfully excluded from the analysis.

Although sample BC43 shows significant Hf contamination and low $^{176}Lu/^{177}Hf$ ratios, the high age precision (652.5 ± 3.6 Ma; Fig. 8a) and good regression line (MSWD = 0.15) indicates low scatter between analyses, suggesting that Hf contamination did not greatly affect the analyses. The poor age precision from sample BA23 (649 ± 16 Ma; Fig. 8c), however, is likely due to low $^{176}Lu/^{177}Hf$ ratios resulting from contamination by Hf-rich mineral inclusions disparately affecting the individual garnet fractions. In contrast, due to the low total Hf and high $^{176}Lu/^{177}Hf$ ratios measured by isotope dilution of sample BB11 (Table 3), the poor precision of the resulting isochron age is likely due to problems with

the outlying data point *Grt1*. This garnet fraction (*Grt1*) was prepared separately from the other two (*Grt2* and *Grt3*) and was subjected to much less rigorous purification by mechanical picking. For this reason, a three-point isochron excluding *Grt1* has been calculated for sample BB11, which gives a more precise age of 660.0 ± 2.3 Ma (Fig. 8b).

If there is significant contribution of Hf from detrital zircon in the isotope dilution analyses, our calculated isochron ages may be skewed from their true ages (Scherer et al., 2000). This type of contamination may be responsible for the disparity between the Lu–Hf ages from samples BC43 and BA23 (ca. 650 Ma) compared with sample BB11 (ca.660 Ma), the latter of which shows little to no evidence of Hf contamination. However, these calculated isochron ages lie relatively close together (within error), and thus it is unlikely that contamination by high-Hf mineral inclusions greatly affected their accuracy. This suggests that Hf-rich mineral phases that were in equilibrium with garnet, such as ilmenite, rutile and metamorphic zircon, were responsible for Hf contamination, and detrital zircon grains were successfully removed during sample preparation.

Isotope dilution analysis from sample BA22 shows Hf concentrations in garnet between ~1.10–1.25 ppm (Table 3), which is higher than estimates from LA-ICP-MS analysis of ~0.1–0.3 ppm, thus suggesting a small amount of Hf contamination. However, considering the high $^{176}Lu/^{177}Hf$ ratios obtained by isotope dilution analysis (Table 3), Hf contamination likely came from inclusions of mineral phases with low-Hf concentrations such as primary metamorphic feldspar (Fig. 8f).

Lu concentrations measured by isotope dilution from all garnet samples (Table 3) correspond well with values as determined by LA-ICP-MS (Fig. 8f–i). Garnet from samples BC43 and BB11 show Lu- and Y-zoning typical of Rayleigh fractionation during prograde growth, with the highest concentrations in the cores and decreasing towards the rims (Fig. 8f & g). Prograde garnet growth is also indicated by major element profiles and pseudosection models, and thus we interpret the ages of 652.5 ± 3.6 and 660.0 ± 2.3 Ma from samples BC43 and BB11, respectively, as recording the timing of early prograde garnet growth in the Brusque Complex. The relatively flat Sm–Nd profiles in garnet from sample BC43 (Fig. 8j) are similarly consistent with Rayleigh-type fractionation during prograde growth (e.g. Lapen et al., 2003), and indicate that the 647 ± 10 Ma Sm–Nd age likely reflects and average growth age,

although the lowest Sm and Nd concentrations in garnet cores suggests it may be slightly biased towards later growth. Thus, the overlap of the Lu–Hf and Sm–Nd ages from sample BC43 suggests that garnet growth was brief, consistent with published estimates of growth duration in medium-grade metapelites (Anczkiewicz et al., 2014; Pollington & Baxter, 2010; Schmidt et al., 2015; Vance & Keith O'Nions, 1992).

Garnet porphyroblasts from samples BA23 and BA22 show mostly flat Lu and Y profiles across garnet grains, with little core–rim variation (Fig. 8h & i). Although the major element zonation profiles from these samples preserve prograde garnet growth (Fig. 5c & d), the small grain size (<0.25mm) indicates possible Lu–Hf diffusion during growth despite the relatively low temperatures of ~540°C (Scherer et al., 2000), which may account for the flat Lu and Y profiles. Based on this, we interpret the ages of 649 ± 16 and 596.9 ± 1.7 Ma from samples BA23 and BA22, respectively, as average ages of garnet growth.

4.1.2 U–Pb monazite ages and their meaning

The 641 ± 8 Ma U–Pb monazite age obtained from sample BC43 shows both poor MSWD and probability of concordance, likely reflecting the low sample size (Fig. 9c). Despite this, the age overlaps within error with the ca. 647 ± 10 Ma garnet Sm-Nd isochron age, supporting coeval growth of monazite and garnet. To test if monazite and garnet grew in equilibrium, we have calculated the apparent monazite/garnet REE distribution coefficients for sample BC43 and compared the results against previously published reference values (Hermann & Rubatto, 2003; Rubatto et al., 2006; Warren et al., 2018). Recent studies have urged for caution when using monazite–garnet partition coefficients from natural samples as evidence of growth in equilibrium (Hagen-Peter et al., 2016; Warren et al., 2018), and there is evidence to suggest that REE partitioning between monazite and garnet is temperature dependent (Warren et al., 2018). However, partitioning values do not appear to differ greatly between sub- and supra-solidus metapelites (Hermann & Rubatto, 2003; Rubatto et al., 2006; Warren et al., 2018).

Due to core–rim compositional variation in garnet, apparent distribution coefficients were calculated using average values measured from four zones identified in a representative garnet grain from sample BC43. In this grain, a plateau in HREE+Y concentration in the mantle was used to define two separate mantle zones, referred to as mantle 1 (M1) and mantle 2 (M2), in addition to core and rim zones (Fig. 11a, & b). The results show that none of the apparent partition coefficients calculated for the high HREE (ca. 584 Ma) monazite match the reference values (Fig. 11c–f). The distribution curves, like the chondrite-normalised REE plots (Fig. 9d), show much higher HREE concentrations compared to the older grains, likely reflecting the dissolution of a HREE-rich phase, such as garnet, prior to or at ca. 584 Ma. Because of this, we interpret the ca. 584 Ma monazite as recording a minor retrograde event.

The apparent partition coefficients calculated for the low HREE (ca. 641 Ma) monazite and garnet core, M1, and M2 zones similarly show a poor fit, plotting well below the reference values (Fig. 11c–e). However, the apparent HREE partition coefficients calculated for garnet rims show a good fit with (Fig. 11f), indicating that the ca. 641 Ma monazite likely grew in equilibrium with garnet rims. These observations confirm the coeval growth of monazite and garnet rims, which we interpret to support that peak regional metamorphism in sample BC43 was reached ca. 645–640 Ma.

4.1.3 Ar–Ar ages and their meaning

Microstructural observations of sample BC43 show biotite to have crystallised during the development of S_1 and estimates from thermodynamic modelling place the peak metamorphic conditions experienced by this sample upwards of ~570°C (Fig. 6b). Considering that the calculated bulk closure temperature of biotite of similar size and composition to that analysed in sample BC43 is ~300 ± 50°C (Grove & Harrison, 1996), the biotite $^{40}Ar/^{39}Ar$ age of 635 ± 4 Ma (Fig. 10a) likely represents a cooling age. However, the step heating experiment shows an almost staircase pattern which could point to a mixture with a relict Ar-reservoir partly escaping outgassing (Bosse & Villa, 2019) or excess Ar not resolved through analysis, thus it is possible this does not represent a pure cooling age.

The three muscovite samples—JBD14, BC30 and JBD09—were collected from rocks showing clear S_2 overprint, and each sample yielded much younger $^{40}Ar/^{39}Ar$ ages compared to sample BC43, between ca. 600 and 545 Ma (Fig. 10b–d). Although we have not obtained reliable temperature constraints for these samples, the mineral assemblages suggest lower-greenschist facies conditions, and the predominance of bulging recrystallisation of quartz suggests maximum temperatures of ~400°C. These conditions are approximately at or below the bulk closure temperature of Ar in muscovite of similar size, at ~400°C (Harrison et al., 2009), suggesting that these ages likely reflect the timing of (re)crystallisation of synkinematic muscovite.

Based on these observations, we interpret the ca. 635 Ma biotite $^{40}Ar/^{39}Ar$ age yielded from sample BC43 as the timing of exhumation of the Brusque Complex and cooling within S_1, whereas the muscovite $^{40}Ar/^{39}Ar$ ages reflect reworking of the flat S_1 foliation by the S_2 fabric. The muscovite ages within the centre of the complex (ca. 600 and 585 Ma) coincide with the timing of granite intrusion between ca. 615–585 Ma (Hueck et al., 2019). These intrusions likely provided heat and fluids for the re-equilibration/recrystallisation of the muscovite during reworking of the S_1 fabric.

4.2 Tectono-metamorphic evolution of the northern Dom Feliciano Belt

4.2.1 Early crustal thickening and peak regional metamorphism (ca. 660 to 640 Ma)

The earliest structural feature preserved in the Brusque Complex is the pervasive, flat-lying metamorphic S_1 foliation. The foliation contains intrafolial folds suggestive of development during progressive simple shearing, and the NW–SE-trending L_1 stretching lineations and associated kinematic indicators indicate that it developed during low-angle NW-directed shearing. As S_1 is the earliest major structure recognised in the complex, it likely developed during early convergence, which is consistent with interpretations from previous studies (e.g. Basei et al., 2011; De Toni, Bitencourt, Konopásek, et

al., 2020). This further suggests that S_1 originally dipped shallowly towards the SE, and the local reorientation of S_1 in Region 1 may be the result of doming after intrusion of the Valsungana Batholith.

Phase equilibria modelling of the medium-grade Brusque Complex metasedimentary rocks suggests that prograde garnet growth culminated at 540–570°C and 5.5–6.7 kbar, corresponding to an apparent geothermal gradient of ~25°C/km (Fig. 12) that is consistent with regional orogenic metamorphism within a medium P/T series typical for crustal thickening (Winter, 2014). The randomly oriented, equidimensional mineral inclusions found in some garnet cores (Fig. 5a & b), together with the oriented inclusions continuous with S_1 found in the majority of garnet, suggests pre- to syn-kinematic garnet growth during S_1 development (Zwart, 1962). Thus, based on the Lu–Hf garnet geochronology from this study, crustal thickening due to progressive thrusting in the Dom Feliciano Belt foreland was likely underway by ca. 660–650 Ma. This corresponds with the timing of convergence and crustal thickening in the hinterland estimated from early melting in the Porto Belo Complex (Chemale et al., 2012; De Toni, Bitencourt, Konopásek, et al., 2020; De Toni, Bitencourt, Nardi, et al., 2020; Hueck, Basei, et al., 2018). The complex reached a regional metamorphic peak between ca. 650–640 Ma, as constrained by garnet Sm–Nd and monazite U–Pb dating.

P–T estimates from sample BA23 in the southern, low-grade part of the Brusque Complex indicate peak regional metamorphic conditions at lower amphibolite facies, between 535–555°C and 4.2–6.0 kbar (Fig. 12a). The lower end of the pressure estimate suggests peak regional metamorphism at a higher crustal position compared to the medium-grade domain, corresponding to a maximum apparent geothermal gradient of ~35°C/km (Fig. 12b). Although this part of the complex is dominated by low-grade, greenschist-facies rocks, these results, and the few relict garnet-bearing outcrops observed in the field, suggest that at least parts of this region may be retrogressed equivalents to the central medium-grade domain. The 649 ± 16 Ma metamorphic age yielded from this sample is within error of those from the two medium-grade metapelites, however the lower pressure conditions and higher apparent thermal gradient suggests that this rock may record a slightly later stage of orogenesis related to increasing thermal input during thrusting in the foreland. This is consistent with thermal relaxation during crustal thickening after burial beneath the hinterland between ca. 660–650 Ma.

4.2.2 Exhumation and progressive switch to partitioned transpression (ca. 635 to 615 Ma)

The Ar–Ar biotite age from sample BC43 indicates that at least the uppermost parts of the Brusque Complex cooled to ~300°C by ca. 635 Ma, suggesting thrust-controlled exhumation of the complex by this time (Fig. 12a). Due to the staircase-like step heating pattern (Fig. 10a), however, 300°C is considered the minimum cooling temperature (Bosse & Villa, 2019), and as the end of exhumation and foreland thrusting is only constrained by this one data point, we consider it a maximum age estimate.

The end of thrusting is marked by the intrusion of post-collisional magmatic bodies into the hinterland (Chemale et al., 2012; Florisbal, Bitencourt, et al., 2012), and the partitioning and localization of strain into the Major Gercino Shear Zone (De Toni, Bitencourt, Konopásek, et al., 2020; Hueck, Basei, et al., 2018). Early syn-tectonic magmatism of the Florianópolis Batholith within the Major Gercino Shear Zone records a transition from flat-lying to upright transcurrent emplacement structures from ca. 625 to 615 Ma, and by ca. 610 Ma the syn-tectonic magmatic intrusions appear to be controlled entirely by sub-vertical transcurrent shear zones (Florisbal, Bitencourt, et al., 2012). Thus, the period between ca. 635–615 Ma has been interpreted as the timing of progressive reorientation of the stress field resulting in the end of thrust-dominated tectonics, and the establishment of the simple shear-dominated Major Gercino Shear Zone and pure shear-dominated deformation in the foreland (De Toni, Bitencourt, Konopásek, et al., 2020). The majority of magmatism in the foreland was delayed by ca. 10 Myr with respect to the Florianópolis Batholith, starting from ca. 615 Ma (Campos et al., 2012; Florisbal, Janasi, Bitencourt, & Heaman, 2012; Hueck et al., 2019), and as the foreland granites crosscut the S_1 foliation the absolute minimum age for the end of thrusting-controlled exhumation in the foreland is constrained to ca. 615 Ma.

4.2.3 Pure shear-dominated deformation, granite intrusion, and retrograde metamorphism (ca. 615 to 550 Ma)

The shift to pure shear contractional deformation in the Brusque Complex is reflected by upright to steeply inclined F_2 folding, and the development of extensive sub-vertical S_2 cleavages and transposition foliations. As previously described, the S_2 structures are associated with retrograde chlorite overgrowth, which is particularly clear in the medium-grade domain (Fig. 4b). Similarly, the S_2 transposition foliations and mylonites in the southern low-grade domain close to the Major Gercino Shear Zone are dominated by chlorite and muscovite, and relict garnet at some outcrops suggest that the apparent low-grade metamorphic conditions may be the result of intense retrograde overprint. However, garnet-bearing outcrops (e.g. locality BA23) are rare, and the reorientation and transposition of previous fabrics makes it difficult to identify earlier structures and mineral assemblages. Thus, the S_2 structures are clearly shown to be retrogressive only in the garnet-bearing schists.

The upper limit for the timing of this deformation in the foreland is constrained by the S_1 biotite Ar–Ar cooling age at ca. 635 Ma. However, the lower-greenschist facies conditions recorded during S_2 development indicate higher temperatures than suggested by this cooling age. This can be explained by increasing thermal input from below by deep-seated melting after the end of thrusting, which is supported by exhumation of the Camboriú Complex and subsequent contact metamorphism of the overlying Brusque Complex (De Toni, Bitencourt, Konopásek, et al., 2020). Furthermore, the foreland granitic bodies, in particular the Valsungana Batholith, are preferentially elongated NE–SW with the main S_2 structural trend (Fig. 2c) and show syn-kinematic magmatic foliation fabrics (Hueck et al., 2016) and overprinting metamorphic contact aureoles (Basei et al., 2011) suggesting that they intruded during or after the actively developing F_2 and S_2 structures. Thus, the development of F_2 and S_2 deformation structures likely started at or before ca. 615 Ma and continued throughout the period of granite intrusion.

Phase equilibria modelling and Lu–Hf dating of sample BA22 show that from at least ca. 600 Ma the Brusque Complex was located at a depth corresponding to ~2–3 kbar. However, *P–T* modelling of this sample estimates temperatures of over 500°C (Fig. 7c), resulting in a high apparent thermal gradient of

up to ~50°C/km (Fig. 12b). Due to its proximity with the Valsungana and Florianópolis batholiths (Fig. 1c), it is likely that the high-T/low-P conditions experienced by this sample reflects high thermal input from adjacent magmatic rocks intruding the hinterland and/or foreland. Based on the preserved ca. 635 Ma cooling age from sample BC43, and the absence of garnet-bearing rocks in the majority of the complex, it is clear that there were large differences in local thermal conditions during the post-collisional period. These differences were likely controlled by proximity to magmatic intrusions, which in many cases have well developed metamorphic contact aureoles (Basei et al., 2011; Campos et al., 2012).

The muscovite Ar–Ar ages indicate that the Brusque Complex was still actively deforming from ca. 600 to 570 Ma. Although most deformation overprinting S_1 is pure shear-dominated F_2 folding and S_2 crenulation cleavage development, high-strain zones within the complex also show phyllonitic S_2 foliation fabrics with horizontal stretching lineations indicative of strike-slip deformation, suggesting that partitioning of the strike-slip component of transpression was not solely confined to the Major Gercino Shear Zone. This lasted until at least ca. 570 Ma (muscovite Ar–Ar sample BC30), which is ca. 15 Myr after the end of granitic magmatism (Chemale et al., 2012; Hueck et al., 2019). Localised ductile deformation in the São Miguel Complex along the northern edge of the Schist Belt, at ca. 545 Ma, seemingly marks the end of contractional deformation in the belt and coincides with late-stage deformation along the Major Gercino Shear Zone between ca. 580–540 Ma (Hueck, Basei, et al., 2018). Such timing supports interpretations that ca. 560 Ma orogenic foreland basin sediments were interleaved with the Brusque Complex during the later stages of orogenic development (Percival et al., 2021).

4.3 Summary of the two-stage tectonic evolution of the Dom Feliciano belt

The structural, metamorphic, and geochronological data presented in this study reveal two distinct stages for the tectonic evolution of the northern Dom Feliciano Belt: 1) early crustal thickening driven by top-to-NW thrusting, and 2) partitioned transpression leading to upright folding of the foreland and strike-

slip shearing at the contact between the hinterland and the foreland. As such, the data mostly support the evolutionary model proposed by De Toni, Bitencourt, Konopásek, et al. (2020) for the north-easternmost part of the Dom Feliciano Belt. Our proposed tectonic model is summarised in Figure 13.

Early orogenic thickening recorded in the northern Dom Feliciano Belt foreland at ca. 660–650 Ma was likely induced by thrusting of the hinterland over pre-orogenic rift sediments deposited on the Luis Alves cratonic basement (Fig. 13a). Internal thrust planes developed within the Brusque Complex, and progressive thrusting towards the foreland led to the juxtaposition of the deeper-seated medium-grade domain over the low-grade domain, and the development of an inverted metamorphic gradient within the Brusque Complex (Fig. 13a). Thickening of the foreland took place at progressively increasing apparent thermal gradients from ~25°C/km to ~35°C/km between ca. 660–650 Ma (Fig. 12b). Thrusting-related exhumation in the foreland was likely finishing by ca. 635 Ma, at which time the foreland crust was sufficiently loaded by the thickened crust that it began to buckle and fold (Fig. 13b), resulting in doming in the foreland and decompressive melting of the foreland basement.

The transition into partitioned transpression from ca. 635 Ma resulted in the development of predominantly upright folds and pure shear-dominated shear zones in the foreland, and dextral strike-slip shearing along its contact with the hinterland (Fig. 13b). The thermal effect of crustal loading in the foreland became apparent at ca. 615 Ma when, with a delay of ca. 15–20 Myr compared to the hinterland, melting in the basement produced the foreland batholiths (Fig. 13b). This is supported by metamorphic data from the supracrustal complex (this work) and the crystalline basement (De Toni, Bitencourt, Konopásek, et al., 2020), which show that high apparent thermal gradients of up to ~50°C/km developed in the period between ca. 635–600 Ma. The intrusion of magmatic rocks into the foreland was coeval with pure shear-dominated deformation, producing contact aureoles in the foreland metasedimentary rocks. From ca. 585 Ma, coinciding with the end of melting and final cooling of the orogen, low-temperature deformation in the Brusque Complex localised entirely into steep shear zones (Fig. 13b & c).

4.4 Implications for the pre-orogenic evolution of the Kaoko–Dom Feliciano–Gariep system

According to subduction-collision models involving the Adamastor Ocean, the Southern Brazilian Shear Belt (including the Major Gercino Shear Zone) represents the suture after ocean closure and thrusting of the magmatic arc—the Granite Belt— over the cratonic passive margin sediments—the Schist Belt (Basei et al., 2018; Basei et al., 2000; Hueck, Oyhantçabal, et al., 2018; Passarelli et al., 2010). This interpretation requires that orogenic crustal thickening in the western foreland post-dates intrusion of the Granite Belt, as continental collision could only occur after closure of the Adamastor Ocean. However, our results show that crustal thickening in the foreland, between ca. 660–650 Ma, occurred ca. 20–30 Myr prior to the onset of large-scale melting and intrusion of the Granite Belt from ca. 630 Ma (Basei et al., 2021; Florisbal, Janasi, Bitencourt, & Heaman, 2012) (Fig. 13a & b). This gap in time corresponds well with observations and modelling from other orogens showing a ca. 20–25 Myr delay between crustal thickening and large-scale melting (England & Thompson, 1986; Jamieson & Beaumont, 2013; Jamieson et al., 2011). Thus, the timing of early orogenic thickening in the western foreland ca. 20–30 Myr prior to large-scale melting in the hinterland precludes the interpretation of the Granite Belt as a supra-subduction zone magmatic arc related to long-lived subduction of a large Adamastor Ocean.

Examples in the literature show that large-scale syn-orogenic melting is typical for hinterland domains in hot orogenic systems (e.g. Cavalcante et al., 2018; Jamieson et al., 2011; Vanderhaeghe, 2009; Vanderhaeghe & Teyssier, 2001). This is consistent with alternative interpretations of the Granite Belt as representing post-collisional magmatism driven by melting in the lower- to middle-crust with connections to the mantle (Bitencourt & Nardi, 2000; Florisbal, Bitencourt, et al., 2012; Florisbal et al., 2009; Florisbal, Janasi, Bitencourt, & Heaman, 2012; Florisbal, Janasi, Bitencourt, Nardi, et al., 2012).

These observations support recent interpretations of the pre-orogenic position of the Kaoko and Dom Feliciano belts within an intracontinental or back-arc rift setting, where the Luis Alves Craton and Nico Pérez Terrane represent parts of the rifted/attenuated margin of the Congo Craton. In such models, orogeny is the result of rift inversion triggered by the end of subduction and closure of an oceanic domain

occurring farther to the west (in today's coordinates), documented by relict magmatic arcs in the São Gabriel Terrane at the western edge of the central Dom Feliciano Belt foreland (De Toni, Bitencourt, Nardi, et al., 2020; Konopásek et al., 2020; Konopásek et al., 2018; Oriolo, Oyhantçabal, Wemmer, Basei, et al., 2016). In the central part of the Dom Feliciano Belt, the potential arc-to-hinterland distance suggests a setting similar to accretionary orogeny (see De Toni, Bitencourt, Nardi, et al., 2020; Konopásek et al., 2018), while in its northern part the distance to a potential controlling subduction zone/arc system was probably large, which is more suggestive of an intracontinental setting (Konopásek et al., 2020).

The geochronological data presented in this study suggest that early crustal thickening in the Dom Feliciano Belt foreland coincides with, or slightly precedes, high temperature thrust-related metamorphism and early (but limited) magmatism in the hinterland between ca. 655–640 Ma (Chemale et al., 2012; Gross et al., 2009; Martil, 2016; Oyhantçabal et al., 2009; Will et al., 2019). Thus, crustal thickening in the hinterland and foreland was largely coeval. Crustal thickening on the South American side of the orogenic system coincides with early syn-orogenic sedimentation in the Kaoko Belt on the African side (Konopásek et al., 2017), implying proximity between the Congo and Luis Alves cratonic margins at ca. 660–650 Ma. Furthermore, the onset of crustal thickening on the western side of the orogen took place during, or shortly after, the end of crustal stretching recorded in the eastern (African) foreland between ca. 660–645 Ma (see discussion in Konopásek et al., 2020; Konopásek et al., 2017). These observations further preclude the presence of a large Adamastor Ocean between the African and South American crustal blocks at this time.

5 Conclusions

The Neoproterozoic orogenic evolution of the northern Dom Feliciano Belt is complex owing to a two-stage tectono-metamorphic history. Early convergence is recorded in the supracrustal rocks of the foreland (the Brusque Complex) by the development of a flat-lying metamorphic foliation (S_1) that formed during top-to-NW directed thrusting and records peak regional metamorphic conditions. Garnet-bearing schists record prograde metamorphism with peak *P–T* conditions estimated at 5.5–6.7 kbar and 540–570°C, indicating a geothermal gradient (~25°C/km) that is consistent with regional orogenic metamorphism during crustal thickening. Early garnet growth is constrained by garnet–whole rock Lu–Hf ages of 660 ± 2 Ma, 652 ± 2 Ma, and 649 ± 16 Ma, and the timing of peak regional metamorphism is constrained by a garnet–whole rock Sm–Nd age of 647 ± 10 Ma and a monazite U–Pb age of 641 ± 8 Ma. Exhumation of the foreland supracrustal rocks likely occurred between ca. 635–615 Ma, during which time deformation transitioned into a partitioned transpressional system with pure shear-dominated deformation localised in the foreland and dextral strike-slip deformation in the hinterland. This is marked by the development of upright, NE–SW trending orogen-parallel folds (F_2), a pervasive axial planar crenulation cleavage (S_2), and pure- to dextral strike-slip shear zones. By ca. 600 Ma, the complex was exhumed to pressures of 2.3–3.3 kbar (~10 km), and the intrusion of large granitic batholiths and metamorphic contact aureoles recording local apparent thermal gradients of up to ~50 °C/km indicate increasing thermal input from below. Deformation within the foreland continued until at least ca. 570 Ma, and along major shear zones until ca. 545 Ma.

Our work shows that supracrustal sequences in the northern Dom Feliciano Belt foreland reached metamorphic conditions typical for crustal thickening between ca. 660–650 Ma. This is ca. 20–30 Myr prior to the onset of massive magmatic activity in the hinterland, which is a typical delay seen in hot internal parts of orogens during collision. This observation contradicts a subduction-related magmatic arc interpretation of massive granitic magmatism in the Dom Feliciano Belt hinterland (the Granite Belt), and instead supports a post-collisional interpretation. This implies the absence of subduction at this time, and further suggests the absence of a large oceanic domain between the foreland and hinterland domains prior to orogenesis. Instead, we interpret orogenesis as being initiated by rift-basin inversion

driven by far-field forces transmitted through the crust, potentially in an intracontinental setting or a back-arc rift setting with subduction and a true arc region located further to the west.

Acknowledgments

This work represents part of a PhD project which received financial support from Diku Norway and CAPES Brazil (project UTF-2018-10004). J. Konopásek appreciates support from the Czech Science Foundation (project no. 18-24281S). This work was also partly supported by the Research Council of Norway through the funding to the Norwegian Research School on Dynamics and Evolution of Earth and Planets (DEEP), project number 249040/F60. Many thanks to D. Sala and M. Koziarska for their help with isotopic analytical work, and R. Škoda, R Čopjaková, and M. Erambert for providing monazite elemental maps and assistance with microprobe analyses. We thank M. Hueck and an anonymous reviewer for their helpful comments and suggestions.

Online supporting information and data availability

Datasets for whole-rock and mineral major element analysis, garnet–whole-rock Lu–Hf and Sm–Nd geochronology, monazite U–Pb geochronology and trace element analysis, and mica Ar–Ar geochronology are available online via DOI (https://doi.org/10.26022/IEDA/112054).

References

Aitken, A. R. A., Raimondo, T., & Capitanio, F. A. (2013). The intraplate character of supercontinent tectonics. *Gondwana Research, 24*(3), 807–814. https://doi.org/10.1016/j.gr.2013.03.005

Anczkiewicz, R., Chakraborty, S., Dasgupta, S., Mukhopadhyay, D., & Kołtonik, K. (2014). Timing, duration and inversion of prograde Barrovian metamorphism constrained by high resolution Lu–Hf garnet dating: A case study from the Sikkim Himalaya, NE India. *Earth and Planetary Science Letters, 407*, 70–81. http://dx.doi.org/10.1016/j.epsl.2014.09.035

Anczkiewicz, R., Platt, J. P., Thirlwall, M. F., & Wakabayashi, J. (2004). Franciscan subduction off to a slow start: evidence from high-precision Lu–Hf garnet ages on high grade-blocks. *Earth and Planetary Science Letters, 225*(1), 147–161. https://doi.org/10.1016/j.epsl.2004.06.003

Anczkiewicz, R., Thirlwall, M., Alard, O., Rogers, N. W., & Clark, C. (2012). Diffusional homogenization of light REE in garnet from the Day Nui Con Voi Massif in N-Vietnam: Implications for Sm–Nd geochronology and timing of metamorphism in the Red River shear zone. *Chemical Geology, 318-319*, 16–30. https://doi.org/10.1016/j.chemgeo.2012.04.024

Anczkiewicz, R., & Thirlwall, M. F. (2003). Improving precision of Sm-Nd garnet dating by H2SO4 leaching: a simple solution to the phosphate inclusion problem. *Geological Society, London, Special Publications, 220*(1), 83–91. https://10.1144/GSL.SP.2003.220.01.05

Basei, M. A. S., Campos Neto, M. C., Castro, N. A., Nutman, A. P., Wemmer, K., Yamamoto, M. T., et al. (2011). Tectonic evolution of the Brusque Group, Dom Feliciano belt, Santa Catarina, Southern Brazil. *Journal of South American Earth Sciences, 32*(4), 324─350. https://doi.org/10.1016/j.jsames.2011.03.016

Basei, M. A. S., Campos Neto, M. d. C., Lopes, A. P., Nutman, A. P., Liu, D., & Sato, K. (2013). Polycyclic evolution of Camboriú Complex migmatites, Santa Catarina, Southern Brazil: integrated Hf isotopic and U-Pb age zircon evidence of episodic reworking of a Mesoarchean juvenile crust. *Brazilian Journal of Geology, 43*(3), 427-443. https://doi.org/10.5327/Z2317-48892013000300002

Basei, M. A. S., Corrêa, V. X., Castro, N. A., & Hueck, M. (2021). U–Pb geochronology and Lu–Hf zircon isotopy of the Santinho Granitic Association: A remnant of the early magmatic stages of the Florianópolis Batholith, Santa Catarina, Brazil. *Journal of South American Earth Sciences, 108*, 103148. https://doi.org/10.1016/j.jsames.2020.103148

Basei, M. A. S., Frimmel, H. E., Campos Neto, M. d. C., de Araujo, C. E. G., de Castro, N. A., & Passarelli, C. R. (2018). The Tectonic History of the Southern Adamastor Ocean Based on a Correlation of the Kaoko and Dom Feliciano Belts. In S. Siegesmund, M. A. S. Basei, P. Oyhantçabal, & S. Oriolo (Eds.), *Geology of Southwest Gondwana* (1st ed., pp. 63─85). https://doi.org/10.1007/978-3-319-68920-3_3

Basei, M. A. S., Grasso, C. B., Vlach, S. R. F., Nutman, A., Siga Jr., O., & Osaki, L. S. (2008). *A-type rift-related granite and the lower cryogenian age for the beginning of the Brusque Belt basin.* Paper presented at the Proceedings of South American Symposium on Isotope Geology, San Carlos de Bariloche, Argentina.

Basei, M. A. S., Nutman, A., Siga Jr, O., Passarelli, C. R., & Drukas, C. O. (2009). The Evolution and Tectonic Setting of the Luis Alves Microplate of Southeastern Brazil: An Exotic Terrane during the Assembly of Western Gondwana. In C. Gaucher, A. N. Sial, H. E. Frimmel, & G. P. Halverson (Eds.), *Developments in Precambrian Geology* (Vol. 16, pp. 273-291): Elsevier.

Basei, M. A. S., Siga Jr, O., Masquelin, H., Harara, O. M., Reis Neto, J. M., & Preciozzi, F. (2000). The Dom Feliciano Belt of Brazil and Uruguay and its Foreland Domain, the Rio de la Plata Craton: framework, tectonic evolution and correlation with similar provinces of Southwestern Africa. In U. G. Cordani, E. J. Milani, A. Thomaz Filho, & D. A. Campos (Eds.), *Tectonic Evolution of South America* (pp. 311─334). Rio de Janeiro, Brazil: Geological Society.

Battisti, M. A., Bitencourt, M. F., De Toni, G. B., Nardi, L. V. S., & Konopásek, J. (2018). Metavolcanic rocks and orthogneisses from Porongos and Várzea do Capivarita complexes: A case for identification of tectonic interleaving at different crustal levels from structural and geochemical data in southernmost Brazil. *Journal of South American Earth Sciences, 88*, 253─274. https://doi.org/10.1016/j.jsames.2018.08.009

Baxter, E. F., & Scherer, E. E. (2013). Garnet Geochronology: Timekeeper of Tectonometamorphic Processes. *Elements, 9*(6), 433─438. https://doi.org/10.2113/gselements.9.6.433

Bitencourt, M. F., & Nardi, L. V. S. (1993). Late- to Post-collisional Brasiliano Magmatism in Southernmost Brazil. *Anais da Academia Brasileira de Ciências, 65*, 3─16. https://10.25249/0375-7536.2000301186189

Bitencourt, M. F., & Nardi, L. V. S. (2000). Tectonic setting and sources of magmatism related to the southern Brazilian shear belt. *Revista Brasileira de Geociências, 30*(1), 186─189.

Bosse, V., & Villa, I. M. (2019). Petrochronology and hygrochronology of tectono-metamorphic events. *Gondwana Research, 71*, 76-90. https://doi.org/10.1016/j.gr.2018.12.014

Campos, R. S., Philipp, R. P., Massonne, H.-J., & Chemale Jr, F. (2012). Early post-collisional Brasiliano magmatism in Botuverá region, Santa Catarina, southern Brazil: Evidence from petrology, geochemistry, isotope geology and geochronology of the diabase and lamprophyre dikes. *Journal of South American Earth Sciences, 37*, 266─278. https://doi.org/10.1016/j.jsames.2012.02.005

Campos, R. S., Philipp, R. P., Massonne, H.-J., Chemale Jr, F., & Theye, T. (2011). Petrology and isotope geology of mafic to ultramafic metavolcanic rocks of the Brusque Metamorphic Complex, southern Brazil. *International Geology Review, 54*(6), 686─713. https://doi.org/10.1080/00206814.2011.569393

Cavalcante, C., Fossen, H., de Almeida, R. P., Hollanda, M. H. B. M., & Egydio-Silva, M. (2019). Reviewing the puzzling intracontinental termination of the Araçuaí-West Congo orogenic belt and its implications for orogenic development. *Precambrian Research, 322*, 85–98. https://doi.org/10.1016/j.precamres.2018.12.025

Cavalcante, C., Hollanda, M. H., Vauchez, A., & Kawata, M. (2018). How long can the middle crust remain partially molten during orogeny? *Geology, 46*(10), 839–842. https://doi.org/10.1130/g45126.1

Cawood, P. A., Kröner, A., Collins, W. J., Kusky, T. M., Mooney, W. D., & Windley, B. F. (2009). Accretionary orogens through Earth history. *Geological Society, London, Special Publications, 318*(1), 1–36. https://doi.org/10.1144/SP318.1

Caxito, F. A., Heilbron, M., Valeriano, C. M., Bruno, H., Pedrosa-Soares, A., Alkmim, F. F., et al. (2021). Integration of elemental and isotope data supports a Neoproterozoic Adamastor Ocean realm. *Geochemical perspectives letters, 17*, 6–10. https://doi.org/10.7185/geochemlet.2106

Chemale, F., Mallmann, G., Bitencourt, M. F., & Kawashita, K. (2012). Time constraints on magmatism along the Major Gercino Shear Zone, southern Brazil: Implications for West Gondwana reconstruction. *Gondwana Research, 22*(1), 184–199. https://doi.org/10.1016/j.gr.2011.08.018

Chemale, F., Philipp, R. P., Dussin, I. A., Formoso, M. L. L., Kawashita, K., & Berttotti, A. L. (2011). Lu–Hf and U–Pb age determination of Capivarita Anorthosite in the Dom Feliciano Belt, Brazil. *Precambrian Research, 186*(1–4), 117–126. https://doi.org/10.1016/j.precamres.2011.01.005

Cheng, H. (2019). Garnet Lu–Hf and Sm–Nd geochronology: a time capsule of the metamorphic evolution of orogenic belts. *Geological Society, London, Special Publications, 474*(1), 47–67. https://doi.org/10.1144/sp474.7

Collins, W. J. (2002). Nature of extensional accretionary orogens. *Tectonics, 21*(4), 6-1–6-12. https://doi.org/10.1029/2000TC001272

Connolly, J. A. D. (2005). Computation of phase equilibria by linear programming: A tool for geodynamic modeling and its application to subduction zone decarbonation. *Earth and Planetary Science Letters, 236*(1–2), 524–541. https://doi.org/10.1016/j.epsl.2005.04.033

Cunningham, D. (2005). Active intracontinental transpressional mountain building in the Mongolian Altai: Defining a new class of orogen. *Earth and Planetary Science Letters, 240*(2), 436–444. https://doi.org/10.1016/j.epsl.2005.09.013

De Toni, G. B., Bitencourt, M. F., Konopásek, J., Battisti, M. A., Oliveira da Costa, E., & Savian, J. F. (2021). Autochtonous origin of the Encruzilhada Block, Dom Feliciano Belt, southern Brazil, based on aerogeophysics, image analysis and PT-paths. *Journal of Geodynamics, 144*, 101825. https://doi.org/10.1016/j.jog.2021.101825

De Toni, G. B., Bitencourt, M. F., Konopásek, J., Martini, A., Andrade, P. H. S., Florisbal, L. M., & Campos, R. S. (2020). Transpressive strain partitioning between the Major Gercino Shear Zone

and the Tijucas Fold Belt, Dom Feliciano Belt, Santa Catarina, southern Brazil. *Journal of Structural Geology, 136*, 104058. https://doi.org/10.1016/j.jsg.2020.104058

De Toni, G. B., Bitencourt, M. F., Nardi, L. V. S., Florisbal, L. M., Almeida, B. S., & Geraldes, M. (2020). Dom Feliciano Belt orogenic cycle tracked by its pre-collisional magmatism: The Tonian (ca. 800 Ma) Porto Belo Complex and its correlations in southern Brazil and Uruguay. *Precambrian Research, 342*, 105702. https://doi.org/10.1016/j.precamres.2020.105702

England, P. C., & Thompson, A. (1986). Some thermal and tectonic models for crustal melting in continental collision zones. *Geological Society, London, Special Publications, 19*(1), 83. https://doi.org/10.1144/GSL.SP.1986.019.01.05

Evans, T. P. (2004). A method for calculating effective bulk composition modification due to crystal fractionation in garnet-bearing schist: Implications for isopleth thermobarometry. *Journal of Metamorphic Geology, 22*(6), 547–557. https://doi.org/10.1111/j.1525-1314.2004.00532.x

Faure, M., Shu, L., Wang, B., Charvet, J., Choulet, F., & Monie, P. (2009). Intracontinental subduction: a possible mechanism for the Early Palaeozoic Orogen of SE China. *Terra Nova, 21*(5), 360–368. https://doi.org/10.1111/j.1365-3121.2009.00888.x

Fischer, G., Fassbinder, E., Barros, C. E. M., & Fossen, H. (2019). The evolution of quartz veins during the tectonometamorphic development of the Brusque Metamorphic Complex, Brazil. *Journal of South American Earth Sciences, 93*, 174–182. https://doi.org/10.1016/j.jsames.2019.04.027

Florisbal, L. M., Bitencourt, M. F., Janasi, V. A., Nardi, L. V. S., & Heaman, L. M. (2012). Petrogenesis of syntectonic granites emplaced at the transition from thrusting to transcurrent tectonics in post-collisional setting: Whole-rock and Sr–Nd–Pb isotope geochemistry in the Neoproterozoic Quatro Ilhas and Mariscal Granites, Southern Brazil. *Lithos, 153*, 53–71. https://doi.org/10.1016/j.lithos.2012.04.031

Florisbal, L. M., Bitencourt, M. F., Nardi, L. V. S., & Conceição, R. V. (2009). Early post-collisional granitic and coeval mafic magmatism of medium- to high-K tholeiitic affinity within the Neoproterozoic Southern Brazilian Shear Belt. *Precambrian Research, 175*(1–4), 135–148. https://doi.org/10.1016/j.precamres.2009.09.003

Florisbal, L. M., Janasi, V. A., Bitencourt, M. F., & Heaman, L. M. (2012). Space–time relation of post-collisional granitic magmatism in Santa Catarina, southern Brazil: U–Pb LA-MC-ICP-MS zircon geochronology of coeval mafic–felsic magmatism related to the Major Gercino Shear Zone. *Precambrian Research, 216–219*, 132–151. https://doi.org/10.1016/j.precamres.2012.06.015

Florisbal, L. M., Janasi, V. A., Bitencourt, M. F., Nardi, L. V. S., & Heaman, L. M. (2012). Contrasted crustal sources as defined by whole-rock and Sr–Nd–Pb isotope geochemistry of neoproterozoic early post-collisional granitic magmatism within the Southern Brazilian Shear Belt, Camboriú, Brazil. *Journal of South American Earth Sciences, 39*, 24–43. https://doi.org/10.1016/j.jsames.2012.06.013

Fossen, H., Cavalcante, C., Konopásek, J., Tieppo Meira, V., Almeida, R., Hollanda, M., & Trompette, R. (2020). A critical discussion of the subduction-collision model for the Neoproterozoic Araçuaí-West Congo orogen. *Precambrian Research*, 105715. https://doi.org/10.1016/j.precamres.2020.105715

Fossen, H., Cavalcante, G. C., & Almeida, R. P. d. (2017). Hot Versus Cold Orogenic Behavior: Comparing the Araçuaí-West Congo and the Caledonian Orogens. *Tectonics, 36*(10), 2159–2178. https://doi.org/10.1002/2017tc004743

Fossen, H., & Cavalcante, G. C. G. (2017). Shear zones – A review. *Earth-Science Reviews, 171*, 434–455. https://doi.org/10.1016/j.earscirev.2017.05.002

Fossen, H., Cavalcante, G. C. G., Pinheiro, R. V. L., & Archanjo, C. J. (2019). Deformation – Progressive or multiphase? *Journal of Structural Geology*. https://doi.org/10.1016/j.jsg.2018.05.006

Frimmel, H. E., Basei, M. A. S., & Gaucher, C. (2011). Neoproterozoic geodynamic evolution of SW-Gondwana: a southern African perspective. *International Journal of Earth Sciences, 100*, 323–354. https://www.doi.org/10.1007/s00531-010-0571-9

Fuhrman, M. L., & Lindsley, D. H. (1988). Ternary-feldspar modeling and thermometry. *American Mineralogist, 73*(3–4), 201–215.

Godet, A., Guilmette, C., Labrousse, L., Smit, M. A., Cutts, J. A., Davis, D. W., & Vanier, M.-A. (2021). Lu–Hf garnet dating and the timing of collisions: Palaeoproterozoic accretionary tectonics revealed in the Southeastern Churchill Province, Trans-Hudson Orogen, Canada. *Journal of Metamorphic Geology*, 1–31. https://doi.org/10.1111/jmg.12599

Gross, A. O. M. S., Droop, G. T. R., Porcher, C. C., & Fernandes, L. A. D. (2009). Petrology and thermobarometry of mafic granulites and migmatites from the Chafalote Metamorphic Suite: New insights into the Neoproterozoic P–T evolution of the Uruguayan—Sul-Rio-Grandense shield. *Precambrian Research, 170*(3–4), 157–174. https://doi.org/10.1016/j.precamres.2009.01.011

Grove, M., & Harrison, T. M. (1996). 40Ar* diffusion in Fe-rich biotite. *American Mineralogist, 81*(7–8), 940–951. https://doi.org/10.2138/am-1996-7-816

Guadagnin, F., Chemale Jr, F., Dussin, I. A., Jelinek, A. R., dos Santos, M. N., Borba, M. L., et al. (2010). Depositional age and provenance of the Itajaí Basin, Santa Catarina State, Brazil: Implications for SW Gondwana correlation. *Precambrian Research, 180*(3–4), 156–182. https://doi.org/10.1016/j.precamres.2010.04.002

Hagen-Peter, G., Cottle, J. M., Smit, M., & Cooper, A. F. (2016). Coupled garnet Lu-Hf and monazite U-Pb geochronology constrain early convergent margin dynamics in the Ross orogen, Antarctica.(Report). *Journal of Metamorphic Geology, 34*(4), 293–319. https://doi.org/10.1111/jmg.12182

Hand, M., & Sandiford, M. (1999). Intraplate deformation in central Australia, the link between subsidence and fault reactivation. *Tectonophysics, 305*(1), 121–140. https://doi.org/10.1016/S0040-1951(99)00009-8

Harrison, T. M., Célérier, J., Aikman, A. B., Hermann, J., & Heizler, M. T. (2009). Diffusion of 40Ar in muscovite. *Geochimica et Cosmochimica Acta, 73*(4), 1039–1051. https://doi.org/10.1016/j.gca.2008.09.038

Hartnady, C., Joubert, P., & Stowe, C. (1985). Proterozoic Crustal Evolution in Southwestern Africa. *International Union of Geological Sciences, 8*(4), 236–244. https://doi.org/10.18814/epiiugs/1985/v8i4/003

Heilbron, M., de Morisson Valeriano, C., Peixoto, C., Tupinambá, M., Neubauer, F., Dussin, I., et al. (2020). Neoproterozoic magmatic arc systems of the central Ribeira belt, SE-Brazil, in the context of the West-Gondwana pre-collisional history: A review. *Journal of South American Earth Sciences, 103*, 102710. https://doi.org/10.1016/j.jsames.2020.102710

Heilbron, M., & Machado, N. (2003). Timing of terrane accretion in the Neoproterozoic–Eopaleozoic Ribeira orogen (se Brazil). *Precambrian Research, 125*(1), 87–112. https://doi.org/10.1016/S0301-9268(03)00082-2

Heine, C., Zoethout, J., & Müller, R. D. (2013). Kinematics of the South Atlantic rift. *Solid Earth, 4*(2), 215–253. https://doi.org/10.5194/se-4-215-2013

Hermann, J., & Rubatto, D. (2003). Relating zircon and monazite domains to garnet growth zones: age and duration of granulite facies metamorphism in the Val Malenco lower crust. *Journal of Metamorphic Geology, 21*(9), 833–852. https://doi.org/10.1046/j.1525-1314.2003.00484.x

Höfig, D. F., Marques, J. C., Basei, M. A. S., Giusti, R. O., Kohlrausch, C., & Frantz, J. C. (2018). Detrital zircon geochronology (U-Pb LA-ICP-MS) of syn-orogenic basins in SW Gondwana: New insights into the Cryogenian-Ediacaran of Porongos Complex, Dom Feliciano Belt, southern Brazil. *Precambrian Research, 306*, 189–208. https://doi.org/10.1016/j.precamres.2017.12.031

Holland, T. J. B., & Powell, R. (2011). An improved and extended internally consistent thermodynamic dataset for phases of petrological interest, involving a new equation of state for solids. *Journal of Metamorphic Geology, 29*(3), 333–383. https://doi.org/10.1111/j.1525-1314.2010.00923.x

Hollister, L. S. (1966). Garnet Zoning: An Interpretation Based on the Rayleigh Fractionation Model. *Science, 154*(3757), 1647–1651.

Hueck, M., Basei, M. A. S., & Castro, N. A. d. (2016). Origin and evolution of the granitic intrusions in the Brusque Group of the Dom Feliciano Belt, south Brazil: Petrostructural analysis and whole-rock/isotope geochemistry. *Journal of South American Earth Sciences, 69*, 131–151. https://doi.org/10.1016/j.jsames.2016.04.004

Hueck, M., Basei, M. A. S., & Castro, N. A. d. (2019). Tracking the sources and the evolution of the late Neoproterozoic granitic intrusions in the Brusque Group, Dom Feliciano Belt, South Brazil: LA-ICP-MS and SHRIMP geochronology coupled to Hf isotopic analysis. *Precambrian Research, 338*, 105566. https://doi.org/10.1016/j.precamres.2019.105566

Hueck, M., Basei, M. A. S., Wemmer, K., Oriolo, S., Heidelbach, F., & Siegesmund, S. (2018). Evolution of the Major Gercino Shear Zone in the Dom Feliciano Belt, South Brazil, and implications for the assembly of southwestern Gondwana. *International Journal of Earth Sciences, 108*(2), 403–425. https://www.doi.org/10.1007/s00531-018-1660-4

Hueck, M., Oyhantçabal, P., Basei, M., & Siegesmund, S. (2018). The Dom Feliciano Belt in Southern Brazil and Uruquay. In S. Siegesmund, M. A. S. Basei, P. Oyhantçabal, & S. Oriolo (Eds.). R. Oberhänsli, M. J. d. Wit, & F. M. Roure (Series Eds.), *Geology of Southwest Gondwana* (1st ed., pp. 267–302). https://doi.org/10.1007/978-3-319-68920-3_11

Jamieson, R. A., & Beaumont, C. (2013). On the origin of orogens. *Geological Society of America Bulletin, 125*(11–12), 1671–1702. https://doi.org/10.1130/b30855.1

Jamieson, R. A., Unsworth, M. J., Harris, N. B. W., Rosenberg, C. L., & Schulmann, K. (2011). Crustal Melting and the Flow of Mountains. *Elements, 7*(4), 253–260. https://doi.org/10.2113/gselements.7.4.253

Jochum, K. P., Weis, U., Schwager, B., Stoll, B., Wilson, S. A., Haug, G. H., et al. (2016). Reference Values Following ISO Guidelines for Frequently Requested Rock Reference Materials. *Geostandards and Geoanalytical Research, 40*(3), 333–350. https://doi.org/10.1111/j.1751-908X.2015.00392.x

Jochum, K. P., Weis, U., Stoll, B., Kuzmin, D., Yang, Q., Raczek, I., et al. (2011). Determination of Reference Values for NIST SRM 610–617 Glasses Following ISO Guidelines. *Geostandards and Geoanalytical Research, 35*(4), 397–429. https://doi.org/10.1111/j.1751-908X.2011.00120.x

Koester, E., Porcher, C. C., Pimentel, M. M., Fernandes, L. A. D., Vignol-Lelarge, M. L., Oliveira, L. D., & Ramos, R. C. (2016). Further evidence of 777 Ma subduction-related continental arc magmatism in Eastern Dom Feliciano Belt, southern Brazil: The Chácara das Pedras Orthogneiss. *Journal of South American Earth Sciences, 68*, 155–166. https://doi.org/10.1016/j.jsames.2015.12.006

Konopásek, J., Cavalcante, C., Fossen, H., & Janoušek, V. (2020). Adamastor – an ocean that never existed? *Earth-Science Reviews, 205*, 103201. https://doi.org/10.1016/j.earscirev.2020.103201

Konopásek, J., Hoffmann, K.-H., Sláma, J., & Košler, J. (2017). The onset of flysch sedimentation in the Kaoko Belt (NW Namibia) – Implications for the pre-collisional evolution of the Kaoko–Dom Feliciano–Gariep orogen. *Precambrian Research, 298*, 220–234. http://dx.doi.org/10.1016/j.precamres.2017.06.017

Konopásek, J., Janoušek, V., Oyhantçabal, P., Sláma, J., & Ulrich, S. (2018). Did the circum-Rodinia subduction trigger the Neoproterozoic rifting along the Congo–Kalahari Craton margin? *International Journal of Earth Sciences, 107*(5), 1859–1894. https://doi.org/10.1007/s00531-017-1576-4

Konopásek, J., Sláma, J., & Košler, J. (2016). Linking the basement geology along the Africa-South America coasts in the South Atlantic. *Precambrian Research, 280*, 221–230. https://doi.org/10.1016/j.precamres.2016.05.011

Lapen, T. J., Johnson, C. M., Baumgartner, L. P., Mahlen, N. J., Beard, B. L., & Amato, J. M. (2003). Burial rates during prograde metamorphism of an ultra-high-pressure terrane: an example from Lago di Cignana, western Alps, Italy. *Earth and Planetary Science Letters, 215*(1), 57–72. https://doi.org/10.1016/S0012-821X(03)00455-2

Lara, P., Oyhantçabal, P., & Belousova, E. (2020). Two distinct crustal sources for Late Neoproterozoic granitic magmatism across the Sierra Ballena Shear Zone, Dom Feliciano Belt, Uruguay: Whole-rock geochemistry, zircon geochronology and Sr-Nd-Hf isotope evidence. *Precambrian Research, 341*, 105625. https://doi.org/10.1016/j.precamres.2020.105625

Leech, M. L., Singh, S., Jain, A. K., Klemperer, S. L., & Manickavasagam, R. M. (2005). The onset of India–Asia continental collision: Early, steep subduction required by the timing of UHP metamorphism in the western Himalaya. *Earth and Planetary Science Letters, 234*(1), 83–97. https://doi.org/10.1016/j.epsl.2005.02.038

Lenz, C., Fernandes, L. A. D., McNaughton, N. J., Porcher, C. C., & Masquelin, H. (2011). U–Pb SHRIMP ages for the Cerro Bori Orthogneisses, Dom Feliciano Belt in Uruguay: Evidences of a ~800Ma magmatic and ~650Ma metamorphic event. *Precambrian Research, 185*(3), 149–163. https://doi.org/10.1016/j.precamres.2011.01.007

Lister, G., & Forster, M. (2009). Tectonic mode switches and the nature of orogenesis. *Lithos, 113*(1), 274–291. https://doi.org/10.1016/j.lithos.2008.10.024

Lugmair, G. W., & Marti, K. (1978). Lunar initial 143Nd/144Nd: Differential evolution of the lunar crust and mantle. *Earth and Planetary Science Letters, 39*(3), 349–357. https://doi.org/10.1016/0012-821X(78)90021-3

Martil, M. M. D. (2016). *O Magmatismo De Arco Continental Pré-colisional (790 Ma) E a Reconstituição Espaço-temporal Do Regime Transpressivo (650 Ma) No Complexo Várzea Do Capivarita, Sul Da Província Mantiqueira.* (PhD thesis). Universidade Federal do Rio Grande do Sul, Available at: https://www.lume.ufrgs.br/handle/10183/149194.

Martil, M. M. D., Bitencourt, M. F., Nardi, L. V. S., Koester, E., & Pimentel, M. M. (2017). Pre-collisional, Tonian (ca. 790 Ma) continental arc magmatism in southern Mantiqueira Province, Brazil: Geochemical and isotopic constraints from the Várzea do Capivarita Complex. *Lithos, 274–275*, 39–52. https://doi.org/10.1016/j.lithos.2016.11.011

McCourt, S., Armstrong, R., Jelsma, H., & Mapeo, R. (2013). New U-Pb SHRIMP ages from the Lubango region, SW Angola: Insights into the Palaeoproterozoic evolution of the Angolan Shield, southern Congo Craton, Africa. *Geological Society London Special Publications, 170*(2), 353–363. https://doi.org/10.1144/jgs2012-059

McDonough, W. F., & Sun, S.-s. (1995). The composition of the Earth. *Chemical Geology, 120*(3), 223─253. https://doi.org/10.1016/0009-2541(94)00140-4

Meira, V. T., Garcia-Casco, A., Hyppolito, T., Juliani, C., & Schorscher, J. H. D. (2019). Tectono-Metamorphic Evolution of the Central Ribeira Belt, Brazil: A Case of Late Neoproterozoic Intracontinental Orogeny and Flow of Partially Molten Deep Crust During the Assembly of West Gondwana. *Tectonics, 38*(8), 3182–3209. https://doi.org/10.1029/2018tc004959

Oliveira, C. H. E., Chemale, F., Jelinek, A. R., Bicca, M. M., & Philipp, R. P. (2014). U–Pb and Lu–Hf isotopes applied to the evolution of the late to post-orogenic transtensional basins of the dom feliciano belt, Brazil. *Precambrian Research, 246*, 240–255. https://doi.org/10.1016/j.precamres.2014.03.008

Oriolo, S., Oyhantçabal, P., Basei, M. A. S., Wemmer, K., & Siegesmund, S. (2016). The Nico Pérez Terrane (Uruguay): From Archean crustal growth and connections with the Congo Craton to late Neoproterozoic accretion to the Río de la Plata Craton. *Precambrian Research, 280*, 147–160. https://doi.org/10.1016/j.precamres.2016.04.014

Oriolo, S., Oyhantçabal, P., Wemmer, K., Basei, M. A. S., Benowitz, J., Pfänder, J., et al. (2016). Timing of deformation in the Sarandí del Yí Shear Zone, Uruguay: Implications for the amalgamation of western Gondwana during the Neoproterozoic Brasiliano-Pan-African Orogeny. *Tectonics, 35*(3), 754–771. https://doi.org/10.1002/2015tc004052

Oriolo, S., Oyhantçabal, P., Wemmer, K., Heidelbach, F., Pfänder, J., Basei, M. A. S., et al. (2016). Shear zone evolution and timing of deformation in the Neoproterozoic transpressional Dom Feliciano Belt, Uruguay. *Journal of Structural Geology, 92*, 59-78. 10.1016/j.jsg.2016.09.010

Oyhantçabal, P., Oriolo, S., Philipp, R. P., Wemmer, K., & Siegesmund, S. (2018). The Nico Pérez Terrane of Uruguay and Southeastern Brazil. In S. Siegesmund, M. A. S. Basei, P. Oyhantçabal, & S. Oriolo (Eds.), *Geology of Southwest Gondwana* (pp. 161-188). Cham: Springer International Publishing.

Oyhantçabal, P., Oriolo, S., Wemmer, K., Basei, M. A. S., Frei, D., & Siegesmund, S. (2021). Provenance of metasedimentary rocks of the western Dom Feliciano Belt in Uruguay: Insights from U–Pb detrital zircon geochronology, Hf and Nd model ages, and geochemical data. *Journal of South American Earth Sciences, 108*, 103139. https://doi.org/10.1016/j.jsames.2020.103139

Oyhantçabal, P., Siegesmund, S., & Wemmer, K. (2011). The Río de la Plata Craton: a review of units, boundaries, ages and isotopic signature. *International Journal of Earth Sciences, 100*(2), 201─220. https://doi.org/10.1007/s00531-010-0580-8

Oyhantçabal, P., Siegesmund, S., Wemmer, K., Frei, R., & Layer, P. (2007). Post-collisional transition from calc-alkaline to alkaline magmatism during transcurrent deformation in the southernmost Dom Feliciano Belt (Braziliano–Pan-African, Uruguay). *Lithos, 98*(1–4), 141─159. https://doi.org/10.1016/j.lithos.2007.03.001

Oyhantçabal, P., Siegesmund, S., Wemmer, K., & Passchier, C. W. (2011). The transpressional connection between Dom Feliciano and Kaoko Belts at 580–550 Ma. *International Journal of Earth Sciences, 100*, 379─390. https://doi.org/10.1007/s00531-010-0577-3

Oyhantçabal, P., Siegesmund, S., Wemmer, K., Presnyakov, S., & Layer, P. (2009). Geochronological constraints on the evolution of the southern Dom Feliciano Belt (Uruguay). *Journal of the Geological Society, 166*(6), 1075─1084. https://doi.org/10.1144/0016-76492008-122

Passarelli, C. R., Basei, M. A. S., Siga, O., Reath, I. M., & Campos Neto, M. d. C. (2010). Deformation and geochronology of syntectonic granitoids emplaced in the Major Gercino Shear Zone, southeastern South America. *Gondwana Research, 17*(4), 688─703. https://doi.org/10.1016/j.gr.2009.09.013

Passchier, C. W., & Trouw, R. A. J. (2005). *Microtectonics*(2nd ed.). https://doi.org/10.1007/3-540-29359-0

Pedrosa-Soares, A. C., Noce, C. M., Wiedemann, C. M., & Pinto, C. P. (2001). The Araçuaí-West-Congo Orogen in Brazil: an overview of a confined orogen formed during Gondwanaland assembly. *Precambrian Research, 110*(1), 307─323. https://doi.org/10.1016/S0301-9268(01)00174-7

Percival, J. J., Konopásek, J., Eiesland, R., Sláma, J., de Campos, R. S., Battisti, M. A., & Bitencourt, M. d. F. (2021). Pre-orogenic connection of the foreland domains of the Kaoko–Dom Feliciano–Gariep orogenic system. *Precambrian Research, 354*, 106060. https://doi.org/10.1016/j.precamres.2020.106060

Pertille, J., Hartmann, L. A., Santos, J. O. S., McNaughton, N. J., & Armstrong, R. (2017). Reconstructing the Cryogenian–Ediacaran evolution of the Porongos fold and thrust belt, Southern Brasiliano Orogen, based on Zircon U–Pb–Hf–O isotopes. *International Geology Review, 59*(12), 1532─1560. https://doi.org/10.1080/00206814.2017.1285257

Peternell, M., Bitencourt, M. d. F., Kruhl, J. H., & Stäb, C. (2010). Macro and microstructures as indicators of the development of syntectonic granitoids and host rocks in the Camboriú region, Santa Catarina, Brazil. *Journal of South American Earth Sciences, 29*(3), 738─750. https://doi.org/10.1016/j.jsames.2009.11.006

Philipp, R. P., & Machado, R. (2005). The Late Neoproterozoic granitoid magmatism of the Pelotas Batholith, southern Brazil. *Journal of South American Earth Sciences, 19*(4), 461─478. https://doi.org/10.1016/j.jsames.2005.06.010

Philipp, R. P., Mallmann, G., Bitencourt, M. F., Souza, E. R., Liz, J. D., Wild, F., et al. (2004). Caracterização Litológica e Evolução Metamórfica da Porção Leste do Complexo Metamórfico Brusque, Santa Catarina. *Revista Brasileira de Geociências, 34*, 21─34. https://doi.org/10.25249/0375-7536.20043412134

Philipp, R. P., Massonne, H.-J., & Campos, R. S. (2013). Peraluminous leucogranites of the Cordilheira Suite: A record of Neoproterozoic collision and the generation of the Pelotas Batholith, Dom Feliciano Belt, Southern Brazil. *Journal of South American Earth Sciences, 43*, 8─24. https://doi.org/10.1016/j.jsames.2012.10.006

Philipp, R. P., Pimentel, M. M., & Basei, M. A. S. (2018). The Tectonic Evolution of the São Gabriel Terrane, Dom Feliciano Belt, Southern Brazil: The Closure of the Charrua Ocean. In S. Siegesmund, M. A. S. Basei, P. Oyhantçabal, & S. Oriolo (Eds.), *Geology of Southwest Gondwana* (pp. 243─265). https://doi.org/10.1007/978-3-319-68920-3_10

Pollington, A. D., & Baxter, E. F. (2010). High resolution Sm–Nd garnet geochronology reveals the uneven pace of tectonometamorphic processes. *Earth and Planetary Science Letters, 293*(1), 63─71. https://doi.org/10.1016/j.epsl.2010.02.019

Porada, H. (1979). The Damara-Ribeira orogen of the Pan-African─Brasiliano cycle in Namibia (Southwest Africa) and Brazil as interpreted in terms of continental collision. *Tectonophysics, 57*(2), 237─265. https://doi.org/10.1016/0040-1951(79)90150-1

Porada, H. (1989). Pan-African rifting and orogenesis in southern to equatorial Africa and eastern Brazil. *Precambrian Research, 44*(2), 103─136. https://doi.org/10.1016/0301-9268(89)90078-8

Raimondo, T., Hand, M., & Collins, W. J. (2014). Compressional intracontinental orogens: Ancient and modern perspectives. *Earth-Science Reviews, 130*, 128─153. https://doi.org/10.1016/j.earscirev.2013.11.009

Rubatto, D., Hermann, J., & Buick, I. S. (2006). Temperature and Bulk Composition Control on the Growth of Monazite and Zircon During Low-pressure Anatexis (Mount Stafford, Central Australia). *Journal of Petrology, 47*(10), 1973─1996. https://doi.org/10.1093/petrology/egl033

Saalmann, K., Gerdes, A., Lahaye, Y., Hartmann, L., Remus, M., & Läufer, A. (2011). Multiple accretion at the eastern margin of the Rio de la Plata craton: the prolonged Brasiliano orogeny in southernmost Brazil. *International Journal of Earth Sciences, 100*, 355─378. https://doi.org/10.1007/s00531-010-0564-8

Scherer, E. E., Cameron, K. L., & Blichert-Toft, J. (2000). Lu–Hf garnet geochronology: closure temperature relative to the Sm–Nd system and the effects of trace mineral inclusions. *Geochimica et Cosmochimica Acta, 64*(19), 3413–3432. https://doi.org/10.1016/S0016-7037(00)00440-3

Scherer, E. E., Munker, C., & Mezger, K. (2001). Calibration of the Lutetium-Hafnium clock. *Science, 293*(5530), 683-687. https://10.1126/science.1061372

Schmidt, A., Pourteau, A., Candan, O., & Oberhänsli, R. (2015). Lu–Hf geochronology on cm-sized garnets using microsampling: New constraints on garnet growth rates and duration of metamorphism during continental collision (Menderes Massif, Turkey). *Earth and Planetary Science Letters, 432*, 24–35. https://doi.org/10.1016/j.epsl.2015.09.015

Silva, L. C., Hartmann, L. A., McNaughton, N. J., & Fletcher, I. (2000). Zircon U-Pb SHRIMP dating of a Neoproterozoic overprint in Paleoproterozoic granitic-gneissic terranes, southern Brazil. *American Mineralogist, 85*(5–6), 649–667. https://doi.org/10.2138/am-2000-5-602

Smit, M. A., Hacker, B. R., & Lee, J. (2014). Tibetan garnet records early Eocene initiation of thickening in the Himalaya. *Geology, 42*(7), 591–594. https://doi.org/10.1130/g35524.1

Stipp, M., Stünitz, H., Heilbronner, R., & Schmid, S. M. (2002). The eastern Tonale fault zone: a 'natural laboratory' for crystal plastic deformation of quartz over a temperature range from 250 to 700°C. *Journal of Structural Geology, 24*(12), 1861–1884. https://doi.org/10.1016/S0191-8141(02)00035-4

Tedeschi, M., Novo, T., Pedrosa-Soares, A., Dussin, I., Tassinari, C., Silva, L. C., et al. (2016). The Ediacaran Rio Doce magmatic arc revisited (Araçuaí-Ribeira orogenic system, SE Brazil). *Journal of South American Earth Sciences, 68*, 167–186. https://doi.org/10.1016/j.jsames.2015.11.011

Thompson, A. B., Schulmann, K., Jezek, J., & Tolar, V. (2001). Thermally softened continental extensional zones (arcs and rifts) as precursors to thickened orogenic belts. *Tectonophysics, 332*(1–2), 115–141. https://doi.org/10.1016/S0040-1951(00)00252-3

Vance, D., & Keith O'Nions, R. (1992). Prograde and retrograde thermal histories from the central Swiss Alps. *Earth and Planetary Science Letters, 114*(1), 113–129. https://doi.org/10.1016/0012-821X(92)90155-O

Vanderhaeghe, O. (2009). Migmatites, granites and orogeny: Flow modes of partially-molten rocks and magmas associated with melt/solid segregation in orogenic belts. *Tectonophysics, 477*(3), 119–134. https://doi.org/10.1016/j.tecto.2009.06.021

Vanderhaeghe, O., & Teyssier, C. (2001). Partial melting and flow of orogens. *Tectonophysics, 342*(3), 451–472. https://doi.org/10.1016/S0040-1951(01)00175-5

Vollmer, F. W. (1990). An application of eigenvalue methods to structural domain analysis. *Geological Society of America Bulletin, 102*(6), 786–791. https://doi.org/10.1130/0016-7606(1990)102<0786:AAOEMT>2.3.CO;2

Vollmer, F. W. (1995). C program for automatic contouring of spherical orientation data using a modified Kamb method. *Computers & Geosciences, 21*(1), 31–49. https://doi.org/10.1016/0098-3004(94)00058-3

Warren, C. J., Greenwood, L. V., Argles, T. W., Roberts, N. M. W., Parrish, R. R., & Harris, N. B. W. (2018). Garnet-monazite rare earth element relationships in sub-solidus Metapelites: A case study from Bhutan. *Geological Society Special Publication, 478*(1), 145–166. https://doi.org/10.1144/SP478.1

White, R. W., Powell, R., & Clarke, G. L. (2002). The interpretation of reaction textures in Fe-rich metapelitic granulites of the Musgrave Block, central Australia: constraints from mineral equilibria calculations in the system K2O–FeO–MgO–Al2O3–SiO2–H2O–TiO2–Fe2O3. *Journal of Metamorphic Geology, 20*(1), 41–55. https://doi.org/10.1046/j.0263-4929.2001.00349.x

White, R. W., Powell, R., Holland, T. J. B., Johnson, T. E., & Green, E. C. R. (2014). New mineral activity–composition relations for thermodynamic calculations in metapelitic systems. *Journal of Metamorphic Geology, 32*(3), 261–286. https://doi.org/10.1111/jmg.12071

White, R. W., Powell, R., Holland, T. J. B., & Worley, B. A. (2000). The effect of TiO2 and Fe2O3 on metapelitic assemblages at greenschist and amphibolite facies conditions: mineral equilibria calculations in the system K2O–FeO–MgO–Al2O3–SiO2–H2O–TiO2–Fe2O3. *Journal of Metamorphic Geology, 18*(5), 497–511. https://doi.org/10.1046/j.1525-1314.2000.00269.x

Whitney, D., & Evans, B. (2010). Abbreviations for Names of Rock-Forming Minerals. *American Mineralogist, 95*, 185–187. https://doi.org/10.2138/am.2010.3371

Will, T. M., Gaucher, C., Ling, X. X., Li, X. H., Li, Q. L., & Frimmel, H. E. (2019). Neoproterozoic magmatic and metamorphic events in the Cuchilla Dionisio Terrane, Uruguay, and possible correlations across the South Atlantic. *Precambrian Research, 320*, 303–322. https://doi.org/10.1016/j.precamres.2018.11.004

Winter, J. D. (2014). *Principles of igneous and metamorphic petrology* (2nd ed.). Harlow: Pearson Education.

Zwart, H. J. (1962). On the determination of polymetamorphic mineral associations, and its application to the Bosost Area (Central Pyrenees). *International Journal of Earth Sciences, 52*(1), 38–65. https://doi.org/10.1007/BF01840064

Figure captions

Figure 1. (a) Schematic reconstruction of the African and South American continental blocks before the opening of the South Atlantic Ocean (modified from Konopásek et al., 2020), with location of the SANOS highlighted in orange. Am. = Amazonia; WA = West Africa; Sa. = Sahara; S = São Francisco; P = Paranapanema; R = Rio de la Plata; Ka. = Kalahari. (b) Simplified geological map of the southern SANOS (based on Bitencourt & Nardi, 2000; De Toni et al., 2021; Konopásek et al., 2017; McCourt et al., 2013; Oyhantçabal, Siegesmund, & Wemmer, 2011), showing the position of the African and South American continents at the onset of the opening of the South Atlantic Ocean (after Heine et al., 2013). LA = Luis Alves Craton; NP = Nico Pérez Terrane; RDLP = Rio de la Plata Craton; SBSB = Southern Brazilian Shear Belt; DFB = Dom Feliciano Belt. (c) Simplified geology of the northern DFB (based on field mapping and collated from Basei et al., 2011; Campos et al., 2011; De Toni, Bitencourt, Nardi, et al., 2020; Florisbal, Janasi, Bitencourt, & Heaman, 2012; Hueck, Basei, et al., 2018). IPSZ = Itajaí–Perimbó Shear Zone; MGSZ = Major Gercino Shear Zone.

Figure 2. (a) Simplified geology of the Brusque Complex (see Fig. 1c for references) showing primary foliation trendlines, orientation measurements, and results of structural domain analysis. (b) Equal-area, lower-hemisphere projections showing contoured poles-to-plane data for the three deformation fabrics identified in the field (S_1, S_2, and S_3), and associated fold axes (F_2 and F_3, red squares), excluding regions 1 to 3. (c) Contoured L_1 and L_2 stretching lineations (across all regions). (d) Contoured poles-to-plane data for S_1 and S_2 in Region 1. (e) Contoured poles-to-plane data for S_1 and S_2 in Region 2. (f) Contoured poles-to-plane data for S_2 in Region 3 – note the dominant group of poles striking ~040, and two subordinate clusters defining a second group of foliations striking ~100. Dotted grey lines and grey dots in S_1 stereonets show best-fit great circles and constructed fold axes, respectively. Contouring of poles-to-plane and lineation data calculated by modified Kamb method at 5 equally spaced density levels (Vollmer, 1995).

Figure 3. Outcrop photographs and interpretative sketches detailing the primary deformation structures in the Brusque Complex. (a) Garnet-mica schist (S 26.94385, W 48.71592) showing the primary metamorphic foliation (S_1) and sigma-shaped stretched quartz veins indicating top-to-WNW shear

sense. (b) Garnet-mica schist (S 27.19278, W 49.04884) showing intrafolial folding (F_1) within S_1 foliation, and overprinting F_2 folds and axial plane-parallel S_2 cleavage. (c) Retrograde garnet-mica schist (S 27.19229, W 49.04803) showing transposition foliation (S_2) with transposed S_1 quartz veins and F_2 fold hinges. (d) Chlorite-mica phyllite (S 27.20600, W 49.15432) deformed by low-strain F_3 conjugate crenulations (S_3 cleavage).

Figure 4. Photomicrographs and sketches detailing metamorphic textures and deformation microstructures in the Brusque Complex and adjacent units (sections with stereonets are cut along in the XZ plane, parallel to lineation and perpendicular to foliation). (a) Garnet-mica schist from the medium-grade, low-strain Brusque Complex (sample BC43) showing a rotated garnet porphyroblast with oriented mineral inclusions (S_i) and quartz-rich pressure shadows indicating top-to-NW shear sense. (b) Garnet-mica schist from the medium-grade Brusque Complex (sample BB11) showing a large retrograde chlorite porphyroblast overgrowing S_1 and elongated parallel to S_2 (note also that the F_2 crenulation is less well-developed within the chlorite suggesting growth during the early stages of S_2 development). (c) Chlorite-mica phyllite from the low-grade, high-strain Brusque Complex (sample BC30) showing sigma-shaped quartz aggregates and shear bands indicating dextral strike-slip shear sense. (d) Mylonitic granite from the Itajaí–Perimbó Shear Zone (sample JBD09) showing stretched quartz sigma-type porphyroclasts indicating mixed dextral strike-slip and top-to-NW thrusting shear sense, and showing evidence of bulging and sub-grain rotation dynamic recrystallisation.

Figure 5. Garnet photomicrographs and SEM image, interpretative sketches, and compositional transects for samples (a) BC43, (b) BB11, (c) BA23, and (d) BA22. Red lines and dots on photomicrographs and sketches show approximate locations of compositional transects.

Figure 6. Pressure–temperature pseudosections calculated for: garnet–mica schist sample BC43 using (a) measured bulk composition and (b) estimated bulk composition after garnet fractionation calculations; garnet–mica schist sample BB11 using (c) measured bulk composition and (d) estimated bulk composition after garnet fractionation calculations. Higher variance fields are shown by darker

shading. Contoured isopleths show observed compositional values with ± 0.01 error. Fields containing the observed mineral assemblages are highlighted in bold and italics.

Figure 7. Pressure–temperature pseudosections calculated for: sample BA23 (garnet–mica schist) using (a) measured bulk composition and (b) estimated bulk composition after garnet fractionation calculations; (c) sample BA22 (felsic metavolcanic rock) using measured bulk composition. Contoured isopleths for sample BA23 show the observed compositional values with ± 0.01 error, and for sample BA22 the entire range of garnet modal compositions are shown.

Figure 8. Results of Lu–Hf and Sm–Nd dating, and trace element analysis. (a–d) Lu–Hf isochron plots (open circle in (b) represents the rejected aliquot for BB11 that was not considered in the isochron). (e) Sm–Nd isochron plot for sample BC43. (f–i) Element distribution profiles of Hf, Lu, Y, Ti and U, measured across representative garnet grains. (j) Element distribution profile of Sm, Nd, U and P, measured across the same grain from sample BC43.

Figure 9. Results of trace element analysis and U–Pb dating (data-point error ellipses are 2σ) of monazite from sample BC43. (a–b) Monazite BSE images and yttrium compositional maps for representative grains from the two age groups. (c) Chondrite-normalised monazite REE plot (after McDonough & Sun, 1995). (d) Concordia diagram showing all monazite U–Pb data. (e) Detail of ca. 640 Ma analyses (ignoring discordant data) and concordia age. (f) Detail of ca. 580 Ma analyses and concordia age.

Figure 10. Mica $^{40}Ar/^{39}Ar$ spectra. (a) Biotite from sample BC43 from the medium-grade Brusque Complex. (b) Muscovite from sample JBD14 from a high-strain zone (S_2) within the low-grade Brusque Complex. (c) Muscovite from sample BC30 from a high-strain zone (S_2) within the low-grade Brusque Complex. (d) Muscovite from sample JBD09 from a mylonitic granite within the Itajaí–Perimbó Shear Zone.

Figure 11. (a) Distribution of Y and Lu across a representative garnet grain from sample BC43, with zoning defining a core, mantle 1 (M1), mantle 2 (M2), and rim. (b) Chondrite-normalised REE plot showing variation from core to rim in the same garnet grain (reference values from McDonough and

Sun, 1995). (c–f) Apparent garnet/monazite REE distribution coefficients for garnet cores, M1, M2, and rims, compared with known published data (Hermann & Rubatto, 2003; Rubatto et al., 2006; Warren et al., 2018). The apparent partition coefficients were calculated using individual monazite REE analyses against averages of each garnet zone.

Figure 12. (a) Summary of P–T–t data. Estimated P–T paths (dashed lines and arrows) show a clockwise evolution. Open and filled rectangles show P–T estimates using measured and fractionated bulk rock compositions, respectively. Depth is calculated using an average crustal density of 2.8 g/cm^3. 1A = increasing P–T during early crustal thickening and prograde garnet growth between ca. 660–650 Ma; 1B = increasing thermal gradient during progressive thrusting at ca. 650 Ma; 1C = further heating and decompressive melting in the basement (CC – Camboriú Complex) after the end of thrusting (De Toni, Bitencourt, Konopásek, et al., 2020); 2 = cooling of Brusque Complex between ca. 635–615 Ma; 3 = granite intrusion into the Brusque Complex and contact metamorphism by at least ca. 600 Ma. (b) Detail of P–T estimates showing increasing apparent thermal gradients in the foreland from ca. 660 to 600 Ma related to intrusion of granitoids from ca. 630 Ma.

Figure 13. Schematic diagram outlining the proposed tectonic evolution of the northern Dom Feliciano Belt. (a) Between ca. 660–635 Ma: early crustal thickening and thrusting of the hinterland over Tonian volcanosedimentary supracrustal rocks (Brusque Complex) and the Luis Alves Craton (stippled lines show future shear zones, stippled polygons show early migmatisation). (b) From ca. 635 Ma: partitioned transpression resulting in simple shear-dominated strike-slip deformation in the hinterland and pure shear-dominated deformation in the foreland; intrusion of the Granite Belt (from ca. 625 Ma) and foreland granites (from ca. 615 Ma). White frame shows location of cross section in Fig. 13c. (c) From ca. 550 Ma: final configuration of the northern Dom Feliciano belt.

Table 1. Representative garnet, biotite, muscovite, plagioclase, and chlorite compositions.

Sample	BC43						BB11							BA23				BA22				
	Grt		Bt	Msc	Pl	Chl	Grt		Bt	Msc	Pl	Chl		Grt		Bt	Msc	Grt		Bt	Msc	Pl
	core	rim					core	rim				early	late	core	rim			core	rim			
wt %																						
SiO_2	36.53	36.71	36.06	46.97	66.39	25.33	37.62	37.75	36.03	46.79	68.06	25.00	25.18	36.93	37.29	38.88	45.61	36.41	36.58	34.37	46.14	66.90
TiO_2	0.06	0.09	1.49	0.26	0.00	0.10	0.08	0.07	1.55	0.34	0.00	0.11	0.09	0.04	0.05	0.32	0.06	0.00	0.00	0.04	0.59	0.01
Cr_2O_3	0.02	0.00	0.04	0.04	0.00	0.04	0.01	0.01	0.02	0.01	0.00	0.00	0.03	0.00	0.03	0.01	0.00	0.00	0.00	0.00	0.00	0.00
Al_2O_3	20.41	20.51	18.91	35.50	21.96	22.58	20.44	20.44	18.17	35.91	20.57	22.39	22.44	20.13	20.33	20.09	31.78	20.55	20.93	14.67	30.57	21.05
Fe_2O_3	1.12	1.13	0.00	0.00	0.00	0.00	0.67	0.66	0.00	0.00	0.00	0.00	0.00	0.60	0.30	0.00	4.85	0.58	0.40	0.00	3.56	0.04
FeO	31.53	35.76	20.88	1.13	0.02	27.16	26.89	33.41	22.66	1.14	0.06	28.30	27.93	9.01	10.82	9.33	0.41	21.81	23.67	24.13	2.01	0.00
MnO	5.15	0.51	0.05	0.00	0.00	0.03	6.65	1.01	0.05	0.00	0.00	0.08	0.06	29.65	26.80	0.77	0.04	19.91	17.84	0.26	0.09	0.03
MgO	1.08	2.30	9.21	0.50	0.00	13.46	0.76	1.48	7.88	0.54	0.00	12.92	12.99	1.48	2.52	15.45	1.04	0.12	0.12	5.24	0.70	0.00
CaO	3.55	2.78	0.04	0.00	2.68	0.04	7.67	6.25	0.03	0.04	1.33	0.03	0.02	1.97	1.70	0.30	0.03	0.95	1.30	0.83	0.00	2.07
Na_2O	0.11	0.01	0.16	1.95	10.36	0.00	0.05	0.03	0.18	1.68	10.95	0.01	0.00	0.00	0.00	0.21	0.57	0.03	0.03	0.25	0.25	10.73
K_2O	0.01	0.00	8.41	8.29	0.07	0.03	0.01	0.00	8.45	9.11	0.08	0.00	0.01	0.00	0.00	6.18	10.48	0.00	0.00	3.61	11.03	0.05
Total	99.56	99.80	95.25	94.65	101.48	88.78	100.85	101.12	95.02	95.54	101.04	88.83	88.75	99.81	99.83	91.53	94.87	100.37	100.87	83.39	94.94	100.87
Si	2.99	2.98	2.83	3.13	2.88	2.67	3.01	3.02	2.87	3.09	2.96	2.65	2.66	3.01	3.02	3.02	3.09	2.99	2.98	3.20	3.15	2.91
Ti	0.00	0.01	0.09	0.01	0.00	0.01	0.00	0.00	0.09	0.02	0.00	0.01	0.01	0.00	0.00	0.02	0.00	0.00	0.00	0.00	0.03	0.00
Cr	0.00	0.00	0.00	0.00	0.00	0.00	0.00	0.00	0.00	0.00	0.00	0.00	0.00	0.00	0.00	0.00	0.00	0.00	0.00	0.00	0.00	0.00
Al	1.97	1.96	1.75	2.79	1.12	2.80	1.93	1.92	1.70	2.79	1.05	2.79	2.80	1.93	1.94	1.84	2.54	1.99	2.01	1.61	2.46	1.08
Fe^{3+}	0.07	0.07	0.00	0.00	0.00	0.00	0.04	0.04	0.00	0.00	0.00	0.00	0.00	0.04	0.02	0.00	0.25	0.04	0.02	0.00	0.18	0.00
Fe^{2+}	2.16	2.43	1.37	0.06	0.00	2.39	1.80	2.23	1.51	0.06	0.00	2.50	2.47	0.61	0.73	0.61	0.02	1.50	1.61	1.88	0.11	0.00
Mn	0.36	0.04	0.00	0.00	0.00	0.00	0.45	0.07	0.00	0.00	0.00	0.01	0.01	2.05	1.84	0.05	0.00	1.38	1.23	0.02	0.01	0.00
Mg	0.13	0.00	1.08	0.05	0.00	2.11	0.09	0.18	0.93	0.05	0.00	2.04	2.05	0.18	0.30	1.79	0.11	0.01	0.01	0.73	0.07	0.00
Ca	0.31	0.28	0.00	0.00	0.12	0.00	0.66	0.54	0.00	0.00	0.06	0.00	0.00	0.17	0.15	0.02	0.00	0.08	0.11	0.08	0.00	0.10
Na	0.02	0.24	0.02	0.25	0.87	0.00	0.01	0.00	0.03	0.22	0.92	0.00	0.00	0.00	0.00	0.03	0.08	0.00	0.00	0.05	0.03	0.91
K	0.00	0.00	0.84	0.70	0.00	0.00	0.00	0.00	0.86	0.77	0.00	0.00	0.00	0.00	0.00	0.61	0.91	0.00	0.00	0.43	0.96	0.00
X_{Sps}	0.12	0.01					0.15	0.02						0.67	0.60			0.46	0.41			
X_{Alm}	0.73	0.81					0.60	0.74						0.20	0.24			0.50	0.55			
X_{Prp}	0.04	0.09					0.03	0.06						0.06	0.10			0.00	0.00			
X_{Grs}	0.11	0.08					0.22	0.18						0.06	0.05			0.03	0.04			
X_{Mg}	0.06	0.10	0.44			0.47	0.05	0.07	0.38			0.45	0.45	0.22	0.29	0.75		0.01	0.01	0.28		
X_{An}					0.12						0.06											0.10

Table 2. Summary of estimated P–T conditions and comparison of observed vs. modelled mineral compositional parameters

	P–T estimates						Mineral modal compositions							
	T (°C)			P (kbar)				X_{Sps}	X_{Alm}	X_{Prp}	X_{Grs}	Grt X_{Mg}	Bt X_{Mg}	Chl X_{Mg}	X_{An}
	min	max	mean	min	max	mean									
BC43 core	540	550	***545***	5.1	6.2	***5.7***	obs.*	0.12	0.73	0.04	0.11	0.06	–	–	–
							mod.†	0.13	0.71	0.06	0.10	0.08	–	–	–
							diff.	*-0.01*	*0.02*	*-0.02*	*0.01*	*-0.02*	–	–	–
BC43 rim	560	570	***565***	5.5	6.5	***6.0***	obs.*	0.01	0.81	0.09	0.08	0.10	0.43	0.47	0.12
							mod.†	0.03	0.81	0.09	0.08	0.10	0.32	0.43	0.31
							diff.	*-0.02*	*0.00*	*0.00*	*0.00*	*0.00*	*0.11*	*0.04*	*-0.19*
BB11 core	510	520	***515***	5.5	6.0	***5.8***	obs.*	0.15	0.60	0.03	0.22	0.05	–	–	–
							mod.†	0.14	0.60	0.04	0.22	0.06	–	–	–
							diff.	*0.01*	*0.00*	*-0.01*	*0.00*	*-0.01*	–	–	–
BB11 rim	540	550	***545***	6.4	6.7	***6.6***	obs.*	0.02	0.74	0.06	0.18	0.07	0.40	0.43	0.07
							mod.†	0.02	0.76	0.06	0.17	0.07	0.25	0.38	0.38
							diff.	*0.00*	*-0.02*	*0.00*	*0.01*	*0.00*	*0.15*	*0.05*	*-0.31*
BA23 core (low-P range)	490	500	***495***	3.0	4.5	***3.8***	obs.*	0.67	0.21	0.06	0.06	0.22	–	–	–
							mod.†	0.69	0.20	0.03	0.05	0.22	–	–	–
							diff.	*-0.02*	*0.01*	*0.03*	*0.01*	*0.00*	–	–	–
BA23 rim	535	555	***545***	4.2	6.0	***5.1***	obs.*	0.60	0.24	0.10	0.05	0.29	0.74	–	–
							mod.†	0.59	0.27	0.10	0.01	0.31	0.72	–	–
							diff.	*0.01*	*-0.03*	*0.00*	*0.04*	*-0.02*	*0.02*	–	–
BA22	510	520	***515***	2.3	3.3	***2.8***	obs.*	0.43	0.53	0.00	0.04	0.01	0.29	–	0.10
							mod.†	0.40	0.52	0.04	0.03	0.08	0.25	–	0.19
							diff.	*0.03*	*0.01*	*-0.04*	*0.01*	*-0.07*	*0.04*	–	*-0.09*

* Representative compositional values of analysed garnet (based on the rims and cores from transects across multiple grains), or the median value from multiple spot analyses (for biotite, chlorite and plagioclase)

† Modelled mineral compositions at mean *P–T* conditions

Table 3. Summary of Lu–Hf and Sm–Nd dating results.

Sample	Fraction	Weight (mg)	Lu (ppm)	Hf (ppm)	$^{176}Lu/^{177}Hf$	$^{176}Hf/^{177}Hf$	Age (Ma)
BC43	Grt1	54.82	4.888	4.546	0.1521	0.283967 ± 3	652.5 ± 3.6
	Grt2	59.41	4.541	4.323	0.1486	0.283924 ± 3	
	Grt3	58.81	4.708	4.125	0.1614	0.284077 ± 3	
	WR	100.79	0.480	5.592	0.0121	0.282250 ± 4	
BB11	Grt1	41.65	5.249	0.211	3.5393	0.325075 ± 17	658 ± 38
	Grt2	51.64	5.260	0.183	4.1126	0.333191 ± 17	(660.9 ± 2.3)*
	Grt3	52.83	6.642	0.213	4.4470	0.337321 ± 11	
	WR	99.56	0.531	3.452	0.0218	0.282465 ± 3	
BA23	Grt1	55.32	2.564	1.703	0.2130	0.284549 ± 4	649 ± 16
	Grt2	56.30	2.252	1.522	0.2093	0.284480 ± 3	
	Grt3	58.42	2.768	1.660	0.2359	0.284804 ± 4	
	WR	100.12	0.186	1.675	0.0157	0.282127 ± 4	
BA22	Grt1	71.08	10.912	1.178	1.3134	0.296635 ± 4	596.9 ± 1.7
	Grt2	70.87	10.629	1.246	1.2094	0.295529 ± 4	
	Grt3	76.35	10.567	1.098	1.3653	0.297305 ± 3	
	WR	100.98	0.034	3.628	0.0013	0.281980 ± 4	
Sample	Fraction	Weight (mg)	Sm (ppm)	Nd (ppm)	$^{147}Sm/^{144}Nd$	$^{143}Nd/^{144}Nd$	Age (Ma)
BC43	Grt1	54.82	2.291	1.177	1.1778	0.516243 ± 10	647 ± 10
	Grt2	59.41	2.262	0.949	1.4422	0.517368 ± 15	
	Grt3	58.81	2.314	1.008	1.3901	0.517177 ± 13	
	WR	100.79	8.414	39.145	0.1299	0.511816 ± 04	

All errors are 2 SE (standard errors) and relate to the last significant digits. 176Lu/177Hf errors are 0.5% and $^{147}Sm/^{144}Nd$ errors are 0.3%. JMC475 yielded $^{176}Hf/^{177}Hf$ = 0.282163 ± 6 (n = 8) and JNd-1 gave $^{143}Nd/^{144}Nd$ = 0.512090 ± 10 (n = 6) over the period of analyses. Mass bias corrections conducted using $^{179}Hf/^{177}Hf$ = 0.7325 and $^{146}Nd/^{144}Nd$ = 0.7129. Decay constants used for age calculations: $\lambda_{176Lu} = 1.865 \times 10^{-11}$ yr^{-1} (Scherer et al., 2001) and $\lambda_{147Sm} = 6.02 \times 10^{-12}$ $year^{-1}$ (Lugmair & Marti, 1978). Age uncertainties are 2σ.

* Age calculated with three-point isochron excluding Grt1.

Figures

Figure 1.

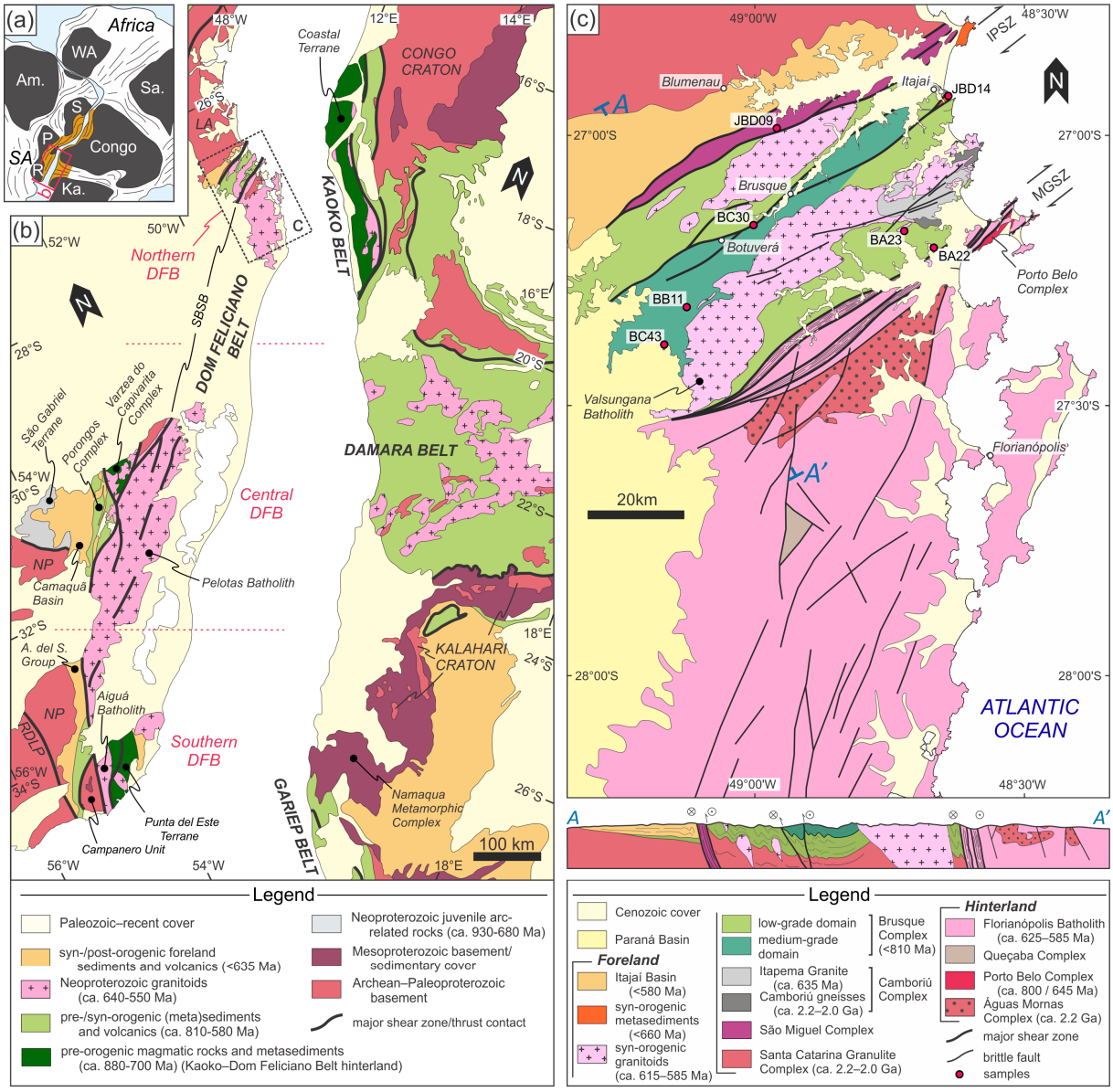

Figure 2.

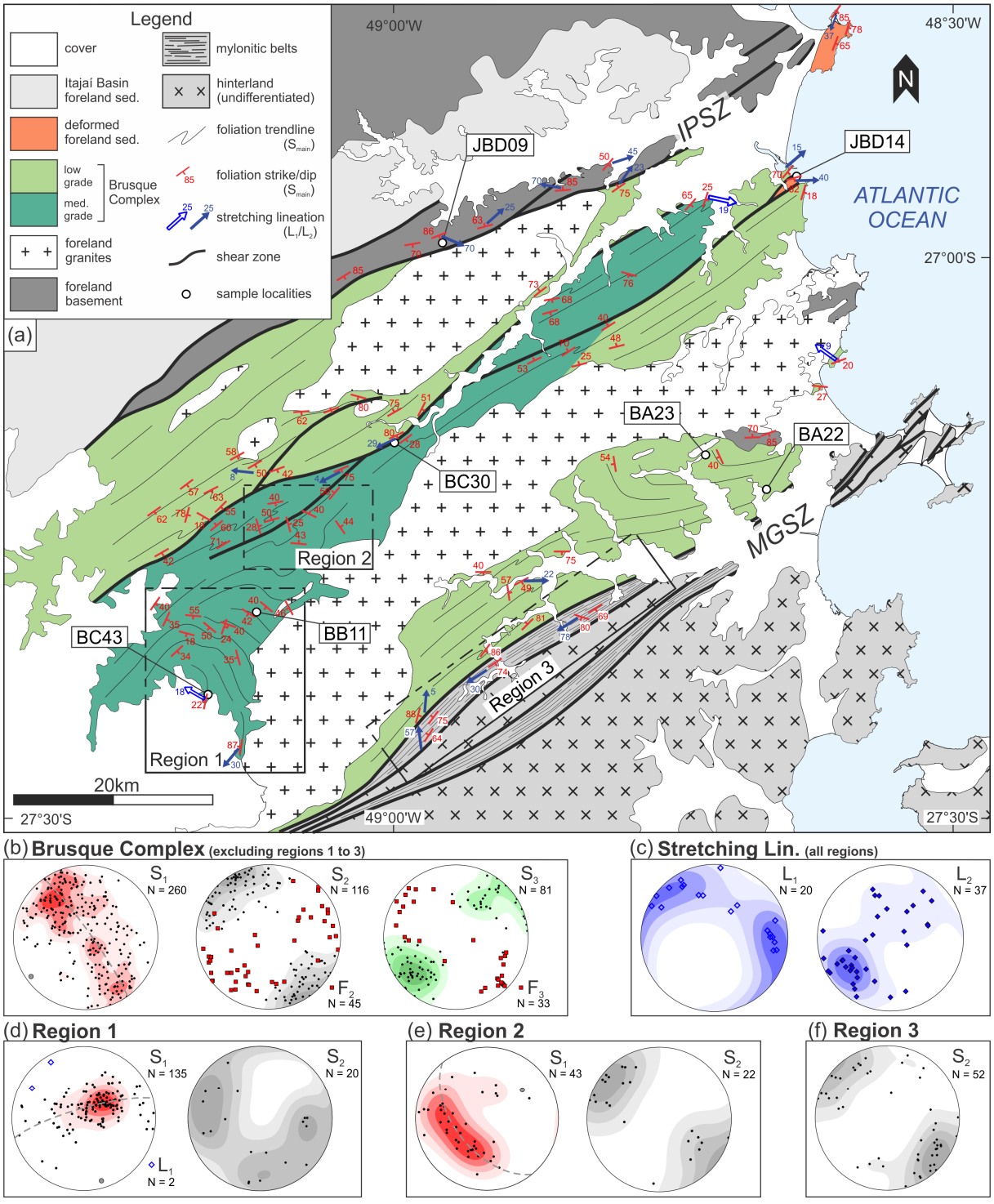
Legend
cover
Itajaí Basin foreland sed.
deformed foreland sed.
low grade
med. grade
Brusque Complex
foreland granites
foreland basement
mylonitic belts
hinterland (undifferentiated)
foliation trendline (S_main)
foliation strike/dip (S_main)
stretching lineation (L1/L2)
shear zone
sample localities
(a)
49°00'W
48°30'W
27°00'S
27°30'S
N
IPSZ
MGSZ
ATLANTIC OCEAN
JBD09
JBD14
BA23
BA22
BC30
BC43
BB11
Region 1
Region 2
Region 3
20km
(b) Brusque Complex (excluding regions 1 to 3)
S1 N = 260
S2 N = 116
S3 N = 81
F2 N = 45
F3 N = 33
(c) Stretching Lin. (all regions)
L1 N = 20
L2 N = 37
(d) Region 1
S1 N = 135
S2 N = 20
L1 N = 2
(e) Region 2
S1 N = 43
S2 N = 22
(f) Region 3
S2 N = 52

Figure. 3

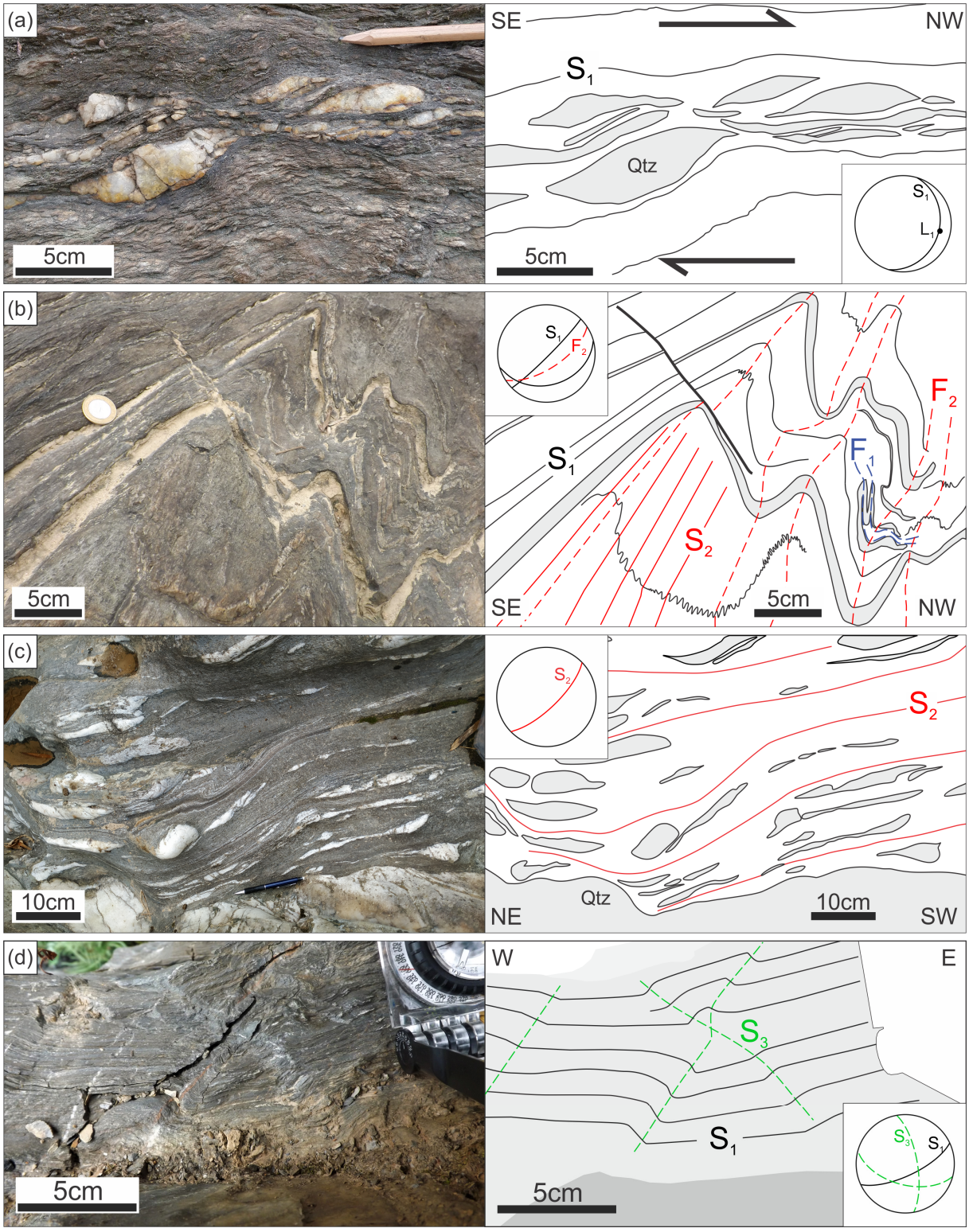
(a)
5cm
SE
NW
S1
Qtz
5cm
S1
L1
(b)
5cm
S1
F2
S1
F2
F1
S2
SE
5cm
NW
(c)
10cm
S2
S2
Qtz
NE
10cm
SW
(d)
5cm
W
E
S3
S1
5cm
S3
S1

Figure 4.

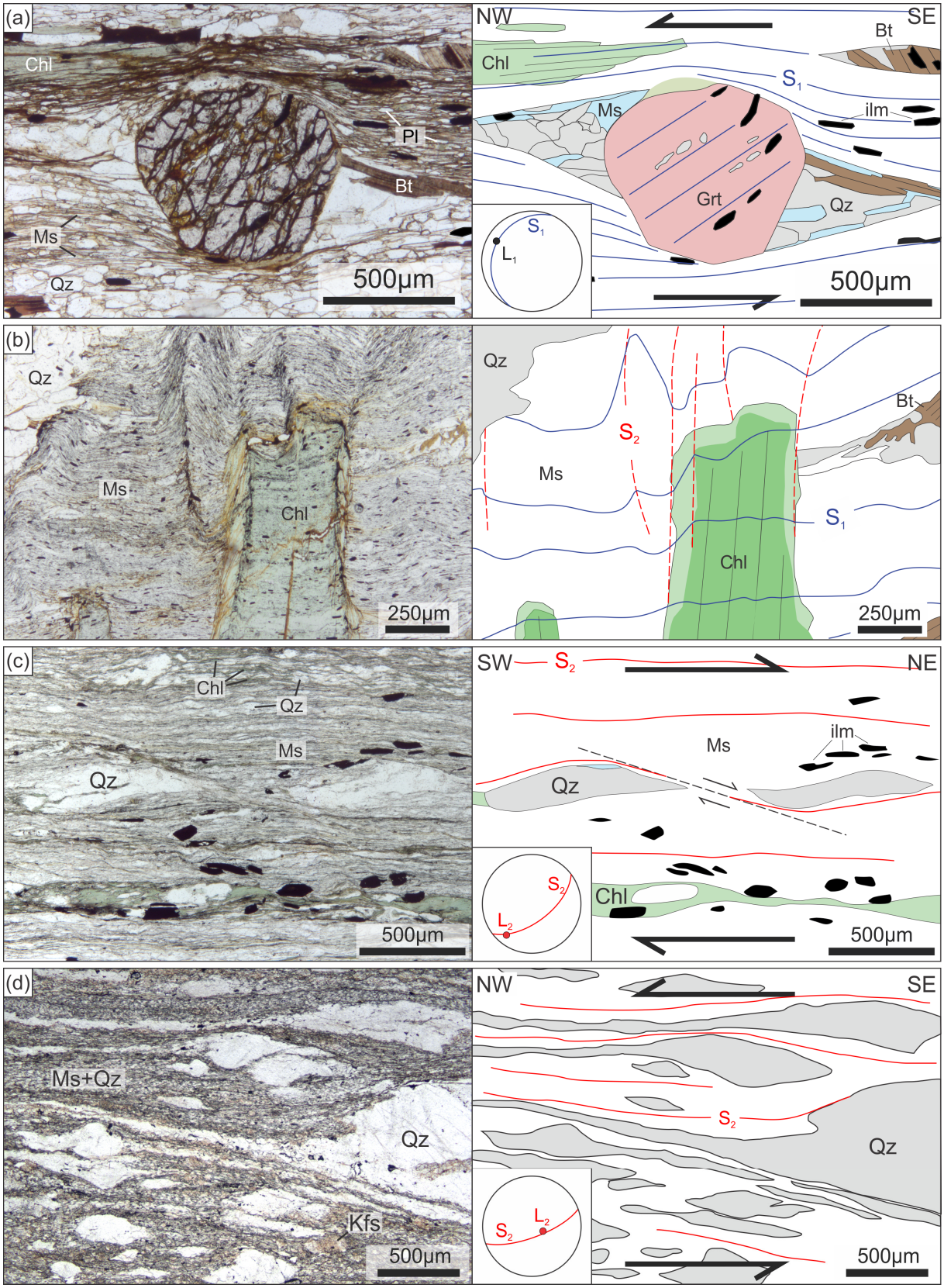
(a)
Chl
Pl
Bt
Ms
Qz
500μm
NW
SE
Chl
Bt
S1
Ms
ilm
Grt
Qz
S1
L1
500μm
(b)
Qz
Ms
Chl
250μm
Qz
Bt
S2
Ms
S1
Chl
250μm
(c)
Chl
Qz
Ms
Qz
500μm
SW
S2
NE
Ms
ilm
Qz
S2
L2
Chl
500μm
(d)
Ms+Qz
Qz
Kfs
500μm
NW
SE
S2
Qz
S2
L2
500μm

Figure 5.

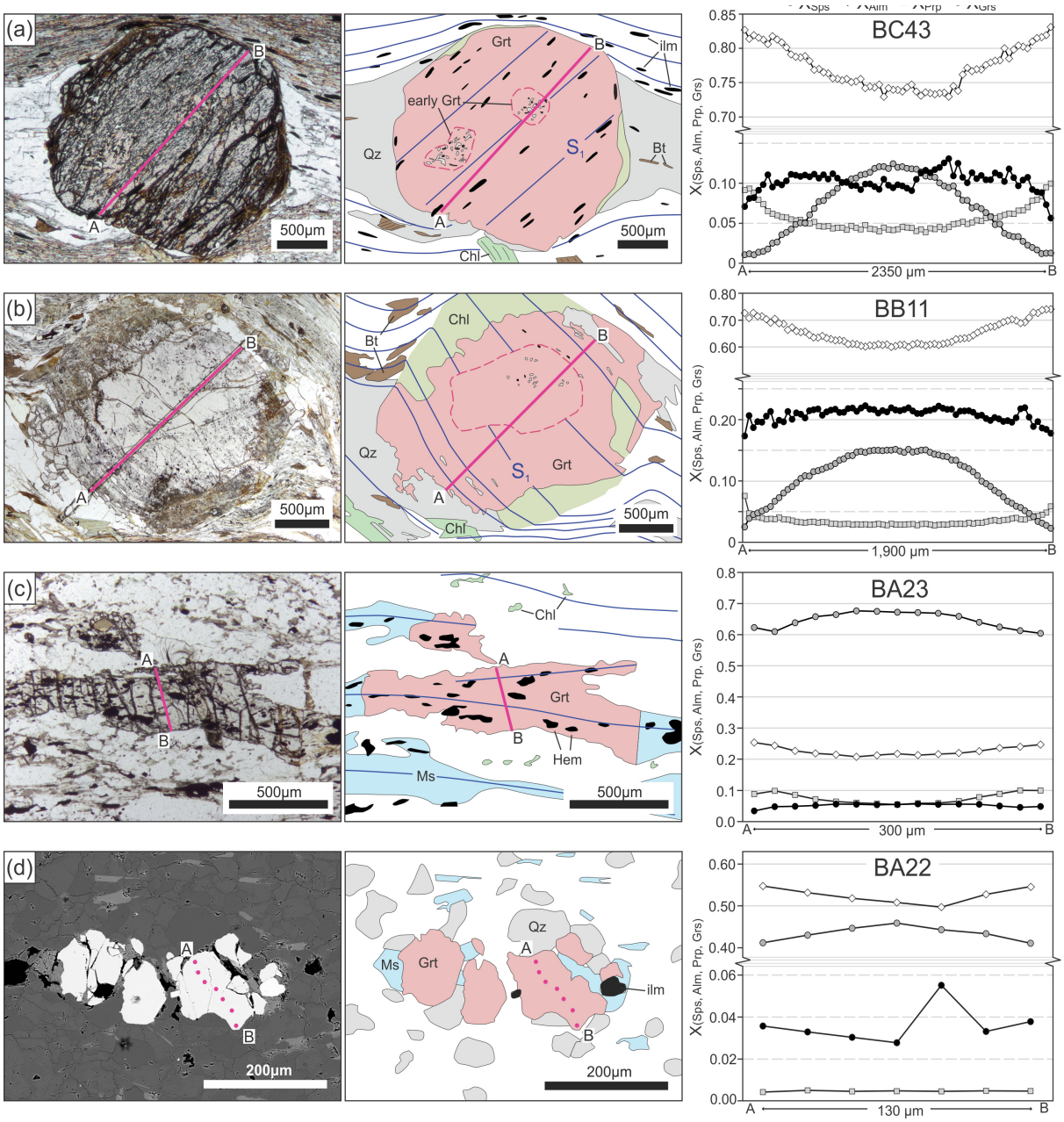
(a)
B
A
500μm
Grt
B
ilm
early Grt
Qz
S1
Bt
A
Chl
500μm
BC43
0.85
0.80
0.75
0.70
0.10
0.05
0
X(Sps, Alm, Prp, Grs)
A
2350 μm
B
(b)
B
A
500μm
Chl
Bt
B
Qz
S1
Grt
A
Chl
500μm
BB11
0.80
0.70
0.60
0.20
0.10
0
X(Sps, Alm, Prp, Grs)
A
1,900 μm
B
(c)
A
B
500μm
Chl
A
Grt
B
Hem
Ms
500μm
BA23
0.8
0.7
0.6
0.5
0.4
0.3
0.2
0.1
0.0
X(Sps, Alm, Prp, Grs)
A
300 μm
B
(d)
A
B
200μm
Qz
Ms
Grt
A
ilm
B
200μm
BA22
0.60
0.50
0.40
0.06
0.04
0.02
0.00
X(Sps, Alm, Prp, Grs)
A
130 μm
B

Figure 6.

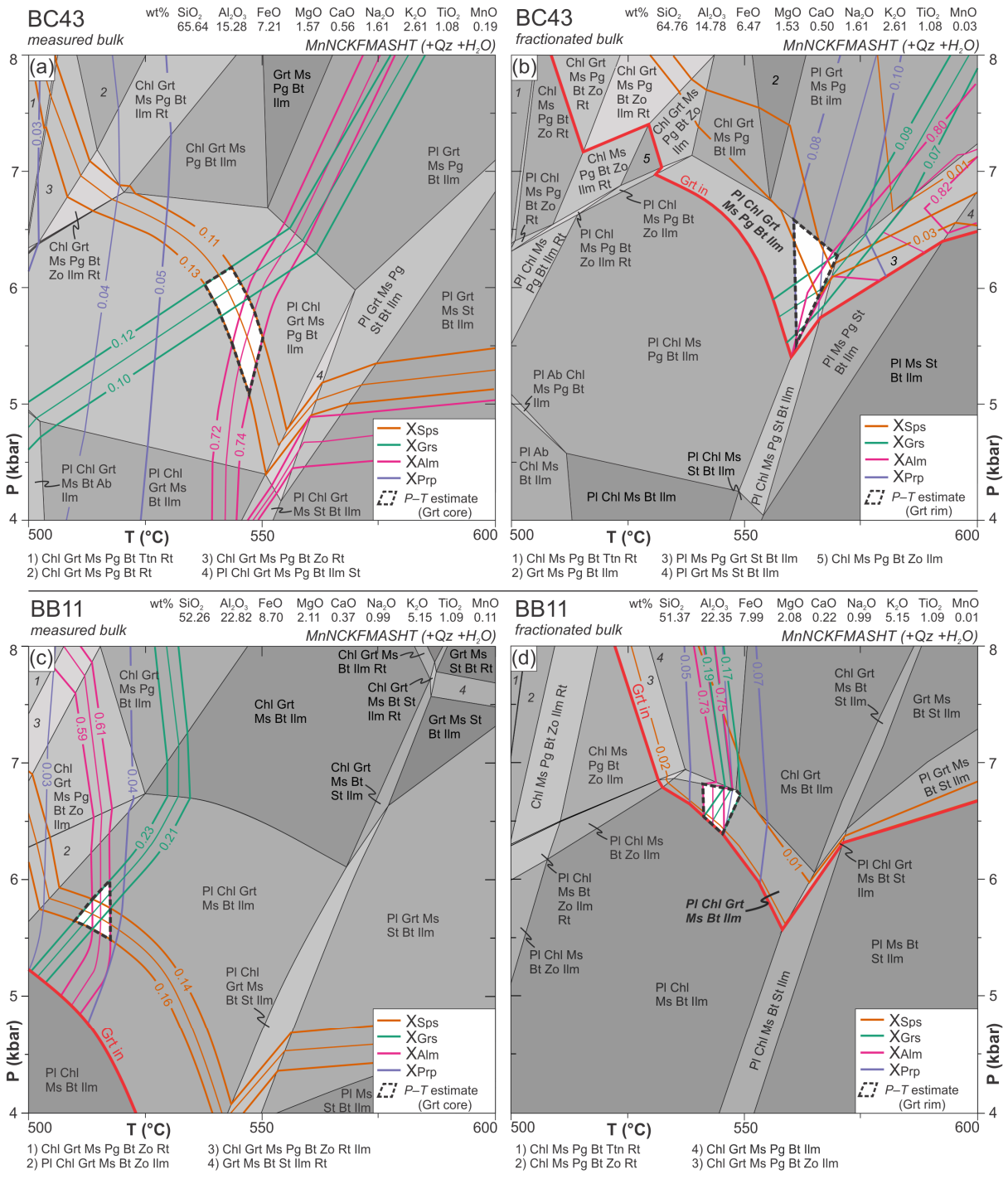
BC43
measured bulk
wt% SiO2 Al2O3 FeO MgO CaO Na2O K2O TiO2 MnO
65.64 15.28 7.21 1.57 0.56 1.61 2.61 1.08 0.19
MnNCKFMASHT (+Qz +H2O)
(a)
Chl Grt Ms Pg Bt Ilm Rt
Grt Ms Pg Bt Ilm
Chl Grt Ms Pg Bt Ilm
Pl Grt Ms Pg Bt Ilm
Chl Grt Ms Pg Bt Zo Ilm Rt
Pl Chl Grt Ms Pg Bt Ilm
Pl Grt Ms Pg St Bt Ilm
Pl Grt Ms St Bt Ilm
Pl Chl Grt Ms Bt Ab Ilm
Pl Chl Grt Ms Bt Ilm
Pl Chl Grt Ms St Bt Ilm
XSps
XGrs
XAlm
XPrp
P–T estimate (Grt core)
P (kbar)
T (°C)
1) Chl Grt Ms Pg Bt Ttn Rt
2) Chl Grt Ms Pg Bt Rt
3) Chl Grt Ms Pg Bt Zo Rt
4) Pl Chl Grt Ms Pg Bt Ilm St
BC43
fractionated bulk
wt% SiO2 Al2O3 FeO MgO CaO Na2O K2O TiO2 MnO
64.76 14.78 6.47 1.53 0.50 1.61 2.61 1.08 0.03
MnNCKFMASHT (+Qz +H2O)
(b)
Chl Ms Pg Bt Zo Rt
Chl Grt Ms Pg Bt Zo Ilm Rt
Chl Grt Ms Pg Bt Zo Ilm
Chl Grt Ms Pg Bt Ilm
Pl Grt Ms Pg Bt Ilm
Pl Chl Ms Pg Bt Zo Rt
Chl Ms Pg Bt Zo Ilm Rt
Grt in
Pl Chl Grt Ms Pg Bt Ilm
Pl Chl Ms Pg Bt Zo Ilm
Pl Chl Ms Pg Bt Zo Ilm Rt
Pl Chl Ms Pg Bt Ilm Rt
Pl Ms Pg St Bt Ilm
Pl Ms St Bt Ilm
Pl Chl Ms Pg Bt Ilm
Pl Ab Chl Ms Pg Bt Ilm
Pl Ab Chl Ms Bt Ilm
Pl Chl Ms St Bt Ilm
Pl Chl Ms Pg St Bt Ilm
Pl Chl Ms Bt Ilm
XSps
XGrs
XAlm
XPrp
P–T estimate (Grt rim)
P (kbar)
T (°C)
1) Chl Ms Pg Bt Ttn Rt
2) Grt Ms Pg Bt Ilm
3) Pl Ms Pg Grt St Bt Ilm
4) Pl Grt Ms St Bt Ilm
5) Chl Ms Pg Bt Zo Ilm
BB11
measured bulk
wt% SiO2 Al2O3 FeO MgO CaO Na2O K2O TiO2 MnO
52.26 22.82 8.70 2.11 0.37 0.99 5.15 1.09 0.11
MnNCKFMASHT (+Qz +H2O)
(c)
Chl Grt Ms Pg Bt Ilm
Chl Grt Ms Bt Ilm Rt
Grt Ms St Bt Rt
Chl Grt Ms Bt Ilm
Chl Grt Ms Bt St Ilm Rt
Grt Ms St Bt Ilm
Chl Grt Ms Bt St Ilm
Chl Grt Ms Pg Bt Zo Ilm
Pl Chl Grt Ms Bt Ilm
Pl Grt Ms St Bt Ilm
Pl Chl Grt Ms Bt St Ilm
Grt in
Pl Chl Ms Bt Ilm
Pl Ms St Bt Ilm
XSps
XGrs
XAlm
XPrp
P–T estimate (Grt core)
P (kbar)
T (°C)
1) Chl Grt Ms Pg Bt Zo Rt
2) Pl Chl Grt Ms Bt Zo Ilm
3) Chl Grt Ms Pg Bt Zo Rt Ilm
4) Grt Ms Bt St Ilm Rt
BB11
fractionated bulk
wt% SiO2 Al2O3 FeO MgO CaO Na2O K2O TiO2 MnO
51.37 22.35 7.99 2.08 0.22 0.99 5.15 1.09 0.01
MnNCKFMASHT (+Qz +H2O)
(d)
Chl Ms Pg Bt Zo Ilm Rt
Grt in
Chl Ms Pg Bt Zo Ilm
Chl Grt Ms Bt St Ilm
Grt Ms Bt St Ilm
Chl Grt Ms Bt Ilm
Pl Grt Ms Bt St Ilm
Pl Chl Ms Bt Zo Ilm
Pl Chl Ms Bt Zo Ilm Rt
Pl Chl Grt Ms Bt Ilm
Pl Chl Grt Ms Bt St Ilm
Pl Ms Bt St Ilm
Pl Chl Ms Bt Ilm
Pl Chl Ms Bt St Ilm
XSps
XGrs
XAlm
XPrp
P–T estimate (Grt rim)
P (kbar)
T (°C)
1) Chl Ms Pg Bt Ttn Rt
2) Chl Ms Pg Bt Zo Rt
3) Chl Grt Ms Pg Bt Zo Ilm
4) Chl Grt Ms Pg Bt Ilm

Figure 7.

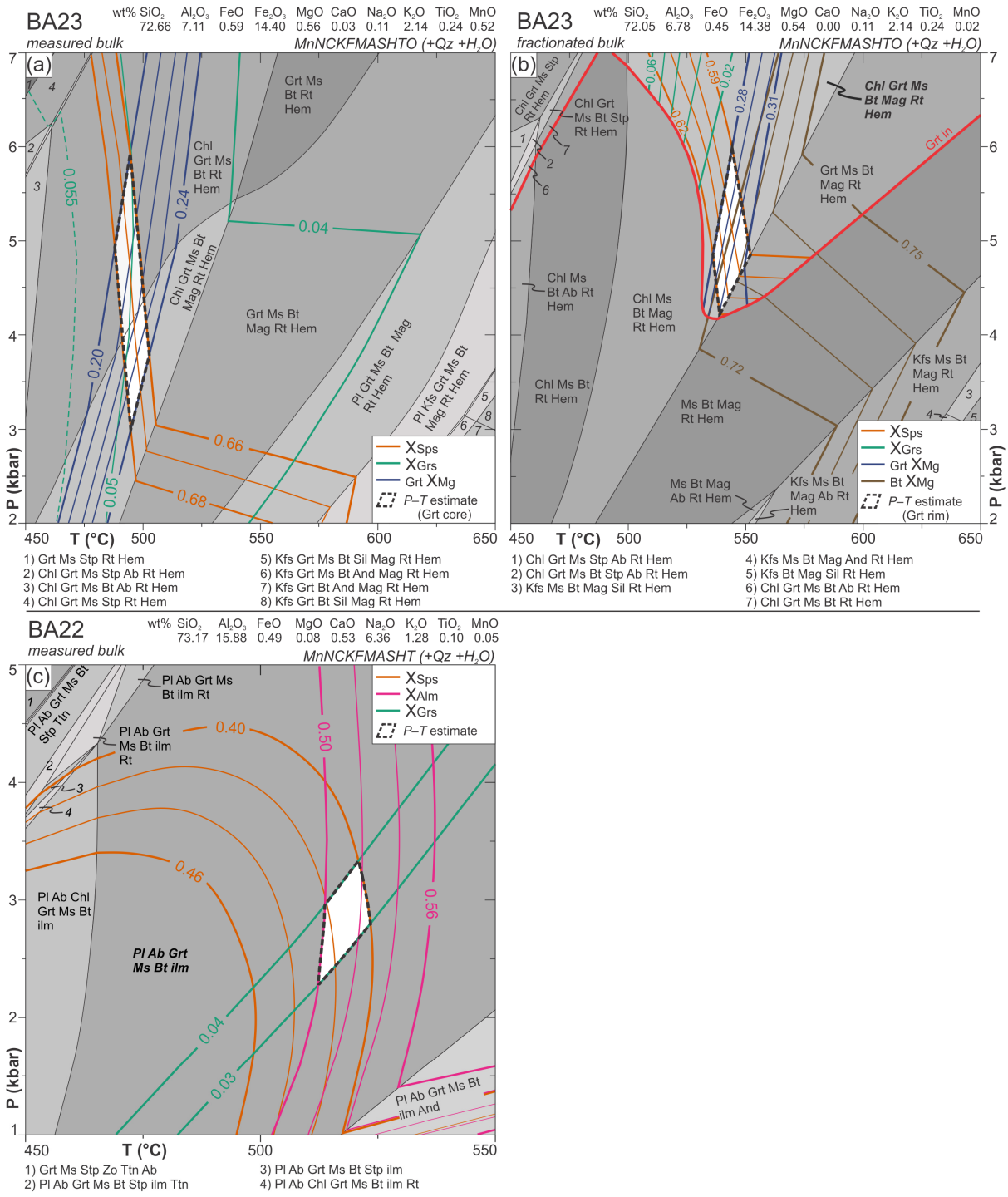
BA23
wt% SiO2 Al2O3 FeO Fe2O3 MgO CaO Na2O K2O TiO2 MnO
72.66 7.11 0.59 14.40 0.56 0.03 0.11 2.14 0.24 0.52
measured bulk
MnNCKFMASHTO (+Qz +H2O)
(a)
Grt Ms Bt Rt Hem
Chl Grt Ms Bt Rt Hem
Chl Grt Ms Bt Mag Rt Hem
Grt Ms Bt Mag Rt Hem
Pl Grt Ms Bt Mag Rt Hem
Pl Kfs Grt Ms Bt Mag Rt Hem
0.055
0.24
0.04
0.20
0.66
0.68
0.05
XSps
XGrs
Grt XMg
P–T estimate (Grt core)
P (kbar)
T (°C)
1) Grt Ms Stp Rt Hem
2) Chl Grt Ms Stp Ab Rt Hem
3) Chl Grt Ms Bt Ab Rt Hem
4) Chl Grt Ms Stp Rt Hem
5) Kfs Grt Ms Bt Sil Mag Rt Hem
6) Kfs Grt Ms Bt And Mag Rt Hem
7) Kfs Grt Bt And Mag Rt Hem
8) Kfs Grt Bt Sil Mag Rt Hem
BA23
wt% SiO2 Al2O3 FeO Fe2O3 MgO CaO Na2O K2O TiO2 MnO
72.05 6.78 0.45 14.38 0.54 0.00 0.11 2.14 0.24 0.02
fractionated bulk
MnNCKFMASHTO (+Qz +H2O)
(b)
Chl Grt Ms Stp Rt Hem
Chl Ms Bt Ab Rt Hem
Chl Ms Bt Mag Rt Hem
Chl Ms Bt Rt Hem
Ms Bt Mag Rt Hem
Ms Bt Mag Ab Rt Hem
Kfs Ms Bt Mag Rt Hem
Kfs Ms Bt Mag Ab Rt Hem
Chl Grt Ms Bt Mag Rt Hem
Grt in
0.06
0.59
0.02
0.28
0.31
0.62
0.75
0.72
XSps
XGrs
Grt XMg
Bt XMg
P–T estimate (Grt rim)
P (kbar)
T (°C)
1) Chl Grt Ms Stp Ab Rt Hem
2) Chl Grt Ms Bt Stp Ab Rt Hem
3) Kfs Ms Bt Mag Sil Rt Hem
4) Kfs Ms Bt Mag And Rt Hem
5) Kfs Bt Mag Sil Rt Hem
6) Chl Grt Ms Bt Ab Rt Hem
7) Chl Grt Ms Bt Rt Hem
BA22
wt% SiO2 Al2O3 FeO MgO CaO Na2O K2O TiO2 MnO
73.17 15.88 0.49 0.08 0.53 6.36 1.28 0.10 0.05
measured bulk
MnNCKFMASHT (+Qz +H2O)
(c)
Pl Ab Grt Ms Bt Stp Ttn
Pl Ab Grt Ms Bt ilm Rt
Pl Ab Grt Ms Bt ilm
Pl Ab Chl Grt Ms Bt ilm
Pl Ab Grt Ms Bt ilm And
0.40
0.50
0.46
0.56
0.04
0.03
XSps
XAlm
XGrs
P–T estimate
P (kbar)
T (°C)
1) Grt Ms Stp Zo Ttn Ab
2) Pl Ab Grt Ms Bt Stp ilm Ttn
3) Pl Ab Grt Ms Bt Stp ilm
4) Pl Ab Chl Grt Ms Bt ilm Rt

Figure 8.

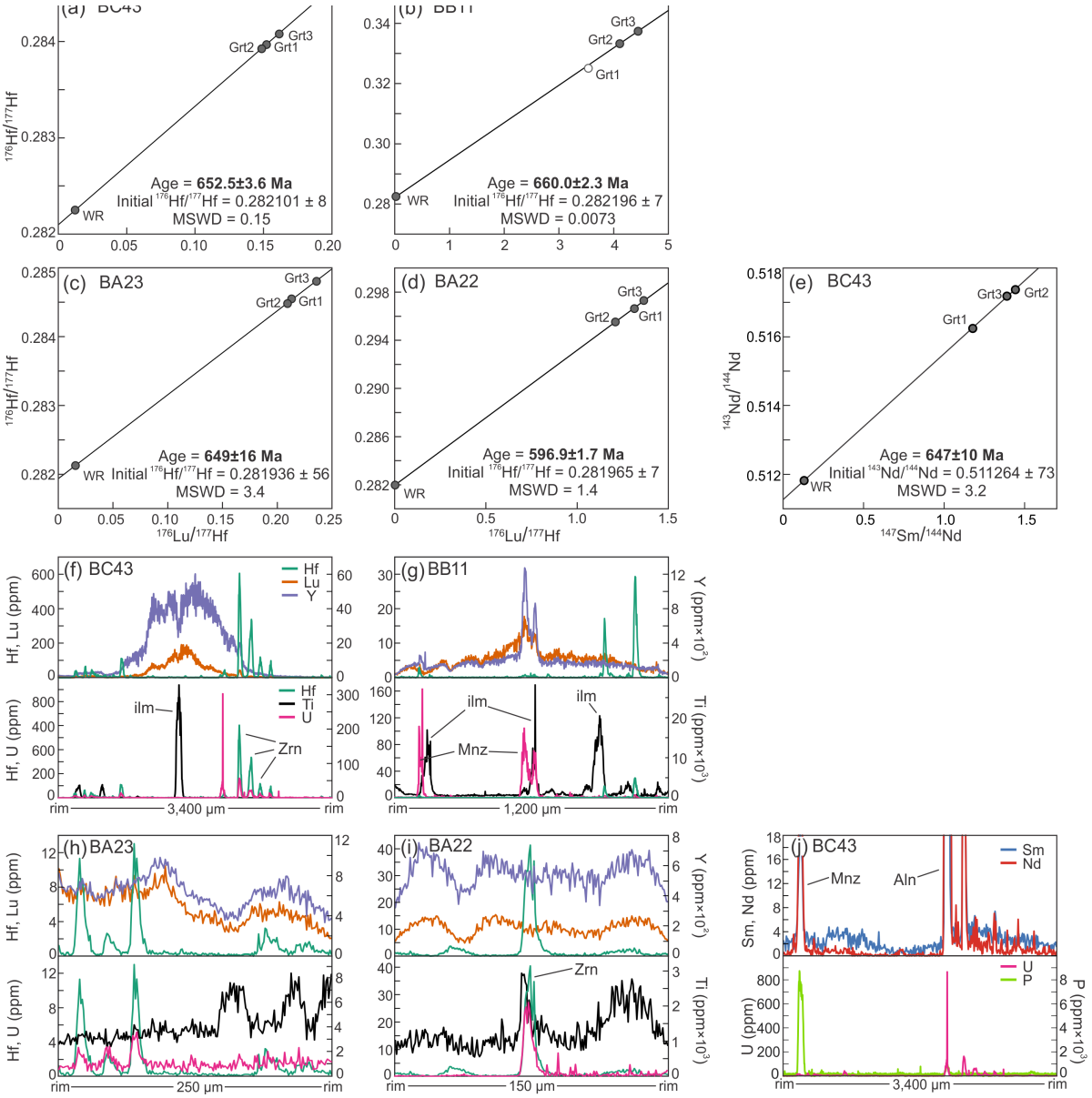
(a) BC43
Grt3
Grt2
Grt1
WR
Age = 652.5±3.6 Ma
Initial 176Hf/177Hf = 0.282101 ± 8
MSWD = 0.15
176Hf/177Hf
(b) BB11
Grt3
Grt2
Grt1
WR
Age = 660.0±2.3 Ma
Initial 176Hf/177Hf = 0.282196 ± 7
MSWD = 0.0073
(c) BA23
Grt3
Grt2
Grt1
WR
Age = 649±16 Ma
Initial 176Hf/177Hf = 0.281936 ± 56
MSWD = 3.4
176Lu/177Hf
(d) BA22
Grt3
Grt2
Grt1
WR
Age = 596.9±1.7 Ma
Initial 176Hf/177Hf = 0.281965 ± 7
MSWD = 1.4
176Lu/177Hf
(e) BC43
Grt3
Grt2
Grt1
WR
Age = 647±10 Ma
Initial 143Nd/144Nd = 0.511264 ± 73
MSWD = 3.2
143Nd/144Nd
147Sm/144Nd
(f) BC43
Hf
Lu
Y
Hf, Lu (ppm)
Hf
Ti
U
ilm
Zrn
Hf, U (ppm)
rim
3,400 μm
rim
(g) BB11
Y (ppm×10³)
ilm
ilm
Mnz
Ti (ppm×10³)
rim
1,200 μm
rim
(h) BA23
Hf, Lu (ppm)
Hf, U (ppm)
rim
250 μm
rim
(i) BA22
Y (ppm×10³)
Zrn
Ti (ppm×10³)
rim
150 μm
rim
(j) BC43
Sm
Nd
Mnz
Aln
Sm, Nd (ppm)
U
P
U (ppm)
P (ppm×10³)
rim
3,400 μm
rim

Figure 9.

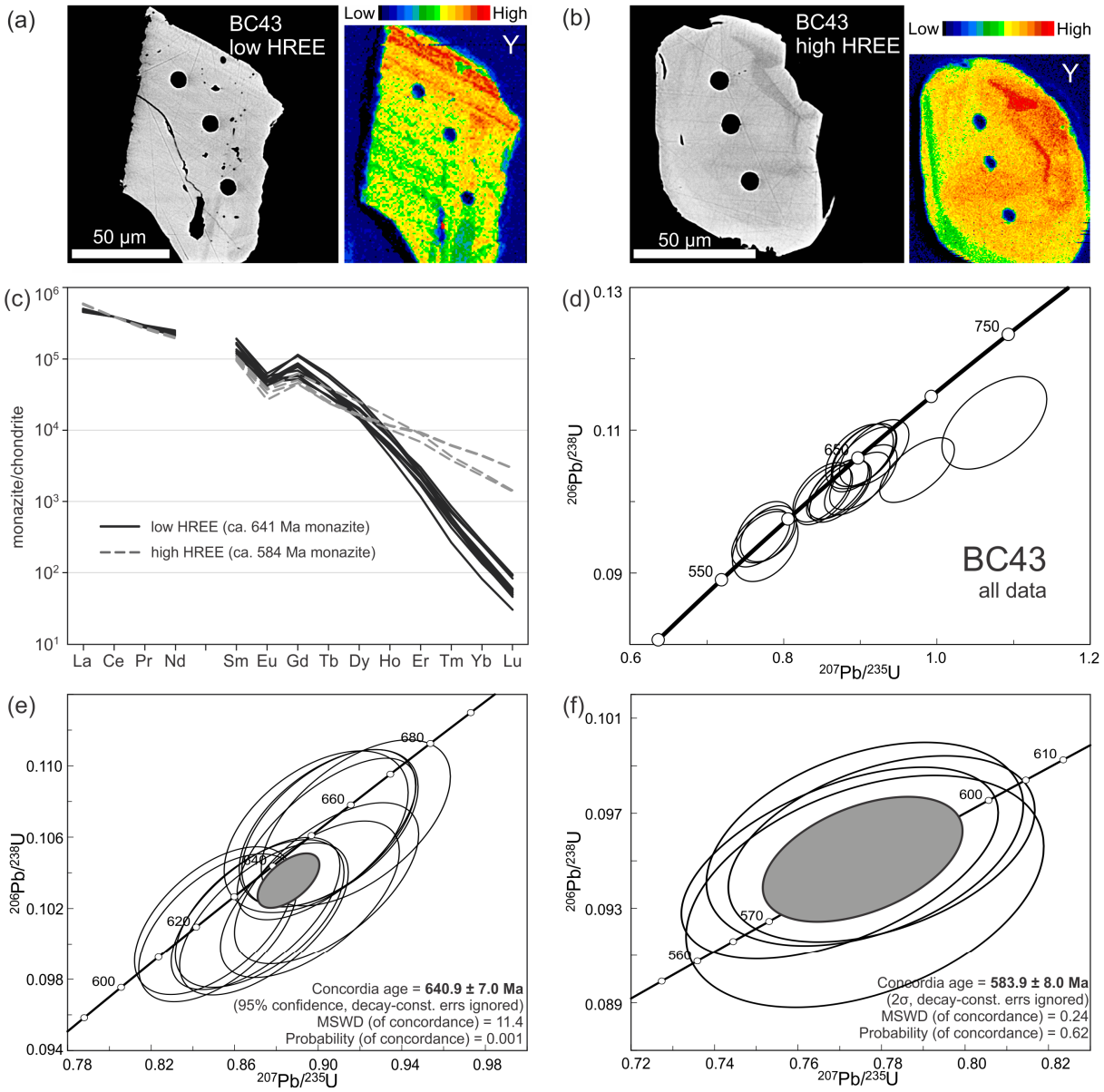
(a)
BC43
low HREE
50 µm
Low
High
Y
(b)
BC43
high HREE
50 µm
Low
High
Y
(c)
monazite/chondrite
low HREE (ca. 641 Ma monazite)
high HREE (ca. 584 Ma monazite)
La Ce Pr Nd Sm Eu Gd Tb Dy Ho Er Tm Yb Lu
(d)
750
650
550
BC43
all data
206Pb/238U
207Pb/235U
(e)
680
660
640
620
600
Concordia age = 640.9 ± 7.0 Ma
(95% confidence, decay-const. errs ignored)
MSWD (of concordance) = 11.4
Probability (of concordance) = 0.001
206Pb/238U
207Pb/235U
(f)
610
600
570
560
Concordia age = 583.9 ± 8.0 Ma
(2σ, decay-const. errs ignored)
MSWD (of concordance) = 0.24
Probability (of concordance) = 0.62
206Pb/238U
207Pb/235U

Figure 10.

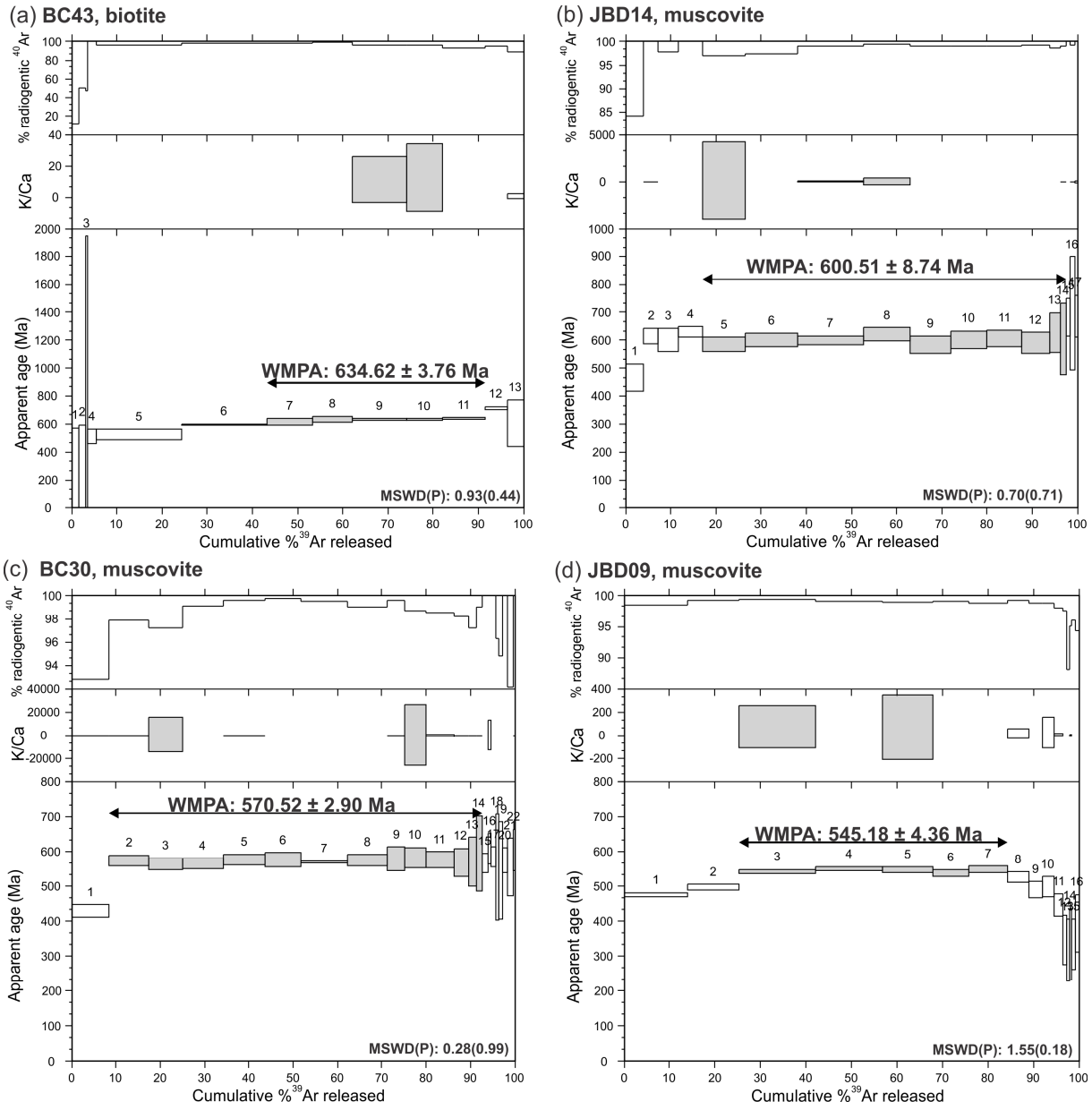
(a) BC43, biotite
% radiogentic ^{40}Ar
K/Ca
Apparent age (Ma)
WMPA: 634.62 ± 3.76 Ma
MSWD(P): 0.93(0.44)
Cumulative %^{39}Ar released
(b) JBD14, muscovite
WMPA: 600.51 ± 8.74 Ma
MSWD(P): 0.70(0.71)
(c) BC30, muscovite
WMPA: 570.52 ± 2.90 Ma
MSWD(P): 0.28(0.99)
(d) JBD09, muscovite
WMPA: 545.18 ± 4.36 Ma
MSWD(P): 1.55(0.18)

Figure 11.

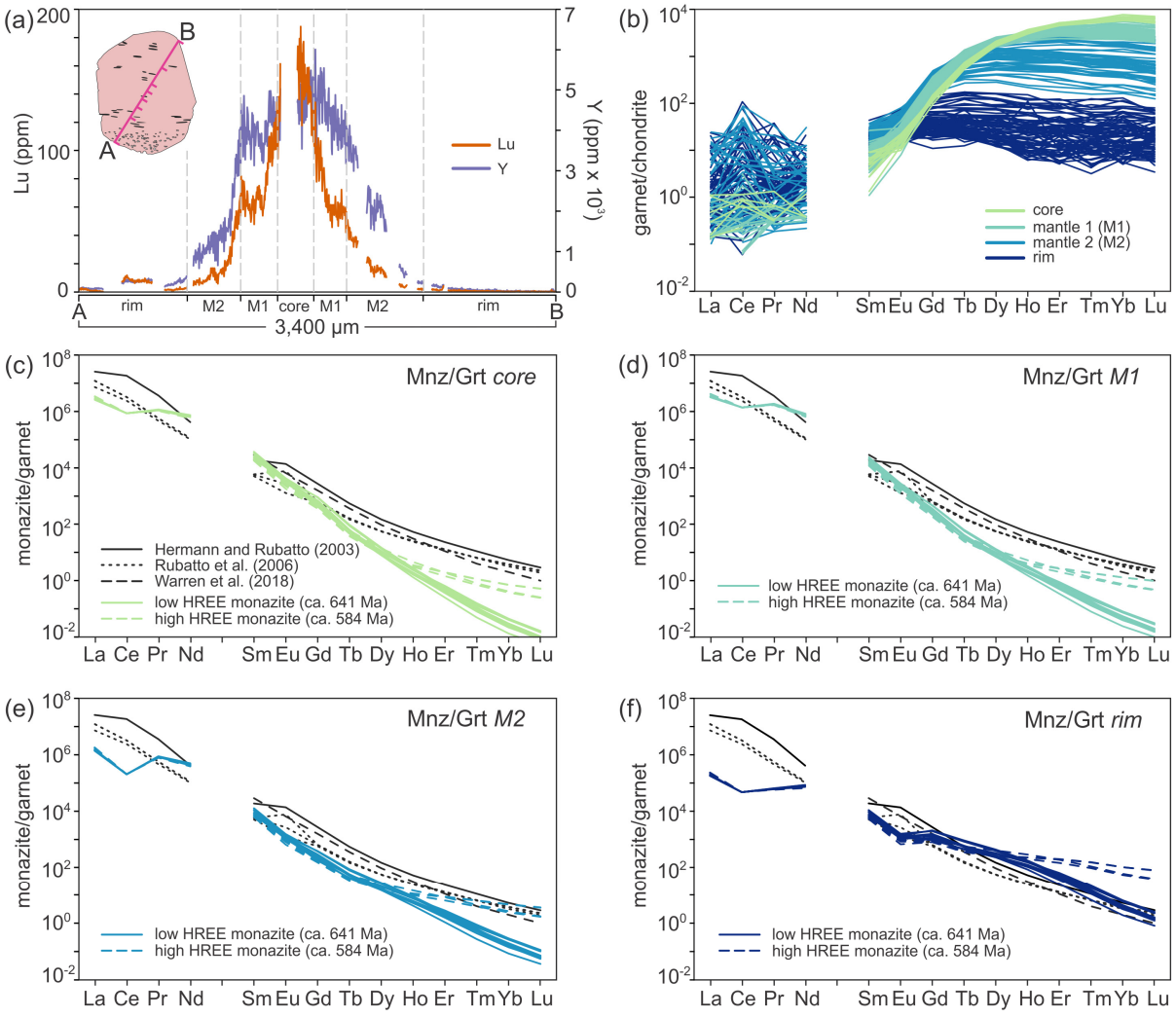
(a)
Lu (ppm)
Y (ppm x 10³)
Lu
Y
A
B
rim
M2
M1
core
M1
M2
rim
3,400 µm
(b)
garnet/chondrite
core
mantle 1 (M1)
mantle 2 (M2)
rim
La Ce Pr Nd Sm Eu Gd Tb Dy Ho Er Tm Yb Lu
(c)
Mnz/Grt core
monazite/garnet
Hermann and Rubatto (2003)
Rubatto et al. (2006)
Warren et al. (2018)
low HREE monazite (ca. 641 Ma)
high HREE monazite (ca. 584 Ma)
(d)
Mnz/Grt M1
(e)
Mnz/Grt M2
(f)
Mnz/Grt rim

Figure 12.

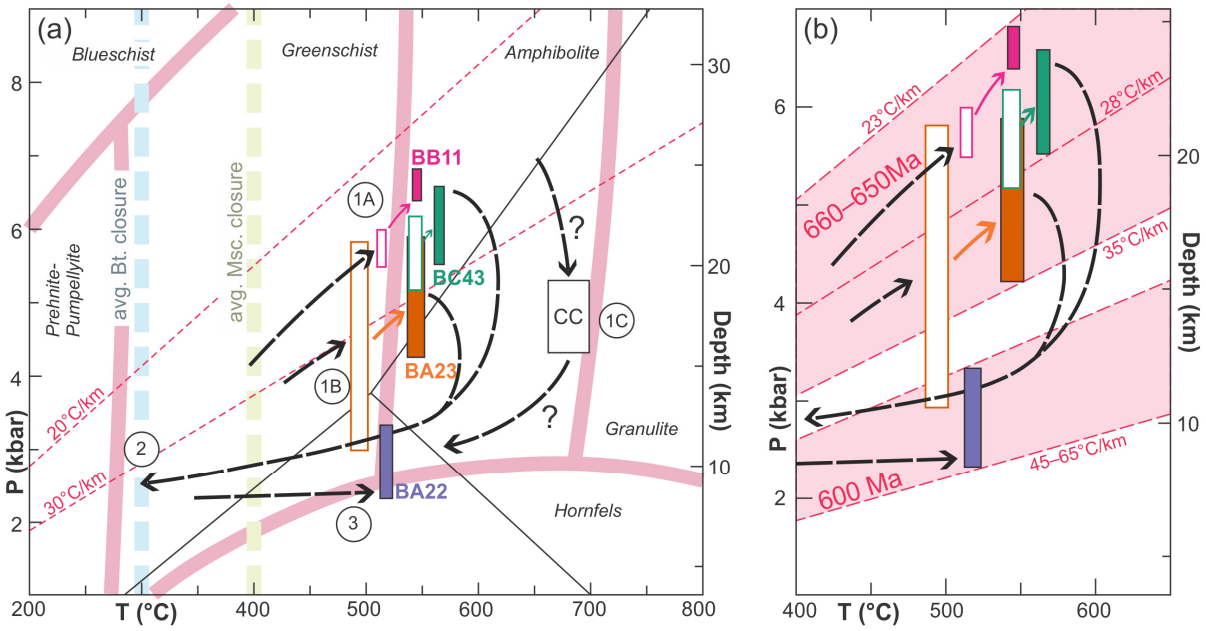
(a)
Blueschist
Greenschist
Amphibolite
Granulite
Hornfels
Prehnite-Pumpellyite
avg. Bt. closure
avg. Msc. closure
BB11
BC43
BA23
BA22
1A
1B
1C
CC
2
3
20°C/km
30°C/km
P (kbar)
T (°C)
Depth (km)
(b)
23°C/km
28°C/km
35°C/km
45–65°C/km
660–650Ma
600 Ma

Figure 13.

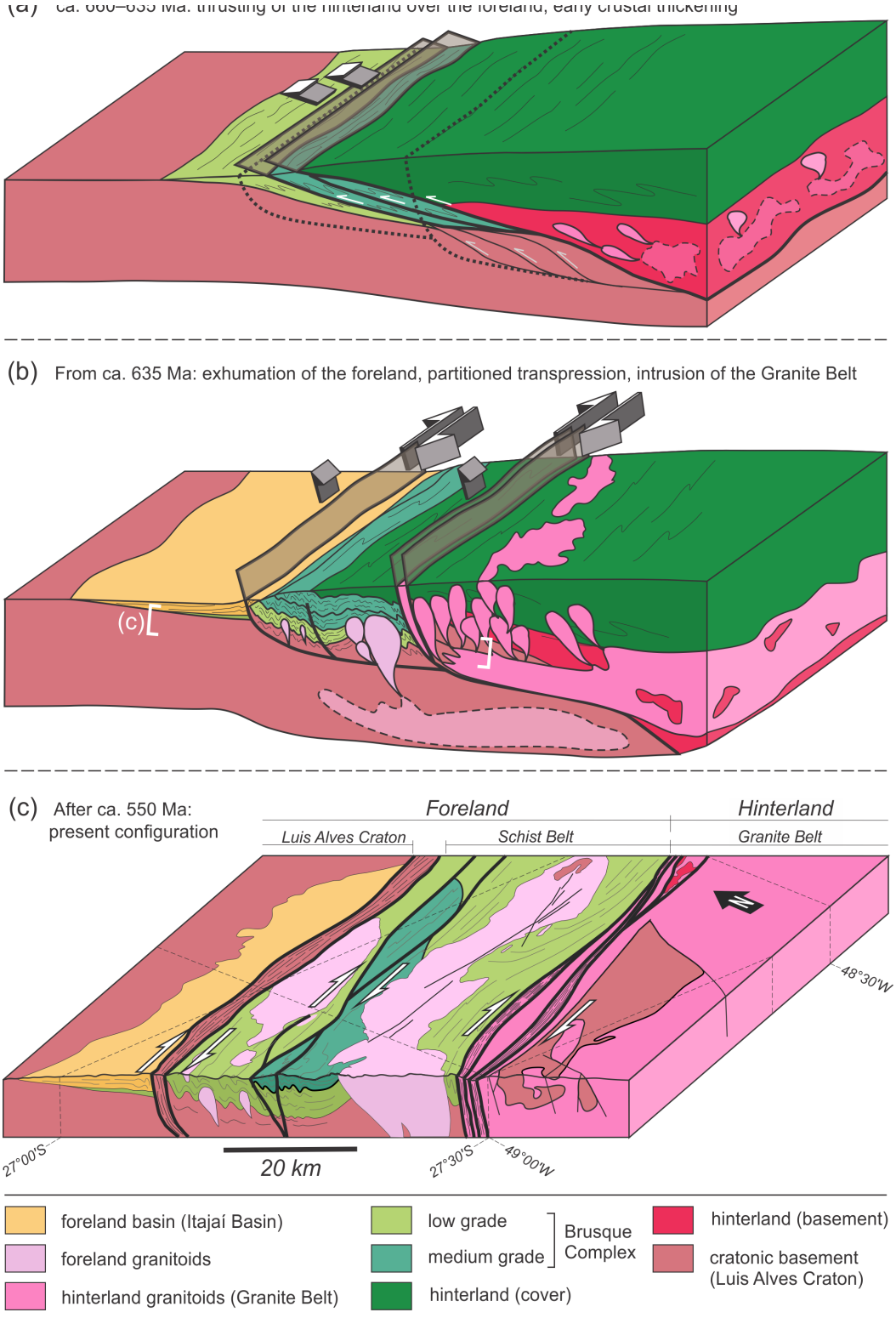
(a) ca. 660–635 Ma: thrusting of the hinterland over the foreland, early crustal thickening
(b) From ca. 635 Ma: exhumation of the foreland, partitioned transpression, intrusion of the Granite Belt
(c)
(c) After ca. 550 Ma: present configuration
Foreland
Hinterland
Luis Alves Craton
Schist Belt
Granite Belt
48°30'W
27°00'S
20 km
27°30'S
49°00'W
foreland basin (Itajaí Basin)
foreland granitoids
hinterland granitoids (Granite Belt)
low grade
medium grade
Brusque Complex
hinterland (cover)
hinterland (basement)
cratonic basement (Luis Alves Craton)

Supporting Information

Introduction

The following text outlines the analytical methods applied for the collection of each dataset used in this study, and which is not described in the main body of the article.

Text S1 – Analytical Methods

Whole rock major element analysis

Whole rock major element analysis was conducted by lithium borate fusion inductively coupled plasma emission spectroscopy (ICP ES) at Bureau Veritas Mineral Laboratories in Vancouver, Canada, and by atomic absorption spectroscopy (AAS) and titration at the Czech Geological Survey, Prague, Czech Republic.

Mineral major element analysis

Mineral major element compositions were analysed using an electron microprobe CAMECA SX100 at the Faculty of Natural Sciences, Masaryk University, Czech Republic, in joint service with the Czech Geological Service. A 15 kV accelerating voltage and 20 nA probe current were applied to garnet, spinel, rutile and ilmenite analyses, using a spot size of 2μm. A 15kV accelerating voltage and 10nA probe current were applied to biotite, muscovite, chlorite and feldspar analyses, using a spot size of 5 μm.

Further garnet major element analyses were conducted using an electron microprobe CAMECA SX100 at the Department of Geosciences, University of Oslo (UiO), Norway. Analytical conditions were 15 kV and 15 nA.

Lu–Hf and Sm–Nd garnet dating and trace element analyis

Garnet–whole-rock Lu–Hf and Sm–Nd geochronology and trace element analysis was conducted at the Institute of Geological Sciences, Polish Academy of Sciences, Kraków Research Centre. Sample preparation and isotopic analysis follow the methods from Anczkiewicz et al. (2004). Isotopic ratios were measured using ICP-MS Neptune by Thermo Scientific. Rim-to-rim trace element profiles were analysed from thin sections by Laser Ablation ICP-MS (Woodhead et al., 2007) across individual garnet grains. Analysis was conducted using an excimer laser-ablation system *RESOlution M50* by Resonetics

coupled with quadrupole ICP-MS *XSeriesII* by Thermo, with further details on the setup found in Anczkiewicz et al. (2012) and references therein. The data was processed using Iolite software (Paton et al., 2011).

Monazite U─Pb dating

Samples were chosen for monazite U─Pb dating to compliment garnet Lu─Hf ages. Thin sections were prepared, and then analysed using polarized-light and scanning electron microscopy for the presence of monazite. Samples containing monazite were then crushed and milled to a grainsize of (maximum) 500μm. Milled samples were then run through a Wilfley shaking table to separate mineral phases based on density. Samples were further processed using LST and DIM heavy liquids, and a Frantz magnetic separator. Monazite grains were individually handpicked under a binocular optical microscope. Ultimately, only one sample (BC43) produced monazite grains of sufficient size and number for analysis. Only seven grains were analysed for U─Pb from the sample, and multiple spots were analysed on each grain. A Thermo Scientific Element 2 sector field ICP-MS coupled to a 193 nm ArF excimer laser (Teledyne Cetac Analyte Excite laser), at the Institute of Geology of the Czech Academy of Sciences, was used to measure the Pb/U, Pb/Th and Pb isotopic ratios in monazite. Full analytical details are presented in the online Supporting Information.

Monazite trace element analysis

A Thermo Scientific Element 2 high-resolution sector field ICP-MS coupled to a 193 nm ArF excimer laser (Teledyne Cetac Analyte Excite laser) at the Institute of Geology of the Czech Academy of Sciences, Prague, Czech Republic, was used to acquire the trace element (TE) data. The laser was fired at a repetition rate of 5 Hz and fluence of 3.5 J/cm2 with a 13 micron laser spot size. He carrier gas was flushed through the two-volume ablation cell at a flow rate of 0.9 L/min and mixed with 0.7 L/min Ar and 0.005 L/min N prior to introduction into the ICP. The in-house glass signal homogenizer (design of Tunheng & Hirata, 2004) was used for mixing all the gases and aerosol resulting in a smooth, spike-free signal. The signal was tuned for maximum sensitivity while keeping low oxide levels, commonly below 0.1 %. Typical acquisitions consisted of 15 seconds of blank measurement followed by the measurement of TE signals from the ablated materials for another 20 seconds. This ablation pattern was repeated on each analytical spot. The following isotopes were collected at low mass resolution mode ($m/\Delta m = 300$): ^{31}P, ^{89}Y, ^{139}La, ^{140}Ce, ^{141}Pr, ^{146}Nd, ^{147}Sm, ^{153}Eu, ^{157}Gd, ^{159}Tb, ^{163}Dy, ^{165}Ho, ^{166}Er, ^{169}Tm, ^{172}Yb and ^{175}Lu. The cell was washed for 30 seconds between each analysis. The measurement sequence consisted of the repeated blocks of 2 analyses of NIST SRM610, one analysis of BCR-2 standard and 10 unknowns.

Trace element data were calibrated against the NIST SRM610 glass using P as internal standard together with concentration values of the measured samples obtained from EMPA analysis.

The minimum detection limit values were calculated by multiplying the variance of the background by 3.25 for individual elements and are listed in the data table. The time-resolved signal data were processed using the Glitter software (van Achterberg et al., 2001). The precision of the analyses (1 RSD) ranges between 5 and 15% for most elements. The accuracy was monitored by a homogenized basalt reference material BCR-2 (USGS).

$^{40}Ar/^{39}Ar$ mica dating

Samples were crushed and sieved to a grainsize of 180─250µm. Fine material from this fraction was decanted in tap water, and then the coarse residue was cleaned in an ultrasonic bath in deionised water. This last cleaning step was repeated until there was no longer dust or discolouration in the water. The optically best grains void of any coating were handpicked under a stereomicroscope. The samples were packed in aluminum capsules together with the PP20 flux monitor standard along with zero age reagent grade K_2SO_4 and optical grade CaF_2 salts for interference corrections. The samples were irradiated at the BNC reactor (Hungary) for c. 6.5 hours, with a nominal fast neutron flux density of c. 5.5×10^{13} n*(cm^{-2} *s^{-1}). The interference correction factors for the production of isotopes from Ca and K are located in the online Supporting Information. The mineral grains were placed in a 3.5mm pit size aluminum sample disk and step heated using a defocused 3.5 mm CO_2 laser beam from Photon Machine Fusions 10.6 with a flat energy spectrum. The extracted gases from the sample cell were expanded into a Piston Free Stirling Cryocooler for trapping potential water vapor and further into a two-stage low volume extraction line (c. 300 cm^3), both stages equipped with SAES GP-50 (st101 alloy) getters, the first running hot (c. 350 °C) and the second running at room temperature. The samples were analyzed with a MAP 215–50 mass spectrometer in static mode, installed at the Geological Survey of Norway. The peaks and baseline (AMU = 36.2) were determined during peak hopping for 10 cycles (15 integrations per cycle, 30 integrations on mass ^{36}Ar) on the different masses ($^{40–36}AMU$) on a Mascom electron multiplier in analogue mode and linearly regressed back to zero inlet time. Blanks were analyzed every third measurement. After blank correction, a correction for mass fractionation, ^{37}Ar and ^{39}Ar decay and neutron-induced interference reactions produced in the reactor was undertaken using in-house software AgeMonster, written by M. Ganerød. It implements the equations of McDougall and Harrison (1999) and the newly proposed decay constant for ^{40}K after (Renne et al., 2010). A $^{40}Ar/^{36}Ar$ ratio of 298.56 ± 0.31 from Lee et al. (2006), was used for the atmospheric argon correction and mass discrimination calculation using a power law distribution of the masses. We calculated J-values relative to an age of 1080.4 ± 1.1 Ma for the PP20 fluence monitor (Renne et al., 2010). We define a plateau

according to the following requirements: at least three consecutive steps overlapping at the 95% confidence level (1.96σ) using the strict test:

$overlap\ if: abs(age_n - age_{n+1}) < 1.96\sqrt{(\sigma_n^2 + \sigma_{n+1}^2)}$ (if errors quoted at 1σ),

>= 50% cumulative ^{39}Ar released, and mean square of weighted deviates (MSWD) less than the two tailed student T critical test statistics for n - 1. Weighted mean ages are calculated by weighting on the inverse of the analytical variance. The uncertainties are expanded in cases where MSWD > 1 using $\sigma * \sqrt{MSWD}$ to account for this excess error contribution.

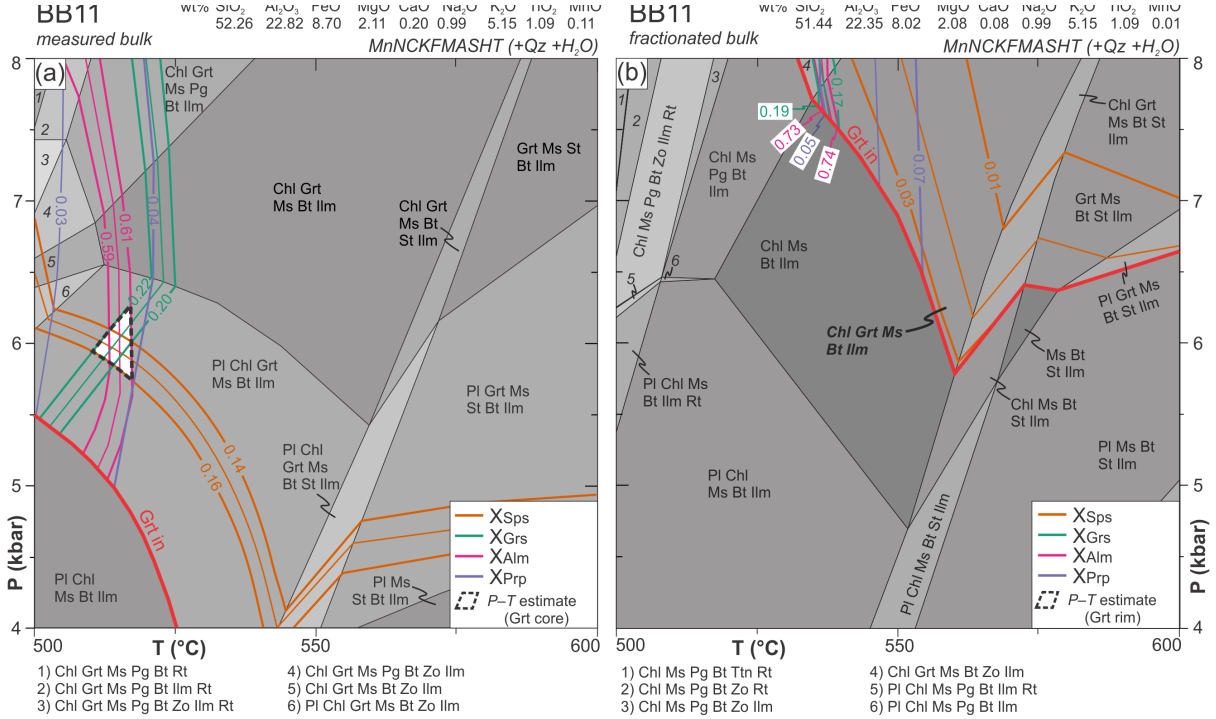

Figure S1. Pressure–temperature pseudosections calculated for garnet–mica schist sample BB11 using (a) measured bulk composition after apatite CaO-adjustment and (b) estimated bulk composition after garnet fractionation calculations. Higher variance fields are shown by darker shading. Contoured isopleths show observed compositional values with ± 0.01 error. Fields containing the observed mineral assemblages are highlighted in bold and italics.

References in Supporting Information

Anczkiewicz, R., Platt, J. P., Thirlwall, M. F., & Wakabayashi, J. (2004). Franciscan subduction off to a slow start: evidence from high-precision Lu–Hf garnet ages on high grade-blocks. *Earth and Planetary Science Letters, 225*(1), 147–161. doi:https://doi.org/10.1016/j.epsl.2004.06.003

Anczkiewicz, R., Thirlwall, M., Alard, O., Rogers, N. W., & Clark, C. (2012). Diffusional homogenization of light REE in garnet from the Day Nui Con Voi Massif in N-Vietnam: Implications for Sm–Nd geochronology and timing of metamorphism in the Red River shear zone. *Chemical Geology, 318-319*, 16–30. doi:https://doi.org/10.1016/j.chemgeo.2012.04.024

Lee, J.-Y., Marti, K., Severinghaus, J. P., Kawamura, K., Yoo, H.-S., Lee, J. B., & Kim, J. S. (2006). A redetermination of the isotopic abundances of atmospheric Ar. *Geochimica et Cosmochimica Acta, 70*(17), 4507-4512. doi:https://doi.org/10.1016/j.gca.2006.06.1563

McDougall, I., & Harrison, T. M. (1999). *Geochronology and thermochronology by the 40Ar/39Ar method*. New York: Oxford University Press.

Paton, C., Hellstrom, J., Paul, B., Woodhead, J., & Hergt, J. (2011). Iolite: Freeware for the visualisation and processing of mass spectrometric data. *Journal of Analytical Atomic Spectrometry, 26*(12), 2508─2518. doi:https://doi.org/10.1039/C1JA10172B

Renne, P. R., Mundil, R., Balco, G., Min, K., & Ludwig, K. R. (2010). Joint determination of 40K decay constants and 40Ar∗/40K for the Fish Canyon sanidine standard, and improved accuracy for 40Ar/39Ar geochronology. *Geochimica et Cosmochimica Acta, 74*(18), 5349-5367. doi:https://doi.org/10.1016/j.gca.2010.06.017

Tunheng, A., & Hirata, T. (2004). Development of signal smoothing device for precise elemental analysis using laser ablation-ICP-mass spectrometry. *Journal of Analytical Atomic Spectrometry, 19*(7), 932-934. doi:https://www.doi.org/10.1039/B402493A

van Achterberg, E., Ryan, C., Jackson, S., & Griffin, W. (2001). Data reduction software for LA-ICP-MS. *Laser Ablation ICP-MS in the Earth Science, 29*, 239-243.

Woodhead, J. D., Hellstrom, J., Hergt, J. M., Greig, A., & Maas, R. (2007). Isotopic and Elemental Imaging of Geological Materials by Laser Ablation Inductively Coupled Plasma-Mass Spectrometry. *Geostandards and Geoanalytical Research, 31*(4), 331–343. doi:https://doi.org/10.1111/j.1751-908X.2007.00104.x

Paper III

Diachronous two-stage Neoproterozoic evolution of the southern Dom Feliciano Belt, Uruguay

Jack James Percival[1]*, Jiří Konopásek[1,2], Pedro Oyhantçabal[3], Jiří Sláma[4], Robert Anczkiewicz[5]

[1] Department of Geosciences, UiT–The Arctic University of Norway, Dramsveien 201, 9037 Tromsø, Norway

[2] Czech Geological Survey, Klárov 3, 118 21 Prague 1, Czech Republic

[3] Departamento de Geodinámica Interna, Facultad de Ciencias, Universidad de La República, Uruguay

[4] Institute of Geology of the Czech Academy of Sciences, Rozvojová 269, 165 00 Prague 6, Czech Republic

[5] Institute of Geological Sciences, Polish Academy of Sciences, Kraków Research Centre, Senacka 1, PL 31-002, Kraków, Poland

*Corresponding author: jack.j.percival@uit.no

Abstract

The Dom Feliciano Belt of southern Brazil and Uruguay represents part of a larger Neoproterozoic orogenic system formed during the amalgamation of Western Gondwana. The hinterland and foreland domains in parts of the belt have been shown to preserve deformation structures and metamorphic assemblages developed during early crustal thickening, although the metamorphic history of the southern foreland, in Uruguay, and its relationship with the hinterland, is not so well understood. Metamorphism in the hinterland is characterised by near-isothermal decompression from ~10 kbar and ~770°C, down to ~6 kbar, reflecting exhumation from depths of ~40 km during thrusting and crustal thickening. This metamorphic event is constrained by garnet Lu–Hf and zircon U–Pb dating to ca. 655–640 Ma, supporting geochronological and thermobarometric constraints from previous studies. Furthermore, ca. 655 Ma melting associated with this high-T event is reported for the first time in this part of the belt. In contrast, prograde metamorphism in the foreland supracrustal rocks reached maximum lower-amphibolite facies conditions (~6–7kbar and ~550–570°C) and is constrained by garnet Lu–Hf dating to 582 ± 23 Ma. Exposed foreland basement rocks reached upper-amphibolite facies conditions, and metamorphism is similarly constrained to ca. 585–570 Ma by monazite U–Pb dating. The data indicate that metamorphism in the foreland occurred during a major sinistral transpressional event ca. 55–85 m.y. after the start of crustal thickening recorded in the hinterland. We propose that strain partitioning during sinistral transpression led to imbrication in the foreland and oblique thrusting of the basement over more distal supracrustal rocks. This event is coeval with transpressional deformation in the Kaoko and Gariep belts, indicating a distinct two-stage tectonic history driven by the three-way convergence between the Congo, Kalahari, and South American cratons.

1 Introduction

The exhumed roots of orogenic belts and their interactions with foreland domains reveal fundamental details about the evolution of orogenic crustal thickening, and assessing the nature of these events requires the integration of structural and metamorphic petrological observations with geochronological data (e.g. Meira et al., 2019; Percival et al., in review; Tajčmanová et al., 2006). The correlation of the growth of dated minerals with specific structures and tectonic events allows the construction of P–T–t paths, which can then be used to interpret the development of orogens on a large scale (e.g. Coelho et al., 2017; Goscombe et al., 2017; Goscombe et al., 2018; Larson et al., 2020; Schulmann et al., 2009).

The Dom Feliciano Belt, outcropping in southern Brazil and Uruguay, is part of the larger South Atlantic Neoproterozoic Orogenic System (SANOS; Konopásek et al., 2020 Fig. 1a). The belt represents the western half of a largely symmetric orogenic structure with a distinct two-stage evolution. Early crustal thickening is characterised by west-directed thick-skinned thrusting and development of a high-grade metamorphosed hinterland, which coincides with early thin-skinned thrusting and development of peak metamorphic conditions in the foreland. After the early compressional movement along the thrust system ended, deformation in the orogen transitioned into a transpressional phase, leading to the development of large sub-vertical shear zones overprinting previous flat-lying deformation fabrics and down-grading peak metamorphic assemblages (Battisti et al., 2018; De Toni et al., 2020a; Percival et al., in review).

Recent studies in the northern and central Dom Feliciano Belt have recognised the coupled tectono-metamorphic evolution of the orogenic foreland and hinterland domains. In the northern Dom Feliciano Belt (Santa Catarina state), recent studies hypothesise that low- to medium-grade metamorphism in the foreland records the progressive west-directed over-thrusting of the hinterland at ca. 660–650 Ma, marking the earliest evidence of crustal thickening in the orogen (Percival et al., in review; De Toni et al., 2020). The same relationship is inferred in the central belt (Rio Grande do Sul state), although there are currently no constraints on the timing of events in the central foreland (Battisti et al., 2018; De Toni et al., 2021). In the southern Dom Feliciano Belt (Uruguay), west-directed thrusting and high

temperature metamorphism at ca. 650–640 Ma is documented only in the Punta del Este Terrane (Gross et al., 2009; Oyhantçabal et al., 2009a), which is defined in this study as part of the orogenic hinterland. The evolution of the southern foreland, however, is more complex, and events are not as well understood, in part owing to strong reworking by post-collisional sub-vertical shear zones during the transpressional stage of orogenesis. Although there are abundant geochronological data from the hinterland and the surrounding shear zones (Lenz et al., 2011; Masquelin et al., 2011; Oriolo et al., 2016a; Oriolo et al., 2016b; Oyhantçabal et al., 2009a; Will et al., 2019), geochronological constraints for the Neoproterozoic metamorphic history of the foreland are lacking. As such, it is difficult to compare the evolutionary histories of the foreland and hinterland domains.

The aim of this work is to investigate the tectono-metamorphic evolution of the southern Dom Feliciano Belt foreland and hinterland domains in Uruguay, in particular the potential relationship between high-grade metamorphic units in both domains and the timing of crustal thickening and metamorphism in the foreland. Using detailed petrological and geochronological data, this work documents, and provides constraints on, the timing and conditions of two distinct tectonic events. Furthermore, the integration of this data with geochronological data from surrounding units is used to present a tectonic model for the evolution the southern Dom Feliciano Belt.

2 Geological setting

The Dom Feliciano Belt is part of the larger Kaoko–Dom Feliciano–Gariep orogenic system, which forms the southernmost part of the SANOS (Fig. 1b). The belt can broadly be divided into orogenic foreland and hinterland domains, which are generally further divided into a series of linear tectonostratigraphic units. From east to west, these are 1) a high-grade metamorphic basement of the hinterland with locally preserved syn-orogenic cover (Cerro Olivo, Várzea do Capivarita, and Porto Belo complexes), 2) the Granite Belt, 3) the Schist Belt, 4) the foreland basins, and 5) the foreland basement (Basei et al., 2000; De Toni et al., 2020b; Gross et al., 2006; Martil et al., 2017; Oyhantçabal et al., 2009a; Preciozzi et al., 1999).

In the southern Dom Feliciano Belt, the foreland consists of cratonic basement overlain by a series of Paleo- to Neoproterozoic supracrustal sequences (Fig. 2a and b). The Nico Pérez Terrane represents the reworked cratonic margin of the belt, which is separated from the relatively unaffected Piedra Alta Terrane, part of the Rio de la Plata Craton, by the Sarandí del Yí Shear Zone along its western boundary (Oriolo et al., 2015; Rapela et al., 2011). The Nico Pérez Terrane is comprised of several Archean to Paleoproterozoic basement units that have been weakly to strongly reworked during the Neoproterozoic (Masquelin et al., 2021; Oyhantçabal et al., 2011a; Oyhantçabal et al., 2012). Recent works have highlighted the allochthonous nature of the Nico Pérez Terrane relative to the Rio de la Plata Craton (Oyhantçabal et al., 2011a; Rapela et al., 2011), and its likely origin as a part of the Congo Craton rifted away prior to orogenesis (Oriolo et al., 2015; Oriolo et al., 2016c; Oyhantçabal et al., 2021; Percival et al., 2021).

The foreland basement is overlain by (now metamorphosed) pre-orogenic sedimentary sequences of the Schist Belt, known as the Lavalleja Complex (*sensu lato*), as well as Ediacaran syn- to post-collisional foreland basin deposits (Basei et al., 2000; Oyhantçabal et al., 2021). Although the litho- and tectono-stratigraphy of the metasedimentary sequences is complex and poorly defined (see Oyhantçabal et al., 2021), the strongly metamorphosed and deformed supracrustal rocks belonging to the Lavalleja Complex (Schist Belt) can generally be divided into two pre-Neoproterozoic units; the Cebollatí and

Zanja del Tigre complexes (Hartmann et al., 2001; Oriolo et al., 2019; Oyhantçabal et al., 2021). The potential correlation of the pre-orogenic sedimentary history of the Lavalleja Complex in Uruguay with the Schist Belt in the central and northern Dom Feliciano Belt is complicated by the apparent predominance of Paleoproterozoic to Mesoproterozoic sedimentary ages (Chiglino et al., 2010; Gaucher et al., 2011; Hartmann et al., 2001; Oriolo et al., 2019; Oyhantçabal et al., 2018). This contrasts with the Schist Belt in Brazil where early-Neoproterozoic (ca. 810–770 Ma) sedimentary ages dominate (Percival et al., 2021; Pertille et al., 2017; Saalmann et al., 2011). The metasedimentary rocks of the Schist Belt in Uruguay show a range in metamorphic grade from lower greenschist to lower amphibolite facies conditions (Hartmann et al., 2001; Sánchez Bettucci et al., 2001). Both the basement and supracrustal units are intruded by syn- to post-collisional granitoids ranging in age from ca. 635 to 585 Ma (Lara et al., 2017; Oyhantçabal et al., 2007; Oyhantçabal et al., 2012).

The Campanero Unit represents a basement inlier of the Nico Pérez Terrane, and consists of ca. 1.7 Ga orthogneisses with subordinate high-temperature amphibolites and metasedimentary migmatites (Mallmann et al., 2007; Sánchez-Bettucci et al., 2004). From previous structural studies, the Campanero Unit is generally accepted to be a basement nappe that has been thrust over the Schist Belt (Mallmann et al., 2007; Oyhantçabal et al., 2018; Rossini and Legrand, 2003). Although the timing of high-T metamorphism in the Campanero Unit is so far unknown, the final cooling below ~500°C and potential exhumation of the unit, and thus the minimum age for metamorphism, is constrained by Ar–Ar in hornblende to ca. 564 ± 4 Ma (Oyhantçabal et al., 2009a).

The Zanja del Tigre Complex forms part of the Schist Belt outcropping immediately to the north and west of the Campanero Unit, and is comprised of a metamorphosed sedimentary sequence including metapelites, metapsammites, marbles, felsic metavolcanics, and gabbros (Oriolo et al., 2019). The metamorphic grade ranges from greenschist facies in the majority of the complex to lower-amphibolite facies conditions close to the contact with the Campanero Unit (Sánchez Bettucci et al., 2001). U–Pb concordia ages from igneous zircon in metavolcanic and metagabbroic rocks within the complex constrain the timing of sedimentation to between ca. 1480–1430 Ma (Gaucher et al., 2011; Oriolo et al., 2019).

The Sierra Ballena Shear Zone separates the foreland in the west from the hinterland to the east. The hinterland is represented by the Punta del Este Terrane, which is comprised of pre-orogenic basement complexes intruded by voluminous syn- to post-collisional granitoids of the Aiguá Batholith, and overlain by late-Neoproterozoic sedimentary successions including the Rocha, Sierra de Aguirre, and San Carlos formations. The basement is comprised of high temperature granulitic orthogneisses, paragneisses, amphibolites and migmatites of the Cerro Olivo Complex. Protolith ages from orthogneisses in this complex record an important magmatic episode during the middle Neoproterozoic at ca. 800–770 Ma (Lenz et al., 2011; Masquelin et al., 2011; Oyhantçabal et al., 2009a). Similar ages are preserved in the Várzea do Capivarita Complex in the central Dom Feliciano Belt and in the Coastal Terrane in the Kaoko Belt (Konopásek et al., 2008; Martil et al., 2017). This magmatic event has been interpreted as recording pre-orogenic rifting, potentially linked to rifting of the Nico Pérez–Luis Alves Terrane from the Congo Craton during the breakup of Rodinia (Konopásek et al., 2018; Oriolo et al., 2016c; Oyhantçabal et al., 2009a; Oyhantçabal et al., 2018; Rapela et al., 2011; Will et al., 2019), or continental arc magmatism (De Toni et al., 2020b; Lenz et al., 2011; Lenz et al., 2013; Masquelin et al., 2011). Central to the latter interpretation is the arc-like geochemical signature preserved in the rocks, although Konopásek et al. (2018) have argued that this may be inherited from crustal sources, and that the geochemical signature can be compatible with either a back-arc or purely continental rift-related setting.

3 Field relationships – structural geology and metamorphism

The primary fabric in the Campanero Unit is a high-grade gneissic to mylonitic foliation (S1; Figs. 2c & 3a). This fabric is predominantly flat-lying and is overprinted by two mutually near-orthogonal foliations, S2 and S3 (Fig. 2c), as well as associated macro-scale folding. Foliation S2 trends E–W and is defined by parallel muscovite and biotite overprinting the high-T S1 gneissic fabric. Foliation S3 is oriented N–S, largely parallel with the Sierra Ballena Shear Zone and thus comparable to S2 in the other units (Fig. 2c–e). The two overprinting foliations (S2 and S3) show similar metamorphic grade and degree of deformation and based on field observations it is difficult to unequivocally determine their relative age.

Two near-orthogonal stretching lineations are observed in the Campanero Unit; one trending NW–SE (L1) and another trending NNE–SSW (L2) (Fig. 2c). Due to similarities in orientation, L1 stretching lineations in the Campanero Unit have been correlated with L1 in the Cerro Olivo Complex (Oyhantçabal et al., 2009a), and thus potentially records early west-directed tangential shearing. Lineation L1 appears to be folded towards parallelism with the Sierra Ballena Shear Zone (see Oyhantçabal et al., 2009b), suggesting it has been deformed by, and thus predates, sinistral shearing along this boundary. Oyhantçabal et al. (2009b) also suggest that this probably indicates the partitioning of strain into contraction and wrench-dominated domains. Lineation L2, on the other hand, lies parallel to the Sierra Ballena Shear Zone suggesting that it developed during this later sinistral transpressional event. L2 is contained predominantly within the N–S-oriented S3 foliation and associated small shear zones, however some outcrops show lineations with similar orientation within the E–W-oriented S2. Considering this, and the potential partitioning of strain within, and adjacent to, the Campanero Unit, it is possible that the development of S2 and S3 was largely contemporaneous.

The dominant fabric in the Zanja del Tigre Complex is a low- to medium-grade schistosity (S1; Figs. 2d, 3c) characterised by lepidoblastic muscovite ± chlorite ± biotite. Foliation S1 is deformed by F2 folds with axes largely parallel to the Sierra Ballena Shear Zone, and is overprinted by an often pervasive

axial planar crenulation cleavage (S2; Figs. 2d & 3c). Sánchez Bettucci et al. (2001) described the same structural features across the whole of the southern part of the Schist Belt in Uruguay, and observed ubiquitous NW-directed thrust faults transecting the supracrustal rocks. They interpret the development of these thrust faults as likely contemporaneous with the development of F2 and S2. Sánchez Bettucci et al. (2001) further reported that the metamorphic grade in the Schist Belt increases from lower-greenschist facies to lower-amphibolite facies towards the southeast and the contact with the Campanero Unit, where the presence of staurolite and garnet marks the highest-grade rocks in this region. However, rocks showing lower-amphibolite facies metamorphic conditions can also be found in the west of the Zanja del Tigre Complex (locality UD17; Fig. 2a), as well as in the northeast within the Cebollatí Complex (Hartmann et al., 2001).

The primary structural feature of the hinterland basement (Cerro Olivo Complex) is a high-temperature deformation fabric trending 060° (S1; Fig. 2e). The fabric is characterised predominantly by granoblastic gneissose granulites varying in structure from strongly banded (Fig. 3d) to weakly foliated and almost massive with large garnet porphyroblasts (Fig. 3e). Stretching lineations (L1) associated with this high-T deformation trend predominantly E–W with shallow to moderate plunge (Figs. 2e and 3d), and include stretched quartz and feldspar aggregates, and oriented metamorphic minerals such as sillimanite (Gross et al., 2009; Masquelin et al., 2011). Minor outcrops of deformed porphyritic granites contain large K-feldspar porphyroclasts stretched and oriented with the main lineation trend (Fig. 3f). The L1 lineations have been interpreted to indicate west-directed tectonic transport during high-T metamorphism and foliation development (Masquelin et al., 2011). The complex is transected by the NE to NNE-trending Cordillera Shear Zone (Fig. 2a), which in some locations show parallel stretching lineations (L2) and evidence of sinistral shear sense, similar to the relationship between Campanero Unit and the Sierra Ballena Shear Zone (Masquelin et al., 2011; Oyhantçabal et al., 2009a).

4 Results

4.1 Sample description and mineral chemistry

Two samples from the Schist Belt, two from the Campanero Unit, and five from the Cerro Olivo Complex were collected for petrological and geochronological analysis (Fig. 2a). For samples used for thermodynamic modelling, mineral major element compositions were analysed using an electron microprobe CAMECA SX100 at the Faculty of Natural Sciences, Masaryk University, Czech Republic. An overview of the data are given in Supporting Information Tables S1 to S3, and analytical methods are given in Supporting Information Text S1. Mineral abbreviations follow Whitney and Evans (2010). Mineral compositions and endmember proportions are reported as follows: X_{Mg}=Mg/(Mg+Fe), X_{Sps}=Mn/(Mn+Fe+Mg+Ca), X_{Alm}=Fe/(Mn+Fe+Mg+Ca), X_{Prp}=Mg/(Mn+Fe+Mg+Ca), X_{Grs}=Ca/(Mn+Fe+Mg+Ca), X_{An}=Ca/(Ca+Na+K).

4.1.1 Samples from the Cerro Olivo Complex

Sample UB02 (S 34.90849°, W 54.82512°) is a fine-grained felsic granulite collected from the Cerro Olivo Complex. The rock shows a strong gneissic fabric (Fig. 3d) and contains the mineral assemblage plagioclase–K-feldspar–garnet–biotite–sillimanite–quartz, with minor ilmenite and rutile. Garnet grains are small (<250 μm) and rounded (Fig. 4e), and there is only minor compositional variation in garnet from core to rim ($Sps_{0.02}Alm_{0.73}Prp_{0.22}Grs_{0.03}$ – $Sps_{0.01}Alm_{0.70}Prp_{0.26}Grs_{0.03}$; Fig. 5b). Biotite grains (X_{Mg} = 0.57–0.66, Ti = 0.17–0.31 p.f.u) are small (<250 μm) and uncommon. The matrix is dominated by quartz and feldspar, showing a granoblastic texture and an average grain-size of ~100–150 μm.

Sample UB22 (S 34.57308°, W 54.470232°) is a medium-grained felsic granulite collected from the Cerro Olivo Complex. The sample contains the mineral assemblage plagioclase–K-feldspar–garnet–biotite–cordierite–ilmenite–quartz. Compositional sub-domains of cordierite enclosing sillimanite, hercynite and ilmenite are common (Fig. 4f), and secondary sericite is often found replacing feldspar (Fig. 4g). Garnet porphyroblasts are anhedral, and reach up to ca. 1.5 mm in width (Fig. 4g). Garnet is Alm-rich, and grains do not vary much in composition from core to rim ($Sps_{0.03}Alm_{0.82}Prp_{0.11}Grs_{0.04}$ –

$Sps_{0.03}Alm_{0.79}Prp_{0.15}Grs_{0.04}$; Fig. 5c). The cores of garnet porphyroblasts contain <100 μm rounded inclusions of biotite (X_{Mg} = 0.44, Ti = 0.31 p.f.u), ilmenite and hercynite. A weak gneissic foliation is defined by alternating cordierite-rich and quartz–feldspar-rich banding, and matrix biotite (X_{Mg} = 0.39–0.0.40, Ti (pfu) = 0.18–0.20) and elongated garnet grains are oriented with this fabric.

Sample UE08 (S 34.29184°, W 54.18184°) is a coarse-grained granulite collected from the Cerro Olivo Complex. The sample contains the mineral assemblage plagioclase–K-feldspar–biotite–garnet–quartz–sillimanite, with accessory ilmenite and rutile, and secondary muscovite. Garnet porphyroblasts are large, reaching up to 7 mm in diameter, and the largest grains contain abundant inclusions of rounded biotite (X_{Mg} = 0.58–0.59, Ti (pfu) = 0.25–0.27), plagioclase, quartz, rutile and ilmenite (Fig. 4H and i). No rutile is found in the matrix. Garnet is Alm-rich and shows prograde compositional zoning from the core through the mantle ($Sps_{0.05}Alm_{0.65}Prp_{0.22}Grs_{0.08}$ – $Sps_{0.04}Alm_{0.62}Prp_{0.22}Grs_{0.12}$; Fig. 5d), and apparent retrograde re-equilibration at the rims ($Sps_{0.06}Alm_{0.76}Prp_{0.14}Grs_{0.04}$). Matrix biotite ($X_{Mg}$ = 0.44–0.46, Ti (pfu) = 0.28–0.31) is randomly oriented, and predominantly located interstitially between larger matrix plagioclase, quartz and garnet grains.

Sample UC73 (S 34.30564°, W 54.17755°) is a coarse-grained, migmatitic, felsic granulite collected from the Cerro Olivo Complex. The sample shows a gneissic foliation defined by alternating quartz-rich and feldspar-rich layers and contains the mineral assemblage quartz–plagioclase–K-feldspar–biotite–garnet–sillimanite–ilmenite. Garnet porphyroblasts are irregularly shaped with rounded edges, reaching up to 3 mm in diameter (Fig. 4j). Most garnet grains contain cores with small (<200 μm), rounded inclusions of quartz, rutile, and biotite (X_{Mg} = 0.67, Ti (pfu) = 0.38), and a small number contain elongate ilmenite inclusions (Fig. 4j and k). There is no rutile in the matrix. Garnet is an Alm- and Prp-rich solid solution ($Sps_{0.01}Alm_{0.60}Prp_{0.32}Grs_{0.07}$ – $Sps_{0.02}Alm_{0.62}Prp_{0.33}Grs_{0.03}$; Fig. 5e), showing a relatively compositionally stable core and mantle. There is a slight increase in the Sps, Alm and Prp components, and a decrease in the Grs component, towards the rim, likely reflecting retrograde re-equilibration. Matrix biotite (X_{Mg} = 0.49–0.60, Ti (pfu) = 0.29) is oriented parallel to the primary foliation.

Sample UA38 (S 34.64827°, W 54.73200°) is from a deformed porphyritic granite of the Cerro Olivo Complex. Large porphyroclasts of K-feldspar (up to several cm; Fig. 3f) are surrounded by a

recrystallized matrix of quartz, plagioclase, K-feldspar, biotite, and an opaque mineral, with accessory apatite and zircon. The coarse-grained nature of recrystallized feldspars and quartz points at high-temperature deformation, likely coeval with the formation of surrounding migmatites. Biotite is occasionally converted to chlorite, suggesting minor retrogression of the high-temperature mineral assemblage.

4.1.2 Samples from the Campanero Unit

Sample UF36 (S 34.63407°, W 55.23149°) is an orthogneiss collected from the Campanero Unit. The sample contains the mineral assemblage biotite–plagioclase–K-feldspar–quartz, with accessory monazite and zircon. The rock is coarse-grained (ca. 500 μm) and equigranular, pointing to deformation at high temperatures, and intergrowths of quartz and feldspar, though uncommon, suggest a degree of partial melting. Monazite grains are large, reaching up to ca. 200 μm. Lepidoblastic biotite crystals define the primary (S1) foliation.

Sample UC40 (S 34.59390°, W 55.17511°) is a metasedimentary migmatite collected from the Campanero Unit. The rock consists of melanocratic–mesocratic (Fig. 3b) and leucocratic parts, with the former showing coarse-grained texture with the mineral assemblage biotite–sillimanite–plagioclase–K-feldspar–quartz with accessory monazite and zircon, and secondary muscovite (Fig. 4d). The leucocratic parts are predominantly quartz-feldspathic with small amounts of biotite and accessory zircon. From field relationships it is not clear whether the leucocratic parts represent leucosomes or dykes that intruded the (meta)sedimentary protolith of the rock.

4.1.3 Samples from the Schist Belt

Sample UE14B (S 34.60547°, W 55.27147°) is a metapelitic schist collected from the Zanja del Tigre Complex. The rock contains the mineral assemblage muscovite–biotite–garnet–staurolite–quartz–ilmenite, with secondary chlorite. Garnet grains are euhedral crystals up to 1mm across (Fig. 4a), and show prograde growth with decreasing Sps, and increasing Alm, Prp and Grs components from core to

rim ($Sps_{0.10}Alm_{0.75}Prp_{0.06}Grs_{0.08}$–$Sps_{0.04}Alm_{0.79}Prp_{0.07}Grs_{0.10}$; Fig. 5a). Garnet is often completely eroded (likely by mechanical processes during thin section preparation), and relict grains commonly show heavy fracturing and replacement by secondary oxide minerals. Despite this, there does not appear to be retrograde replacement of garnet by chlorite. Garnet porphyroblasts show concentric zoning delineated by micro inclusions of opaque oxides with no evidence of preferred orientation, suggesting growth prior to the development of a strong foliation. However, few fresh garnet porphyroblasts remain to study. Staurolite grains (X_{Mg} = 0.10–0.14), in contrast, contain larger and more abundant visible inclusions (Fig. 4b), including ilmenite oriented to a previous fabric suggesting syn- to post-kinematic growth. Biotite (X_{Mg} = 0.36–0.38, Ti = 0.06–0.09 p.f.u) is commonly overgrown by S2-parallel muscovite, and very occasionally replaced by secondary chlorite. The dominant fabric is a strong crenulation cleavage oriented 035/70E, likely transposing S1 and apparently coeval with the peak metamorphic assemblage at this locality.

Sample UD17 (S 34.17881°, W 55.28727°) is a metapelitic schist collected from the north-western Schist Belt, close to the contact with the Sarandí del Yí Shear Zone (Fig. 2a). The rock contains the same mineral assemblage as sample UE14B, and ~1mm euhedral garnet grains show similar prograde zoning with decreasing Sps and Grs and increasing Alm and Prp from core to rim ($Sps_{0.11}Alm_{0.73}Prp_{0.06}Grs_{0.1}$ – $Sps_{0.07}Alm_{0.80}Prp_{0.07}Grs_{0.06}$). Staurolite ($X_{Mg}$ = 0.09–0.11) and biotite (X_{Mg} = 0.35, Ti (pfu) = 0.09–0.10) grains show similar size, shape, and composition to those in sample UE14B (Fig. 4c).

4.2 Phase equilibria modelling

P–T estimates were calculated using the PerpleX software package of Connolly (2005) (ver. 6.9.0) with the thermodynamic dataset DS6.22 of Holland and Powell (2011). The following solution models were used for all pseudosections: garnet, chlorite, chloritoid, cordierite, white mica, biotite and staurolite from White et al. (2014), ternary feldspar from Fuhrman and Lindsley (1988), and ilmenite from White et al. (2000) as modified by White et al. (2014). In addition, the melt model from White et al. (2014) was used to calculate pseudosections for the high temperature samples (UE08, UB02, UB22, UC73 and UC40), and the spinel model from White et al. (2002) was used for sample UB22.

All pseudosections were modelled in the $MnO–Na_2O–CaO–K_2O–MgO–Al_2O_3–SiO_2–H_2O–TiO_2$ (MnNCKFMASHT) system. Bulk rock compositions used for calculations were estimated by whole-rock powders, conducted by lithium borate fusion inductively coupled plasma emission spectroscopy (ICP ES) at Bureau Veritas Mineral Laboratories in Vancouver, Canada, and are presented with the pseudosection figures. None of the analysed samples contain minerals with a significant Fe_2O_3 component, so the system was simplified by excluding O_2/Fe_2O_3. Samples that show evidence of supra-solidus metamorphic equilibration (samples UE08, UB02, UC73 and UB22) were modelled in H_2O-constrained conditions, as to model melt-present phase fields. Samples UE14B and UD17, which are both sub-solidus metapelites, were modelled in H_2O-saturated conditions. Mineral compositional contours were calculated for each pseudosection, and compared with the observed values as determined by microprobe analysis to better constrain the estimated P─T conditions (e.g. Stüwe and Powell, 1995). Contours are presented with a spacing of 0.01 units and show only the compositional range of a given mineral as measured by microprobe ± 0.01 units.

Prograde metamorphic garnet growth up to upper amphibolite-facies conditions has been shown to fractionate elements faster than diffusional processes can maintain equilibrium, resulting in the progressive removal of elements from metamorphic reactions in the rock matrix (Caddick et al., 2010; Marmo et al., 2002). Using the X_{Sps} component as an indicator of Rayleigh fractionation during prograde growth (Hollister, 1966), only garnet from samples UE14B and UD17 show evidence of typical prograde growth without significant diffusional re-equilibration. For this reason, garnet fractionation calculations

were conducted for samples UE14B and UD17 to better constrain peak metamorphic conditions during matrix and garnet rim equilibration.

Granulites commonly reflect the residuum product of melting processes. As such, partial melt extraction from granulitic rocks has the potential to fractionate elements from their protolith compositions, potentially obfuscating estimates of P–T conditions for garnet core growth and early prograde metamorphic histories (Bartoli, 2017; Indares et al., 2008; White et al., 2004). Melt-reintegration calculations can be used to investigate these early prograde histories. Of the granulite-facies samples in this study, however, only garnet cores from sample UE08 show evidence of prograde growth, so inferring a P–T path for melt reintegration is difficult or ineffective for the remaining samples. Melt reintegration calculations for sample UE08 (data not shown), following the single-step method of Indares et al. (2008), provide an estimate that the rock underwent only minor melt loss (<5 wt%), and models calculated using the resulting protolith (pre melt-loss) bulk composition do not have significant effects on mineral compositional isopleths or the shapes of relevant stability fields when compared to calculations using the measured bulk rock.

4.2.1 Modelling samples from the Schist Belt

To estimate P–T conditions for both samples UE14B and UD17, phase equilibria models were calculated using measured bulk rock compositions (Table S1) to constrain conditions of early garnet growth. For both samples, garnet compositional isopleths for observed Sps, Alm, Prp and Grs compositions constrain the temperature of early core garnet growth to between ~525–540°C (Fig. 6a and d). The intersecting isopleths do not provide a reliable pressure constraint, but the Grt-in line provides a minimum pressure constraint of ~4kbar. We infer that the garnet core compositions measured by microprobe record true early growth, and thus it is unlikely that the pressure conditions lie above ~6 kbar where the Grt-in line deviates from the modelled compositional isopleths (Fig. 6b and e). To estimate peak matrix equilibration conditions, multiple exploratory garnet fractionation calculations and pseudosections were made using varying P–T values for the garnet core starting point (data not shown), based on the above-

mentioned estimated P–T range. Garnet fractionation was observed to rapidly raise the pressure of the Grt-in line but did not significantly affect the position of calculated mineral isopleths for garnet rims and matrix minerals, or the shapes of stability fields. The results of modelling with and without fractionation were thus seen to be nearly identical, and we conclude that the results using measured bulk compositions without garnet fractionation provide accurate estimates of matrix equilibration conditions.

For sample UE14B, mineral isopleths for X_{Sps} and X_{Mg} in garnet, X_{Mg} in staurolite, and Ti (pfu) in biotite all intersect in the phase field containing the mineral assemblage Chl–Ms–Bt–Grt–St–Ilm, indicating peak P–T conditions of 6.0–7.0 kbar and 550–570°C (Fig. 6a). However, the observed mineral assemblage does not contain primary chlorite, suggesting that the true P–T conditions lie at slightly higher temperatures past the chl-out line.

For sample UD17, contoured mineral isopleths for X_{Sps}, X_{Alm}, X_{Prp} and X_{Grs} content in garnet, X_{Mg} in staurolite, and Ti (pfu) content in biotite all intersect within the phase field containing the mineral assemblage Chl–Ms–Bt–Grt–St–Ilm, indicating peak P–T conditions of 5.5–6.5 kbar and 545–560°C (Fig. 6d). Like sample UE14B, the observed mineral assemblage does not contain primary chlorite, and so we infer that the true P–T conditions reached slightly higher peak temperatures than is indicated in these models, at least past the Chl-out line.

4.2.2 Modelling samples from the Campanero Unit

Figure 7 shows a pseudosection calculated in H2O-undersaturated conditions for sample UC40 (Fig. 7a) and contoured for X_{Mg} and Ti (pfu) in biotite (Fig. 7b), and X_{An} in plagioclase (Fig. 7c). There is no garnet in the sample to help constrain P–T conditions, but the isopleths for biotite and plagioclase intersect within the phase field containing the observed mineral assemblage biotite—plagioclase—K-feldspar—sillimanite—melt and constrain peak metamorphic conditions to within ~4.2–9.0 kbar and 670–770°C (dashed white line in Fig. 7a).

4.2.3 Modelling samples from the Cerro Olivo Complex

Figure 8a shows a pseudosection calculated in H2O-undersaturated conditions for sample UB02, and is contoured for X_{Sps}, X_{Alm}, X_{Prp} and X_{Grs} content in garnet rims (Fig. 8b), X_{An} in plagioclase, and Ti (pfu) in biotite (Fig. 8c). All of the isopleths intersect within the phase field containing the observed mineral assemblage Bt–Grt–Pl–Kfs–Sill–Ilm–Liq and constrain metamorphic P–T conditions to within 5.2–7.2 kbar and 780–800°C (dashed white line in Fig. 8a).

Figure 9a shows a pseudosection calculated for sample UB22 in H2O-undersaturated conditions, and is contoured for observed X_{Sps}, X_{Alm}, X_{Prp} and X_{Grs} in garnet rims (Fig. 9b), X_{An} in matrix plagioclase, X_{Mg} and Ti (pfu) in matrix biotite, and X_{Mg} in matrix cordierite (Fig. 9c). These contoured isopleths intersect within the phase fields containing the observed dominant assemblage of Bt–Grt–Pl–Kfs–Crd–Ilm–Liq ± Sil, constraining metamorphic equilibration conditions to 3.9–4.5 kbar and 745–760°C (dashed white line in Fig. 9a). A separate pseudosection was calculated for the hercynite-bearing sub-domains using an estimated composition calculated by measuring the volume-proportion of each phase from thin section BSE images. The resulting model estimated similar P–T conditions, and so is not shown.

Figure 10 shows a pseudosection calculated for sample UE08 in H2O-undersaturated conditions and shows contours for the observed garnet core composition and matrix assemblage. Contoured isopleths calculated for X_{Sps}, X_{Alm}, X_{Prp} and X_{Grs} content in garnet cores, and X_{Mg} in biotite inclusions within garnet, intersect within error at 9.7–11.4 kbar and 760–780°C (Fig. 10b). Isopleths for X_{Sps}, X_{Alm} and X_{Grs} content in garnet rims, X_{Mg} in matrix biotite, and X_{An} in matrix plagioclase (not shown), all intersect within the phase fields containing the assemblage Bt–Grt–Pl–Kfs–Sill–Liq ± Rt ± Ilm, constraining matrix equilibration conditions to 5.5–8.5 kbar and 740–790°C (Fig. 10c).

Figure 11a shows a pseudosection calculated in H2O-undersaturated conditions for sample UC73 and is contoured for garnet rim (Fig. 11b) and matrix assemblage minerals (Fig. 11c). The contours for garnet core end-member compositions and biotite X_{Mg} (not shown) are vertical and parallel, with no pressure constraints, but suggest temperatures between 810–840°C. Furthermore, rutile inclusions within garnet suggest higher-pressure conditions, above ~7kbar, during early garnet growth. Isopleths calculated for observed X_{Sps}, X_{Alm}, X_{Prp} and X_{Grs} in garnet rims, X_{An} in matrix plagioclase, and X_{Mg} in biotite rims

intersect within the phase field containing the observed assemblage Bt–Grt–Pl–Kfs–Sill–Ilm–Liq at 5.2–6.9 kbar and 775–790°C.

4.3 Geochronology

4.3.1 Garnet Lu-Hf geochronology and trace element chemistry

The results of Lu–Hf dating are summarised in Table 1 and Figure 12a–c. Sample preparation and analytical methods are summarised in Anczkiewicz et al. (2004) and Anczkiewicz and Thirlwall (2003). Standards reproducibility and constants used for calculations are given in the footnote to Table 1. Lu–Hf isotope dilution analysis of three to four garnet and one whole-rock fractions were used to define isochron ages for two granulites from the Cerro Olivo Complex (samples UE08 and UB02) and one metapelitic schist from the Zanja del Tigre Formation (sample UE14B). The obtained isochron ages are 654 ± 23 Ma (MSWD = 10.0) for sample UE08, 638.5 ± 2.2 Ma (MSWD = 1.13) for sample UB02, and 582 ± 23 Ma (MSWD = 8.3) for sample UE14B (Table 1; Fig. 12a–c).

Trace element concentrations were analysed along transects across representative garnet grains to determine the potential influence of mineral inclusions on isotope dilution results, and the influence of compositional zonation on the age interpretation. Analytical methods are detailed in Supporting Information Text S1. The results of trace element analysis from representative grains in samples UE08, UB02 and UE14B are summarised in Figure 12d–f. The garnet from sample UB02 does not appear to show consistent core–rim zonation, although there is minor variation in relevant trace element concentrations across the transects (Fig. 12d). Hf concentrations are high, predominantly ranging between 1.0–3.0 ppm despite an apparent lack of hf-rich inclusions. Garnet porphyroblasts from sample UE08 show roughly M-shaped Lu and Y zonation, with slowly increasing concentrations from the core into the mantle, a sharp increase at the edge of the mantle, and then a sharp decrease towards the rim (Fig. 12e). Regular gaps in the profile are due to mineral inclusions such as quartz, plagioclase and biotite (Fig. 4i). Hf concentrations in inclusion-free parts of the garnet from sample UE08 are typically between 0.1–0.2 ppm, characteristic of metamorphic garnet (Anczkiewicz et al., 2014; Cheng, 2019;

Scherer et al., 2000), whereas large spikes represent Hf-rich micro- to sub-micro- mineral inclusions. Garnet porphyroblasts from sample UE14B show strong bell-shaped Lu and Y zonation, with the highest concentration in the cores, and decreasing dramatically towards the rims (Fig. 12f). Hf concentrations are highly variable, but typically range between 0.2–0.5 ppm in clean parts of the garnet. Higher Hf concentrations are predominantly correlated with alteration zones within cracks, but also regions with high concentrations of sub-micron inclusions of opaque oxides, likely ilmenite (Fig. 12f).

4.3.2 Interpretation of Lu-Hf garnet ages

Sample UB02 shows good agreement between estimates of Hf concentration from isotope dilution versus LA-ICP-MS analysis (Fig. 12, Table 1), indicating that the analytical results for this sample were not significantly affected by contamination from Hf-rich inclusions. Trace element profiles show relatively flat Lu and Y trends (Fig. 12d). Theoretical studies show that the closure temperature of Lu in garnet is lower for smaller grain sizes (Dodson, 1973; Ganguly and Tirone, 1999), such as those in sample UB02, which combined with the high temperatures experienced by the sample may be responsible for intracrystalline Lu diffusion (Anczkiewicz et al., 2012). Similarly, recrystallisation of garnet during peak metamorphic conditions may be responsible for the homogeneous trace element transect. Despite possible complications concerning diffusion or recrystallisation, we interpret the Lu–Hf age obtained from sample UB02 as reflecting the timing of peak, or near peak, metamorphism recorded in the rock.

Samples UE08 and UE14B, in contrast, show an order of magnitude difference in Hf concentration between isotope dilution analysis and LA-ICP-MS analysis of clean garnet. For sample UE08, the high Hf concentrations obtained by isotope dilution are likely due to Hf-rich inclusions in garnet such as titanite and zircon (Fig. 12e). It is thus likely that inclusions in garnet are responsible for the low $^{176}Lu/^{177}Hf$ ratios from sample UE08, which is in turn responsible for the low precision of the isochron age (Table 1). This large error makes it impossible to compare the Lu–Hf garnet age with metamorphic zircon ages. However, considering the differing P–T conditions between core growth and rim

equilibration, it is possible that the high imprecision is the result of age disparity between the different garnet zone domains, and thus the age of 654 ± 23 Ma may represent an average age of prolonged growth and/or the effects of diffusive relaxation of garnet rims at high temperatures. Despite these complications, the ages obtained from samples UB02 and UE08 overlap within error.

Sample UE14B similarly shows higher Hf concentration from isotope dilution analysis compared with LA-ICP-MS analysis of clean garnet. Contamination from alteration products in micro cracks is unlikely, considering the effort to remove impure fragments by manual picking, ultrasonic bath treatment, and through acid leaching. It is more likely that Hf contamination comes from high-density sub-micro inclusions of ilmenite, which have a higher chance of evading removal but which should not pose a problem in the accuracy of the isochron age. Furthermore, due to high Lu concentrations in the garnet (Table 1, Fig. 12f), we obtained high $^{176}Lu/^{177}Hf$ ratios, meaning that it is unlikely that Hf contamination had a significant effect on age precision. Despite this, the resulting four point isochron shows a large error and large MSWD, which appears to be due to a single garnet fraction (Grt3). Removing this anomalous fraction results in a higher precision age of 584.0 ± 2.4 Ma (Table 1), although analytically there is no known problem with this fraction and so the low precision age will be considered throughout the rest of the text. Considering the prograde, bell-shaped distribution of Lu in garnet, we interpret the isochron age of 582 ± 23 Ma as representing the timing of early garnet growth in sample UE14B.

4.3.3 U–Pb dating - sample descriptions and results

Zircon and monazite grains were analysed for U–Pb age dating to complement garnet Lu–Hf ages in the Cerro Olivo Complex, as well as to determine the timing of metamorphism in the Campanero Unit. Before analysis, cathodoluminescence (CL) images of zircon grains were taken to allow the targeting of specific areas and structures. Zircon U–Pb data were analysed at the Institute of Geology of the Czech Academy of Sciences, Prague, Czech Republic, using laser ablation inductively coupled plasma mass spectrometry (LA-ICP-MS). Analytical methods are presented in Supporting Information Text S1 and Table S4. Monazite U–Pb data, and zircon U–Pb data from one sample (UA38), were analysed at the

NordSIM facility at the Swedish Museum of Natural History in Stockholm using secondary ion mass spectrometry (SIMS).

4.3.3.1 Zircon U–Pb ages from the Cerro Olivo Complex

Zircon grains from sample UB02 are ~150–250 μm in length and are predominantly rounded and anhedral in shape (Fig. 13). Most grains show weak, patchy zoning (Fig. 13a and b), or show no zoning at all (Fig. 13c), although grains with oscillatory zoning are not uncommon. Grains with oscillatory zoning almost always have overgrowth rims of varying thickness (Fig. 13d). From LA-ICP-MS isotopic analysis of 56 spots on zircon, 6 provided >10% discordant dates and were not considered further. From the remaining 50 dates (Fig. 14a), 40 closely clustered dates combine to give a concordia age of 649 ± 6 Ma (Fig. 14b). The remaining dates are individually scattered up to ca. 800 Ma, with a minority of individual dates younger than ca. 640 Ma that are considered as outliers and not significant. The ca. 650 Ma dates come from the weakly-zoned to un-zoned grains and from overgrowth rims, whereas the older dates come from grains and cores with well-defined, oscillatory zoning (Fig. 13a–d). Based on these observations, we interpret the ca. 649 Ma concordia age as reflecting the timing of granulite-facies metamorphism, whereas the remaining older dates are likely relict grains from the igneous protolith.

Zircon grains from sample UE08 are between ~100–250 μm in length, and are predominantly long, euhedral crystals, although a subordinate number of grains are short and oval-shaped, occasionally with rounded edges (Fig. 13e–h). A few grains show no internal zoning, or very small, zoned cores (Fig. 13e and f), whereas most of the grains show oscillatory zoning with thin, amorphous overgrowth rims (Fig. 13g and h). From LA-ICP-MS isotopic analysis of 70 spots, 10 provided >10% discordant dates and thus were not considered further. From the remaining 60 dates (Fig. 14c), two clusters of dates are observed at ca. 650 and ca. 1250 Ma. The younger discordant cluster produced a discordia line with a lower intercept of 642 ± 3 Ma (Fig. 14d). A small cluster (six analyses) of <1% discordant dates produced a concordia age of 646 ± 6 Ma (Fig. 14e), overlapping within error with the intercept age. The younger cluster of dates (<700 Ma) come from zircon grains with only weak zoning, or from overgrowth rims around strongly-zoned cores (Fig. 13e–h). The older dates are from zircon grains showing

oscillatory zoning, both with and without overgrowth rims. Based on these observations, we interpret the concordia and discordia ages as reflecting the timing of metamorphism, whereas the remaining older dates are likely inherited detrital grains.

Zircon grains extracted from sample UA38 are ca. 100–170 μm long (Fig. 13i–l). CL images revealed that the grains are mostly oscillatory-zoned and have no significant inherited cores. Some grains have CL-bright and mostly <10 m thick rims that may represent metamorphic overgrowths (Fig. 13i and l). LA-ICP-MS isotopic analysis of the zircon (25 analytical spots) yielded a concordia U–Pb age of 656 ± 4 Ma (Fig. 14f), whereas nine SIMS analyses in oscillatory-zoned parts of the grains combine in a concordia U–Pb age of 654 ± 3 Ma (Fig. 14g). Both ages are indistinguishable within error and are interpreted as the igneous protolith age of the sample.

4.3.3.2 Monazite and zircon U–Pb ages from the Campanero Unit

Monazite grains from sample UF36 reach ~100–200 μm in length, and predominantly show rounded edges. Irregular, cloudy internal zoning (Fig. 13m–p) suggests growth during metamorphism (Schulz, 2021). SIMS analysis of 21 analytical spots from 16 grains provided data that combine to give a U–Pb concordia age of 583 ± 6 Ma (Fig. 14h). We interpret this age as reflecting the timing of peak metamorphism.

Monazite grains from the melanocratic part of sample UC40 are ca. 100–190 μm in length, and often show concentric or sector zoning, with rounded to euhedral crystal shapes (Fig. 13q–t). Despite the chemical zonation observed in BSE images, there is no distinct age zonation in any of the grains. SIMS analysis of 19 analytical spots from 10 grains provided data that combine in a concordia U–Pb age of 572 ± 5 Ma (Fig. 14i). We interpret this age as reflecting the timing of peak metamorphism during partial melting.

Zircon grains separated from the leucocratic portion of sample UC40 rock are ca. 130–300 μm long. CL imaging reveals that all grains are either entirely oscillatory-zoned, or they show oscillatory-zoned outer parts surrounding indistinct sector-zoned or featureless cores. From 46 grains analysed by LA-ICP-MS,

20 of them provided >10% discordant dates and these were not considered further. The remaining 26 analytical spots yielded a spectrum of dates, with one cluster around ca. 630 Ma and the rest spread across the Mesoproterozoic–Archean (Fig. 14j). The scatter of the Neoproterozoic cluster did not allow calculation of a concordia age (Fig. 14k). However, the $^{206}Pb/^{238}U$ dates of the youngest cluster combine into a weighted average mean age of 633 ± 8 Ma (95% conf.), which we interpret as being rather imprecise and probably inaccurate but still the best estimate of the crystallization of the leucocratic part of the rock (Fig. 14l). The remaining dates between ca. 1.36 and 3.00 Ga are interpreted as coming from inherited, xenocrystic grains.

5 Discussion

5.1 P–T–t paths and the tectonic evolution of the southern Dom Feliciano Belt

5.1.1 The hinterland – Cerro Olivo Complex

The P–T–t data collected in this study are summarised in Figure 15. Thermodynamic modelling of metamorphic conditions for granulites of the Cerro Olivo Complex suggests their near-isothermal decompression at ~750–800°C, from upwards of ~10–11 kbar down to ~5.5–8 kbar. The pressure estimate from modelling of garnet cores from sample UE08, of ~10–11 kbar, is the only preserved record of earlier peak pressure conditions in these rocks, and suggests burial to a depth of ~35–40 km. Otherwise, all but one of the analysed samples record matrix equilibration at the latter pressure conditions of ~5.5–8 kbar, implying that this metamorphic event is ubiquitous across the complex and is likely associated with the observed dominant S1 high-temperature deformation fabric. Evidence of further decompression is recorded in one sample (UB22), which shows peak matrix equilibration conditions of ~750–780 and ~1.5–3.5 kbar. This sample shows no record of previous metamorphic equilibration conditions, within mineral cores or otherwise, and so decompression from higher pressures (~5.5–8 kbar) is inferred from temperature estimates in other granulitic samples and the absence of any geochronological evidence supporting a later high-T metamorphic event. Our data generally support previous P–T estimates of Gross et al. (2009), who found the same three-stage clockwise metamorphic path using combined conventional thermobarometry and phase equilibria modelling, although with somewhat differing results. Notably, their data suggest higher peak temperatures (830–950°C), and lower temperatures for the late decompression phase (600–750°C), but despite this their P–T estimates mostly overlap with those from this study. Similarly, high peak pressures of >10 kbar are in line with estimates from Will et al. (2020).

The two garnet Lu–Hf isochron ages, despite high imprecision from one of the samples (UE08; 654 ± 23 Ma), provide strong evidence for garnet growth, and thus metamorphism, between ca. 655–640 Ma. Considering the preservation of elevated pressure conditions during early garnet growth in sample UE08, the earlier age of 654 ± 23 Ma may correspond to the timing of earliest crustal thickening in the hinterland domain. As pre-orogenic rifting is estimated to have ended only by ca. 680–660 Ma (Konopásek et al., 2018), convergence and crustal thickening likely shortly followed crustal thinning. Thus, the burial of the hinterland domain to depths of at least ca. 40 km (Fig. 15), together with the intrusion of porphyritic granites (e.g., sample UA38), suggests significant thickening of already hot, thinned crust at ca. 655 Ma. The garnet from sample UB02, on the other hand, does not show evidence for the preservation of an earlier higher-pressure metamorphic event, and thus the age of 639 ± 2 Ma from this sample is the best estimate for the timing of the main metamorphic episode responsible for the development of S1 and L1; namely high-T/low-P metamorphism during decompression and E–W directed tectonic transport. The overlapping 641 ± 2 Ma U–Pb zircon intercept age, and similar 646 ± 3 Ma concordia age, from sample UE08 likely records this same event, during re-equilibration of the matrix. The U–Pb zircon age of 649 ± 1 Ma derived from sample UB02 is a noticeable discrepancy, as it is ca. 10 m.y. older than the Lu–Hf garnet age from the same sample, and shows a closer fit to the protolith age obtained from the orthogneiss sample UA38 (654 ± 3 SIMS and 656 ± 4 Ma LA-ICP-MS. However, considering that most zircon grains in sample UB02 contain ca. 800 Ma cores, the shift towards a slightly higher U–Pb concordia age can be explained by incomplete lead loss from protolith zircon. The same situation is seen in the discordant dates from sample UE08, but as the protolith zircon grains in this sample are much older it is clearer that the younger, re-equilibrated metamorphic dates are discordant and plotting away from the true age.

The data as presented point towards high temperature metamorphism and partial melting between ca. 655–640 Ma. The intrusion of porphyritic granites (such as sample UA38, and at localities UB26 and UA42) at ca. 655 Ma, and coeval medium-P/high-T granulite-facies metamorphism, marks the earliest phase of crustal thickening during orogeny (Fig. 16a). We interpret the subsequent isothermal decompression as following a clockwise P–T path, reflecting the exhumation of the orogenic hinterland

during progressive thrusting over the foreland. Calculating the difference between the peak and re-equilibration pressures (using UE08 garnet core and UB02 matrix P–T estimates) gives a decompression path between 2.5–6.2 kbar, which translates to a vertical exhumation of about 10–20 km (using an average crustal density of 2.8g/cm^3). Dividing these values by the duration of exhumation (17 ± 6 Ma; using the more precise 656 ± 4 Ma (UA38) age, and 639 ± 2 Ma (UB02) age) results in an estimated exhumation rate of between 0.6 (+0.3/-0.2) and 1.2 (+0.6/-0.3) km Myr^{-1} (Fig. 15a). These rates are relatively slow (e.g. Štípská et al., 2004; Tajčmanová et al., 2006), supporting the fact that almost no relict higher-P mineral assemblages are preserved.

Our geochronological data closely match metamorphic age constraints from Lenz et al. (2011) and Oyhantçabal et al. (2009a), who presented zircon U–Pb concordia ages from metamorphic rims in Cerro Olivo Complex gneisses of 653 ± 4 and 641 ± 17, respectively. Will et al. (2019) presented similar U–Pb zircon rim concordia ages of between ca. 655–642 Ma, as well as closely matching U–Pb monazite intercept ages of 647 ± 11, 639 ± 9, and 632 ± 12. We interpret the few individual zircon grains in sample UB02 that record ages between ca. 660–670 Ma as not statistically significant, and thus we do not consider them to be an adequate estimate of earliest metamorphism and crustal thickening, such as is suggested by Lenz et al. (2011) and Masquelin et al. (2011) based on similar age distributions in their samples. Furthermore, and as previously mentioned, the shift towards higher ages in some of these samples likely represent incomplete lead loss from Tonian-aged cores, and thus do not record true metamorphic ages.

Following exhumation, cooling of the hinterland below ~400°C was reached by ca. 630–620 Ma (Figs. 15a, b and 16b), as constrained by K–Ar cooling ages in muscovite and Ar–Ar cooling ages in hornblende (Oyhantçabal et al., 2009a; Will et al., 2019). The cooling rate is difficult to estimate due to overlapping age estimates, but it was likely quite rapid (Fig. 15b). However, by using the Lu-Hf garnet age and temperature estimate from sample UB02 (639 ± 2 Ma, ~790°C), and ignoring the errors associated with the two muscovite K–Ar cooling ages from Oyhantçabal et al. (2009a) (628 and 621 Ma, ignoring errors), we obtain a rough estimated cooling rate of between 20–45°C Myr^{-1} (Fig. 15b).

5.1.2 The foreland – Campanero Unit and Schist Belt

Thermodynamic modelling of the migmatitic Campanero Unit indicates metamorphic equilibration conditions between ~700–770°C and ~4–9 kbar, showing that the unit reached high enough temperatures for partial melting. Although the results overlap with those from the dominant P–T conditions recorded in the Cerro Olivo Complex (Fig. 15), the estimate is largely imprecise. In contrast with the Cerro Olivo Complex, the rocks in the Campanero Unit are not granulites, having the appearance of uppermost amphibolite-facies gneisses, and thus it is likely the true temperature conditions are on the lower end of this estimate. The imprecise and low-accuracy weighted mean zircon U–Pb age of 633 ± 8 from the leucocratic parts of sample UC40 suggests an early partial melting event recorded in the Campanero Unit that may be temporally close to the high-T metamorphism in the hinterland formed during early crustal thickening. This could explain the NW–SE orientation of stretching lineation L1 preserved in the Campanero gneisses (Fig. 2c), which likely formed during roughly E–W-directed tectonic transport like within the Cerro Olivo Complex. However, this age more closely matches the timing of earliest post-collisional granitic magmatism in the foreland at ca. 630 Ma (Hartmann et al., 2002; Lara et al., 2017; Oyhantçabal et al., 2009a), suggesting that these leucocratic veins may simply be minor dykes associated with early post-collisional melting in the foreland and are unrelated to metamorphism during early crustal thickening in the hinterland. More likely, the ca. 630 Ma dykes, and perhaps all of the magmatism of this age in the Nico Pérez Terrane, reflects the end of early orogenic loading of the foreland, as it coincides with the timing of exhumation and cooling of the hinterland determined by K–Ar ages (Oyhantçabal et al., 2009a) Unfortunately, the poor outcrop situation makes it difficult to accurately ascertain this relationship in the field. Instead, based on the monazite U–Pb concordia age from the melanocratic part of the same sample, and from another sample from the Campanero Unit (UF36), we infer that pervasive high-T metamorphism most likely occurred between ca. 585–570 Ma. This is ca. 65–80 Ma after the high-T metamorphic event during early crustal thickening recorded in the Cerro Olivo Complex.

Based on the garnet Lu–Hf age from sample UE14B (582 ± 23 Ma), metamorphism in the Zanja del Tigre Formation similarly occurred ca. 60 ± 20 Myr after early crustal thickening and high-T

metamorphism in the hinterland. Although the age is imprecise, it overlaps within error with the metamorphic ages from the Campanero Unit, suggesting that metamorphism in the Campanero and metasedimentary cover units was likely coeval. The estimated P–T conditions from the Schist Belt (samples UE14B and UD17, respectively) show that metamorphism in the metasedimentary cover units of the foreland followed a prograde path along an apparent geothermal gradient of ~25°C/km, reaching lower amphibolite facies at ~6–7kbar and ~550–560°C (Fig. 15). This contrasts with the high-T conditions recorded in the Campanero Unit. Metamorphism in the foreland at ca. 580–570 Ma is contemporaneous with much of the post-collisional magmatic rocks intruding the Nico Pérez Terrane and adjacent shear zones (Lara et al., 2017; Oyhantçabal et al., 2007; Oyhantçabal et al., 2009a; Oyhantçabal et al., 2012; Rapalini et al., 2015), suggesting that metamorphism may have been driven by thermal input from voluminous magmatic intrusions. However, despite the high apparent thermal gradient recorded in the Campanero Unit, the thermal gradient recorded in the metasedimentary cover units indicates prograde Barrovian-type metamorphism that is more consistent with tectonic burial than with the elevated geothermal gradients associated with thermal metamorphism (Fig. 15). Furthermore, pre- to syn-tectonic garnet and staurolite growth in the metapelites show that metamorphism was contemporaneous with deformation. Thus, we interpret this metamorphic event to confirm observations in the field that the Campanero Unit is thrust over the metasedimentary cover units of the foreland, with the Campanero Unit representing a deep, hot part of the foreland basement exhumed and thrust over the more external foreland between ca. 585–570 Ma (Fig. 16c), which supports field observations and structural analysis presented in previous studies.

This thrusting event, from ca. 585 Ma, is coeval with sinistral reactivation of major dextral orogen-parallel shear zones in the region. Sinistral deformation is recorded along the Sierra Ballena Shear Zone at 586 ± 2 Ma (Oyhantçabal et al., 2009b), and similarly along the Sarandí del Yí Shear Zone at ca. 595–585 (Oriolo et al., 2016b; Oyhantçabal et al., 2009b), which both show evidence of previous dextral movement starting from ca. 630 Ma. Based on the absence of clear asymmetric structures in many regions within the Sierra Ballena Shear Zone, and the presence of both sub-vertical and sub-horizontal stretching lineations, Oyhantçabal et al. (2009b) described deformation in the shear zone as

predominantly pure-shear flattening within a sinistral transpressional system. Similar observations have been made in the Sarandi del Yí Shear Zone (Oyhantçabal et al., 2001; Oyhantçabal et al., 2007). Thus, coeval sub-horizontal tangential shearing within the foreland between these two major transpressional shear zones suggests the partitioning of strain into pure shear- and tangential simple shear-dominated domains, which is consistent with studies demonstrating that sinistral tectonics in the southern Dom Feliciano Belt occurred within a transpressional regime (Oriolo et al., 2016a; Oyhantçabal et al., 2011b).

5.2 Tectonic implications

Our data support previous studies showing that peak metamorphism and associated melting in the hinterland occurred at roughly the same time everywhere along the Dom Feliciano Belt—in the Porto Belo, Várzea do Capivarita and Cerro Olivo complexes (Chemale et al., 2012; Lenz et al., 2011; Martil, 2016; Oyhantçabal et al., 2009a)—as well as in the Coastal Terrane of the Kaoko Belt (Franz et al., 1999; Goscombe et al., 2005a; Konopásek et al., 2008; Kröner et al., 2004; Seth et al., 1998). We also report, for the first time, evidence of the ca. 655 Ma magmatic activity associated with early crustal thickening and high-T metamorphism in the southern Dom Feliciano Belt, which has otherwise only been recorded in the Porto Belo Complex and the Coastal Terrane (Chemale et al., 2012; Kröner et al., 2004; Seth et al., 1998). This result implies a tectonic environment already capable of sustaining high temperatures at ca. 655 Ma, which is consistent with burial beneath continental crust. Furthermore, near-simultaneous crustal thickening along the hinterland of the Dom Feliciano Belt at the start of orogenesis implies the presence of converging continental crust eastward of the entire length of the orogen at ca. 660–650 Ma (De Toni et al., 2020b; Lenz et al., 2011; Martil, 2016; Oyhantçabal et al., 2009a; Percival et al., in review; and this work). Thus, as the rift-drift transition between the Congo and Kalahari Cratons did not start until ca. 650 Ma (Hoffman, 2021), both the Kalahari and Congo cratons were likely involved in early orogenesis. The data therefore support the interpretation that early crustal thickening and dextral transpression in the Dom Feliciano Belt was driven by high-angle to oblique convergence of the Congo and Kalahari cratons with the South American cratonic bodies (Rio de la Plata Craton, Luis Alves Craton, and Nico Pérez Terrane) by at least ca. 660–650 Ma (Fig. 16a).

Our data show that there is so far no record of coeval ca. 650 Ma metamorphism in the Schist Belt of the southern Dom Feliciano Belt foreland, such as is seen in the Brusque Complex of the northern foreland (Percival et al., in review). Instead, peak metamorphic conditions recorded in the southern foreland were reached between ca. 585–570 Ma, during the later transpressional phase of orogenesis that affected the Dom Feliciano, Kaoko, and Gariep belts (Frimmel, 2018; Goscombe et al., 2003b; Gresse, 1994; Hueck et al., 2018b). There are a few possible explanations for this discrepancy. Firstly, the record of early crustal thickening in the southern foreland may have been obliterated during the ca. 580–570 Ma transpressional event. The imbrication of the foreland basement and oblique thrusting over the more distal parts of the foreland, and the subsequent metamorphism of the pre-orogenic sedimentary cover, could have led to the complete overprint of any previous metamorphic fabrics. Secondly, the currently exposed parts of the foreland supracrustal rocks may have never contained an earlier metamorphic record to begin with, potentially due to the foreland failing to reach the conditions needed for the development of a strong metamorphic overprint during early crustal thickening and subsequent tectonic burial. However, considering that the garnet-bearing metamorphic assemblage in the schists closest to the Campanero Unit (sample UE14B) appears to be coeval with the S2 transposition foliation, the S1 foliation likely represents an earlier fabric and thus the former scenario is the most likely. Although with no geochronological constraints for this earlier event, the interpretation remains speculative.

The ca. 580 Ma sinistral transpressive event represents a switch from earlier, predominantly dextral shearing across the major orogen-parallel shear zones in the southern Dom Feliciano Belt, marking a significant geodynamic change within the orogen (Oriolo et al., 2016a; Oriolo et al., 2016b). This switch was potentially driven by the northward convergence of the Kalahari Craton from ca. 580 Ma (Frimmel and Frank, 1998; Oriolo et al., 2016b; Oyhantçabal et al., 2011b; Rapela et al., 2011). This interpretation is supported by Hoffman (2021), who suggests that the Kalahari Craton continued to drift away from the Congo Craton after the end of rifting at ca. 650 Ma, opening the Damara basins prior to their eventual closure and inversion during the Damaran orogeny from ca. 580 Ma (Fig. 16b & c).

In contrast with the southern Dom Feliciano Belt, sinistral deformation is almost completely absent from the major shear zones of the northern Dom Feliciano Belt, and there is only minor reactivation along these shear zones after ca. 580 Ma (Hueck et al., 2018a; Percival et al., in review). Instead, it appears that deformation in the northern extension of the system at ca. 580 was confined almost completely to the eastern half of the orogen (Fig. 16c). This was expressed by the development of the Kaoko Belt, where earliest metamorphism (east of the Coastal Terrane hinterland) is constrained to ca. 580 Ma, and the main transpressional phase of orogenesis lasted until ca. 550 Ma (Goscombe et al., 2003b; Goscombe et al., 2005a; Seth et al., 1998; Ulrich et al., 2011). Furthermore, just like in the southern Dom Feliciano Belt, sinistral transpression dominated in the Kaoko Belt during this time (Goscombe et al., 2003a; Goscombe et al., 2003b; Goscombe et al., 2005b; Konopásek et al., 2005).

Thus, the data presented in this study support the hypothesis advanced by Oyhantçabal et al. (2011b) that ca. 580 Ma sinistral transpressional reactivation of previous dextral shear structures in the Dom Feliciano Belt, as well as transpressional deformation in the Kaoko and Gariep belts, was driven by the oblique convergence of the Kalahari Craton (relative to the South American cratonic blocks) from ca. 580 Ma. Deformation during this event was expressed more strongly in the southern and central Dom Feliciano Belt than in the north.

6 Conclusions

- The foreland and hinterland domains of the southern Dom Feliciano Belt in Uruguay share some similarities in deformation structures: both show a dominant high-T fabric (S1) with a generally E–W trending stretching lineation (L1). This fabric is overprinted by folds (F2) and an associated sub-vertical axial plane-parallel foliation (S2) containing a stretching lineation (L2), which are all oriented parallel to major N–S- to NE–SW-trending shear zones. The foreland basement differs slightly, showing also a sub-vertical E–W trending foliation (S3).
- Granulites from the Cerro Olivo Complex (hinterland) record prograde metamorphism with a peak at ~9.5–11.5 kbar and ~760–780°C, and subsequent near-isothermal decompression down to ~5.5–7.0 kbar and ~770–790°C. A garnet Lu–Hf age of 654 ± 23 Ma reflects the average age of garnet growth across these two metamorphic stages, whereas a 638.5 ± 2.2 Ma age records the timing of decompression-related, high-T metamorphism.
- A deformed porphyritic granite from the Cerro Olivo Complex records zircon U–Pb LA-ICP-MS and SIMS ages of 656 ± 4 Ma and 654 ± 3 Ma, respectively, which reflects the igneous protolith age. The rock represents the first evidence of early orogenic melting in the Dom Feliciano Belt of Uruguay.
- Supracrustal rocks in the foreland Schist Belt record prograde metamorphism with a peak at 5.5–7.0 kbar and 550–575°C, and a garnet Lu–Hf age constrains this event to 582 ± 23 Ma. Metamorphism in the Campanero Unit gneisses (foreland basement) reached peak conditions of 4–9 kbar and 670–770°C and is constrained by monazite U–Pb ages of 583 ± 6 and 572 ± 5 Ma. Metamorphism in the foreland was coeval with sinistral transpression recorded along major shear zones in the belt.
- The P–T–t paths recorded in the hinterland and foreland indicate: 1) early west-directed imbrication and thrusting of the hinterland at ca. 655–640 Ma (D1), and 2) late imbrication and thrusting of the foreland basement over the more distal supracrustal foreland rocks during sinistral transpression at ca. 585–570 Ma (D2).

- This two-stage tectonic evolution event is likely driven by the three-way convergence between the Congo, Kalahari, and South American cratons.

Acknowledgements

This work represents part of a PhD project which received financial support from Diku Norway and CAPES Brazil (project UTF-2018-10004). Thanks to D. Sala and M. Koziarska for their help with isotopic analytical work, and R. Škoda and R Čopjaková for assistance with microprobe analyses. We thank Martin Whitehouse and Heejin Jeon for their support while using the Nordsim ion probe in Stockholm.

References

Anczkiewicz R. & Thirlwall M. F., 2003. Improving precision of Sm-Nd garnet dating by H2SO4 leaching: a simple solution to the phosphate inclusion problem. Geological Society, London, Special Publications, vol. 220, no. 1, pp. 83–91. https://10.1144/GSL.SP.2003.220.01.05.

Anczkiewicz R., Platt J. P., Thirlwall M. F. & Wakabayashi J., 2004. Franciscan subduction off to a slow start: evidence from high-precision Lu–Hf garnet ages on high grade-blocks. Earth Planet. Sci. Lett., vol. 225, no. 1, pp. 147–161. https://doi.org/10.1016/j.epsl.2004.06.003.

Anczkiewicz R., Thirlwall M., Alard O., Rogers N. W. & Clark C., 2012. Diffusional homogenization of light REE in garnet from the Day Nui Con Voi Massif in N-Vietnam: Implications for Sm–Nd geochronology and timing of metamorphism in the Red River shear zone. Chem. Geol., vol. 318-319, pp. 16–30. https://doi.org/10.1016/j.chemgeo.2012.04.024.

Anczkiewicz R., Chakraborty S., Dasgupta S., Mukhopadhyay D. & Kołtonik K., 2014. Timing, duration and inversion of prograde Barrovian metamorphism constrained by high resolution Lu–Hf garnet dating: A case study from the Sikkim Himalaya, NE India. Earth Planet. Sci. Lett., vol. 407, pp. 70–81. http://dx.doi.org/10.1016/j.epsl.2014.09.035.

Bartoli O., 2017. Phase equilibria modelling of residual migmatites and granulites: An evaluation of the melt-reintegration approach. Journal of Metamorphic Geology, vol. 35, no. 8, pp. 919-942. 10.1111/jmg.12261.

Basei M. A. S., Siga Jr O., Masquelin H., Harara O. M., Reis Neto J. M. & Preciozzi F., 2000. The Dom Feliciano Belt of Brazil and Uruguay and its Foreland Domain, the Rio de la Plata Craton: framework, tectonic evolution and correlation with similar provinces of Southwestern Africa. In Cordani U. G., et al. eds. Tectonic Evolution of South America. pp. 311─334. Rio de Janeiro, Brazil: Geological Society http://10.13140/RG.2.1.5109.4567.

Battisti M. A., Bitencourt M. F., De Toni G. B., Nardi L. V. S. & Konopásek J., 2018. Metavolcanic rocks and orthogneisses from Porongos and Várzea do Capivarita complexes: A case for identification of tectonic interleaving at different crustal levels from structural and geochemical data in southernmost Brazil. J. S. Am. Earth Sci., vol. 88, p. 253─274. https://doi.org/10.1016/j.jsames.2018.08.009.

Bitencourt M. F. & Nardi L. V. S., 2000. Tectonic setting and sources of magmatism related to the southern Brazilian shear belt. Revista Brasileira de Geociencias, vol. 30, no. 1, p. 186─189.

Caddick M., Konopasek J. & Thompson A., 2010. Preservation of Garnet Growth Zoning and the Duration of Prograde Metamorphism. J. Petrol., vol. 51, pp. 2327-2347. 10.1093/petrology/egq059.

Chemale F., Jr, Mallmann G., Bitencourt M. F. & Kawashita K., 2012. Time constraints on magmatism along the Major Gercino Shear Zone, southern Brazil: Implications for West Gondwana reconstruction. Gondwana Res., vol. 22, no. 1, pp. 184–199. https://doi.org/10.1016/j.gr.2011.08.018.

Cheng H., 2019. Garnet Lu–Hf and Sm–Nd geochronology: a time capsule of the metamorphic evolution of orogenic belts. Geological Society, London, Special Publications, vol. 474, no. 1, pp. 47–67. https://doi.org/10.1144/sp474.7.

Chiglino L., Gaucher C., Sial A. N., Bossi J., Ferreira V. P. & Pimentel M. M., 2010. Chemostratigraphy of Mesoproterozoic and Neoproterozoic carbonates of the Nico Pérez Terrane, Río de la Plata Craton, Uruguay. Precambrian Res., vol. 182, no. 4, pp. 313-336. https://doi.org/10.1016/j.precamres.2010.06.002.

Coelho M. B., Trouw R. A. J., Ganade C. E., Vinagre R., Mendes J. C. & Sato K., 2017. Constraining timing and P-T conditions of continental collision and late overprinting in the Southern Brasília Orogen (SE-Brazil): U-Pb zircon ages and geothermobarometry of the Andrelândia Nappe System. Precambrian Res., vol. 292, no. Supplement C, pp. 194-215. https://doi.org/10.1016/j.precamres.2017.02.001.

Connolly J. A. D., 2005. Computation of phase equilibria by linear programming: A tool for geodynamic modeling and its application to subduction zone decarbonation. Earth Planet. Sci. Lett., vol. 236, no. 1–2, pp. 524–541. https://doi.org/10.1016/j.epsl.2005.04.033.

De Toni G. B., Bitencourt M. F., Konopásek J., Martini A., Andrade P. H. S., Florisbal L. M. & Campos R. S., 2020a. Transpressive strain partitioning between the Major Gercino Shear Zone and the Tijucas Fold Belt, Dom Feliciano Belt, Santa Catarina, southern Brazil. J. Struct. Geol., vol. 136, p. 104058. https://doi.org/10.1016/j.jsg.2020.104058.

De Toni G. B., Bitencourt M. F., Nardi L. V. S., Florisbal L. M., Almeida B. S. & Geraldes M., 2020b. Dom Feliciano Belt orogenic cycle tracked by its pre-collisional magmatism: The Tonian (ca. 800 Ma) Porto Belo Complex and its correlations in southern Brazil and Uruguay. Precambrian Res., vol. 342, p. 105702. https://doi.org/10.1016/j.precamres.2020.105702.

De Toni G. B., Bitencourt M. F., Konopásek J., Battisti M. A., Oliveira da Costa E. & Savian J. F., 2021. Autochtonous origin of the Encruzilhada Block, Dom Feliciano Belt, southern Brazil, based on aerogeophysics, image analysis and PT-paths. JGeo, vol. 144, p. 101825. https://doi.org/10.1016/j.jog.2021.101825.

Dodson M. H., 1973. Closure temperature in cooling geochronological and petrological systems. Contributions to Mineralogy and Petrology, vol. 40, no. 3, pp. 259-274. 10.1007/BF00373790.

Franz L., Romer R. L. & Dingeldey D. P., 1999. Diachronous Pan-African granulite-facies metamorphism (650 Ma and 550 Ma) in the Kaoko Belt, NW Namibia. European Journal of Mineralogy, vol. 11, no. 1, pp. 167-180. https://doi.org/10.1127/ejm/11/1/0167.

Frimmel H. E. & Frank W., 1998. Neoproterozoic tectono-thermal evolution of the Gariep Belt and its basement, Namibia and South Africa. Precambrian Res., vol. 90, no. 1, pp. 1-28. https://doi.org/10.1016/S0301-9268(98)00029-1.

Frimmel H. E., 2018. The Gariep Belt. In Siegesmund S., et al. eds. Geology of Southwest Gondwana. pp. 353-386. 1st ed. Cham: Springer International Publishing https://www.doi.org/10.1007/978-3-319-68920-3_13.

Fuhrman M. L. & Lindsley D. H., 1988. Ternary-feldspar modeling and thermometry. Am. Mineral., vol. 73, no. 3–4, pp. 201–215.

Ganguly J. & Tirone M., 1999. Diffusion closure temperature and age of a mineral with arbitrary extent of diffusion: theoretical formulation and applications. Earth Planet. Sci. Lett., vol. 170, no. 1, pp. 131-140. https://doi.org/10.1016/S0012-821X(99)00089-8.

Gaucher C., Frei R., Chemale Jr F., Frei D., Bossi J., Martínez G., Chiglino L. & Cernuschi F., 2011. Mesoproterozoic evolution of the Río de la Plata Craton in Uruguay: at the heart of Rodinia? Int. J. Earth Sci., vol. 100, no. 2, pp. 273-288. https://www.doi.org/10.1007/s00531-010-0562-x.

Goscombe B., Hand M. & Gray D., 2003a. Structure of the Kaoko Belt, Namibia: progressive evolution of a classic transpressional orogen. J. Struct. Geol., vol. 25, no. 7, pp. 1049-1081. https://www.doi.org/10.1016/S0191-8141(02)00150-5.

Goscombe B., Hand M., Gray D. & Mawby J. O., 2003b. The Metamorphic Architecture of a Transpressional Orogen: the Kaoko Belt, Namibia. J. Petrol., vol. 44, no. 4, pp. 679-711. https://www.doi.org/10.1093/petrology/44.4.679.

Goscombe B., Gray D., Armstrong R., Foster D. A. & Vogl J., 2005a. Event geochronology of the Pan-African Kaoko Belt, Namibia. Precambrian Res., vol. 140, no. 3–4, pp. 103.e1–103.e41. https://doi.org/10.1016/j.precamres.2005.07.003.

Goscombe B., Gray D. & Hand M., 2005b. Extrusional Tectonics in the Core of a Transpressional Orogen; the Kaoko Belt, Namibia. J. Petrol., vol. 46, no. 6, pp. 1203-1241. https://www.doi.org/10.1093/petrology/egi014.

Goscombe B., Foster D. A., Gray D. & Wade B., 2017. Metamorphic response and crustal architecture in a classic collisional orogen: The Damara Belt, Namibia. Gondwana Res., https://doi.org/10.1016/j.gr.2017.07.006.

Goscombe B., Foster D., Gray D. & Wade B., 2018. The Evolution of the Damara Orogenic System: A Record of West Gondwana Assembly and Crustal Response. pp. 303-352. 10.1007/978-3-319-68920-3_12.

Gresse P. G., 1994. Strain partitioning in the southern Gariep Arc as reflected by sheath folds and stretching directions. S. Afr. J. Geol., vol. 97, no. 1, pp. 52-61.

Gross A. O. M. S., Porcher C. C., Fernandes L. A. D. & Koester E., 2006. Neoproterozoic low-pressure/high-temperature collisional metamorphic evolution in the Varzea do Capivarita

Metamorphic Suite, SE Brazil: Thermobarometric and Sm/Nd evidence. Precambrian Res., vol. 147, no. 1, pp. 41-64. https://doi.org/10.1016/j.precamres.2006.02.001.

Gross A. O. M. S., Droop G. T. R., Porcher C. C. & Fernandes L. A. D., 2009. Petrology and thermobarometry of mafic granulites and migmatites from the Chafalote Metamorphic Suite: New insights into the Neoproterozoic P–T evolution of the Uruguayan—Sul-Rio-Grandense shield. Precambrian Res., vol. 170, no. 3–4, pp. 157–174. https://doi.org/10.1016/j.precamres.2009.01.011.

Harrison T. M., Célérier J., Aikman A. B., Hermann J. & Heizler M. T., 2009. Diffusion of 40Ar in muscovite. Geochimica et Cosmochimica Acta, vol. 73, no. 4, pp. 1039–1051. https://doi.org/10.1016/j.gca.2008.09.038.

Hartmann L. A., Campal N., Santos J. O. S., McNaughton N. J., Bossi J., Schipilov A. & Lafon J.-M., 2001. Archean crust in the Rio de la Plata Craton, Uruguay — SHRIMP U–Pb zircon reconnaissance geochronology. J. S. Am. Earth Sci., vol. 14, no. 6, pp. 557-570. https://doi.org/10.1016/S0895-9811(01)00055-4.

Hartmann L. A., Santos J. O. S., Bossi J., Campal N., Schipilov A. & McNaughton N. J., 2002. Zircon and titanite U–Pb SHRIMP geochronology of Neoproterozoic felsic magmatism on the eastern border of the Rio de la Plata Craton, Uruguay. J. S. Am. Earth Sci., vol. 15, no. 2, pp. 229-236. https://doi.org/10.1016/S0895-9811(02)00030-5.

Heine C., Zoethout J. & Müller R. D., 2013. Kinematics of the South Atlantic rift. Solid Earth, vol. 4, no. 2, pp. 215–253. https://doi.org/10.5194/se-4-215-2013.

Hoffman P. F., 2021. On the kinematics and timing of Rodinia breakup: a possible rift–transform junction of Cryogenian age at the southwest cape of Congo Craton (northwest Namibia). S. Afr. J. Geol., vol. 124, no. 2, pp. 401-420. 10.25131/sajg.124.0038.

Holland T. J. B. & Powell R., 2011. An improved and extended internally consistent thermodynamic dataset for phases of petrological interest, involving a new equation of state for solids. Journal of Metamorphic Geology, vol. 29, no. 3, pp. 333–383. https://doi.org/10.1111/j.1525-1314.2010.00923.x.

Hollister L. S., 1966. Garnet Zoning: An Interpretation Based on the Rayleigh Fractionation Model. Science, vol. 154, no. 3757, pp. 1647–1651.

Hueck M., Basei M. A. S., Wemmer K., Oriolo S., Heidelbach F. & Siegesmund S., 2018a. Evolution of the Major Gercino Shear Zone in the Dom Feliciano Belt, South Brazil, and implications for the assembly of southwestern Gondwana. Int. J. Earth Sci., vol. 108, no. 2, pp. 403–425. https://www.doi.org/10.1007/s00531-018-1660-4.

Hueck M., Oyhantçabal P., Basei M. & Siegesmund S., 2018b. The Dom Feliciano Belt in Southern Brazil and Uruquay. In Siegesmund S., et al. eds. Geology of Southwest Gondwana. pp. 267–302. 1st ed. Cham: Springer International Publishing https://doi.org/10.1007/978-3-319-68920-3_11.

Indares A., White R. W. & Powell R., 2008. Phase equilibria modelling of kyanite-bearing anatectic paragneisses from the central Grenville Province. Journal of Metamorphic Geology, vol. 26, no. 8, pp. 815-836. 10.1111/j.1525-1314.2008.00788.x.

Konopásek J., Kröner S., Kitt S. L., Passchier C. W. & Kröner A., 2005. Oblique collision and evolution of large-scale transcurrent shear zones in the Kaoko belt, NW Namibia. Precambrian Res., vol. 136, no. 2, pp. 139-157. 10.1016/j.precamres.2004.10.005.

Konopásek J., Kosler J., Tajčmanová L., Ulrich S. & Kitt S., 2008. Neoproterozoic igneous complex emplaced along major tectonic boundary in the Kaoko Belt (NW Namibia): ion probe and LA-ICP-MS dating of magmatic and metamorphic zircons. J. Geol. Soc. Lond., vol. 165, no. 1, pp. 153–165. https://doi.org/10.1144/0016-76492006-192.

Konopásek J., Hoffmann K.-H., Sláma J. & Košler J., 2017. The onset of flysch sedimentation in the Kaoko Belt (NW Namibia) – Implications for the pre-collisional evolution of the Kaoko–Dom Feliciano–Gariep orogen. Precambrian Res., vol. 298, pp. 220–234. http://dx.doi.org/10.1016/j.precamres.2017.06.017.

Konopásek J., Janoušek V., Oyhantçabal P., Sláma J. & Ulrich S., 2018. Did the circum-Rodinia subduction trigger the Neoproterozoic rifting along the Congo–Kalahari Craton margin? Int. J. Earth Sci., vol. 107, no. 5, pp. 1859–1894. https://doi.org/10.1007/s00531-017-1576-4.

Konopásek J., Cavalcante C., Fossen H. & Janoušek V., 2020. Adamastor – an ocean that never existed? Earth-Sci. Rev., vol. 205, p. 103201. https://doi.org/10.1016/j.earscirev.2020.103201.

Kröner S., Konopásek J., Kröner A., Passchier C. W., Poller U., Wingate M. T. D. & Hofmann K. H., 2004. U-Pb and Pb-Pb zircon ages for metamorphic rocks in the Kaoko Belt of Northwestern Namibia: A Palaeo- to Mesoproterozoic basement reworked during the Pan-African orogeny. S. Afr. J. Geol., vol. 107, no. 3, pp. 455-476. https://www.doi.org/10.2113/107.3.455.

Lara P., Oyhantçabal P. & Dadd K., 2017. Post-collisional, Late Neoproterozoic, high-Ba-Sr granitic magmatism from the Dom Feliciano Belt and its cratonic foreland, Uruguay: Petrography, geochemistry, geochronology, and tectonic implications. Lithos, vol. 277, pp. 178-198. https://doi.org/10.1016/j.lithos.2016.11.026.

Larson K. P., Shrestha S., Soret M. & Smit M., 2020. The P-T-t-D evolution of the Mahabharat, east-central Nepal: The out-of-sequence development of the Himalaya. Geoscience Frontiers, https://doi.org/10.1016/j.gsf.2020.08.001.

Lenz C., Fernandes L. A. D., McNaughton N. J., Porcher C. C. & Masquelin H., 2011. U–Pb SHRIMP ages for the Cerro Bori Orthogneisses, Dom Feliciano Belt in Uruguay: Evidences of a ∼800Ma magmatic and ∼650Ma metamorphic event. Precambrian Res., vol. 185, no. 3, pp. 149–163. https://doi.org/10.1016/j.precamres.2011.01.007.

Lenz C., Porcher C., Fernandes L., Masquelin H., Koester E. & Conceição R., 2013. Geochemistry of the Neoproterozoic (800–767 Ma) Cerro Bori orthogneisses, Dom Feliciano Belt in Uruguay: tectonic evolution of an ancient continental arc. Mineral. Petrol., vol. 107, pp. 785–806. https://doi.org/10.1007/s00710-012-0244-4.

Mallmann G., Chemale Jr F., Ávila J. N., Kawashita K. & Armstrong R. A., 2007. Isotope geochemistry and geochronology of the Nico Pérez Terrane, Rio de la Plata Craton, Uruguay. Gondwana Res., vol. 12, no. 4, pp. 489-508. https://doi.org/10.1016/j.gr.2007.01.002.

Marmo B. A., Clarke G. L. & Powell R., 2002. Fractionation of bulk rock composition due to porphyroblast growth: effects on eclogite facies mineral equilibria, Pam Peninsula, New Caledonia. Journal of Metamorphic Geology, vol. 20, no. 1, pp. 151-165. https://doi.org/10.1046/j.0263-4929.2001.00346.x.

Martil M. M. D., 2016. O Magmatismo De Arco Continental Pré-colisional (790 Ma) E a Reconstituição Espaço-temporal Do Regime Transpressivo (650 Ma) No Complexo Várzea Do Capivarita, Sul Da Província Mantiqueira. Universidade Federal do Rio Grande do Sul, Available at: https://www.lume.ufrgs.br/handle/10183/149194.

Martil M. M. D., Bitencourt M. F., Nardi L. V. S., Koester E. & Pimentel M. M., 2017. Pre-collisional, Tonian (ca. 790 Ma) continental arc magmatism in southern Mantiqueira Province, Brazil: Geochemical and isotopic constraints from the Várzea do Capivarita Complex. Lithos, vol. 274–275, pp. 39–52. https://doi.org/10.1016/j.lithos.2016.11.011.

Masquelin H., Fernandes L., Lenz C., Porcher C. C. & McNaughton N. J., 2011. The Cerro Olivo Complex: A pre-collisional Neoproterozoic magmatic arc in Eastern Uruguay. Int. Geol. Rev., vol. 54, pp. 1161-1183. https://www.doi.org/10.1080/00206814.2011.626597.

Masquelin H., Aïfa T., Scaglia F. & Basei M. A. S., 2021. The Archean Pavas Block in Uruguay: Extension and tectonic evolution based on LA-ICP-MS U–Pb ages and airborne geophysics. J. S. Am. Earth Sci., vol. 110, p. 103364. https://doi.org/10.1016/j.jsames.2021.103364.

McCourt S., Armstrong R., Jelsma H. & Mapeo R., 2013. New U-Pb SHRIMP ages from the Lubango region, SW Angola: Insights into the Palaeoproterozoic evolution of the Angolan Shield, southern Congo Craton, Africa. Geol. Soc. Spec. Publ., vol. 170, no. 2, pp. 353–363. https://doi.org/10.1144/jgs2012-059.

McDougall I. & Harrison T. M., 1999. Geochronology and thermochronology by the 40Ar/39Ar method. Oxford University Press, New York.

Meira V. T., Garcia-Casco A., Hyppolito T., Juliani C. & Schorscher J. H. D., 2019. Tectono-Metamorphic Evolution of the Central Ribeira Belt, Brazil: A Case of Late Neoproterozoic Intracontinental Orogeny and Flow of Partially Molten Deep Crust During the Assembly of West Gondwana. Tectonics, vol. 38, no. 8, pp. 3182–3209. https://doi.org/10.1029/2018tc004959.

Oriolo S., Oyhantçabal P., Heidelbach F., Wemmer K. & Siegesmund S., 2015. Structural evolution of the Sarandí del Yí Shear Zone, Uruguay: kinematics, deformation conditions and tectonic

significance. GR Geologische Rundschau, vol. 104, no. 7, pp. 1759-1777. 10.1007/s00531-015-1166-2.

Oriolo S., Oyhantçabal P., Wemmer K., Heidelbach F., Pfänder J., Basei M. A. S., Hueck M., Hannich F., Sperner B. & Siegesmund S., 2016a. Shear zone evolution and timing of deformation in the Neoproterozoic transpressional Dom Feliciano Belt, Uruguay. J. Struct. Geol., vol. 92, pp. 59-78. https://doi.org/10.1016/j.jsg.2016.09.010.

Oriolo S., Oyhantçabal P., Wemmer K., Basei M. A. S., Benowitz J., Pfänder J., Hannich F. & Siegesmund S., 2016b. Timing of deformation in the Sarandí del Yí Shear Zone, Uruguay: Implications for the amalgamation of western Gondwana during the Neoproterozoic Brasiliano-Pan-African Orogeny. Tectonics, vol. 35, no. 3, pp. 754–771. https://doi.org/10.1002/2015tc004052.

Oriolo S., Oyhantçabal P., Basei M. A. S., Wemmer K. & Siegesmund S., 2016c. The Nico Pérez Terrane (Uruguay): From Archean crustal growth and connections with the Congo Craton to late Neoproterozoic accretion to the Río de la Plata Craton. Precambrian Res., vol. 280, pp. 147–160. https://doi.org/10.1016/j.precamres.2016.04.014.

Oriolo S., Oyhantçabal P., Konopásek J., Basei M. A. S., Frei R., Sláma J., Wemmer K. & Siegesmund S., 2019. Late Paleoproterozoic and Mesoproterozoic magmatism of the Nico Pérez Terrane (Uruguay): Tightening up correlations in southwestern Gondwana. Precambrian Res., vol. 327, pp. 296-313. https://doi.org/10.1016/j.precamres.2019.04.012.

Oyhantçabal P., Heimann A. & Miranda S., 2001. Measurement and interpretation of strain in the syntectonic Solís de Mataojo Granitic Complex, Uruguay. J. Struct. Geol., vol. 23, no. 5, pp. 807-817. https://doi.org/10.1016/S0191-8141(00)00152-8.

Oyhantçabal P., Siegesmund S., Wemmer K., Frei R. & Layer P., 2007. Post-collisional transition from calc-alkaline to alkaline magmatism during transcurrent deformation in the southernmost Dom Feliciano Belt (Braziliano–Pan-African, Uruguay). Lithos, vol. 98, no. 1–4, p. 141─159. https://doi.org/10.1016/j.lithos.2007.03.001.

Oyhantçabal P., Siegesmund S., Wemmer K., Presnyakov S. & Layer P., 2009a. Geochronological constraints on the evolution of the southern Dom Feliciano Belt (Uruguay). Journal of the Geological Society, vol. 166, no. 6, p. 1075─1084. https://doi.org/10.1144/0016-76492008-122.

Oyhantçabal P., Siegesmund S., Wemmer K. & Layer P., 2009b. The Sierra Ballena Shear Zone in the southernmost Dom Feliciano Belt (Uruguay): evolution, kinematics, and deformation conditions. Int. J. Earth Sci., vol. 99, no. 6, pp. 1227-1246. 10.1007/s00531-009-0453-1.

Oyhantçabal P., Siegesmund S. & Wemmer K., 2011a. The Río de la Plata Craton: a review of units, boundaries, ages and isotopic signature. Int. J. Earth Sci., vol. 100, no. 2, p. 201─220. https://doi.org/10.1007/s00531-010-0580-8.

Oyhantçabal P., Siegesmund S., Wemmer K. & Passchier C. W., 2011b. The transpressional connection between Dom Feliciano and Kaoko Belts at 580–550 Ma. Int. J. Earth Sci., vol. 100, p. 379─390. https://doi.org/10.1007/s00531-010-0577-3.

Oyhantçabal P., Wagner-Eimer M., Wemmer K., Schulz B., Frei R. & Siegesmund S., 2012. Paleo- and Neoproterozoic magmatic and tectonometamorphic evolution of the Isla Cristalina de Rivera (Nico Pérez Terrane, Uruguay). Int. J. Earth Sci., vol. 101, no. 7, pp. 1745-1762. https://doi.org/10.1007/s00531-012-0757-4.

Oyhantçabal P., Oriolo S., Philipp R. P., Wemmer K. & Siegesmund S., 2018. The Nico Pérez Terrane of Uruguay and Southeastern Brazil. In Siegesmund S., et al. eds. Geology of Southwest Gondwana. pp. 161-188. Cham: Springer International Publishing https://doi.org/10.1007/978-3-319-68920-3_7.

Oyhantçabal P., Oriolo S., Wemmer K., Basei M. A. S., Frei D. & Siegesmund S., 2021. Provenance of metasedimentary rocks of the western Dom Feliciano Belt in Uruguay: Insights from U–Pb detrital zircon geochronology, Hf and Nd model ages, and geochemical data. J. S. Am. Earth Sci., vol. 108, p. 103139. https://doi.org/10.1016/j.jsames.2020.103139.

Percival J. J., Konopásek J., Eiesland R., Sláma J., de Campos R. S., Battisti M. A. & Bitencourt M. d. F., 2021. Pre-orogenic connection of the foreland domains of the Kaoko–Dom Feliciano–Gariep orogenic system. Precambrian Res., vol. 354, p. 106060. https://doi.org/10.1016/j.precamres.2020.106060.

Percival J. J., Konopásek J., Anczkiewicz R., Ganerød M., Sláma J., Sacks de Campos R. & Bitencourt M. F., in review. Tectono-metamorphic evolution of the northern Dom Feliciano Belt foreland, Santa Catarina, Brazil: Implications for models of subduction-driven orogenesis. Tectonics.

Pertille J., Hartmann L. A., Santos J. O. S., McNaughton N. J. & Armstrong R., 2017. Reconstructing the Cryogenian–Ediacaran evolution of the Porongos fold and thrust belt, Southern Brasiliano Orogen, based on Zircon U–Pb–Hf–O isotopes. Int. Geol. Rev., vol. 59, no. 12, p. 1532─1560. https://doi.org/10.1080/00206814.2017.1285257.

Preciozzi F., Masquelin H. & Basei M., 1999. The namaqua/grenville terrane of eastern Uruguay: 2nd South American symposium on isotope geology. Argentina, pp. 338-340.

Rapalini A. E., Tohver E., Bettucci L. S., Lossada A. C., Barcelona H. & Pérez C., 2015. The late Neoproterozoic Sierra de las Ánimas Magmatic Complex and Playa Hermosa Formation, southern Uruguay, revisited: Paleogeographic implications of new paleomagnetic and precise geochronologic data. Precambrian Res., vol. 259, pp. 143-155. https://doi.org/10.1016/j.precamres.2014.11.021.

Rapela C. W., Fanning C. M., Casquet C., Pankhurst R. J., Spalletti L., Poiré D. & Baldo E. G., 2011. The Rio de la Plata craton and the adjoining Pan-African/brasiliano terranes: Their origins and incorporation into south-west Gondwana. Gondwana Res., vol. 20, no. 4, pp. 673-690. http://dx.doi.org/10.1016/j.gr.2011.05.001.

Rossini C. A. & Legrand J. M., 2003. Tecto-metamorphic events in the Carapé group: a model for its Neoproterozoic evolution. Revista de la Sociedad Uruguaya de Geología, vol. 1, p. 49─67.

Saalmann K., Gerdes A., Lahaye Y., Hartmann L., Remus M. & Läufer A., 2011. Multiple accretion at the eastern margin of the Rio de la Plata craton: the prolonged Brasiliano orogeny in southernmost Brazil. Int. J. Earth Sci., vol. 100, p. 355─378. https://doi.org/10.1007/s00531-010-0564-8.

Sánchez-Bettucci L., Oyhantçabal P., Loureiro J., Ramos V. A., Preciozzi F. & Basei M. A. S., 2004. Mineralizations of the Lavalleja Group (Uruguay), a Probable Neoproterozoic Volcano-sedimentary Sequence. Gondwana Res., vol. 7, no. 3, pp. 745-751. https://www.doi.org/10.1016/S1342-937X(05)71060-1.

Sánchez Bettucci L., Cosarinsky M. & Ramos V. A., 2001. Tectonic Setting of the Late Proterozoic Lavalleja Group (Dom Feliciano Belt), Uruguay. Gondwana Res., vol. 4, no. 3, pp. 395-407. https://doi.org/10.1016/S1342-937X(05)70339-7.

Scherer E. E., Cameron K. L. & Blichert-Toft J., 2000. Lu–Hf garnet geochronology: closure temperature relative to the Sm–Nd system and the effects of trace mineral inclusions. Geochimica et Cosmochimica Acta, vol. 64, no. 19, pp. 3413–3432. https://doi.org/10.1016/S0016-7037(00)00440-3.

Scherer E. E., Munker C. & Mezger K., 2001. Calibration of the Lutetium-Hafnium clock. Science, vol. 293, no. 5530, pp. 683-7. https://10.1126/science.1061372

Schulmann K., Konopásek J., Janoušek V., Lexa O., Lardeaux J.-M., Edel J.-B., Štípská P. & Ulrich S., 2009. An Andean type Palaeozoic convergence in the Bohemian Massif. Comptes Rendus Geoscience, vol. 341, no. 2, pp. 266-286. https://doi.org/10.1016/j.crte.2008.12.006.

Schulz B., 2021. Monazite Microstructures and Their Interpretation in Petrochronology. Frontiers in Earth Science, vol. 9, no. 241, 10.3389/feart.2021.668566.

Seth B., Kröner A., Mezger K., Nemchin A. A., Pidgeon R. T. & Okrusch M., 1998. Archaean to Neoproterozoic magmatic events in the Kaoko belt of NW Namibia and their geodynamic significance. Precambrian Res., vol. 92, no. 4, pp. 341-363. https://doi.org/10.1016/S0301-9268(98)00086-2.

Spoturno J. J., Loureiro J., Oyhantçabal P. & Pascale A., 2012. Mapa geológico del Departamento de Maldonado escala 1:100,000. Facultad de Ciencias (UdelaR)-Dirección Nacional de Minería y Geología (MIEM), Montevideo.

Spoturno J. J., Oyhantçabal P. & Faraone M., 2019. Mapa geológico del Departamento de Lavalleja escala 1:100,000. Facultad de Ciencias (UdelaR)-Ministerio de Industria, Energía Y Minería (MIEM), Montevideo.

Štípská P., Schulmann K. & Kröner A., 2004. Vertical extrusion and middle crustal spreading of omphacite granulite: A model of syn-convergent exhumation (Bohemian Massif, Czech

Republic). Journal of Metamorphic Geology, vol. 22, pp. 179-198. 10.1111/j.1525-1314.2004.00508.x.

Stüwe K. & Powell R., 1995. PT Paths from modal proportions: application to the Koralm Complex, Eastern Alps. Contributions to Mineralogy and Petrology, vol. 119, no. 1, pp. 83-93. https://doi.org/10.1007/BF00310719.

Tajčmanová L., Konopásek J. & Schulmann K., 2006. Thermal evolution of the orogenic lower crust during exhumation within a thickened Moldanubian root of the Variscan belt of Central Europe. Journal of Metamorphic Geology, vol. 24, no. 2, pp. 119-134. https://doi.org/10.1111/j.1525-1314.2006.00629.x.

Ulrich S., Konopásek J., Jeřábek P. & Tajčmanová L., 2011. Transposition of structures in the Neoproterozoic Kaoko Belt (NW Namibia) and their absolute timing. Int. J. Earth Sci., vol. 100, no. 2, pp. 415–429. https://doi.org/10.1007/s00531-010-0573-7.

White R. W., Powell R., Holland T. J. B. & Worley B. A., 2000. The effect of TiO2 and Fe2O3 on metapelitic assemblages at greenschist and amphibolite facies conditions: mineral equilibria calculations in the system K2O–FeO–MgO–Al2O3–SiO2–H2O–TiO2–Fe2O3. Journal of Metamorphic Geology, vol. 18, no. 5, pp. 497–511. https://doi.org/10.1046/j.1525-1314.2000.00269.x.

White R. W., Powell R. & Clarke G. L., 2002. The interpretation of reaction textures in Fe-rich metapelitic granulites of the Musgrave Block, central Australia: constraints from mineral equilibria calculations in the system K2O–FeO–MgO–Al2O3–SiO2–H2O–TiO2–Fe2O3. Journal of Metamorphic Geology, vol. 20, no. 1, pp. 41–55. https://doi.org/10.1046/j.0263-4929.2001.00349.x.

White R. W., Powell R. & Halpin J. A., 2004. Spatially-focussed melt formation in aluminous metapelites from Broken Hill, Australia. Journal of Metamorphic Geology, vol. 22, no. 9, pp. 825-845. 10.1111/j.1525-1314.2004.00553.x.

White R. W., Powell R., Holland T. J. B., Johnson T. E. & Green E. C. R., 2014. New mineral activity–composition relations for thermodynamic calculations in metapelitic systems. Journal of Metamorphic Geology, vol. 32, no. 3, pp. 261–286. https://doi.org/10.1111/jmg.12071.

Whitney D. & Evans B., 2010. Abbreviations for Names of Rock-Forming Minerals. Am. Mineral., vol. 95, pp. 185–187. https://doi.org/10.2138/am.2010.3371.

Will T. M., Gaucher C., Ling X. X., Li X. H., Li Q. L. & Frimmel H. E., 2019. Neoproterozoic magmatic and metamorphic events in the Cuchilla Dionisio Terrane, Uruguay, and possible correlations across the South Atlantic. Precambrian Res., vol. 320, pp. 303–322. https://doi.org/10.1016/j.precamres.2018.11.004.

Will T. M., Höhn S., Frimmel H. E., Gaucher C., le Roux P. J. & Macey P. H., 2020. Petrological, geochemical and isotopic data of Neoproterozoic rock units from Uruguay and South Africa: Correlation of basement terranes across the South Atlantic. Gondwana Res., vol. 80, pp. 12-32. https://doi.org/10.1016/j.gr.2019.10.012.

Figure captions

Figure 1. (a) Schematic reconstruction of Western Gondwana showing the location of the SANOS (modified from Konopásek et al., 2020). S. Fr. – São Francisco Craton, Par. – Paranapanema Craton. (b) Simplified geological map of the southern SANOS (modified from Bitencourt and Nardi, 2000; De Toni et al., 2021; Konopásek et al., 2017; McCourt et al., 2013; Oyhantçabal et al., 2011a), showing the position of the African and South American continents at the onset of the opening of the South Atlantic Ocean (after Heine et al., 2013). LA – Luis Alves Craton.

Figure 2. (a) Simplified geological map of the Dom Feliciano Belt in Uruguay (modified and compiled from Oriolo et al. (2016b); Oyhantçabal et al. (2009b); Spoturno et al. (2012); Spoturno et al. (2019)). Abbreviations for shear zones: SYSZ – Sarandi del Yí Shear Zone; PPASZ – Puntas del Pan de Azúcar; SBSZ – Sierra Ballena Shear Zone; CSZ – Cordillera Shear Zone. (b) Simplified tectonic map of the same area, showing 1 – Rio de la Plata Craton, 2 – Nico Pérez Terrane (foreland), and 3 – Punta del Este Terrane (hinterland). Equal area lower hemisphere stereographic projections showing poles to plane and lineation structural data from selected units: (c) Campanero Unit (contours in L1 and circles in L2 from Oyhantçabal et al. (2009b), filled diamonds from this study); (d) Zanja del Tigre Complex; (e) Cerro Olivo Complex (contours in L1 from Gross et al. (2009), filled diamonds from this study). N* denotes the number of data from other datasets.

Figure 3. Main outcrop-scale textural and structural features of the Campanero Unit, Zanja del Tigre Complex, and Cerro Olivo Complex. (a) Orthogneiss from the Campanero Unit showing S1 (S 34.90377°, W 55.23678°). (b) Melanocratic–mesocratic part of metasedimentary migmatite in the Campanero Unit (S 34.59390°, W 55.17511°, locality UC40). Inset shows textural detail of sample UC40. (c) F2 folding and S2 crenulation cleavage in phyllite of the Zanja del Tigre Complex (E 34.58506°, W 55.15748°). Inset shows stereoplot of poles to plane S1 data (black dots) fitting along a girdle (dashed line), showing F2 folding (fold axis is open circle) consistent with axial plane-parallel cleavage S2 (red line). (d) Strongly foliated granulite from the Cerro Olivo Complex (S 34.90849°, W 54.82512°, locality UB02), with stereoplot inset showing the orientation of S1 (black line) and L1 (red circle). (e) Weakly foliated granulite from the Cerro Olivo Complex, showing coarse-grained texture and large garnet porphyroblasts (S 34.30564°, W 54.17755°, locality UC73). (f) Deformed porphyritic granite of the Cerro Olivo Complex (S 34.64827°, W 54.73200°, locality UA38), showing stretched K-feldspar porphyroblasts.

Figure 4. Photomicrographs of thin sections from samples in this study: (a) garnet from sample UE14B (line A–A' shows transect from Fig. 5a; line A–B shows transect from Fig. 12d). General texture of samples (b) UE14B and (c) UD17 in both plane-polarised light (PPL) and cross-polarised light (XPL), and (d) UC40 in XPL. (e) Garnet from sample UB02 (line A–B shows transect from Fig. 12e). (f)

Hercynite–sillimanite–cordierite sub-domain in sample UB22. (g) Garnet and general texture of sample UB22 (line A–B shows transect from Fig. 5c). (h) Garnet and general texture from sample UE08 (line A–B shows transect from Fig. 5d). (i) Garnet from sample UE08 showing biotite and rutile inclusions (line A–B shows transect from Fig. 12f). (j) Garnet from sample UC73 (line A–B shows transect from Fig. 5e). (k) General texture of sample UC73, showing rutile inclusion in garnet.

Figure 5. Compositional profiles of garnet from samples (a) UE14B, (b) UB02, (c) UB22, (d) UE08, and (e) UC73. Note that profiles (a) and (e) are from core to rim, while the rest are rim to rim.

Figure 6. P–T pseudosections calculated using measured bulk rock compositions of metasedimentary rocks from the Schist Belt. (a) Pseudosection calculated for sample UE14B showing estimated P–T conditions for garnet cores and peak metamorphic assemblage (dashed white lines), using the intersection of (b) garnet core compositional isopleths and (c) garnet rim and matrix staurolite and biotite compositional isopleths. (d) Pseudosection calculated for sample UD17 showing estimated P–T conditions for garnet cores and peak metamorphic assemblage (dashed white lines), using the intersection of (e) garnet core compositional isopleths and (f) garnet rim and matrix staurolite and biotite compositional isopleths.

Figure 7. (a) Pseudosection calculated for sample UC40 showing estimated peak P–T conditions (dashed white lines), using the intersection of (b) biotite compositional isopleths and (c) plagioclase compositional isopleths.

Figure 8. (a) Pseudosection calculated for sample UB02 showing estimated P–T conditions and metamorphic assemblage (dashed white lines), using the intersection of (b) garnet compositional isopleths and (c) matrix biotite and plagioclase compositional isopleths.

Figure 9. (a) Pseudosection calculated for sample UB22 showing estimated P–T conditions (dashed white line) and metamorphic assemblage (in italics and bold), using the intersection of (b) garnet rim compositional isopleths and (c) matrix biotite, plagioclase, and cordierite compositional isopleths.

Figure 10. (a) Pseudosection calculated for sample UE08 showing estimated P–T conditions (dashed white lines) for garnet cores (at top) and the matrix metamorphic assemblage (at bottom, italics and bold), using the intersection of (b) garnet core compositional isopleths and (c) garnet rim and matrix biotite compositional isopleths.

Figure 11. (a) Pseudosection calculated for sample UC73 showing estimated P–T conditions (dashed white line) within the observed metamorphic assemblage (in italics and bold), using the intersection of (b) garnet rim compositional isopleths and (c) matrix biotite and plagioclase compositional isopleths.

Figure 12. Garnet–whole-rock Lu–Hf isochrons for samples (a) UB02, (b) UE08 and (c) UE14B. LA-ICP-MS scans along representative garnet grains in samples (d) UB02, (e) UE08 and (f) UE14B.

Figure 13. (a–l) Cathodoluminescence images of analysed zircon from samples UB02 (a–d), UE08 (e–f) and UA38 (i–l) from the Cerro Olivo Complex, with analysed spots and $^{206}Pb/^{238}U$ ages (2σ error) indicated for samples UB02 and UE08. (m–t) Back-scattered electron (BSE) images of monazite from samples UF36 (m–p) and UC40 (q–t) from the Campanero Unit, with analysed spots and $^{206}Pb/^{238}U$ ages (2σ error) indicated.

Figure 14. Results of U–Pb dating in zircon and monazite for samples from the Cerro Olivo Complex (a–g) and the Campanero Unit (h–l). Wetherill concordia diagrams are as follows: (a) overview of all zircon data (<10% discordant) in sample UB02; (b) concordia age for sample UB02; (c) overview of all zircon data (<10% discordant) in sample UE08; (d) discordia age for sample UE08 (with calculated excess variance); (e) concordia age for sample UE08 (with calculated excess variance); (f) concordia age for zircon in sample UA38 (SIMS data); (g) concordia age for zircon in sample UA38 (LA-ICP-MS data); (h) concordia age for monazite in sample UF36; (i) concordia age for monazite in sample UC40; (j) overview of all zircon data (<10% discordant) in sample UC40; (k) young cluster of data in sample UC40. (l) Weighted mean $^{206}Pb/^{235}U$ age from zircon in sample UC40. Error ellipses and error bars are plotted at 2σ level. MSWD is the mean square of weighted deviates.

Figure 15. (a) Summary of P–T–t paths based on pseudosections and geochronological data from this study. D1 – prograde garnet growth records peak pressures in the hinterland, followed by near complete re-equilibration of rocks during exhumation. Cooling in the hinterland by ca. 630 Ma based on Oyhantçabal et al. (2009a) and Will et al. (2019). D2 – prograde garnet growth recorded in foreland supracrustal rocks, following a geothermal gradient of ~25°C/km. Evidence of D1 not observed in the foreland. (b) Cooling paths for the hinterland and foreland (* denotes K–Ar ages from Oyhantçabal et al. (2009a); closure temperature ranges from Harrison et al. (2009); McDougall and Harrison (1999)). Note the fast cooling path in the hinterland following exhumation, and intersection of the cooling path of the foreland basement with the foreland Schist Belt.

Figure 16. Schematic interpretation of the Neoproterozoic evolution of the southern Dom Feliciano Belt (block diagrams on left) and the wider Kaoko–Dom Feliciano–Gariep orogenic system (map view diagrams on right).

Tables

Table 1. Summary of Lu–Hf dating results.

Sample	Sample weight (mg)	Lu (ppm)	Hf (ppm)	$^{176}Lu/^{177}Hf$	$^{176}Hf/^{177}Hf$	Age (Ma)
UE08						
Grt1	80.27	4.587	3.562	0.1822	0.284262 ± 4	654 ± 23
Grt2	81.49	4.147	2.846	0.2061	0.284590 ± 4	
Grt3	82.52	4.020	3.118	0.1824	0.284313 ± 3	
Grt4	83.01	4.016	3.048	0.1864	0.284351 ± 4	
WR	101.33	0.449	2.853	0.0223	0.282327 ± 3	
UB02						
Grt1	68.90	6.736	2.052	0.4647	0.287730 ± 6	638.5 ± 2.2
Grt2	66.02	7.059	2.157	0.4633	0.287730 ± 4	
Grt3	79.39	8.674	2.744	0.4475	0.287554 ± 4	
WR	99.61	0.474	1.430	0.0468	0.282735 ± 3	
UE14B						
Grt1	62.15	26.094	2.131	1.7349	0.301051 ± 5	582 ± 23
Grt2	62.14	25.681	2.068	1.7624	0.301201 ± 3	(584.0 ± 2.4)†
Grt3	67.56	23.333	1.962	1.6890	0.300227 ± 5	
WR	100.48	0.336	3.881	0.0123	0.282065 ± 4	

All errors are 2 SE (standard errors) and relate to the last significant digits. 176Lu/177Hf errors are 0.5%. JMC475 yielded 176Hf/177Hf = 0.282164 ± 4 (n = 8) over the period of analysis. Mass bias corrections conducted using 179Hf/177Hf = 0.7325. Decay constants used for age calculations: λ176Lu = 1.865 × 10−11 yr−1 (Scherer et al., 2001). Age uncertainties are 2σ.

† Age calculated with three point isochron excluding Grt3.

Figures

Figure 1.

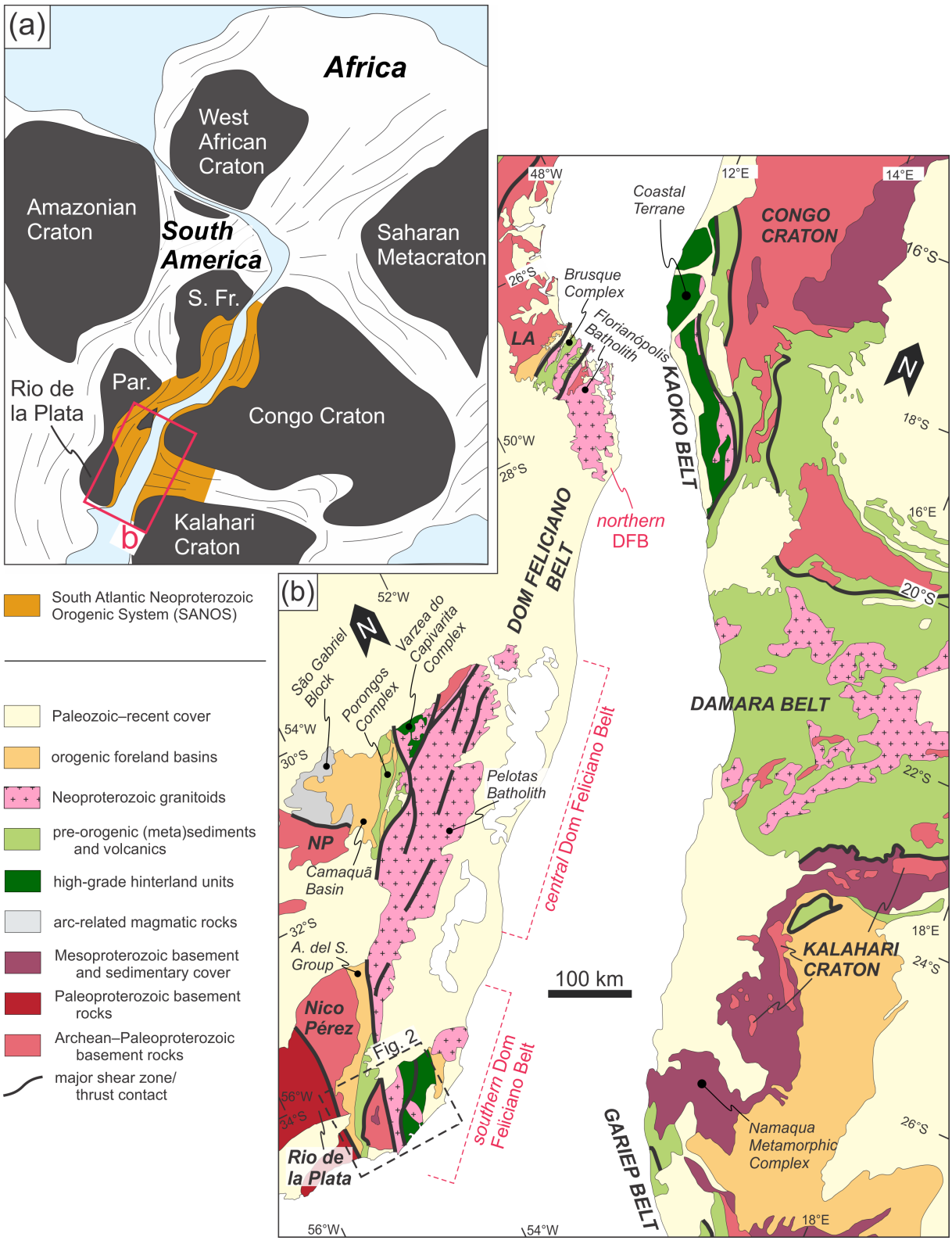

Figure 2.

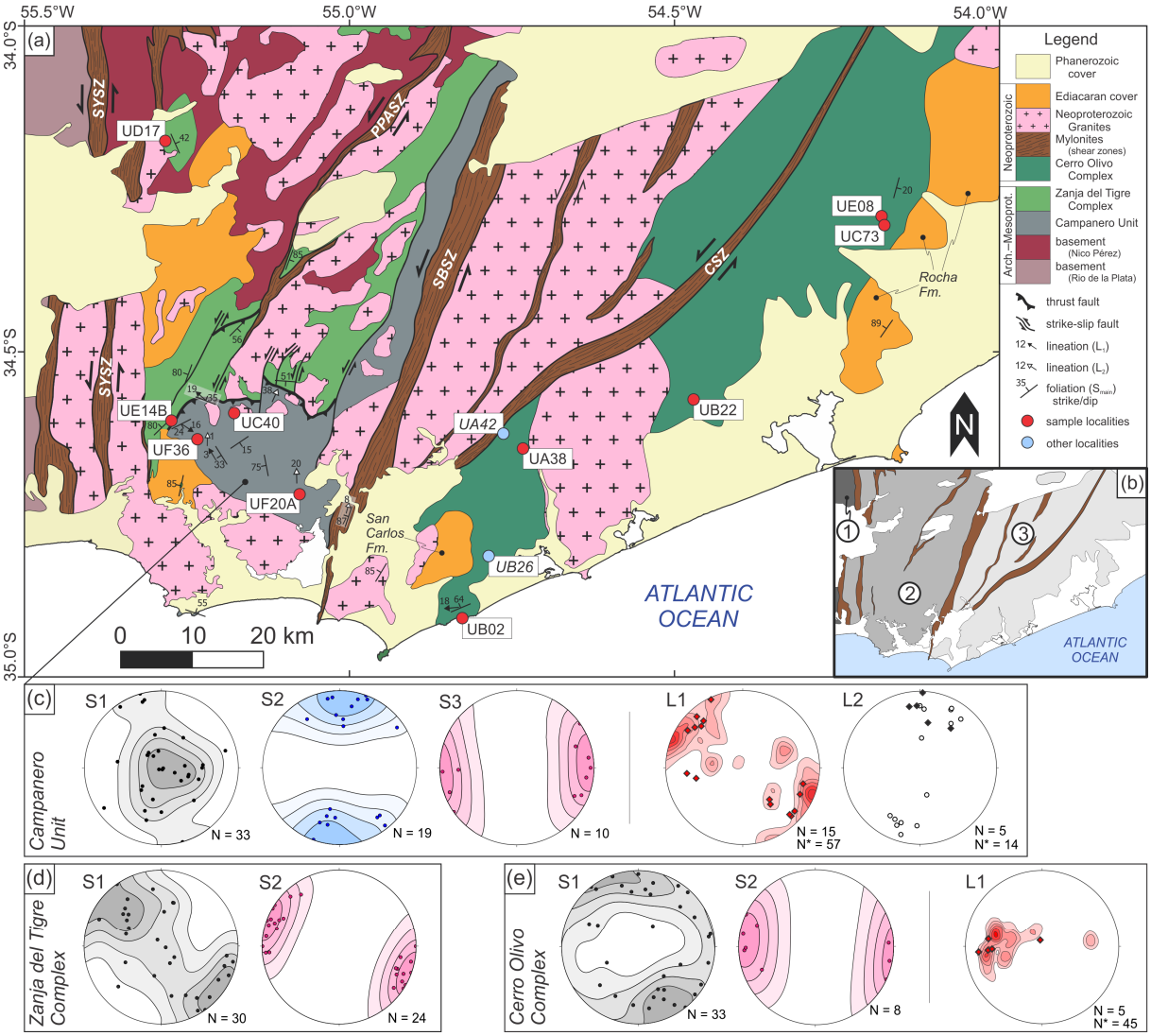
55.5°W
55.0°W
54.5°W
54.0°W
34.0°S
34.5°S
35.0°S
(a)
SYSZ
PPASZ
SBSZ
CSZ
UD17
UE08
UC73
Rocha Fm.
UE14B
UC40
UF36
UF20A
UA42
UA38
UB22
San Carlos Fm.
UB26
UB02
ATLANTIC OCEAN
0 10 20 km
N
Legend
Phanerozoic cover
Ediacaran cover
Neoproterozoic Granites
Mylonites (shear zones)
Cerro Olivo Complex
Zanja del Tigre Complex
Campanero Unit
basement (Nico Pérez)
basement (Rio de la Plata)
Neoproterozoic
Arch.–Mesoprot.
thrust fault
strike-slip fault
lineation (L1)
lineation (L2)
foliation (Sn) strike/dip
sample localities
other localities
(b)
1
2
3
ATLANTIC OCEAN
(c)
Campanero Unit
S1
N = 33
S2
N = 19
S3
N = 10
L1
N = 15
N* = 57
L2
N = 5
N* = 14
(d)
Zanja del Tigre Complex
S1
N = 30
S2
N = 24
(e)
Cerro Olivo Complex
S1
N = 33
S2
N = 8
L1
N = 5
N* = 45

Figure 3.

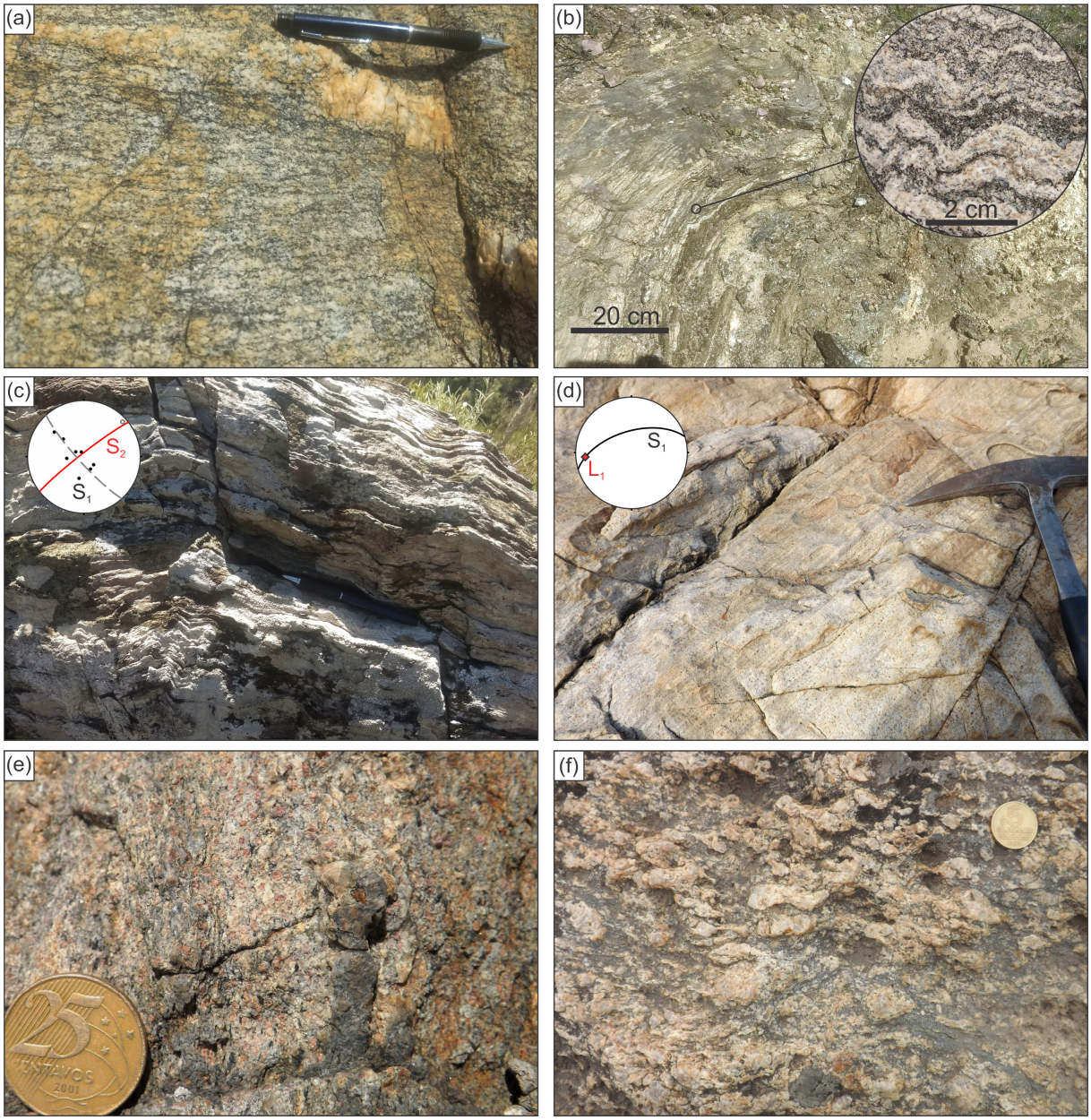

Figure 4.

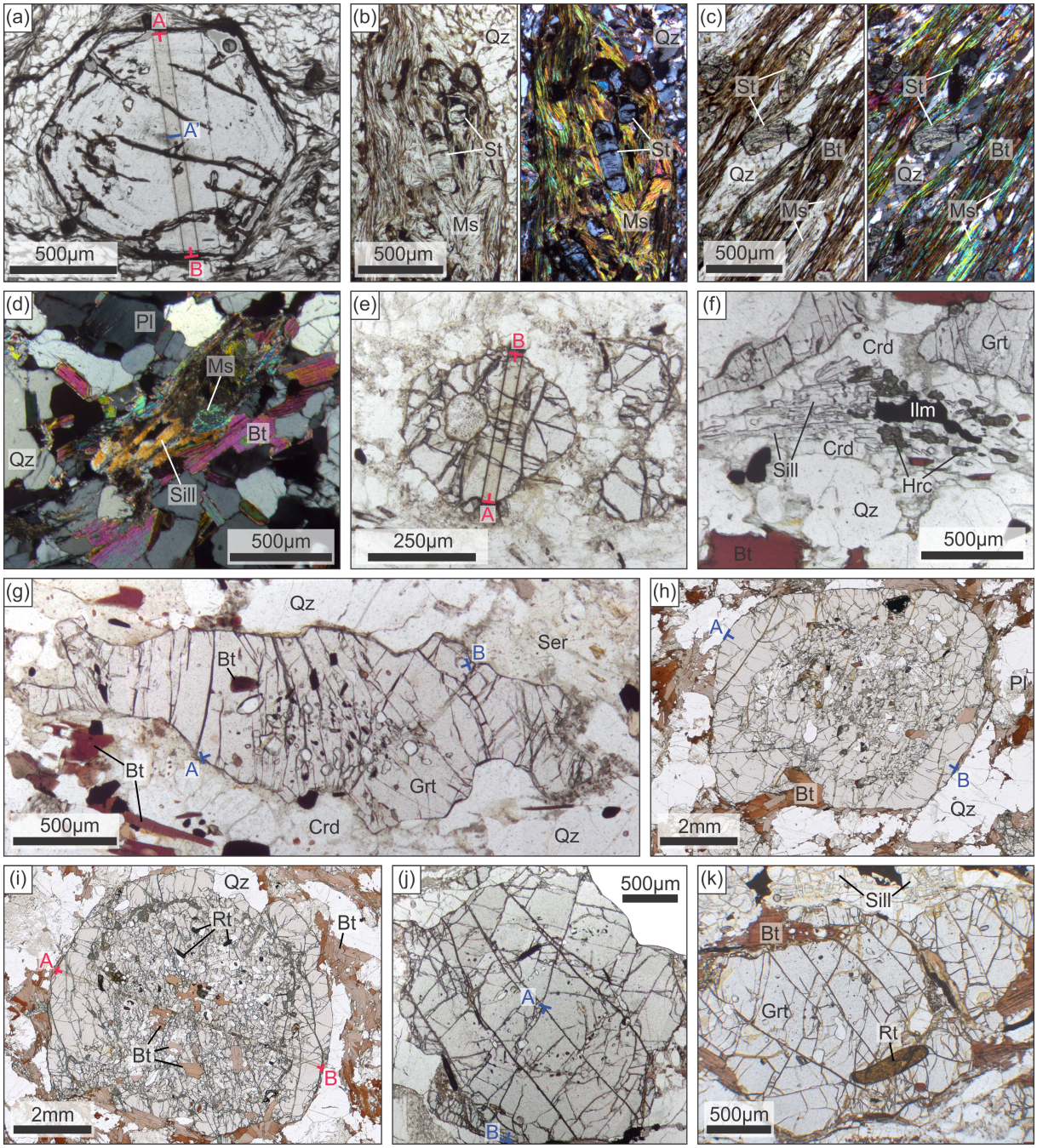
(a)
A
A'
B
500μm
(b)
Qz
St
Ms
500μm
Qz
St
Ms
(c)
St
Bt
Qz
Ms
500μm
St
Bt
Qz
Ms
(d)
Pl
Ms
Bt
Qz
Sill
500μm
(e)
B
A
250μm
(f)
Crd
Grt
Ilm
Crd
Sill
Hrc
Qz
Bt
500μm
(g)
Qz
Ser
Bt
B
Bt
A
Grt
500μm
Crd
Qz
(h)
A
Pl
B
Bt
Qz
2mm
(i)
Qz
Rt
Bt
A
Bt
B
2mm
(j)
500μm
A
B
(k)
Sill
Bt
Grt
Rt
500μm

Figure 5.

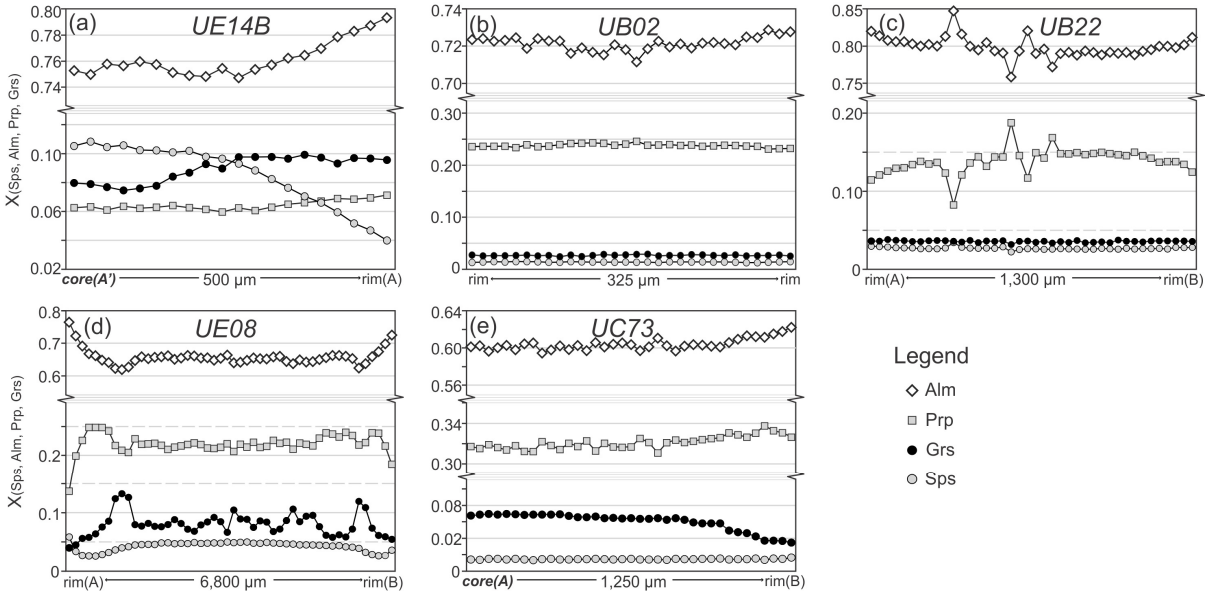
(a)
UE14B
(b)
UB02
(c)
UB22
(d)
UE08
(e)
UC73
X(Sps, Alm, Prp, Grs)
core(A')
500 μm
rim(A)
rim
325 μm
rim
rim(A)
1,300 μm
rim(B)
rim(A)
6,800 μm
rim(B)
core(A)
1,250 μm
rim(B)
Legend
Alm
Prp
Grs
Sps

Figure 6.

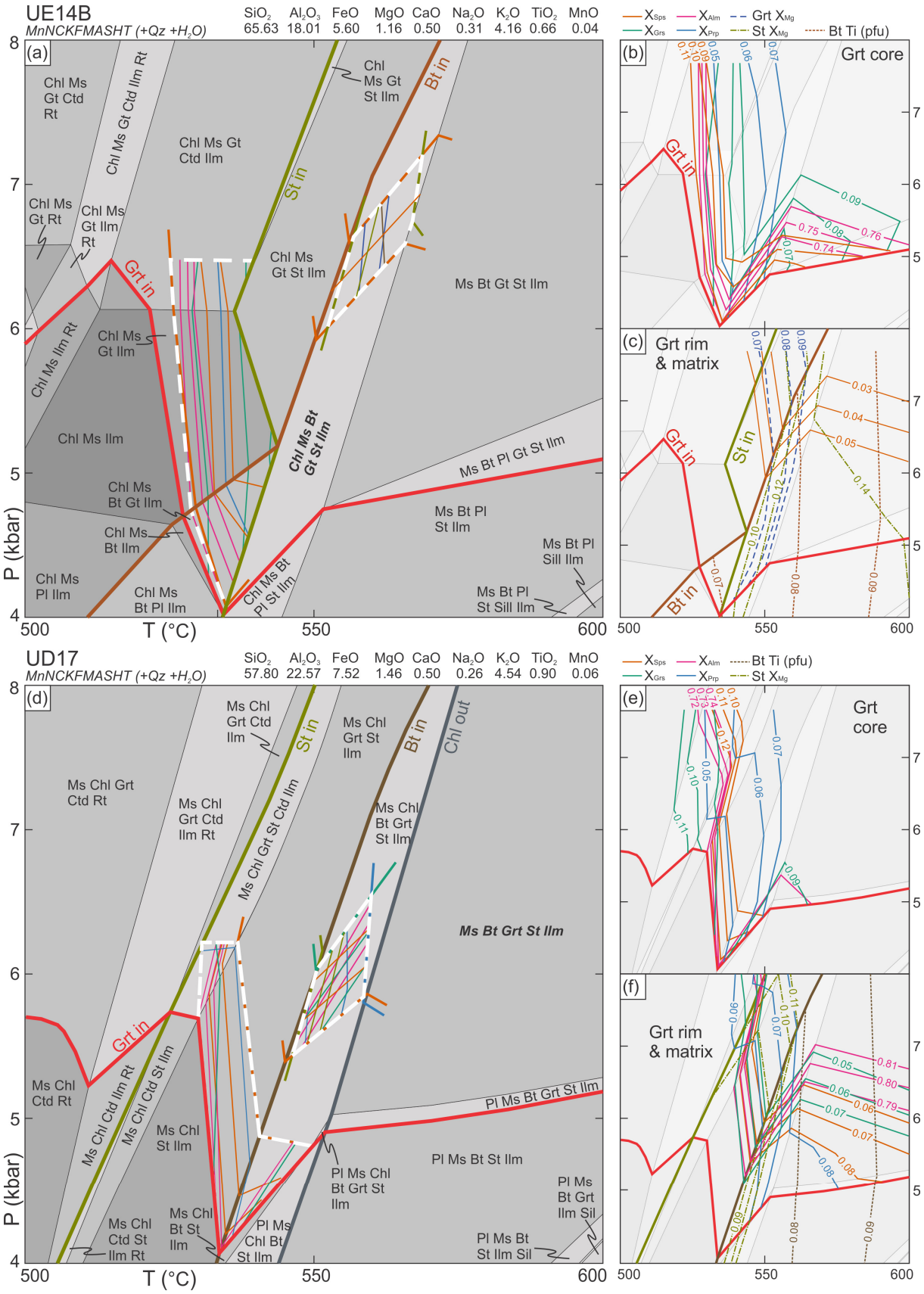
UE14B
MnNCKFMASHT (+Qz +H2O)
SiO2 65.63 Al2O3 18.01 FeO 5.60 MgO 1.16 CaO 0.50 Na2O 0.31 K2O 4.16 TiO2 0.66 MnO 0.04
(a)
Chl Ms Gt Ctd Rt
Chl Ms Gt Ctd Ilm Rt
Chl Ms Gt Ctd Ilm
Chl Ms Gt Rt
Chl Ms Gt Ilm Rt
Chl Ms Gt Ilm
Chl Ms Ilm Rt
Chl Ms Ilm
Chl Ms Bt Gt Ilm
Chl Ms Bt Ilm
Chl Ms Pl Ilm
Chl Ms Bt Pl Ilm
Chl Ms Gt St Ilm
Chl Ms Gt Ilm
Chl Ms Bt Gt St Ilm
Chl Ms Bt Pl St Ilm
Ms Bt Gt St Ilm
Ms Bt Pl Gt St Ilm
Ms Bt Pl St Ilm
Ms Bt Pl Sill Ilm
Ms Bt Pl St Sill Ilm
Grt in
St in
Bt in
P (kbar)
T (°C)
XSps XAlm Grt XMg
XGrs XPrp St XMg
Bt Ti (pfu)
(b)
Grt core
(c)
Grt rim & matrix
UD17
MnNCKFMASHT (+Qz +H2O)
SiO2 57.80 Al2O3 22.57 FeO 7.52 MgO 1.46 CaO 0.50 Na2O 0.26 K2O 4.54 TiO2 0.90 MnO 0.06
(d)
Ms Chl Grt Ctd Rt
Ms Chl Grt Ctd Ilm Rt
Ms Chl Grt Ctd Ilm
Ms Chl Ctd Rt
Ms Chl Ctd Ilm Rt
Ms Chl Ctd St Ilm
Ms Chl St Ilm
Ms Chl Ctd St Ilm Rt
Ms Chl Bt St Ilm
Ms Chl Grt St Ctd Ilm
Ms Chl Grt St Ilm
Ms Chl Bt Grt St Ilm
Ms Bt Grt St Ilm
Pl Ms Bt Grt St Ilm
Pl Ms Bt St Ilm
Pl Ms Chl Bt Grt St Ilm
Pl Ms Chl Bt St Ilm
Pl Ms Bt Grt Ilm Sil
Pl Ms Bt St Ilm Sil
Chl out
(e)
Grt core
(f)
Grt rim & matrix

Figure 7.

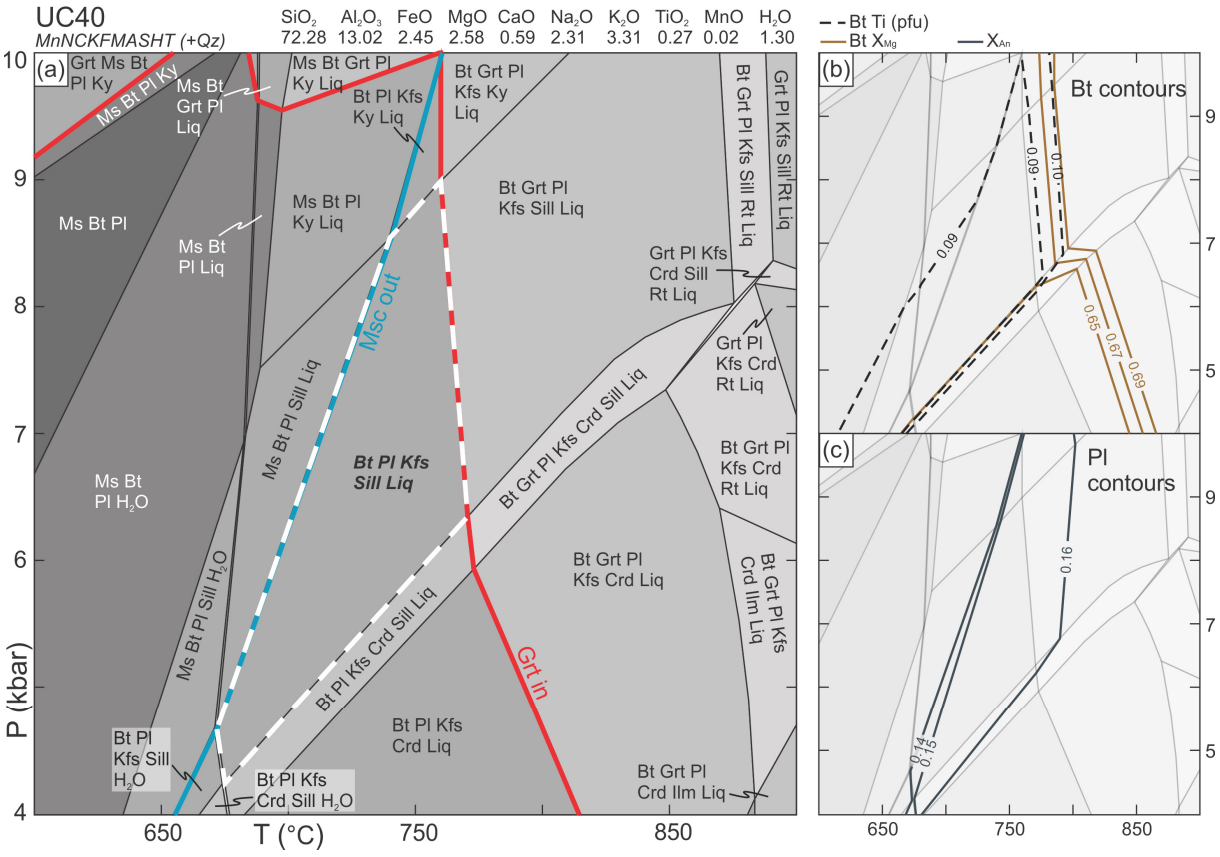
UC40
MnNCKFMASHT (+Qz)
SiO2 72.28 Al2O3 13.02 FeO 2.45 MgO 2.58 CaO 0.59 Na2O 2.31 K2O 3.31 TiO2 0.27 MnO 0.02 H2O 1.30
(a)
Grt Ms Bt Pl Ky
Ms Bt Pl Ky
Ms Bt Grt Pl Liq
Ms Bt Grt Pl Ky Liq
Bt Pl Kfs Ky Liq
Bt Grt Pl Kfs Ky Liq
Ms Bt Pl
Ms Bt Pl Liq
Ms Bt Pl Ky Liq
Bt Grt Pl Kfs Sill Liq
Bt Grt Pl Kfs Sill Rt Liq
Grt Pl Kfs Sill Rt Liq
Grt Pl Kfs Crd Sill Rt Liq
Msc out
Ms Bt Pl Sill Liq
Bt Pl Kfs Sill Liq
Grt Pl Kfs Crd Rt Liq
Bt Grt Pl Kfs Crd Sill Liq
Ms Bt Pl H2O
Bt Grt Pl Kfs Crd Rt Liq
Ms Bt Pl Sill H2O
Bt Grt Pl Kfs Crd Liq
Bt Grt Pl Kfs Crd Ilm Liq
Bt Pl Kfs Crd Sill Liq
Grt in
Bt Pl Kfs Crd Liq
Bt Pl Kfs Sill H2O
Bt Pl Kfs Crd Sill H2O
Bt Grt Pl Crd Ilm Liq
P (kbar)
T (°C)
650
750
850
10
9
8
7
6
5
4
(b)
Bt Ti (pfu)
Bt XMg
XAn
Bt contours
0.09
0.10
0.09
0.65
0.67
0.69
(c)
Pl contours
0.16
0.14
0.15

Figure 8.

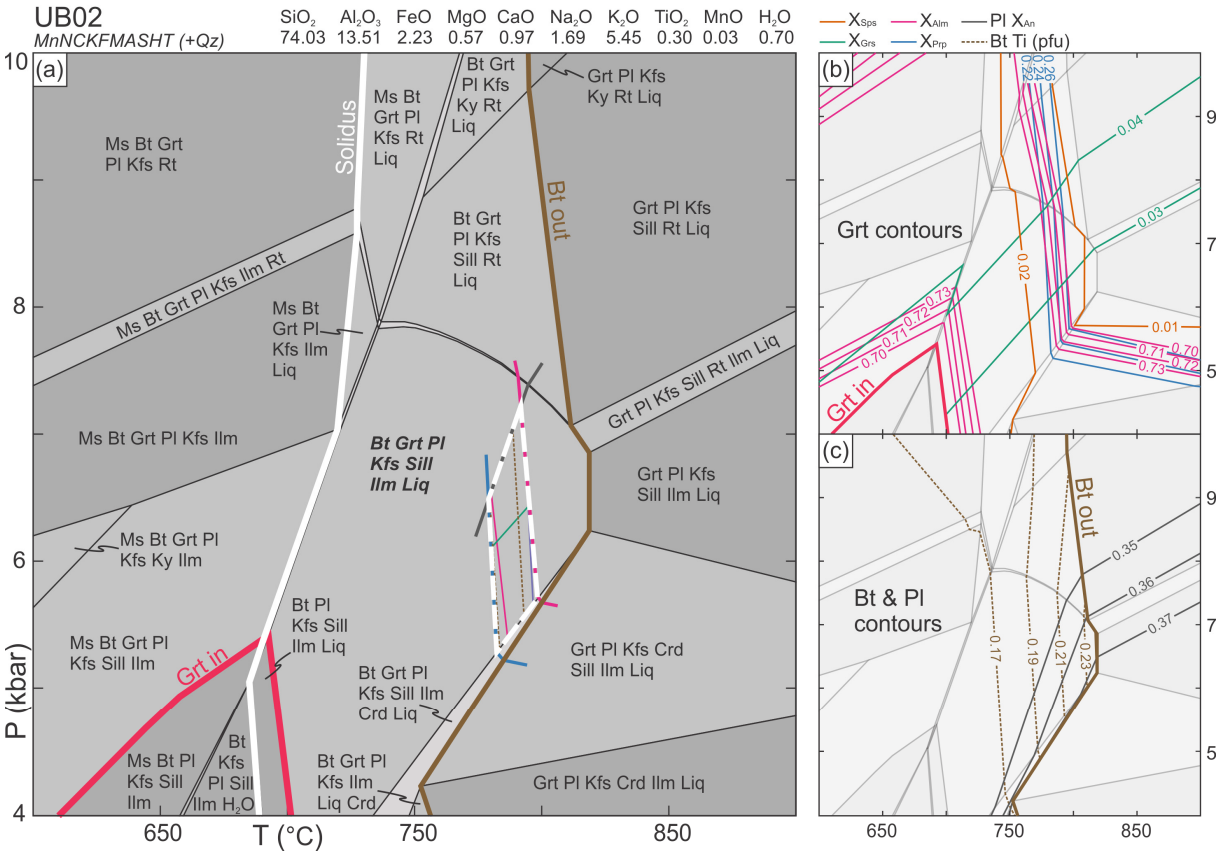
UB02
MnNCKFMASHT (+Qz)
SiO2 74.03 Al2O3 13.51 FeO 2.23 MgO 0.57 CaO 0.97 Na2O 1.69 K2O 5.45 TiO2 0.30 MnO 0.03 H2O 0.70
(a)
Ms Bt Grt Pl Kfs Rt
Solidus
Ms Bt Grt Pl Kfs Rt Liq
Bt Grt Pl Kfs Ky Rt Liq
Grt Pl Kfs Ky Rt Liq
Bt out
Bt Grt Pl Kfs Sill Rt Liq
Grt Pl Kfs Sill Rt Liq
Ms Bt Grt Pl Kfs Ilm Rt
Ms Bt Grt Pl Kfs Ilm Liq
Grt Pl Kfs Sill Rt Ilm Liq
Ms Bt Grt Pl Kfs Ilm
Bt Grt Pl Kfs Sill Ilm Liq
Grt Pl Kfs Sill Ilm Liq
Ms Bt Grt Pl Kfs Ky Ilm
Bt Pl Kfs Sill Ilm Liq
Ms Bt Grt Pl Kfs Sill Ilm
Grt in
Bt Grt Pl Kfs Sill Ilm Crd Liq
Grt Pl Kfs Crd Sill Ilm Liq
Bt Kfs Pl Sill Ilm H2O
Ms Bt Pl Kfs Sill Ilm
Bt Grt Pl Kfs Ilm Liq Crd
Grt Pl Kfs Crd Ilm Liq
P (kbar)
T (°C)
650
750
850
10
8
6
4
(b)
XSps XAlm Pl XAn
XGrs XPrp Bt Ti (pfu)
Grt contours
Grt in
0.04
0.03
0.02
0.01
0.70
0.71
0.72
0.73
(c)
Bt & Pl contours
Bt out
0.35
0.36
0.37
0.17
0.19
0.21
0.23
9
7
5

Figure 9.

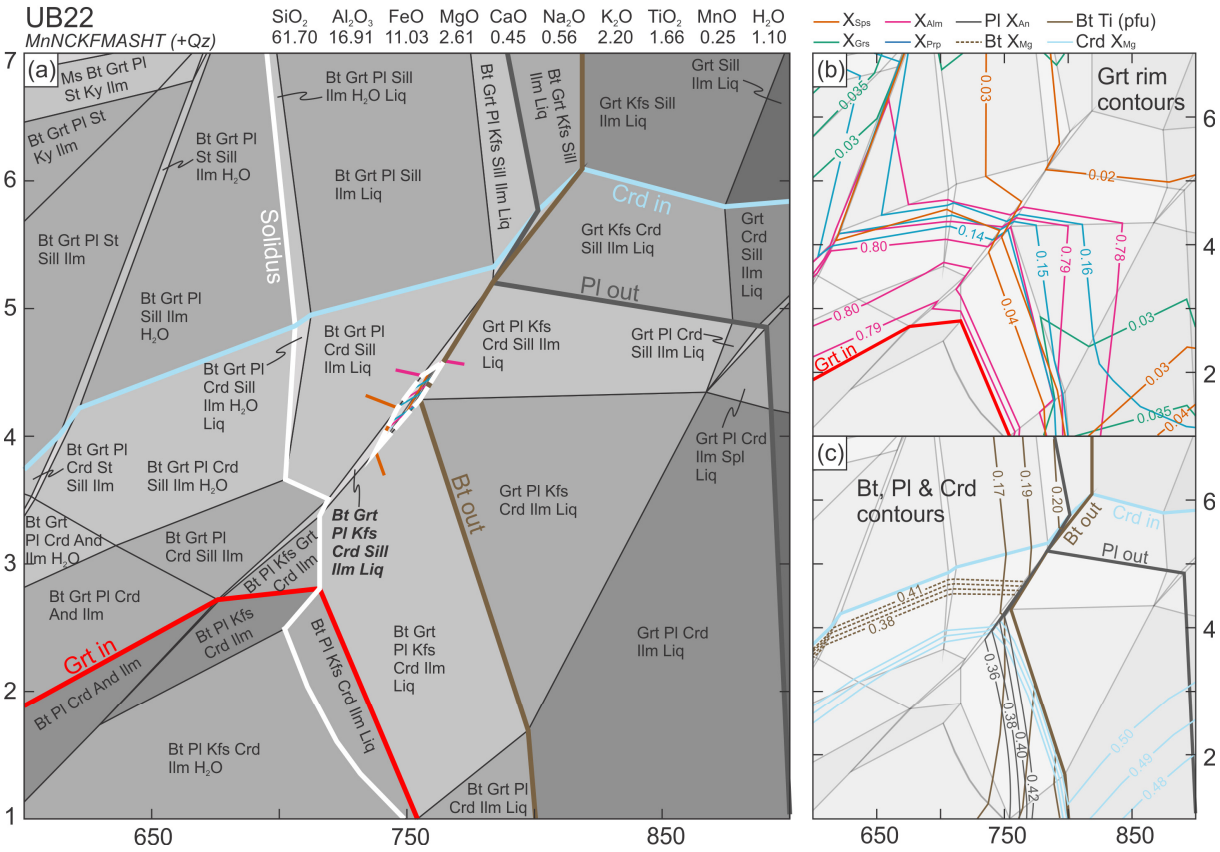
UB22
MnNCKFMASHT (+Qz)
SiO2 61.70 Al2O3 16.91 FeO 11.03 MgO 2.61 CaO 0.45 Na2O 0.56 K2O 2.20 TiO2 1.66 MnO 0.25 H2O 1.10
(a)
(b)
(c)
Grt rim contours
Bt, Pl & Crd contours
Solidus
Crd in
Pl out
Grt in
Bt out
Bt Grt Pl Kfs Crd Sill Ilm Liq
650
750
850

Figure 10.

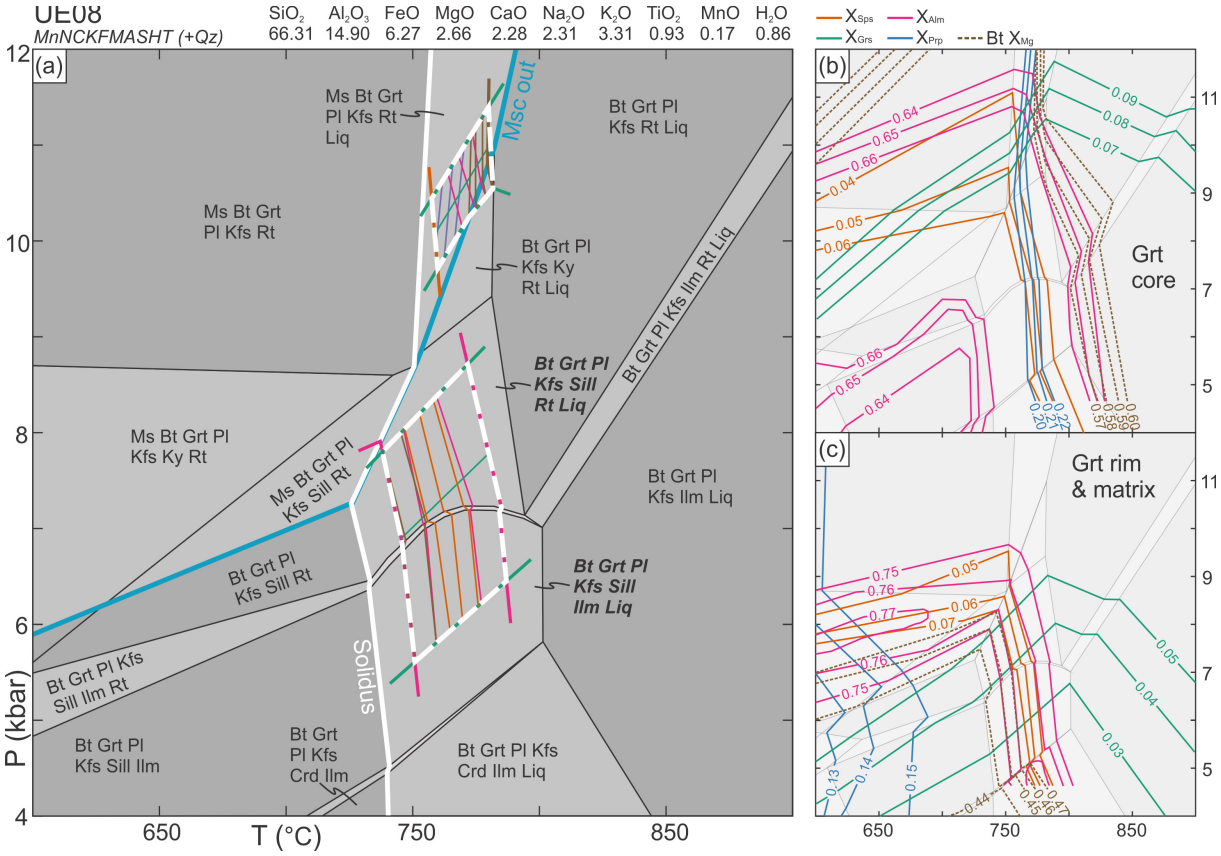
UE08
MnNCKFMASHT (+Qz)
SiO2 66.31
Al2O3 14.90
FeO 6.27
MgO 2.66
CaO 2.28
Na2O 2.31
K2O 3.31
TiO2 0.93
MnO 0.17
H2O 0.86
(a)
Ms Bt Grt Pl Kfs Rt Liq
Msc out
Bt Grt Pl Kfs Rt Liq
Ms Bt Grt Pl Kfs Rt
Bt Grt Pl Kfs Ky Rt Liq
Bt Grt Pl Kfs Sill Rt Liq
Bt Grt Pl Kfs Ilm Rt Liq
Ms Bt Grt Pl Kfs Ky Rt
Ms Bt Grt Pl Kfs Sill Rt
Bt Grt Pl Kfs Ilm Liq
Bt Grt Pl Kfs Sill Rt
Bt Grt Pl Kfs Sill Ilm Liq
Bt Grt Pl Kfs Sill Ilm Rt
Solidus
Bt Grt Pl Kfs Sill Ilm
Bt Grt Pl Kfs Crd Ilm
Bt Grt Pl Kfs Crd Ilm Liq
P (kbar)
T (°C)
XSps XAlm
XGrs XPrp
Bt XMg
(b)
Grt core
(c)
Grt rim & matrix

Figure 11.

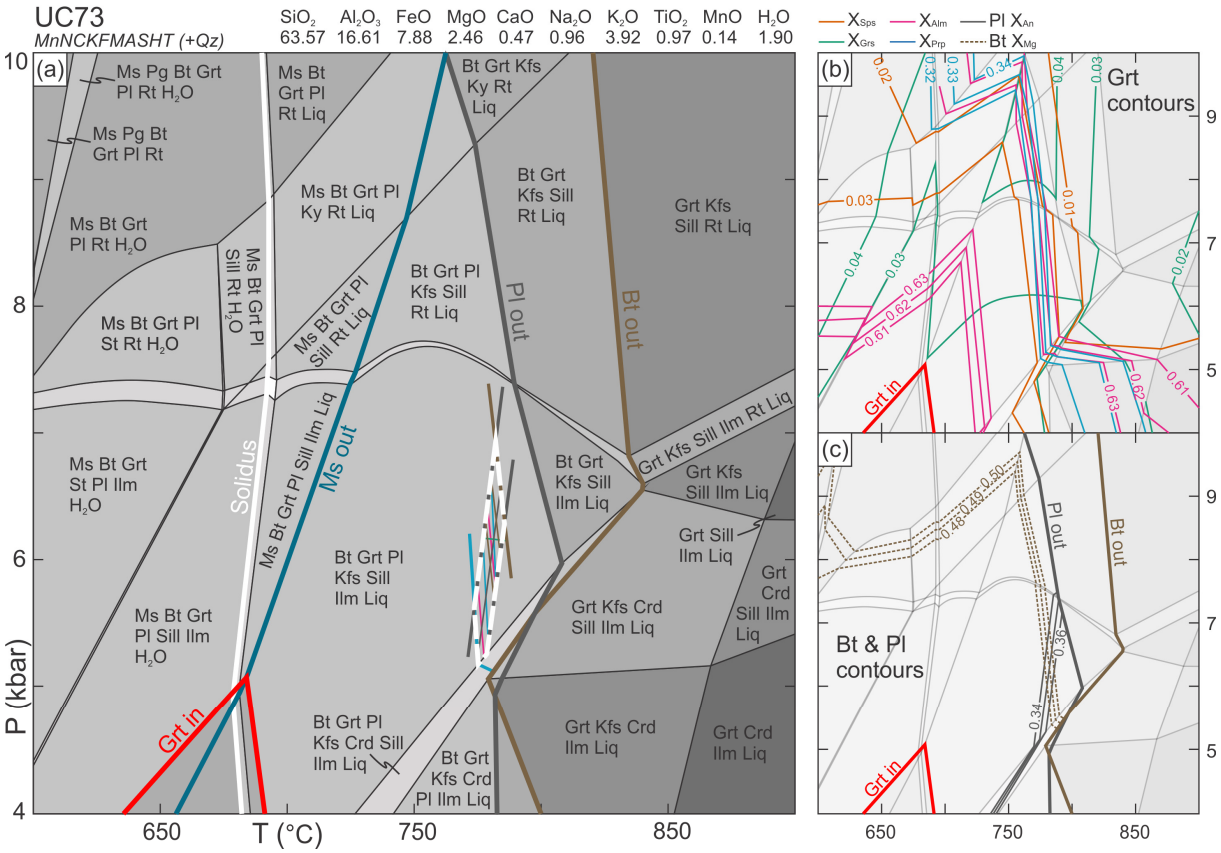
UC73
MnNCKFMASHT (+Qz)
SiO2 Al2O3 FeO MgO CaO Na2O K2O TiO2 MnO H2O
63.57 16.61 7.88 2.46 0.47 0.96 3.92 0.97 0.14 1.90
(a)
Ms Pg Bt Grt Pl Rt H2O
Ms Pg Bt Grt Pl Rt
Ms Bt Grt Pl Rt H2O
Ms Bt Grt Pl St Rt H2O
Ms Bt Grt St Pl Ilm H2O
Ms Bt Grt Pl Sill Ilm H2O
Ms Bt Grt Pl Sill Rt H2O
Ms Bt Grt Pl Rt Liq
Ms Bt Grt Pl Ky Rt Liq
Ms Bt Grt Pl Sill Rt Liq
Bt Grt Kfs Ky Rt Liq
Bt Grt Pl Kfs Sill Rt Liq
Bt Grt Kfs Sill Rt Liq
Grt Kfs Sill Rt Liq
Grt Kfs Sill Ilm Rt Liq
Bt Grt Kfs Sill Ilm Liq
Grt Kfs Sill Ilm Liq
Grt Sill Ilm Liq
Bt Grt Pl Kfs Sill Ilm Liq
Grt Kfs Crd Sill Ilm Liq
Grt Crd Sill Ilm Liq
Bt Grt Pl Kfs Crd Sill Ilm Liq
Bt Grt Kfs Crd Pl Ilm Liq
Grt Kfs Crd Ilm Liq
Grt Crd Ilm Liq
Solidus
Ms out
Pl out
Bt out
Grt in
P (kbar)
T (°C)
650
750
850
4
6
8
10
(b)
Grt contours
Grt in
(c)
Bt & Pl contours
Pl out
Bt out
Grt in
XSps XAlm Pl XAn
XGrs XPrp Bt XMg

Figure 12.

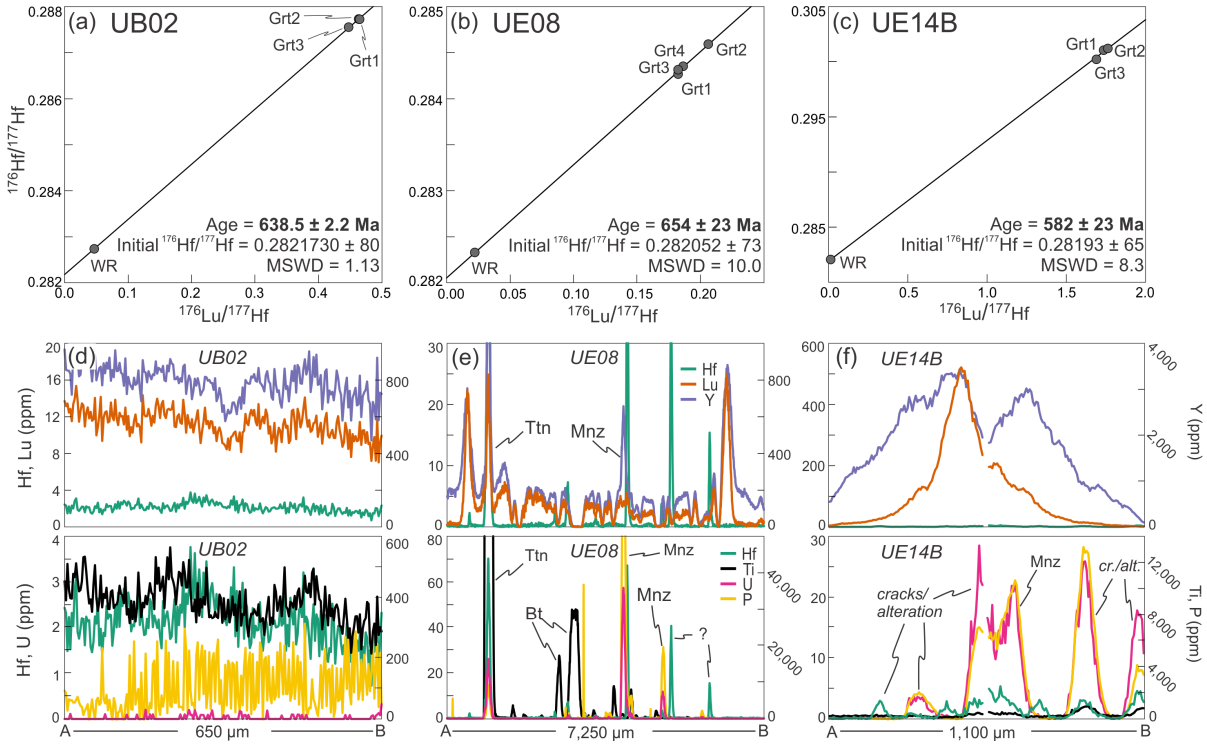
(a) UB02
Grt2
Grt3
Grt1
WR
Age = 638.5 ± 2.2 Ma
Initial 176Hf/177Hf = 0.2821730 ± 80
MSWD = 1.13
(b) UE08
Grt4
Grt3
Grt2
Grt1
WR
Age = 654 ± 23 Ma
Initial 176Hf/177Hf = 0.282052 ± 73
MSWD = 10.0
(c) UE14B
Grt1
Grt2
Grt3
WR
Age = 582 ± 23 Ma
Initial 176Hf/177Hf = 0.28193 ± 65
MSWD = 8.3
176Hf/177Hf
176Lu/177Hf
(d) UB02
(e) UE08
(f) UE14B
Hf, Lu (ppm)
Y (ppm)
Hf
Lu
Y
Ttn
Mnz
Hf, U (ppm)
Ti, P (ppm)
Hf
Ti
U
P
Bt
?
cracks/
alteration
cr./alt.
A
650 µm
B
7,250 µm
1,100 µm

Figure 13.

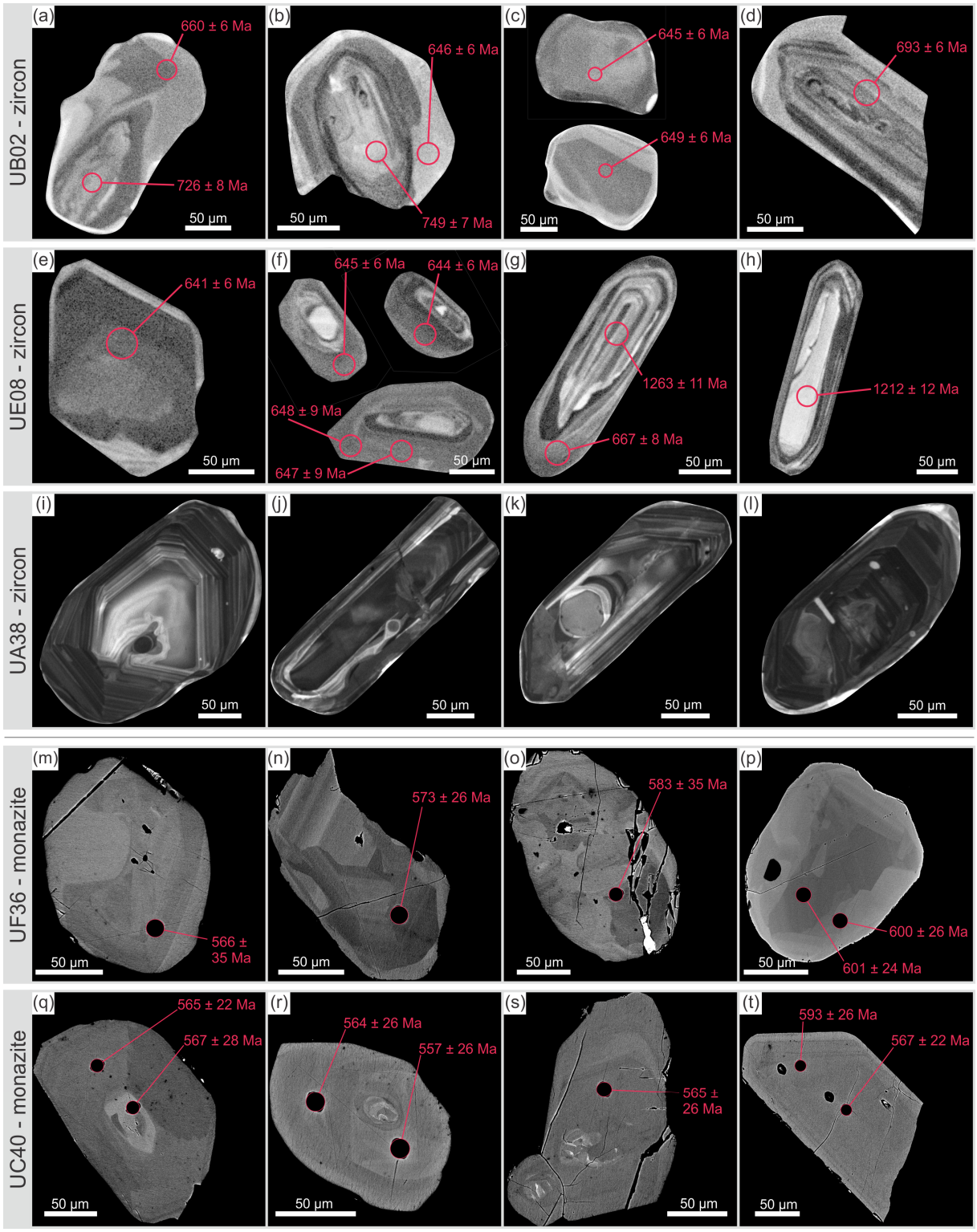
UB02 - zircon
(a)
660 ± 6 Ma
726 ± 8 Ma
50 µm
(b)
646 ± 6 Ma
749 ± 7 Ma
50 µm
(c)
645 ± 6 Ma
649 ± 6 Ma
50 µm
(d)
693 ± 6 Ma
50 µm
UE08 - zircon
(e)
641 ± 6 Ma
50 µm
(f)
645 ± 6 Ma
644 ± 6 Ma
648 ± 9 Ma
647 ± 9 Ma
50 µm
(g)
1263 ± 11 Ma
667 ± 8 Ma
50 µm
(h)
1212 ± 12 Ma
50 µm
UA38 - zircon
(i)
50 µm
(j)
50 µm
(k)
50 µm
(l)
50 µm
UF36 - monazite
(m)
566 ± 35 Ma
50 µm
(n)
573 ± 26 Ma
50 µm
(o)
583 ± 35 Ma
50 µm
(p)
600 ± 26 Ma
601 ± 24 Ma
50 µm
UC40 - monazite
(q)
565 ± 22 Ma
567 ± 28 Ma
50 µm
(r)
564 ± 26 Ma
557 ± 26 Ma
50 µm
(s)
565 ± 26 Ma
50 µm
(t)
593 ± 26 Ma
567 ± 22 Ma
50 µm

Figure 14.

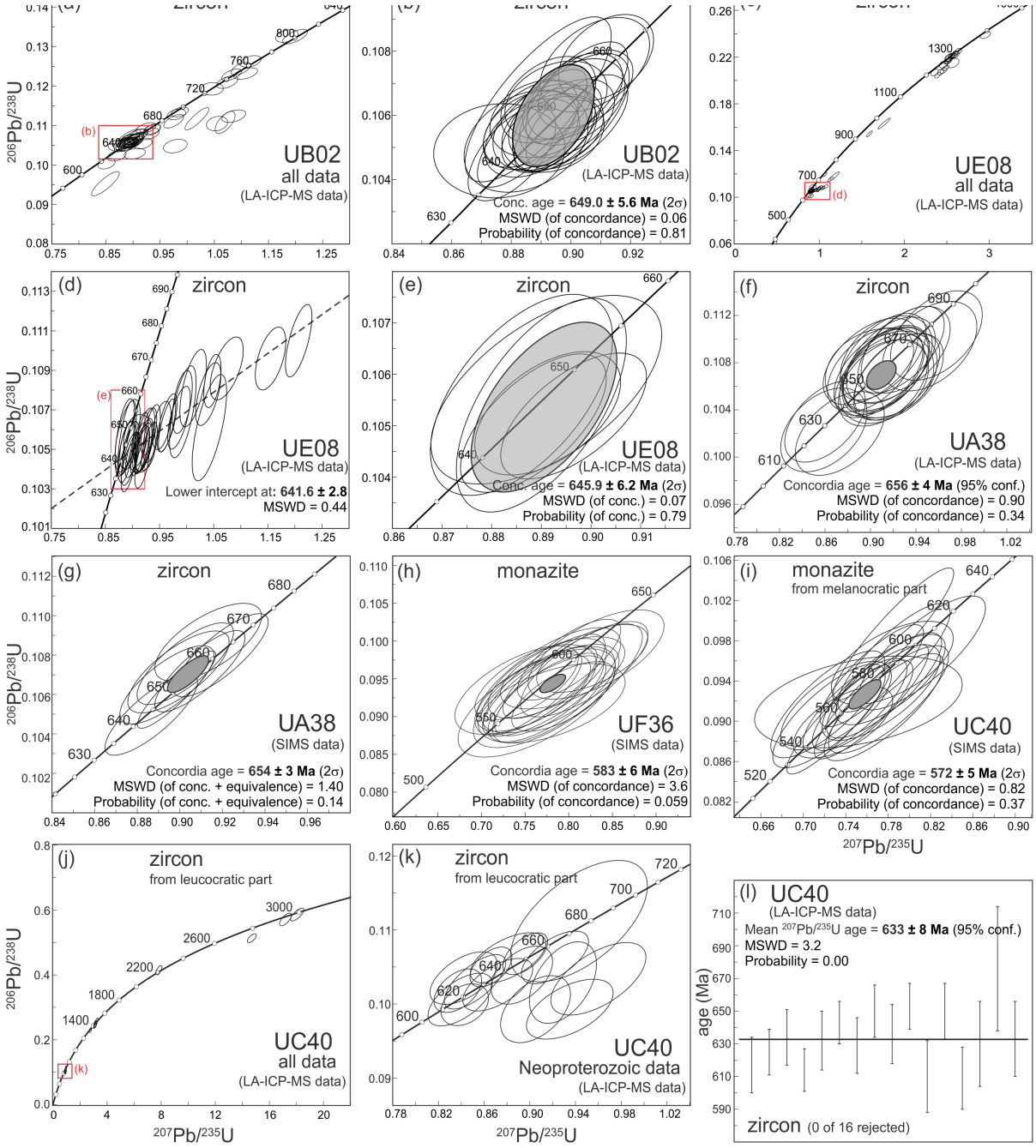
(a)
zircon
UB02
all data
(LA-ICP-MS data)
(b)
UB02
(LA-ICP-MS data)
Conc. age = 649.0 ± 5.6 Ma (2σ)
MSWD (of concordance) = 0.06
Probability (of concordance) = 0.81
UE08
all data
(LA-ICP-MS data)
(d)
zircon
UE08
(LA-ICP-MS data)
Lower intercept at: 641.6 ± 2.8
MSWD = 0.44
(e)
zircon
UE08
(LA-ICP-MS data)
Conc. age = 645.9 ± 6.2 Ma (2σ)
MSWD (of conc.) = 0.07
Probability (of conc.) = 0.79
(f)
zircon
UA38
(LA-ICP-MS data)
Concordia age = 656 ± 4 Ma (95% conf.)
MSWD (of concordance) = 0.90
Probability (of concordance) = 0.34
(g)
zircon
UA38
(SIMS data)
Concordia age = 654 ± 3 Ma (2σ)
MSWD (of conc. + equivalence) = 1.40
Probability (of conc. + equivalence) = 0.14
(h)
monazite
UF36
(SIMS data)
Concordia age = 583 ± 6 Ma (2σ)
MSWD (of concordance) = 3.6
Probability (of concordance) = 0.059
(i)
monazite
from melanocratic part
UC40
(SIMS data)
Concordia age = 572 ± 5 Ma (2σ)
MSWD (of concordance) = 0.82
Probability (of concordance) = 0.37
(j)
zircon
from leucocratic part
UC40
all data
(LA-ICP-MS data)
(k)
zircon
from leucocratic part
UC40
Neoproterozoic data
(LA-ICP-MS data)
(l) UC40
(LA-ICP-MS data)
Mean 207Pb/235U age = 633 ± 8 Ma (95% conf.)
MSWD = 3.2
Probability = 0.00
zircon (0 of 16 rejected)
206Pb/238U
207Pb/235U
age (Ma)

Figure 15.

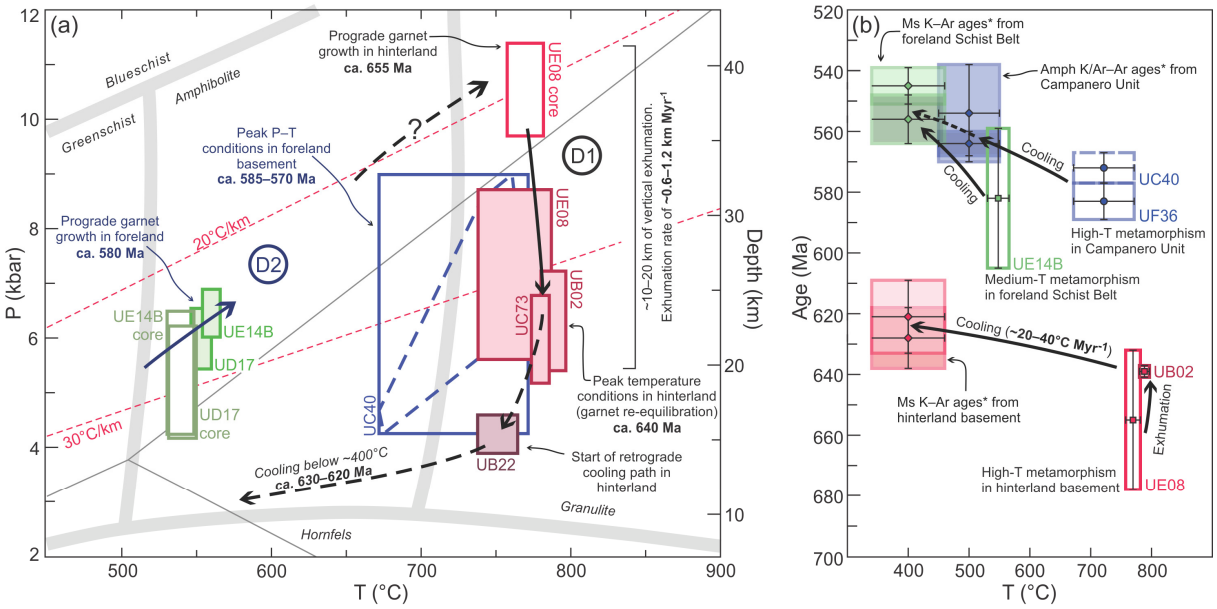
(a)
Blueschist
Amphibolite
Greenschist
Prograde garnet growth in hinterland
ca. 655 Ma
UE08 core
Peak P–T conditions in foreland basement
ca. 585–570 Ma
D1
UE08
UC73
UB02
~10–20 km of vertical exhumation.
Exhumation rate of ~0.6–1.2 km Myr⁻¹
Prograde garnet growth in foreland
ca. 580 Ma
20°C/km
D2
UE14B core
UE14B
UD17
UD17 core
30°C/km
UC40
Peak temperature conditions in hinterland (garnet re-equilibration)
ca. 640 Ma
Start of retrograde cooling path in hinterland
UB22
Cooling below ~400°C
ca. 630–620 Ma
Granulite
Hornfels
P (kbar)
T (°C)
Depth (km)
(b)
Ms K–Ar ages* from foreland Schist Belt
Amph K/Ar–Ar ages* from Campanero Unit
Cooling
Cooling
UC40
UF36
High-T metamorphism in Campanero Unit
UE14B
Medium-T metamorphism in foreland Schist Belt
Cooling (~20–40°C Myr⁻¹)
UB02
Exhumation
Ms K–Ar ages* from hinterland basement
High-T metamorphism in hinterland basement
UE08
Age (Ma)
T (°C)

Figure 16.

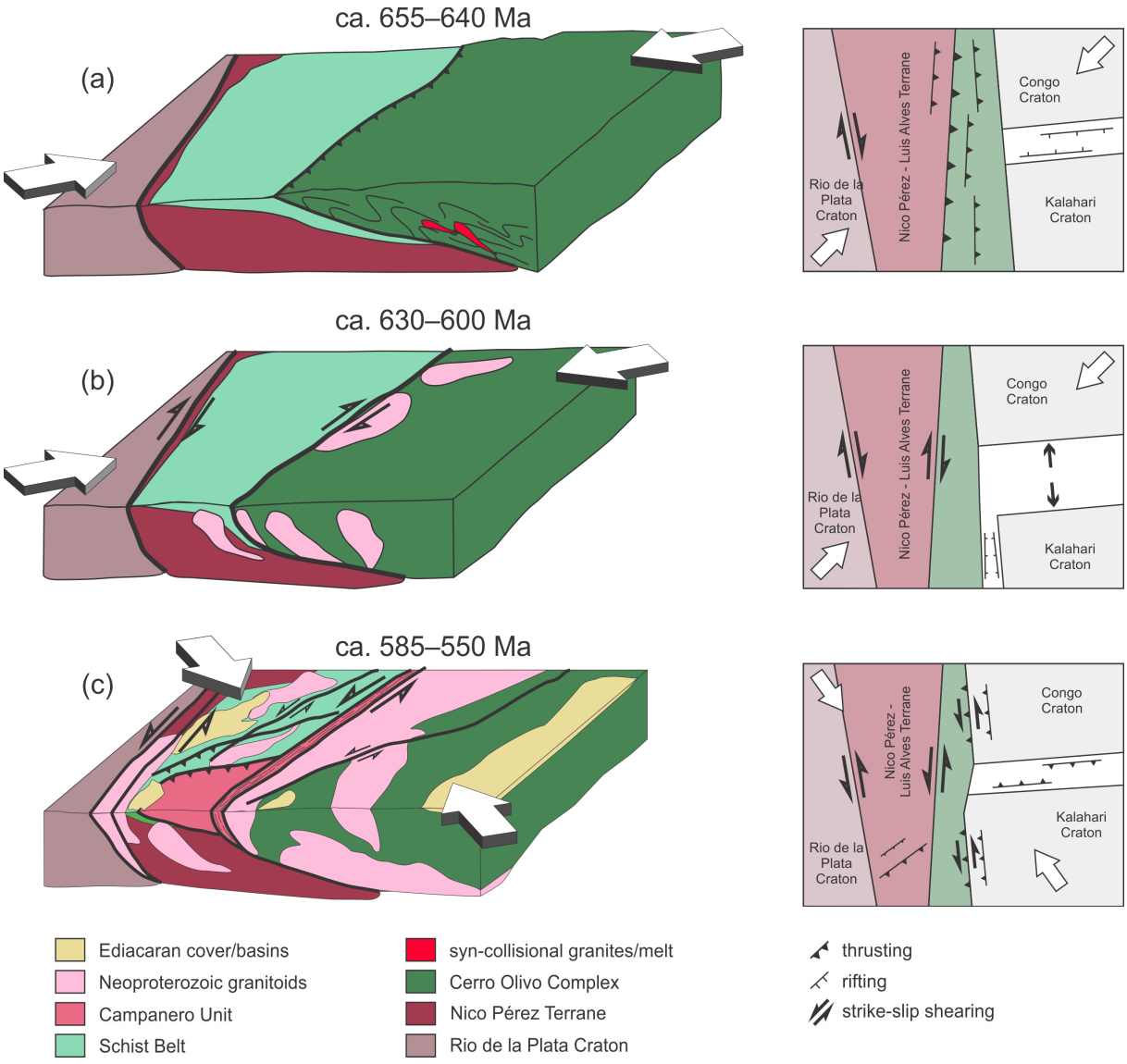
ca. 655–640 Ma
(a)
Rio de la Plata Craton
Nico Pérez - Luis Alves Terrane
Congo Craton
Kalahari Craton
ca. 630–600 Ma
(b)
Rio de la Plata Craton
Nico Pérez - Luis Alves Terrane
Congo Craton
Kalahari Craton
ca. 585–550 Ma
(c)
Rio de la Plata Craton
Nico Pérez - Luis Alves Terrane
Congo Craton
Kalahari Craton
Ediacaran cover/basins
Neoproterozoic granitoids
Campanero Unit
Schist Belt
syn-collisional granites/melt
Cerro Olivo Complex
Nico Pérez Terrane
Rio de la Plata Craton
thrusting
rifting
strike-slip shearing

Supporting Information

Text S1 – Analytical Methods

Whole rock major element analysis:

Whole rock major element analysis was conducted by lithium borate fusion inductively coupled plasma emission spectroscopy (ICP ES) at Bureau Veritas Mineral Laboratories in Vancouver, Canada, and by atomic absorption spectroscopy (AAS) and titration at the Czech Geological Survey, Prague, Czech Republic.

Mineral major element analysis:

Mineral major element compositions were analysed using an electron microprobe CAMECA SX100 at the Faculty of Natural Sciences, Masaryk University, Czech Republic, in joint service with the Czech Geological Service. A 15 kV accelerating voltage and 20 nA probe current were applied to garnet, spinel, rutile and ilmenite analyses, using a spot size of 2μm. A 15kV accelerating voltage and 10nA probe current were applied to biotite, muscovite, chlorite and feldspar analyses, using a spot size of 5 μm.

Lu─Hf and Sm─Nd garnet dating and trace element analysis:

Garnet─whole-rock Lu─Hf geochronology and trace element analysis was conducted at the Institute of Geological Sciences, Polish Academy of Sciences, Kraków Research Centre. Sample preparation and isotopic analysis follow the methods from Anczkiewicz et al. (2004). Isotopic ratios were measured using ICP-MS Neptune by Thermo Scientific. Rim-to-rim trace element profiles were analysed from thin sections by Laser Ablation ICP-MS (Woodhead et al., 2007) across individual garnet grains. Analysis was conducted using an excimer laser-ablation system *RESOlution M50* by Resonetics coupled with quadrupole ICP-MS *XSeriesII* by Thermo, with further details on the setup found in Anczkiewicz et al. (2012) and references therein. The data was processed using Iolite software (Paton et al., 2011).

Monazite U─Pb dating:

Samples were chosen for monazite U─Pb dating to compliment garnet Lu─Hf ages. Thin sections were prepared and then analysed using polarized-light and scanning electron microscopy for the presence of monazite. Samples containing monazite were then crushed and milled to a grainsize of (maximum) 500μm. Milled samples were then run through a Wilfley shaking table to separate mineral phases based on density. Samples were further processed using LST and DIM heavy liquids, and a Frantz magnetic

separator. Monazite grains were individually handpicked under a binocular optical microscope, mounted in epoxy, and coated with ~30 nm of gold. Monazite grains were analysed for isotopes of U, Pb and interfering molecules on a Cameca IMS 1280 ion probe at NordSIM at the Swedish Museum of Natural History in Stockholm. The instrument parameters, analytical methods, and calibrations and corrections follow those in Whitehouse & Kamber (2005) and Kirkland et al. (2009). The instrument was operated in automated mode with a ~18 μm diameter ion beam. Measured Pb/U ratios were calibrated against reference monazite 44069 that has a TIMS age of 424.9 ± 0.4 Ma (Aleinikoff et al. 2006). Common lead corrections assumed a modern-day average terrestrial common Pb composition (Stacey & Kramers, 1975).

Zircon U─Pb dating:

Each sample was crushed to a grain size of <500 μm using first a jaw crusher and then a hammer mill. The milled samples were processed using a Wilfley table to concentrate the heavy minerals, and then dried at 40°C. Highly magnetic minerals were removed from the heavy fraction using a weak iron magnet, and the remaining magnetic minerals were removed using a Frantz Isodynamic Separator. The heavy fractions were then processed with heavy liquids sodium polytungstate (SPT) and diiodomethane (DIM) to further concentrate the heavy minerals. Zircon was then hand-picked under ethanol and transferred in ethanol to double-sided tape using a pipette. The zircon grains were then mounted in epoxy-filled blocks and polished using diamond paste to attain even surfaces for cathodoluminescence imaging and laser ablation ICP–MS analysis.

For ICP–MS analysis, samples were analysed at the Institute of Geology of the Czech Academy of Sciences, Prague, Czech Republic, using Thermo Scientific Element 2 sector field ICP–MS coupled to a 193 nm ArF excimer laser (Teledyne Cetac Analyte Excite laser). The analytical details are given in Table S4 according to the format of Horstwood et al (2016).

For SIMS analysis, samples were coated with c. 30 nm of gold and analysed for isotopes of U, Pb and interfering molecules on a Cameca IMS 1280 ion probe at the Swedish Museum of Natural History in Stockholm (NordSIM facility). The instrument parameters, analytical method, calibration, and correction procedures were similar to those described by Whitehouse *et al.* (1999), Whitehouse & Kamber (2005), and Jeon and Whitehouse (2015). The instrument was operated in automated mode with 18 μm ion beam diameter. The measured Pb/U ratios were calibrated against the reference zircon 91500, which has an age of 1065.4 ± 0.3 Ma and U and Pb concentrations of 80 and 15 ppm, respectively (Wiedenbeck *et al.*, 1995). Common lead corrections assumed a modern-day average terrestrial common Pb composition (Stacey & Kramers, 1975).

Table S1. Representative mineral analyses and recalculated compositions (samples UD17. UE14B and UC40).

Sample	UD17						UE14B						UC40			
Mineral	Grt		Bt	St	St	Msc	Grt		Bt	St		Msc	Bt	Bt	Pl	Kfs
	core	rim					core	rim		core	rim					
wt%																
SiO_2	37.05	36.85	35.87	27.26	27.52	46.43	36.74	37.81	33.23	28.18	28.67	46.57	37.38	37.75	65.02	65.44
TiO_2	0.08	0.00	1.63	0.66	0.50	0.45	0.03	0.02	0.90	0.41	0.46	0.26	1.40	1.42	0.00	0.00
Cr_2O_3	0.02	0.01	0.06	0.04	0.04	0.02	0.00	0.00	0.02	0.03	0.04	0.00	0.01	0.00	0.00	0.40
Al_2O_3	20.89	20.81	19.72	54.50	54.59	36.61	20.65	20.95	18.60	54.76	54.23	35.56	19.62	19.30	21.73	18.65
Fe_2O_3	0.00	0.00	0.00	0.00	0.00	0.00	0.29	0.15	0.00	0.00	0.00	0.00	0.00	0.00	0.00	0.03
FeO	32.31	35.08	21.15	14.26	14.41	1.05	32.88	35.74	24.46	13.12	12.91	0.97	12.41	12.01	0.00	0.00
MnO	4.79	2.99	0.07	0.13	0.20	0.02	4.54	1.78	0.01	0.04	0.03	0.00	0.11	0.08	0.00	0.00
NiO	0.00	0.00	0.00	0.04	0.06	0.00	0.00	0.00	0.00	0.00	0.00	0.00	0.04	0.00	0.00	0.00
MgO	1.49	1.75	6.28	0.97	0.81	0.43	1.53	1.80	7.61	1.18	0.84	0.58	13.81	14.25	0.00	0.00
CaO	3.44	2.15	0.05	0.01	0.00	0.04	2.71	3.36	0.08	0.03	0.04	0.00	0.03	0.01	3.14	0.04
Na_2O	0.00	0.00	0.12	0.00	0.02	0.73	0.05	0.03	0.12	0.00	0.01	1.05	0.37	0.27	9.65	1.65
K_2O	0.01	0.01	8.62	0.00	0.01	9.93	0.02	0.01	5.41	0.00	0.03	9.86	9.68	9.53	0.27	14.70
Total	100.08	99.65	93.55	97.87	98.15	95.69	99.43	101.64	90.43	97.74	97.25	94.85	94.87	94.61	99.80	100.91
No. Ox.																
Si	3.00	3.00	2.91	3.87	3.90	3.08	3.00	3.01	2.80	3.99	4.09	3.11	2.83	2.86	2.88	2.99
Ti	0.01	0.00	0.10	0.07	0.05	0.02	0.00	0.00	0.06	0.04	0.05	0.01	0.08	0.08	0.00	0.00
Cr	0.00	0.00	0.00	0.00	0.00	0.00	0.00	0.00	0.00	0.00	0.00	0.00	0.00	0.00	0.00	0.01
Al	2.00	2.00	1.88	9.13	9.12	2.86	1.99	1.97	1.85	9.15	9.12	2.80	1.75	1.72	1.13	1.00
Fe^{3+}	0.00	0.00	0.00	0.00	0.00	0.00	0.02	0.01	0.00	0.00	0.00	0.00	0.00	0.00	0.00	0.00
Fe^{2+}	2.19	2.39	1.43	1.69	1.71	0.06	2.25	2.38	1.72	1.55	1.54	0.05	0.79	0.76	0.00	0.00
Mn	0.33	0.21	0.00	0.02	0.02	0.00	0.31	0.12	0.00	0.00	0.00	0.00	0.01	0.00	0.00	0.00
Ni	0.00	0.00	0.00	0.00	0.01	0.00	0.00	0.00	0.00	0.00	0.00	0.00	0.00	0.00	0.00	0.00
Mg	0.18	0.21	0.76	0.21	0.17	0.04	0.19	0.21	0.96	0.25	0.18	0.06	1.56	1.61	0.00	0.00
Ca	0.30	0.19	0.00	0.00	0.00	0.00	0.24	0.29	0.01	0.00	0.01	0.00	0.00	0.00	0.15	0.00
Na	0.00	0.00	0.02	0.00	0.00	0.09	0.01	0.01	0.02	0.00	0.00	0.14	0.05	0.04	0.83	0.15
K	0.00	0.00	0.89	0.00	0.00	0.84	0.00	0.00	0.58	0.00	0.01	0.84	0.93	0.92	0.02	0.86
Total	8.00	8.00	8.00	15.00	15.00	7.00	8.00	8.00	8.00	15.00	15.00	7.00	8.00	8.00	5.00	5.00
X_{Sps}	0.11	0.07					0.10	0.04								
X_{Alm}	0.73	0.80					0.75	0.79								
X_{Prp}	0.06	0.07					0.06	0.07								
X_{Grs}	0.10	0.06					0.08	0.10								
X_{Mg}	0.08	0.08	0.35	0.11	0.09		0.08	0.08	0.36	0.14	0.10		0.66	0.68		
X_{An}															0.15	

Table S2. Representative mineral analyses and recalculated compositions (samples UE08, UC73 and UB02).

Sample	UE08						UC73							UB02					
Mineral	Grt		Bt	Bt	Pl	Pl	Grt		Bt			Pl	Kfs	Grt		Bt	Bt	Pl	Kfs
	core	rim	Grt incl.	matrix	Grt Incl.	matrix	core	rim	Grt incl.	core	rim			core	rim				
wt%																			
SiO_2	38.28	37.92	37.07	35.92	57.34	60.51	38.86	38.93	37.03	36.99	36.14	60.26	65.36	38.04	37.90	37.49	38.21	58.62	64.24
TiO_2	0.03	0.01	4.42	5.31	0.00	0.00	0.03	0.10	6.56	5.07	4.95	0.00	0.00	0.05	0.04	5.29	2.96	0.05	0.04
Cr_2O_3	0.07	0.04	0.06	0.08			0.01	0.03	0.14	0.13	0.15	0.02	0.32	0.00	0.00	0.00	0.00	0.02	0.00
Al_2O_3	21.47	21.16	16.87	18.91	26.90	25.42	21.93	21.86	17.21	16.90	16.92	25.37	19.06	21.42	21.54	15.50	15.46	25.78	18.74
Fe_2O_3	0.00	0.00	0.00	0.00	0.00	0.00	0.58	0.34	0.00	0.00	0.00	0.00	0.01	0.79	0.00	0.00	0.00	0.04	0.05
FeO	29.71	34.22	16.02	18.27	0.00	0.00	27.95	29.01	11.70	14.62	18.03	0.00	0.00	32.08	32.83	15.56	13.05	0.00	0.00
MnO	2.21	2.58	0.07	0.07	0.03	0.00	0.64	0.75	0.01	0.02	0.08	0.00	0.00	0.63	0.68	0.01	0.00	0.02	0.00
NiO	0.00	0.00	0.00	0.00			0.00	0.00	0.01	0.06	0.03	0.00	0.00	0.00	0.00	0.00	0.00	0.00	0.00
MgO	5.51	3.43	12.58	8.56	0.02	0.00	8.27	8.54	13.16	12.15	9.62	0.00	0.00	6.54	5.66	11.62	14.44	0.00	0.01
CaO	2.99	1.39	0.03	0.03	9.57	7.22	2.45	1.27	0.00	0.02	0.00	7.31	0.18	0.91	1.00	0.01	0.07	7.61	0.23
Na_2O	0.03	0.02	0.25	0.25	6.09	7.60	0.00	0.00	0.33	0.19	0.23	7.33	2.15	0.00	0.00	0.11	0.10	7.37	2.47
K_2O	0.01	0.00	9.43	9.79	0.35	0.32	0.01	0.02	9.44	9.68	9.51	0.22	13.86	0.00	0.00	9.90	9.42	0.18	13.39
Total	100.31	100.78	96.79	97.19	100.30	101.07	100.75	100.85	95.60	95.83	95.66	100.49	100.93	100.45	99.65	95.50	93.71	99.69	99.17
No. Ox.																			
Si	3.01	3.02	2.82	2.78	2.57	2.67	2.99	2.99	2.84	2.85	2.83	2.68	2.97	2.98	3.01	2.91	2.96	2.62	2.96
Ti	0.00	0.00	0.25	0.31	0.00	0.00	0.00	0.01	0.38	0.29	0.29	0.00	0.00	0.00	0.00	0.31	0.17	0.00	0.00
Cr	0.00	0.00	0.00	0.01			0.00	0.00	0.01	0.01	0.01	0.00	0.01	0.00	0.00	0.00	0.00	0.00	0.00
Al	1.99	1.99	1.51	1.72	1.42	1.32	1.99	1.98	1.55	1.53	1.56	1.33	1.02	1.98	2.01	1.42	1.41	1.36	1.02
Fe^{3+}	0.00	0.00	0.00	0.00	0.00	0.00	0.03	0.02	0.00	0.00	0.00	0.00	0.00	0.05	0.00	0.00	0.00	0.00	0.00
Fe^{2+}	1.95	2.28	1.02	1.18	0.00	0.00	1.80	1.86	0.75	0.94	1.18	0.00	0.00	2.10	2.18	1.01	0.84	0.00	0.00
Mn	0.15	0.17	0.00	0.00	0.00	0.00	0.04	0.05	0.00	0.00	0.01	0.00	0.00	0.04	0.05	0.00	0.00	0.00	0.00
Ni	0.00	0.00	0.00	0.00			0.00	0.00	0.00	0.00	0.00	0.00	0.00	0.00	0.00	0.00	0.00	0.00	0.00
Mg	0.65	0.41	1.43	0.99	0.00	0.00	0.95	0.98	1.50	1.39	1.12	0.00	0.00	0.76	0.67	1.35	1.67	0.00	0.00
Ca	0.25	0.12	0.00	0.00	0.46	0.34	0.20	0.10	0.00	0.00	0.00	0.35	0.01	0.08	0.08	0.00	0.01	0.36	0.01
Na	0.00	0.00	0.04	0.04	0.53	0.65	0.00	0.00	0.05	0.03	0.04	0.63	0.19	0.00	0.00	0.02	0.02	0.64	0.22
K	0.00	0.00	0.92	0.97	0.02	0.02	0.00	0.00	0.92	0.95	0.95	0.01	0.80	0.00	0.00	0.98	0.93	0.01	0.79
Total	8.00	8.00	8.00	8.00	5.00	5.00	8.00	8.00	8.00	8.00	8.00	5.00	5.00	8.00	8.00	8.00	8.00	5.00	5.00
X_{Sps}	0.05	0.06					0.01	0.02						0.01	0.02				
X_{Alm}	0.65	0.76					0.60	0.62						0.70	0.73				
X_{Prp}	0.22	0.14					0.32	0.33						0.26	0.22				
X_{Grs}	0.08	0.04					0.07	0.03						0.03	0.03				
X_{Mg}	0.25	0.15	0.58	0.46			0.35	0.34	0.67	0.60	0.49			0.27	0.24	0.57	0.66		
X_{An}					0.46	0.34						0.35						0.36	

Table S3. Representative mineral analyses and recalculated compositions (sample UB22).

Sample	UB22												
Mineral	Grt		Bt	Bt		Pl	Pl	Kfs	Kfs	Spinel	Spinel	Cordierite	Ilmenite
	core	rim	Grt incl.	core	rim					Crd zone			
wt%													
SiO_2	36.85	37.45	35.92	35.26	35.62	59.61	58.15	67.09	65.44	0.17	0.21	48.15	0.08
TiO_2	0.01	0.01	5.25	3.05	3.32	0.00	0.00	0.00	0.00	0.05	0.02	0.00	52.18
Cr_2O_3	0.03	0.03	0.07	0.24	0.23	0.00	0.00	0.00	0.00	0.30	0.69		0.11
Al_2O_3	20.95	21.08	16.73	18.90	20.01	25.93	26.13	19.18	18.88	57.37	56.21	32.13	0.00
Fe_2O_3	0.83	0.20	0.00	0.00	0.00	0.00	0.00	0.00	0.00	1.59	1.38		0.99
FeO	36.12	35.37	19.77	20.13	19.83	0.00	0.20	0.05	0.15	32.68	32.60	11.37	46.48
MnO	1.28	1.17	0.01	0.05	0.03	0.00	0.00	0.00	0.00	0.06	0.12	0.13	0.25
NiO	0.00	0.00	0.09	0.09	0.06	0.00	0.00	0.00	0.00				0.00
MgO	2.83	3.72	8.86	7.52	7.03	0.00	0.00	0.00	0.00	3.10	2.06	6.17	0.15
CaO	1.24	1.24	0.03	0.04	0.00	7.76	8.49	0.23	0.03	0.01	0.00	0.04	0.01
Na_2O	0.00	0.00	0.11	0.22	0.20	7.44	6.39	7.44	1.24			0.17	0.00
K_2O	0.01	0.00	9.33	9.27	9.20	0.12	0.13	5.58	14.71			0.02	0.00
ZnO										4.10	5.71		
V_2O_3										0.30	0.71		
Total	100.16	100.26	96.17	94.76	95.51	100.87	99.49	99.57	100.45	99.74	99.70	98.18	100.25
No. Ox.													
Si	2.98	3.00	2.83	2.81	2.82	2.64	2.62	3.01	3.00	0.00	0.01	5.03	0.00
Ti	0.00	0.00	0.31	0.18	0.20	0.00	0.00	0.00	0.00	0.00	0.00	0.00	0.99
Cr	0.00	0.00	0.00	0.01	0.01	0.00	0.00	0.00	0.00	0.01	0.02		0.00
Al	1.99	1.99	1.55	1.77	1.87	1.35	1.39	1.01	1.02	1.94	1.92	3.96	0.00
Fe^{3+}	0.05	0.01	0.00	0.00	0.00	0.00	0.00	0.00	0.00	0.03	0.03		0.02
Fe^{2+}	2.44	2.37	1.30	1.34	1.31	0.00	0.01	0.00	0.01	0.78	0.79	0.99	0.98
Mn	0.09	0.08	0.00	0.00	0.00	0.00	0.00	0.00	0.00	0.00	0.00	0.01	0.01
Ni	0.00	0.00	0.01	0.01	0.00	0.00	0.00	0.00	0.00				0.00
Mg	0.34	0.44	1.04	0.89	0.83	0.00	0.00	0.00	0.00	0.13	0.09	0.96	0.01
Ca	0.11	0.11	0.00	0.00	0.00	0.37	0.41	0.01	0.00	0.00	0.00	0.00	0.00
Na	0.00	0.00	0.02	0.03	0.03	0.64	0.56	0.65	0.11			0.03	0.00
K	0.00	0.00	0.94	0.94	0.93	0.01	0.01	0.32	0.86			0.00	0.00
Z										0.09	0.12		
V										0.01	0.02		
Total	8.00	8.00	8.00	8.00	8.00	5.00	5.00	5.00	5.00	3.00	3.00	11.00	2.00
X_{Sps}	0.03	0.03											
X_{Alm}	0.82	0.79											
X_{Prp}	0.11	0.15											
X_{Grs}	0.04	0.04											
X_{Mg}	0.12	0.16	0.44	0.40	0.39					0.14	0.10	0.49	
X_{An}						0.36	0.42						

Table S4. Zircon LA-ICP-MS U-(Th-)Pb analytical details (template according to Horstwood et al. 2016)

Laboratory and Sample Preparation	
Laboratory name	Institute of Geology of the Czech Academy of Sciences, Prague, Czech Republic
Sample type/mineral	zircon
Sample preparation	Conventional mineral separation, 1 inch resin mount, 0.05 μm polish to finish
Imaging	CL, JEOL JXA-8530F Field Emission EPMA, Institute of Petrology and Structural Geology, Charles University in Prague
Laser ablation system	
Make, Model and type	Teledyne Cetac Analyte Excite laser
Ablation cell and volume	built-in 2- volume cell HelEx II, 100x100 mm
Laser wavelength (nm)	193 nm
Pulse width (ns)	< 4 ns
Fluence (J cm-2)	3.5 J cm-2
Repetition rate (Hz)	5 Hz
Ablation duration (s)	35 s
Spot diameter (μm)	25 μm
Sampling mode/pattern	Static spot ablation
Carrier gas	100% He + little addition N2 in the cell, Ar make-up gas combined using a Y-piece along the sample transport line to the torch. All gases and aerosole are mixed in the in-house glass signal homogenizer (design of Tunheng and Hirata, 2004) right before entering torch
Cell carrier gas flow (l min-1)	0.9 l min-1
N2 flow (ml min-1)	4.5 ml min-1
Ar make-up gas flow (l min-1)	0.66 l min-1
ICP-MS Instrument	
Make, Model and type	Thermo Scientific double-focusing magnetic sector field Element 2 HR-ICP-MS
Sample introduction	Dry ablation aerosol
RF power (W)	1200 W
Detection system	discrete dynode, dual mode secondary electron multiplier (SEM); analysis possible in 3 modes (cps-analog-both)
Masses measured (mode)	204 (cps), 206 (both), 207 (cps), 208 (cps), 232 (both), 235 (cps), 238 (both)
Integration time per peak/dwell times (ms)	204 (10 ms), 206 (15 ms), 207 (30 ms), 208 (10 ms), 232 (10 ms), 235 (20 ms), 238 (10 ms)
Total integration time per output data point (s)	~ 0.12 s (time resolution of the data)
Data Processing	
initial calculation	The accuracy of 238 mass measured in "both" mode is dependent on the correctly determined ACF (Analog Correction Factor). In order to correct for this variability, the data are pre-processed using a Python routine for decoding the Thermo Element ICPMS dat files (Hartman et al., 2017) and an in-house Excel macro. As a result, the intensities of 238 are left unchanged if measured in a counting mode and recalculated from 235U intensities (using the natural 138U/135U of 137.818) in all cases the 238U was acquired in analog mode, thus eliminating the non-linearity between pulse counting and analog detecting modes.
Gas blank	15 s on-peak zero subtracted
Calibration strategy	Plešovice used as primary reference material, 91500 and GJ1 used as secondaries/validation
Reference Material information, reference age	Plešovice (***Sláma et al. 2008***), 337 Ma (Concordia age) 91500 (Wiedenbeck et al. 1995), 1065 Ma (Concordia age)
Data processing package used/Correction for LIEF	Iolite v3.5 software (***Paton et al. 2010***) with the VizualAge utility (***Petrus and Kamber, 2012***) used for data normalisation, uncertainty propagation and export blank intensities and instrumental bias interpolated using an automatic spline function; down-hole inter-element fractionation (LIEF) corrected using an exponential function. LIEF correction assumes reference material and samples behave identically. Isoplot v4_16 (Ludwig, 2008) used for pooled age uncertainty propagation, age calculation and plotting.
Common-Pb correction, composition and uncertainty	No common-Pb correction applied to the data
Uncertainty level and propagation	Ages are quoted at 2s absolute, propagation is by quadratic addition. Reproducibility and age uncertainty of reference material are propagated where appropriate following the recommendation of ***Horstwood et al. (2016)***
Quality control/Validation	91500 – Concordia age = 1063 ± 5 Ma (2s, MSWD = 1.0, n = 30) Systematic uncertainty for propagation is 1.2% (2s).
Other information	20 s wait time between ablations.

References in Supporting Information

Aleinikoff, J.N., Schenck, W.S., Plank, M.O., Srogi, L., Fanning, C.M., Kamo, S.L. & Bosbyshell, H. 2006. Deciphering igneous and metamorphic events in high-grade rocks of the Wilmington Complex, Delaware: Morphology, cathodoluminescence and backscattered electron zoning, and SHRIMP U–Pb geochronology of zircon and monazite. Geological Society of America Bulletin, 118, 39–64.

Anczkiewicz, R., Platt, J. P., Thirlwall, M. F., & Wakabayashi, J. (2004). Franciscan subduction off to a slow start: evidence from high-precision Lu–Hf garnet ages on high grade-blocks. Earth and Planetary Science Letters, 225(1), 147–161. https://doi.org/10.1016/j.epsl.2004.06.003

Anczkiewicz, R., Thirlwall, M., Alard, O., Rogers, N. W., & Clark, C. (2012). Diffusional homogenization of light REE in garnet from the Day Nui Con Voi Massif in N-Vietnam: Implications for Sm–Nd geochronology and timing of metamorphism in the Red River shear zone. Chemical Geology, 318-319, 16–30. https://doi.org/10.1016/j.chemgeo.2012.04.024

Hartman, J., Franks, R., Gehrels, G., Hourigan, J., Wenig, P., 2017. Decoding dat files from a Thermo ElementTM ICP Mass Spectrometer. 15p. manual available online at https://github.com/jhh67/extractdat.git

Horstwood, M.S.A., Košler, J., Gehrels, G., Jackson, S.E., McLean, N.M., Paton, C., Pearson, N.J., Sircombe, K., Sylvester, P., Vermeesch, P., Bowring, J.F., Condon, D.J. and Schoene, B. (2016), Community-Derived Standards for LA-ICP-MS U-(Th-)Pb Geochronology – Uncertainty Propagation, Age Interpretation and Data Reporting. Geostand Geoanal Res, 40: 311-332.

Jeon H, Whitehouse M (2015) A critical evaluation of U–Pb calibration schemes used in SIMS zircon geochronology. Geostand Geoanal Res 39:443–452

Kirkland, C.L., Whitehouse, M.J. & Slagstad, T. 2009. Fluid-assisted zircon and monazite growth within a shear zone: a case study from Finnmark, Arctic Norway. Contributions to Mineralogy and Petrology, 158, 637–657.

Lee, J.-Y., Marti, K., Severinghaus, J. P., Kawamura, K., Yoo, H.-S., Lee, J. B., & Kim, J. S. (2006). A redetermination of the isotopic abundances of atmospheric Ar. Geochimica et Cosmochimica Acta, 70(17), 4507-4512. https://doi.org/10.1016/j.gca.2006.06.1563

Ludwig, K.R., 2008. User's manual for Isoplot 3.70: a geochronological toolkit for Microsoft Excel. Berkeley Geochronological Center, Special Publication 4, 1–76.

McDougall, I., & Harrison, T. M. (1999). Geochronology and thermochronology by the 40Ar/39Ar method. New York: Oxford University Press.

Paton, C., Hellstrom, J., Paul, B., Woodhead, J., & Hergt, J. (2011). Iolite: Freeware for the visualisation and processing of mass spectrometric data. Journal of Analytical Atomic Spectrometry, 26(12), 2508─2518. https://doi.org/10.1039/C1JA10172B

Paton, C., Woodhead, J.D., Hellstrom, J.C., Hergt, J.M., Greig, A., Maas, R., 2010. Improved laser ablation u-pb zircon geochronology through robust downhole fractionation correction. Geochemistry Geophysics Geosystems, 11.

Renne, P. R., Mundil, R., Balco, G., Min, K., & Ludwig, K. R. (2010). Joint determination of 40K decay constants and 40Ar∗/40K for the Fish Canyon sanidine standard, and improved accuracy for 40Ar/39Ar geochronology. Geochimica et Cosmochimica Acta, 74(18), 5349-5367. https://doi.org/10.1016/j.gca.2010.06.017

Sláma, J., Kosler, J., Condon, D.J., Crowley, J.L., Gerdes, A., Hanchar, J.M., Horstwood, M.S.A., Morris, G.A., Nasdala, L., Norberg, N., Schaltegger, U., Schoene, B., Tubrett, M.N., Whitehouse, M.J., 2008. Plesovice zircon – a new natural reference material for U-Pb and Hf isotopic microanalysis. Chemical Geology 249, 1–35.

Stacey JS, Kramers JD (1975) Approximation of terrestrial lead isotope evolution by a two-stage model. Earth and Planetary Science Letters 26:207–221

Tunheng, A., & Hirata, T. (2004). Development of signal smoothing device for precise elemental analysis using laser ablation-ICP-mass spectrometry. Journal of Analytical Atomic Spectrometry, 19(7), 932-934. https://www.doi.org/10.1039/B402493A

van Achterberg, E., Ryan, C., Jackson, S., & Griffin, W. (2001). Data reduction software for LA-ICP-MS. Laser Ablation ICP-MS in the Earth Science, 29, 239-243.

Whitehouse M.J., Kamber B.S. (2005) Assigning dates to thin gneissic veins in high-grade metamorphic terranes: a cautionary tale from Akilia, southwest Greenland. J Petrol 46:291–318

Whitehouse M.J., Kamber B.S., Moorbath, S. (1999) Age significance of U–Th–Pb zircon data from early Archaean rocks of west Greenland – a reassessment based on combined ion-microprobe and imaging studies. Chem Geol 160:201–224

Wiedenbeck M., Alle P., Corfu F., Griffin W.L., Meier M., Oberli F., von Quadt A., Roddick J.C., Speigel W. (1995) Three natural zircon standards for U–Th–Pb, Lu–Hf, trace-element and REE analyses. Geostandard Newslett 19:1–23

Woodhead, J. D., Hellstrom, J., Hergt, J. M., Greig, A., & Maas, R. (2007). Isotopic and Elemental Imaging of Geological Materials by Laser Ablation Inductively Coupled Plasma-Mass Spectrometry. Geostandards and Geoanalytical Research, 31(4), 331–343. https://doi.org/10.1111/j.1751-908X.2007.00104.x